Experimental and Theoretical Studies of Molecular Complexes

By

Maganthran Ganesan Govender

A Thesis Submitted to the Faculty of Science, University of Natal, Durban, in Partial Fulfilment of the Requirements for the Degree of Doctor of Philosophy

Durban, 1999

ABSTRACT

The binary complexes comprising the molecules hydrogen fluoride, hydrogen chloride, water, hydrogen sulphide, ammonia, phosphine, methane and silane have been studied by *ab initio* molecular orbital theory thus generating a matrix of eight by eight molecular complexes. The structures, energetics and vibrational spectra of these molecular complexes, both homodimers and heterodimers, have been studied at the second order level of Møller-Plesset perturbation theory using the 6-31G** basis set, by means of the Gaussian 92 computer program. The self consistent field interaction energies have been further dissected into their various components according to the Morokuma scheme, using the Monstergauss computer program. An analysis of the computed interaction energies of the complexes has also been carried out.

A complete normal mode analysis, identifying the normal modes of vibration, has been carried out using the Vibra program.

The infrared spectra of some of the associated species have also been determined experimentally by means of the matrix isolation technique using argon and nitrogen as matrix gases.

The combined use of the theoretical and experimental approaches has enabled reliable vibrational assignments to be made, which have been used in determining the molecular structures of the aggregates formed on complexation.

Declaration

I declare that this thesis is my own, unaided work. It is being submitted for the degree of Doctor of Philosophy in the University of Natal, Durban. It has not been submitted before for any degree or examination in any other University.

.....

M.G. Govender

.....day of .....1999.

Table of Contents

List of Tables

List of Figures

Acknowledgements

I wish to express my deepest thanks to my supervisor, Professor T.A. Ford, for his counsel, encouragement and support throughout the duration of this research project and not to mention the numerous stimulating and enlightening discussions.

I am also indebted to the following people:

Messrs J. Couling, R. Sushipersad, L. Murugas, K.P. Singh and G. Moodley of the School of Pure and Applied Chemistry and the glassblower, Mr P Seigling, who all contributed to the practical section of this project. A special thanks to Dr. W. Klotzbuecher of the Max Planck Institute, Mulheim, for his valuable suggestions regarding the experimental matrix isolation experiments.

Mr D. Lee and the staff of the Computer Services Division for their support in the implementation of the Gaussian and Monstergauss computer programs.

I am also grateful to Dr. D. Steele, of the Royal Holloway College, London, for making available the Vibra computer program and for the valuable communications. Thanks to Messrs K. Bissetty, B.C. Bricknell and T.M. Tshehla for their suggestions during our group discussions.

Thanks to my colleagues Drs. W.C.M.H. Meyer and J.C. Barry of the Atomic Energy Corporation and Mr. G.W. Lok of Eskom for their continued encouragement and support.

I am grateful to the FRD for funding the project and the University of Natal for a graduate scholarship.

Lastly, I would like to thank my wife and family for their emotional support and patience throughout this project.

Chapter One

1.1 *Molecular Interactions*

Molecules interact either reactively, resulting in the formation and breaking of covalent bonds, or non-reactively, in the formation of a molecular complex which may also be a reaction intermediate. The latter type of interaction is termed a weak, non-chemical, physical or van der Waals (vdW) interaction.[1]

The nature of intermolecular forces is well documented[1-6]. Forces occurring at large distances are classified as long-range and those at short distances, short-range interactions. The long-range forces are the classical electrostatic and induction, and the quantum mechanical London dispersion forces. These are attractive forces that lead to condensation to the liquid or solid phases. At shorter distances repulsive forces come into play; these arise from the exchange forces due to slight electronic overlap of the separate molecules. Short range interactions originate mostly from exchange repulsion, when two molecules approach so closely together that their electron clouds overlap. The total energy of interaction between the molecules is described by a potential energy surface, which is a function of the relative positions of the molecules. If the potential energy minimum for the complex formed is sufficiently deep it may support bound vibrational levels and it is these bound molecules that make up a vdW complex.[6] Upper bounds in the binding energy of 60 kJ mol^{-1}, and in the bond length of 250 pm, can be roughly considered as the limits separating classical molecules from vdW molecules.[4]

1.1.1 *Electrostatic Contribution*

This type of interaction arises mostly from the electrostatic interaction between the dipole moments. Such an interaction occurs with no distortion of the electron distribution on either side of the molecule. Higher order moments also contribute to the electrostatic interaction, viz. quadrupole, octupole, etc. The electrostatic energy of the interaction at long range can be written as the sum of terms of the form

$$E^{ES} = \frac{q_A q_B}{r} + \frac{q_A \mu_B}{r^2} + \ldots + \frac{\mu_A \mu_B}{r^3} + \ldots + \frac{Q_A Q_B}{r^5} + \ldots, \qquad (1.1)$$

where q, μ and Q are the monopole, dipole and quadrupole moments respectively of the system A or B, and r is the vector distance between the poles.

The electrostatic interactions can be classified as :

(a) *Ion-Ion*

These comprise the interaction between two ions having electric charges $z_A e$ and $z_B e$. The energy, U(r), is given as

$$U(r) = \frac{z_A z_B e^2}{\epsilon r} \qquad (1.2)$$

where z_A and z_B are the valencies of ions A and B, ϵ is the permittivity of the medium between the ions and r is the distance between the ions.

(b) *Ion - Dipole*

This type of interaction involves a molecule with a dipole moment, μ, inclined at an angle θ to the direction of a field of strength E, due to the ion of valency z, resulting in the following expression for the energy:

$$U(r) = \frac{zE\mu\cos\theta}{\epsilon r^2} \qquad (1.3)$$

(c) *Dipole - Dipole*

In the case of molecular interaction between two dipolar molecules, whose dipole moments, μ_A and μ_B, are aligned in the same direction, with r being the distance between the dipoles, the energy is given as

$$U(r) = -\frac{2\mu_A\mu_B}{\epsilon r^3} \tag{1.4}$$

(d) *Dipole - Quadrupole*

This type of interaction occurs in heterodimers, having dipole moments μ_A and μ_B, and quadrupole moments, Q_A and Q_B, separated by a distance r. The interaction energy is

$$U(r) = \frac{3(Q_A\mu_B - \mu_A Q_B)}{\epsilon r^4} \tag{1.5}$$

(e) *Quadrupole - Quadrupole*

In the case of molecular interaction between centrosymmetric molecules having quadrupole moments Q_A and Q_B, separated by a distance r, the interaction energy is represented as

$$U(r) = \frac{6Q_AQ_B}{\epsilon r^5} \tag{1.6}$$

(f) *Dipole - Induced Dipole*

This type of interaction occurs between the dipole moment of one molecule, A, and a polarizable molecule, B. If the two molecules have dipole moments μ_A and μ_B, with polarizabilites α_A and α_B, separated by a distance r, the resultant interaction energy becomes

$$U(r) = -\frac{(\alpha_A\mu_A^2 + \alpha_B\mu_B^2)}{\epsilon r^6} \tag{1.7}$$

1.1.2 *Induction Contribution*

This interaction occurs when one molecule has a permanent dipole moment and the other is non-polar. An instantaneous dipole is induced in the non-polar molecule. The induced dipole then interacts with the permanent dipole to produce an attractive force. Here, distortion of the electron clouds results when such an interaction take place, and the energy is termed a second order energy. This induction contribution is present with the electrostatic contribution in the case of the interaction of two polar molecules.[3]

1.1.3 *Dispersion Contribution*

An interaction of this type occurs both when the interacting molecules have no permanent dipole moments, and when they are polar in nature. However the electrons are in continuous motion so that the electron density in a molecule oscillates continuously in time and space. Thus at any instant in time the molecule may possess an instantaneous electric dipole which fluctuates as the electron density fluctuates. This instantaneous dipole in one molecule induces an instantaneous dipole in the second molecule. The induced dipole in the second and the inducing dipole in the first molecule interact to produce an attractive energy called dispersion energy. This form of intermolecular attractive interaction was first identified by London in 1930.[2]

1.1.4 *Exchange Repulsion*

When two closed shell molecules approach each other sufficiently closely for their electronic clouds to interact, the positively charged nuclei are then de-shielded from each other and are mutually repelled. This interaction is termed exchange repulsion.

1.2 Types of Molecular Complexes

1.2.1 *Hydrogen Bonded Complexes*

A typical hydrogen bond is represented as A-H..B, where A and B are atoms with electronegativities greater than that of hydrogen.[7,8] A relatively strong attractive interaction energy may then be observed in the A-H..B system, having magnitude up to 250 kJ mol^{-1}, with the AH..B bond angle usually close to 180°.[4] Structural studies usually indicate that the A-H bond becomes slightly longer than in the non-bonded state, whilst the H..B distance usually exceeds that of a covalent bond. Hydrogen bond strengths may be classified approximately as weak, with magnitudes less than about 15 kJ mol^{-1} and strong, with magnitudes greater than 50 kJ mol^{-1}.[1]

Hydrogen bonds can be classed as intramolecular, in which the A-H..B interaction occurs within the molecule itself, and intermolecular, in which an association of two or more identical or different molecules takes place.[1]

Hydrogen bonding[6-10] in an AH..B system is strongly dependent on the electronegativity of atom A. The higher the electronegativity of atom A, the more acidic the proton and the stronger is the AH..B bond.[9] The hydrogen bond has been studied by both spectroscopic and non-spectroscopic techniques. Most of the emphasis has been on the use of spectroscopic techniques. Historically, vibrational spectroscopy has been the most important method, because of the sensitivity of the vibrational modes to the presence of hydrogen bonds. The AH stretching mode and its harmonics are shifted to lower frequencies on bond formation. The infrared (IR) intensity of the fundamental AH band increases many-fold. The bending modes are shifted to frequencies higher than those of the isolated molecules. Numerous new vibrational modes also appear on hydrogen bond formation, viz. stretching, bending, torsion and shearing modes of the hydrogen bond itself, which are found in the region below 1000 cm^{-1}. The observation of the broadening

of the AH stretching band and the appearance of complex structure has been attributed to anharmonic effects and coupling with the low frequency modes of the hydrogen bond. The anharmonic coupling of the AH stretching mode with either a combination or overtone vibration represents a special case of Fermi resonance.[1]

1.2.2 *Electron Donor - Acceptor Complexes*

This type of complex was discovered by Benesi and Hildebrand[11] in 1949, by the observation of new absorption bands in the ultraviolet (UV) spectrum of the I_2.benzene complex, originating from a charge-transfer type interaction.[12]

The electron donor-acceptor molecular complexes result from interactions between molecules, one having a low ionization potential (the electron donor) and the other having a high electron affinity (the electron acceptor). The distortion which occurs when the electron clouds of both molecules approach each other gives rise to a charge transfer from the donor to the acceptor molecule[10]. The attractive charge transfer, together with the electrostatic and dispersion contributions, can outweigh the repulsive term to give strong stable complex formation. This family of molecular complexes have binding energies typically larger than those of the vdW type complexes.

1.2.3 *Van der Waals Complexes*

Van der Waals complexes are weakly bound assemblies of atoms or molecules, having large amplitude vibrational motions, which are held together by dispersion, induction, charge-transfer or hydrogen bonding interactions.[13] Experimentally the advent of supersonic free expansion enabled a wide variety of different complexes to be probed using molecular spectroscopy.[14,15] Theoretically many advances have been made in analyzing the intermolecular potentials, including Stone's distributed multipole analysis

(DMA).[16] Furthermore, in cases governed by electrostatic interaction the geometries of van der Waals complexes can be predicted by the Buckingham-Fowler hard sphere model.[17-19] Legon and Millen[20,21] have devised a set of rules facilitating the prediction of the molecular geometries of vdW complexes. However these models predict the geometries very well for small molecular systems only, and the distortion on complexation is neglected. The binding energies of vdW complexes are typically no greater than 2.5 kJ mol^{-1}, being approximately the thermal energy of molecules at room temperature. Another consequence of vdW interactions is that there is very little redistribution of electronic charge. As a result the individual molecules retain their separate characters. Van der Waals forces are responsible for complex formation in inert and non polar molecules at low temperatures. The stability of vdW complexes depends on a balance between the exchange repulsion, which decreases exponentially with the intermolecular distance, r, and the attractive forces due to electrostatic, induction and dispersion interactions, which decrease as r^{-n} at large distances[22].

1.3 **Experimental Methods for Studying Molecular Complexes**

1.3.1 *Diffraction Methods*

X-ray diffraction analysis, which can only be carried out in the solid phase, yields inaccurate positions for the hydrogen atoms and thus the use of this method in determining the structure of intermolecular complexes, particularly hydrogen bonded complexes, is limited. In X-ray diffraction experiments, X-rays are scattered by electrons, thus approximating the centroid of the electron density rather than the internuclear distances[23]. As a result, the total length R(A..B) in the AH..B system is obtained, rather than the hydrogen bond length. Neutron diffraction, on the other hand, allows for the determination of the R(A..B), r(H..B) and r(AH) distances and the A-H..B angle. This

is possible as a result of neutron scattering by the nuclei themselves, hence providing the internuclear distances.

1.3.2 *Spectroscopic Methods*

1.3.2.1 *Microwave Spectroscopy*

In the microwave region tunable monochromatic radiation is produced by a Klystron oscillator, which is tunable over a small frequency range. Absorption measurements are usually carried out in the gas phase. Stark modulation is often used to increase sensitivity, which also allows the determination of the dipole moment of the absorbing sample. These spectra are usually recorded at ambient temperatures and low pressures. This method is ideal for the study of strong complexes. The bond lengths and angles may be determined from the rotational constants. The rotational spectra of a number of HF-containing complexes have been extensively studied by Millen et al, e.g. $H_2O.HF$[24], $CH_3OH.HF$[25] and $N_2.HF$[20]. The molecular beam electric resonance (MBER) spectroscopic technique was later developed and has been widely applied by Klemperer and co-workers[14]. This method is extremely effective and yields accurate values for the dipole moments and nuclear hyperfine coupling constants for both strong and weak molecular complexes. The method involves the formation of vdW complexes during the adiabatic expansion of a mixture of the subsystems through a supersonic nozzle. The translationally monoenergetic beam obtained is deflected in a non-homogeneous electric field (the Stark effect). The microwave spectra are then recorded at zero external field. After passing through this region the molecular beam enters a mass spectrometer, which serves as a beam detector. The following systems are among those which have been studied by the Klemperer group using this method: $(HF)_2$,[14] $HCl.N_2$ and $HCl.Ar$[15].

The pulsed Fourier transform molecular beam microwave technique is the most recent

spectroscopic technique which has been employed in the studies of molecular complexes by Flygare and co-workers.[26] In these gas phase experiments the molecular beam is directed into a cavity where a several microsecond microwave pulse polarises the system with a rotational-translational transition corresponding to the bandwidth of the cavity. After dissipation of the microwave pulse, the microwave signal is detected by the superheterodyne method and the frequency spectrum is obtained by Fourier transformation. Numerous vdW-type complexes have been studied by this method, including $HF.PH_3$ and $C_2H_2.HCl$.[27]

1.3.2.2 *Infrared Spectroscopy*

The advent of Fourier transform instruments has had a striking influence on the resolution and sensitivity of infrared analysis. New molecular species formed can now be observed by vibrational spectroscopy, by the observation of new vibrational bands. On the basis of the resulting map of the vibrational transition moment direction, it is possible to predict detailed assignments of the relevant vibrational modes. Such studies leave little room for doubt on the correctness of both structural and vibrational interpretation of the spectroscopic results. However, difficulties in making reliable assignments arise when there are no gas-phase results available for comparison, particularly for the reactive species. To overcome this problem, isotopic studies and normal coordinate analysis can be used to aid in the vibrational assignments, but with the development of computational chemistry, mode assignments and the identification of new species are greatly simplified, since the theoretically predicted vibrational modes give a reasonable guide to the region where the new complex bands should appear in the spectrum.

1.3.2.3 **Raman Spectroscopy**

This technique requires very intense light sources and very efficient detectors for use in studying very dilute samples. The Raman technique is most useful for the study of vibrations that do not give rise to infrared bands for reasons of symmetry. Raman spectra complement IR spectra and also give access to low frequency transitions.

1.3.2.4 **The Matrix Isolation Technique**

The matrix isolation technique offers a means of preserving chemical species by embedding them at high dilution in a rigid host. The host used must be transparent to whatever radiation is being used for analysis. In principle the noble gases are ideal but other cryogenic solids such as nitrogen are also alternatives. Matrix isolation was pioneered by Pimentel[28]. The experimental technique of matrix isolation involves the deposition of a gas mixture on a cold surface. The composition of the matrix can then be studied by infrared or Raman, or by other types of spectroscopy.[29-31]

This project researches the molecular interactions of the hydrides of the elements of groups 14 to 17 in the second and third rows of the periodic table, with each other and between themselves. These groups were selected since they show trends of strong to weak molecular complexes thus providing a wider range for the study of molecular interactions. Further those systems involving the molecular interactions of the hydrides of the elements of the third period and beyond were excluded solely on the basis of computation economy. The results may be summarized by the entries in Table 1.1, the crosses indicating those particular complexes which have been successfully characterized in this study.

Table 1.1. Complexes of the Hydrides of the Elements of Groups 14 to 17 in the Second and Third Rows of the Periodic Table Characterized in this Work

Electron Donor	Proton Donor: CH_4	NH_3	H_2O	HF	SiH_4	PH_3	H_2S	HCl
CH_4	x		x	x			x	x
NH_3	x	x	x	x	x		x	x
H_2O	x		x	x			x	x
HF				x				x
SiH_4				x				x
PH_3	x			x	x	x	x	x
H_2S				x			x	x
HCl	x			x				x

Chapter Two

2.1 *Theoretical Methods in Computational Chemistry*

The application of quantum mechanics to the calculation of molecular properties requires detailed mathematical procedures embedded in computational programs. Of the three computational tools, molecular mechanics, semi-empirical and *ab initio* molecular orbital theory, the first two rely on the use of empirical parameters, whilst the third is capable of reproducing experimentally obtained results without such parameters. The term *ab initio* implies a rigorous, non-parametrised molecular orbital evaluation based on first principles in solving the Schrödinger wave equation.[32] The full Schrödinger wave equation has never been solved exactly for any but the simplest model problems. *Ab initio* methods rely on two approaches. In the calibrated approach the full exact equations of the *ab initio* method are used without approximations. The basis set describing the system under study is fixed in a semi-empirical way. This is different from the converged approach, in which a sequence of calculations with improving basis sets is used until acceptable results are obtained. Of the three methods used, molecular mechanics[33,34] can reproduce bond lengths to an accuracy of $\pm$ 0.5 pm in molecules, while minimal level Hartree-Fock *ab initio* methods require significantly more time and computer resources to achieve this level of accuracy. Some molecular mechanics force fields are currently being parametrised with *ab initio* results because of the lack of experimental data for particular classes of compounds.[35] Semi-empirical methods such as MNDO are parametrised to reproduce heats of formation with an accuracy of $\pm$ 36 kJ mol^{-1} for a selected group of compounds.[36] Again, high level *ab initio* calculations can reduce this error to $\pm$ 8 kJ mol^{-1} or less. *Ab initio* theory can be applied in principle to any geometry in the ground state or an excited state of a molecular species.[35] The molecular mechanics methods generally seek to provide information about the molecular structure and relative

energies, however some programs can also compute the vibrational normal modes[35]. Semi-empirical methods are parametrised on experimental heats of formation at 25 °C, and also provide information on the dipole moments and molecular geometries. Even though molecular mechanics and semi-empirical methods can describe many such molecular properties, certain other molecular properties are beyond the scope of either approach.[35] In such cases *ab initio* methods may be the only theoretical model capable of providing a solution. The *ab initio* method is, however, more expensive than the semi-empirical or molecular mechanics methods in terms of computational time, and thus only small molecules can be treated accurately at present. Similar to semi-empirical methods, *ab initio* theory also makes use of the Born-Oppenheimer approximation,[37] in which nuclear motions are assumed to take place on much longer time scales than those of the electrons. This is a good approximation except for systems having very flat potential energy surfaces, as in some Jahn-Teller systems, where there is coupling between the vibrational and electronic wavefunctions.[38]

In summary, computational *ab initio* quantum chemistry attempts to solve the electronic Schrödinger wave equation for the potential energy surface and wave functions on a grid where the nuclear motions are frozen. The wave functions contain the information required to compute the energies, structures, electron densities, dipole moments, polarizabilities and transition properties among the different energy states. The application of an external perturbation to the system under study is also possible, giving valuable data on vibrational frequencies and reaction paths. This study uses the Møller-Plesset (MP2) level of theory (discussed in section 2.4.6) with the 6-31G** basis set (discussed in section 2.4.7) since it provides a good compromise between mathematical rigour and ease of computation.

2.2 *Molecular Mechanics Method*[39]

Molecular mechanics methods are based on simple classical-mechanical models of molecular structures. This approximation treats the molecule as an array of atoms governed by a set of classical-mechanical potential functions, containing the bond stretches, angle bends and torsions. A potential function containing the above three parameters is called a valence force field, because it accounts for the chemical properties attributed to chemical bonds. The valence force field is however inadequate for high quality quantitative calculations. Force fields intended for such calculations should include the van der Waals potentials, which account for steric interactions. The steric repulsions can never be completely separated from other interactions, therefore they are difficult to define, and they are also strongly dependent on the other potential functions. The Urey-Bradley force field[40] does account for these repulsions but generally does not give reliable results. The MM2 (Molecular Mechanics version 2) force field of Allinger[33,34] is currently most widely used since the results obtained compare well with experiment.

2.3 *Semi-Empirical Methods*[41]

The Dewar semi-empirical molecular orbital methods, MINDO (Moderate Intermediate Neglect of Differential Overlap), MINDO/2, MINDO/3 and MNDO (Moderate Neglect of Differential Overlap), have played a major role in organic chemistry. The main aim of these methods was to provide accurate chemical structures for large organic and bio-organic molecules at a reasonable cost of computer time[41]. The earlier semi-empirical methods, CNDO (Complete Neglect of Differential Overlap), INDO (Intermediate Neglect of Differential Overlap) and NDDO (Neglect of Diatomic Differential Overlap), developed by Pople and co-workers,[42-44] were intended to reproduce only electronic properties such as dipole moments. Only now are the merits of semi-empirical methods becoming accepted and their ability to treat large systems with low usage of computer facilities being

appreciated by experimentalists and theoretically oriented chemists. This is partly because the modern NDDO-based methods, Austin model 1 (AM1) and parametric method 3 (PM3), do not have many of the disadvantages of the previous methods and the computer hardware available makes impressive semi-empirical calculations possible. The configuration interaction calculations which are performed within the NDDO framework provide an excellent tool for multiconfigurational effects and for predicting ultraviolet spectra within reasonable accuracy. Molecular electrostatic potentials can also be calculated quickly and accurately, which can then be used for the simulation of solvent effects. There are also semi-empirical packages available for the calculation of the properties of molecules containing lanthanides and actinides, e.g. MOLFDIR.[45]

2.4 *ab initio Molecular Orbital Theory*

Most methods used in *ab initio* molecular orbital theory are based on the linear combination of atomic orbitals (LCAO) approximation and the determination of the electronic wavefunctions using the self-consistent field (SCF) method by the Hartree-Fock (HF) formalism[46a]. The HF method assumes that the electrons move independently of each other, hence ignoring electron correlation. This assumption leads to incorrect behaviour of the wavefunction as the molecule dissociates. Electron correlation is taken into account by configuration interaction (CI) or Møller-Plesset (MP) perturbation methods.[47]

2.4.1 *The Schrödinger Wave Equation*

The Schrödinger wave equation, expressed as

$$\hat{H}\Psi = E\Psi \qquad (2.1)$$

comprises $\hat{H}$, the Hamiltonian, a differential operator representing the total energy, E, of the stationary state of the molecule, which is the numerical value of the energy of that

particular state and Ψ, the wavefunction of the system, which depends on the orientation and the spin coordinates of all particles. The square of the wavefunction represents the probability distribution of particles within the molecule. In quantum mechanics Ψ must behave as a quadratic-integrable function that goes to zero at infinity for a bound state. The wavefunction, if operated on by an appropriate operator, results in a particular property for the system under study. The Hamiltonian, $\hat{H}$, can be classically described as the sum of the kinetic and potential energies,[46b] i.e.

$$\hat{H} = \hat{T} + \hat{V} \tag{2.2}$$

where the kinetic energy operator, $\hat{T}$, is a sum of differential operators,

$$\hat{T} = -\frac{h^2}{8\pi^2} \sum_i \frac{1}{m_i} \left(\frac{\partial^2}{\partial x_i^2} + \frac{\partial^2}{\partial y_i^2} + \frac{\partial^2}{\partial z_i^2} \right) \tag{2.3}$$

The sum is over all particles i (nuclei and electrons) having masses m_i, with h being Planck's constant. The potential energy operator, $\hat{V}$, is the Coulomb interaction, represented as

$$\hat{V} = \sum_{i<j} \sum \frac{(e_i e_j)}{r_{ij}} \tag{2.4}$$

the summations being over all pairs of particles (i,j) with electric charges, e_i and e_j, separated by a distance r_{ij}. For electrons, $e_i = -e$, and for a nucleus with atomic number Z_i, $e_i = +Z_i e$.[46b] The Hamiltonian function described above is non-relativistic, and ceases to be appropriate as the particles under study reach the speed of light. The only solutions to (2.1) that are acceptable are those with appropriate symmetry under interchange of identical particles. The wavefunctions of the electrons are antisymmetric

with respect to interchange of coordinates, hence the wavefunction must be multiplied by -1. This is termed the antisymmetry principle.[46b] The Schrödinger equation for any system under study has many solutions, of which those corresponding to the lowest energy (the ground state) are most applicable. In order to simplify the physical constants from the above equations, the atomic units of length and energy are usually defined as follows:

(a) The bohr, a_0, the atomic unit of length, equivalent to the Bohr radius,

$$a_0 = \frac{h^2}{4\pi^2 me^2} = 52.92\ pm \tag{2.5}$$

(b) The hartree, E_H, the atomic unit of energy, defined as the Coulomb repulsion between two electrons separated by a distance of 1 bohr is represented as

$$E_H = \frac{e^2}{a_0} = 4.3598 \times 10^{-18}\ J \tag{2.6}$$

2.4.2 *The Born-Oppenheimer Approximation*

The general molecular Schrödinger equation, neglecting electron spin effects, is

$$(\hat{T}_n + \hat{T}_e + \hat{V}_{nn} + \hat{V}_{ee} + \hat{V}_{en})\Psi = \hat{E}\Psi \tag{2.7}$$

the operators in the equation being the kinetic and potential energy terms between the nuclei, the electrons, and between both nuclei and electrons. The explicit forms of these operators are given as

$$\hat{T}_n = -\sum_{\alpha}^{nuclei} \frac{h^2}{8\pi^2 M_\alpha}\nabla_\alpha^2 \tag{2.8}$$

$$\hat{T}_e = -\sum_{i}^{electrons} \frac{h^2}{8\pi^2 m_e}\nabla_i^2 \tag{2.9}$$

$$\hat{V}_{nn} = \sum_{\alpha>\beta} \frac{Z_\alpha Z_\beta e^2}{R_{\alpha\beta}} \tag{2.10}$$

$$\hat{V}_{ee} = \sum_{i<j} \frac{e^2}{r_{ij}} \tag{2.11}$$

and

$$\hat{V}_{en} = -\sum_{\alpha}\sum_{i} \frac{Z_\alpha e^2}{r_{\alpha i}} \tag{2.12}$$

There is a repulsive interaction among the nuclear charges and a repulsive charge-charge interaction among the electrons. However the interaction potential between electrons and nuclei is attractive, since the particles are oppositely charged. This particular interaction couples the motions of the electrons and of the nuclei. The wavefunctions that satisfy eq.(2.7) must be functions of both the electron position coordinates and the nuclear position coordinates, and this differential equation is not separable. In principle, true solutions could be found, but the task is difficult. An alternative is an approximate separation of the differential equation based upon the difference in the mass of an electron and the masses of the nuclei. The difference suggests that the nuclei will be sluggish in their motions relative to the electron motions. Over a time period the electrons "see" the nuclei as if they were fixed in space. The nuclei, on the other hand, will "see" the electrons as something of a blur, resulting from their rapid motions.[48a] The Born-Oppenheimer approximation leads to a separation of the molecular Schrödinger equation into a part for the electronic wavefunction and a part for the nuclear motions, which is the Schrödinger equation for vibration and rotation. The physical idea is that the light, fast-moving electrons readjust to the nuclear displacements instantaneously. This is the reason

that the approximation produces an electronic Schrödinger equation for each possible geometrical arrangement of the nuclei in the molecule. The approximation involves "clamping" the nuclei of a molecule, then solving for the electronic Schrödinger wavefunction. This process is repeated for a number of different structures until the electronic energy dependence on the structural parameters is well known.[48b]

2.4.3 *The Linear Combination of Atomic Orbitals (LCAO) Approximation*

Molecular orbital theory uses one-electron functions to approximate the full wavefunction describing the molecular orbital. The molecular orbital, $\psi(x, y, z)$, is a function of the cartesian coordinates x, y, z of a single electron. The square of the molecular orbital, $|\Psi|^2$, is interpreted as the probability distribution of the electron in space, even if Ψ is a complex function. For a closed shell molecule in its ground state with n (even) electrons, doubly occupying n/2 orbitals, a many-electron wavefunction can be constructed as a single determinant called the Slater determinant,

$$\psi = (n!)^{-1/2} \begin{vmatrix} \psi_1(1)\alpha(1) & \psi_1(1)\beta(1) & \psi_2(1)\alpha(1)\ldots & \psi_{n/2}(1)\beta(1) \\ \psi_1(2)\alpha(2) & \psi_1(2)\beta(2) & \psi_2(2)\alpha(2)\ldots & \psi_{n/2}(2)\beta(2) \\ \vdots & \vdots & \vdots & \vdots \\ \psi_1(n)\alpha(n) & \psi_1(n)\beta(n) & \psi_2(n)\alpha(n)\ldots & \psi_{n/2}(n)\beta(n) \end{vmatrix} \qquad (2.13)$$

Here α and β are the spin wavefunctions, with α being the spin wavefunction for electron spin aligned along the positive z-axis and β the spin wavefunction for spin aligned along the negative z-axis. The individual molecular orbitals are written in terms of a linear combination of a finite set of *N* one-electron functions known as basis functions,[46a]

$$\psi = \sum_{\mu=1}^{N} c_{\mu i}\phi_{\mu} \tag{2.14}$$

where $c_{\mu i}$ are the molecular orbital expansion coefficients and $i=1,2,3...N$.

If the basis functions used are atomic orbitals of the atoms, then the wavefunction is described in terms of a LCAO.[46a]

2.4.4 *Hartree-Fock Theory*

The determinantal wavefunction may be defined in terms of molecular orbitals, which may be further expanded in terms of one-electron functions. On selecting the one-electron functions, the coefficients of the functions, $c_{\mu i}$, are adjusted to minimize the energy of the system, which is represented as the expectation value of the many electron Hamiltonian, $\hat{H}$,

$$E' = \int \phi^* \hat{H} \phi d\tau \tag{2.15}$$

where the integration is over the coordinates of all the electrons. We are now left to solve for the $c_{\mu i}$. This is done by using the variational principle[46c], which simply means searching for an upper bound of the exact wavefunction. This implies the variational equations

$$\frac{\partial E'}{\partial c_{\mu i}} = 0 \tag{2.16}$$

for all (μ,i).

This principle leads to a set of equations for the $c_{\mu i}$ called the Roothaan-Hall equations,[49,50] describing the molecular orbital expansion coefficients,

$$\sum_{\nu=1}^{N} (F_{\mu\nu} - \epsilon_i S_{\mu\nu}) = 0 \tag{2.17}$$

where ϵ_i is the one-electron energy of the molecular orbital ϕ_i and $S_{\mu\nu}$ are the elements of the overlap matrix describing the overlap between orbitals. The elements of the Fock matrix, $F_{\mu\nu}$, represent the average effect of the field of all the electrons on each orbital,

$$F_{\mu\nu} = H_{\mu\nu} + \sum_{\lambda=1}^{N}\sum_{\sigma=1}^{N} P_{\lambda\sigma}[(\mu\nu|\lambda\sigma) - \frac{1}{2}(\mu\lambda|\nu\sigma)] \qquad (2.18)$$

$H_{\mu\nu}$ is a matrix representing the energy of a single electron in a field of bare nuclei and the term $(\mu\nu|\lambda\sigma)$ represents the two-electron repulsion integrals, which are further multiplied by the elements of the one-electron density matrix, $P_{\lambda\sigma}$, given by

$$P_{\lambda\sigma} = 2\sum_{i=1}^{occ} c_{\lambda i}^{*} c_{\sigma i} \qquad (2.19)$$

where the summation is over the occupied molecular orbitals only.[46c]

The Fock matrix, through the density matrix, depends on the $c_{\mu i}$ as well. Hence this equation is non-linear and has to be solved iteratively through a process called the self-consistent field (SCF) method. The orbital energies provide a basis for chemical energetics. The ionization potential energy is also an example of an energetic feature, where one electron is removed from the molecule. In this method, the Hartree-Fock method, each electron "sees" the other electrons as an average field with no interactions. This limitation is overcome by using Møller-Plesset (MP) perturbation theory or configuration interaction (CI).

2.4.5 *Electron Correlation*[46d]

The exact wavefunction described by a single determinant is the major weakness of single determinant molecular orbital theory, since the electronic motions are completely

neglected. This leads to the Hartree-Fock energies being significantly higher than the exact values. Correlation effects span through the energies, structural parameters and vibrational frequencies. There are various ways to incorporate correlation effects, e.g. through either CI methods or MP perturbation theory.

2.4.6 *Møller-Plesset Perturbation Theory*

This model aims to find the lowest eigenvalue and corresponding eigenvectors of the full Hamiltonian matrix. These models are formulated by first introducing a generalised electronic Hamiltonian. MP perturbation theory adds higher excitations to HF theory as a non-iterative correction. Perturbation theory is based upon dividing the Hamiltonian into two parts,

$$\hat{H}_\lambda = \hat{H}_o + \lambda \hat{V} \tag{2.20}$$

where $\hat{H}_0$ is exactly soluble and $\hat{V}$ is the perturbation applied to $\hat{H}_0$, which is small in magnitude. Since $\hat{V}$ is a small perturbation to $\hat{H}_0$, the perturbed wavefunction and energy can be expressed as a power series expansion of $\hat{V}$ in terms of a dimensionless parameter, λ, i.e.

$$\psi = \psi_0 + \lambda\psi^{(1)} + \lambda^{(2)}\psi^{(2)} + \lambda^{(3)}\psi^{(3)} + ... \tag{2.21}$$

and

$$E = E^{(0)} + \lambda E^{(1)} + \lambda^{(2)}E^{(2)} + \lambda^{(3)}E^{(3)} + ... \tag{2.22}$$

Substituting the perturbed wavefunction and energy into the Schrödinger equation results in eq. (2.23),

$$(H_0 + \lambda V)(\psi^{(0)} + \lambda\psi^{(1)} + ...) = (E^{(0)} + \lambda E^{(1)} + ...)(\psi^{(0)} + \lambda\psi^{(1)} + ...) \tag{2.23}$$

After expanding the products and equating coefficients on each side of the equation for each power of λ, a series of expressions is established, corresponding to powers of 0, 1 and 2 as shown below:

$$(H_0 - E^{(0)})\psi^{(0)} = 0 \tag{2.24}$$

$$(H_0 - E^{(0)})\psi^{(1)} = (E^{(1)} - V)\psi^{(0)} \tag{2.25}$$

$$(H_0 - E^{(0)})\psi^{(2)} = (E^{(1)} - V)\psi^{(1)} + E^{(2)}\psi^{(0)} \tag{2.26}$$

The above gives a general description of perturbation theory. For MP perturbation theory, $\hat{H}_0$ is defined as the sum of one-electron Fock operators.[46e]

2.4.7 *Basis Set Representations*

Each of the molecular orbitals is represented as a linear combination of one-electron functions, known as basis functions, i.e.

$$\psi_i = \sum_{\mu=1}^{N} c_{\mu i}\phi_\mu \tag{2.27}$$

where the $c_{\mu i}$ are the molecular orbital coefficients and ϕ_μ the basis functions.

2.4.7.1 **Basis Sets**

Most *ab initio* calculations expand the wavefunction in terms of Gaussian basis functions.[51] Cartesian Gaussian-type orbitals are expressed as follows:

$$\chi_{GTO} = Nx^l y^m z^n \exp(-\zeta r^2) \tag{2.28}$$

In this equation ζ is a constant called the orbital exponent, determining the size (radial

extent) of the function. In the Gaussian function, $\exp(-\zeta r^2)$ is multiplied by powers of x, y and z which are the Cartesian coordinates relative to the centre of the function and a constant *N*, the normalisation constant. Thus, for example, s-type functions behave as $\exp(-\zeta r^2)$, p_x functions behave as $x\exp(-\zeta r^2)$ and d_{xy} functions behave as $xy\exp(-\zeta r^2)$. Earlier ab initio calculations used Slater type functions (STFs)[52] as basis functions, which in spherical polar coordinates take the following form:

$$\chi_{STO} = Nr^{n-1}\exp(-\zeta r)Y_{lm}(\theta,\phi) \qquad (2.29)$$

where Y_{lm} is the spherical harmonic, n, l and m are principal, angular and magnetic quantum numbers and ζ is the orbital exponent, with *N* again the normalisation constant. A linear combination of the STFs is used to describe the atomic orbitals (AOs). The advantage of the use of Gaussian type functions over Slater type functions lies in the time taken in computation. STFs may be approximated by summing a number of GTFs with different exponents and coefficients. Gaussian type functions which depend on r^2 are called primitive Gaussians. For the proper representation of molecular calculations the primitive GTFs are contracted[46d], i.e. linear combinations of GTFs have to be summed to represent the basis functions.

2.4.7.2 **Types of Basis Sets**[46d]

Minimal Basis Sets

These basis sets are used to describe the minimum number of basis functions required for each atom in a molecule, e.g. STO-3G, which uses three primitive Gaussians per basis function, and it approximates STFs with GTFs.

Split-Valence and Polarization Basis Sets

In the minimal basis set only the exact number of functions needed for each electron in

the atom is used. An extension of the minimal basis set is to double the number of functions representing the valence region. In a split-valence basis set, hydrogen and helium atoms are represented by two s-type functions and the first- and second-row atoms by two complete sets of valence s and p functions. The type of split-valence basis set used in this project is the 6-31G** basis set, comprising the inner shell functions expanded in terms of six primitive Gaussian functions. The valence shell (2s, 2p) is split into an "inner" part, which is expanded in terms of three primitive Gaussians, and an "outer", more diffuse, part written in terms of one primitive Gaussian. In addition the basis used must also have flexibility to account for the deformations which atoms undergo when a molecule is formed, and must also account for the change in the wavefunction caused by an external perturbation. This flexibility is accounted for by the inclusion of polarization functions. These functions have angular momenta of higher magnitude than those occupied in an atomic calculation. Polarization functions simulate the distortion of hydrogen atoms by means of adding a set of p orbital functions, and similarly for the non-hydrogen atoms a set of d orbital functions is added. However, the principal quantum number on the polarization functions can be changed, as in the 6-31G(2d,2p) and the 6-31G(3d,2p) basis sets, for example.

Diffuse Basis Sets

Basis sets with diffuse functions are useful for systems containing electrons which are far from the nucleus, e.g. molecules with lone pair electrons, and ions. These types of functions contain larger s and p orbital type functions, thus allowing the orbitals to occupy larger regions of space. The 6-31+G basis set adds diffuse functions to heavy atoms, whilst the 6-31++G basis adds diffuse functions to the heavy atoms and the hydrogen atoms as well. These basis sets often require more computer resources.

2.4.8 *Basis Set Superposition Error (BSSE) Calculation*

This error occurs when a finite basis set is used, since the electronic description of either sub-unit in a complex is improved when the basis set for the supermolecule makes use of orbitals associated with the other monomer unit. The inclusion of functions from one monomer with those functions of the other results in a lowering of the interaction energy. This energy lowering is known as the BSSE. An approximate method for accounting for this error is the CPC (counterpoise correction)[53] in which the energies of each monomer unit are calculated using the full basis set.[54] There have been many studies criticizing the CPC[55-57], and alternative suggestions have been made, however the CPC still produces acceptably accurate results.[58-61]

2.5 ***Introduction to Vibrational Theory***

The vibrational spectra of molecules may be observed by two fundamental spectroscopic techniques[62], infrared spectroscopy, first systematically used by Coblentz[63], and Raman spectroscopy, which was theoretically predicted by Smekal[64] in 1923 and first observed experimentally in 1928 by Raman and Krishnan[65].

These techniques give information regarding the orientation of the atoms within a molecule. The experimentally observed spectra may be sometimes difficult to interpret, hence a complete vibrational analysis is required. The procedure involves the evaluation of the ground state potential energy surface around the equilibrium geometry from which the force constants, frequencies and potential energy distributions amongst the vibrational normal modes are obtained within the harmonic approximation. Comprehensive and extensive theoretical work has been done on scaling factors by Scott and Radom[66] to give a better comparison between the computed and the experimentally observed vibrational properties. With recent advances in computational hardware and techniques, *ab initio*

molecular orbital studies have become important in studying molecular vibrational force fields. The *ab initio* molecular orbital calculations yield the vibrational force constants in a Cartesian coordinate system. These Cartesian force constants do not provide a physical description of the vibrational force field, however. The force constants therefore have to be transformed into another frame of reference, the internal coordinate system. In order to accomplish this a set of linearly independent coordinates should be defined. However, geometrical considerations show that these linearly independent coordinates may not all be independent of each other, thus leading to redundancies, which have to be removed, since in any molecule the number of internal coordinates may then be larger than that of the vibrational degrees of freedom. A set of local coordinates defined as having no redundancies is therefore particularly useful. This set of local coordinates, described as being a linear combination of the internal coordinates, is called symmetry coordinates. The redundancies are now defined as combinations of stretching, bending, torsional and linear bending motions[67a].

2.5.1 *Cartesian Displacement Coordinates, X*

This coordinate system measures the displacements from the equilibrium position of each nuclear mass using Cartesian coordinates. Each atom has its own set of Cartesian coordinates with the origin defined by the position of the centre of mass of the molecule.

2.5.2 *Internal Coordinates, R*

Internal coordinates measure the change in shape of a molecule compared with its equilibrium shape, disregarding the position or orientation of the molecule in space. The relative positions of the nuclei are fixed by 3n-6 (or 3n-5 for linear molecules) internal coordinates. The transformation between internal and Cartesian displacement coodinates

is given by the B matrix, defined as

$$R = BX \tag{2.28}$$

The internal coordinates are characterised as follows:[67b]

2.5.2.1 **Bond Stretching**

The change in bond length, Δr, during the stretching of a bond.

2.5.2.2. **Angle Bending**

A bending coordinate is defined as a change in the angle between two bonds. This change is given the symbol $\Delta\delta$.

2.5.2.3. **Rocking**

A rocking coordinate is a particular case of the bending coordinate comprising a change in the angle between one bond and a group of atoms. The rocking coordinate is labelled as $\Delta\rho$.

2.5.2.4. **Wagging**

A wagging coordinate is defined as a change in the angle between a bond and a plane, with the symbol $\Delta\omega$.

2.5.2.5. **Torsion**

In this type of vibration, labelled $\Delta\tau$, there is a change in the angle between two planes.

2.5.2.6. **Out of plane deformation**

In this mode, labelled $\Delta\pi$, an atom moves into and out of a plane, usually a symmetry plane.

2.5.3 *Symmetry Coordinates, S*

For symmetrical molecules the most efficient way of characterising the vibrational modes is by using symmetry coordinates, a linear combination of the internal coordinates represented as

$$S = UR \tag{2.29}$$

where U is the transformation matrix.

2.5.4 *Normal Coordinates, Q*

Normal coordinates are described as linear combinations of symmetry coordinates. For every normal mode of vibration all the coordinates vary periodically with the same frequency and go through their equilibrium positions simultaneously. The form of the normal mode of vibration is defined by specifying the relative amplitudes of the various coordinates in the set being used. The normal coordinates, Q, are related to the symmetry coordinates, S, by the transformation

$$Q = L^{-1}S \tag{2.30}$$

where L^{-1} is the transformation matrix.

The aim of normal mode computations is the calculation of the eigenvalues and atomic displacements for each normal mode of vibration from the structural geometry, the atomic masses and the force field, or alternatively, the determination of the force field from the experimental vibrational spectra. These amplitudes cannot be determined explicitly, however the normal mode calculations yield the relative amplitudes of the motions in terms of the potential energy distribution describing a given normal mode. These calculations follow the format developed by Schachtschneider[68], who wrote the first set of modern computer programs for normal coordinate analysis[69].

2.5.5 *Normal Modes of Vibration*[9a]

Let the displacements from the equilibrium position of each of the N atoms be represented by a set of coordinates x_1, y_1, z_1, for atom 1, x_2, y_2, z_2 for atom 2,... x_N, y_N, z_N for atom N, or more generally by the use of mass weighted coordinates q_1, q_2, q_3, q_4,...,q_{3N}. The 3N coordinates, q_i, where i=1,2,3...3N, may be used to define the potential energy V and the kinetic energy T. The appropriate relations are

$$2V = \sum_{i=1}^{3N} \sum_{j=1}^{3N} f_{ij} q_i q_j \tag{2.31}$$

$$2T = \sum_{i=1}^{3N} \sum_{j=1}^{3N} m_{ij} \dot{q}_i \dot{q}_j \tag{2.32}$$

where

$$\dot{q} = \frac{dq}{dt} \tag{2.33}$$

and q_i and q_j are the ith and jth coordinates, and are not necessarily the same for the general case (i = j or i≠j). The f_{ij} are force constants and the m_{ij} are functions of the atomic masses. Newton's equation of motion written in the Lagrange form is

$$\frac{d}{dt}\left(\frac{\partial T}{\partial \dot{q}_i}\right) + \frac{\partial V}{\partial q_i} = 0 \tag{2.34}$$

From eq. (2.28) and eq. (2.29) we obtain, for each value of q_i,

$$\frac{\partial V}{\partial q_i} = \sum_{j=1}^{3N} f_{ij} q_j \tag{2.35}$$

$$\frac{\partial T}{\partial \dot{q}_i} = \sum_{j=1}^{3N} m_{ij}\dot{q}_j \tag{2.36}$$

$$\frac{d}{dt}\left(\frac{\partial T}{\partial \dot{q}_i}\right) = \sum_{j=1}^{3N} m_{ij}\ddot{q}_j \tag{2.37}$$

Substituting eq. (2.34) and eq. (2.36) into eq. (2.33) yields, for each of the 3N values for i,

$$\sum_{j=1}^{3N} m_{ij}\ddot{q}_j + \sum_{j=1}^{3N} f_{ij}q_j = 0 \tag{2.38}$$

These 3N equations have the general solution

$$q_j = A_j(\sin\sqrt{\lambda}t + \alpha) \tag{2.39}$$

where

$$\sqrt{\lambda} = 2\pi\nu \tag{2.40}$$

where A_j are the amplitude factors, α are the phase angles, and λ is a frequency factor which is determined by the force constants.

Differentiating eq. (2.39) twice with respect to time results in the following expressions

$$\dot{q}_j = \sqrt{\lambda}\ A_j\cos(\sqrt{\lambda}t + \alpha) \tag{2.41}$$

and

$$\ddot{q}_j = -\lambda\ A_j\sin(\sqrt{\lambda}t + \alpha) \tag{2.42}$$

Substituting the values for eq. (2.36) and eq. (2.38) into eq. (2.35) results for each of the 3N values for i,

$$\sum_{j=1}^{3N}(f_{ij}-m_{ij}\lambda)A_j=0 \qquad (2.43)$$

The expanded form of the above equation is called a set of secular equations. When the secular equations are expanded, a 3N order characteristic equation for λ is obtained, which can be solved for the 3N characteristic values for ν in terms of the f and m values. Each value of ν is then substituted into the secular equation to calculate the ratios of A_j, which are the ratios of amplitudes for each ν. The result indicates that each atom oscillates about its equilibrium position with amplitude A_j, generally different for each coordinate, but with the same frequency and phase constant. This type of motion is called a normal mode of vibration. The difficulty that arises from using Cartesian coordinates is that the 3N solutions for ν include six non-genuine vibrations with zero frequency, which are the translations and rotations, and the interpretation of the force constants in terms of Cartesian coordinates thus becomes difficult. The use of symmetry coordinates aids in the problems of redundancies and force constant interpretation. If the molecule under study has symmetry, then the secular determinantal equation becomes simpler to solve by factorizing into symmetry blocks. The symmetry coordinates must be orthogonal and normalized. The symmetry coordinate as the following form :

$$S=\sum_{k}U_{jk}R_k \qquad (2.44)$$

which are not unique, hence a general method cannot be given to determine these coordinates. The kinetic and potential energy terms are represented as follows using symmetry coordinates :

$$2V=S^tFS \qquad (2.45)$$

and

$$2T=\dot{S}^tG^{-1}\dot{S} \qquad (2.46)$$

where S^t and $\dot{S}$ are the transpose and time derivative of the symmetry coordinate matrix. The force constant matrix F characterizes the restoring forces for the distorted coordinates in S. G^{-1} is the inverse of the G matrix, which is a function of the atomic masses and the geometrical parameters. The secular equation for the symmetry species, using symmetry coordinates, takes the following form :

$$|G_a F_a - I\lambda| = 0 \qquad (2.47)$$

Similar equations result for the b, e, f and other symmetry species, consisting of square blocks in the secular determinant.

2.5.5.1 **The G- Matrix** [9b]

The Cartesian displacement coordinates, X,.and the internal coordinates, R, are related as follows:

$$R = BX \qquad (2.48)$$

where the B matrix is the linear transformation between the internal and Cartesian displacement coordinates.

Wilson et al[70] have shown the G matrix to be represented as

$$G = B\, M^{-1}\, B^t \qquad (2.49)$$

where M^{-1} is the diagonal matrix consisting the reciprocal of the atomic masses repeated three times. The G matrix elements are independent of the bond orientation in the Cartesian reference frame, thus $|GF - I\lambda| = 0$ becomes

$$(\sum_i \frac{1}{M_i})F - \lambda = 0 \qquad (2.50)$$

using $\nu_i = \frac{\sqrt{\lambda_i}}{2\pi}$ and replacing for λ_i from the above equation one can solve for ν_i.

The complete description of the *G*-matrix elements using a vectorial method is given by Wilson, Decius and Cross[70]. Having determined the frequencies, the forms of the normal modes of vibration in terms of the internal coordinates need to be obtained to give a physical description of the actual vibrational motions incorporating the internal coordinates. To accomplish this, the *L* matrix needs to be evaluated.

2.5.5.2 **The L- Matrix** [9c]

The *L* matrix is obtained by reconstructing the secular determinant, substituting $GF = H$ and subtracting λ from the diagonal elements, thus resulting in a system of equations with L_{ij} as the coefficients.[9b] These values cannot be individually determined but their ratios characterise the vibrations relative to the specific distortion in each internal coordinate. The dimensions of the L_{ij} elements are different for stretches, bends and the other internal coordinates, hence it is preferable to use the potential energy distribution to characterize the forms of the normal coordinates. The potential energy takes the following form :

$$2V_k = Q_k^2 \sum_{i\,j} F_{ij} L_{ik} L_{jk} \qquad (2.51)$$

with the potential energy distribution being the fractional part of the potential energy of a normal mode of vibration contributed by the force constant F_{ij} and is represented by dividing each $F_{ij}\ L_{ik}\ L_{jk}$ by $2V_k$ in eq. (2.51).

Chapter Three

The use of *ab initio* molecular orbital theory coupled with experimental techniques has become particularly useful in the elucidation of the nature of molecular interactions. These types of calculations usually predict the equilibrium geometries, interaction energies and vibrational spectra for comparison with the experimental results. Over the past few years there has been a great improvement in the power, efficiency and availability of *ab initio* computer programs as evident from the numerous publications reporting the use of such programs. For relatively small molecular complexes the use of the MP2 level of theory with the 6-31G** basis set reproduces the experimentally determined properties with reasonable accuracy. Recent studies by Del Bene[71] suggest the implementation of diffuse functions, e.g. 6-31+G** and 6-31++G**, to improve the accuracy of the theoretical studies. This project was carried out using the 6-31G** basis set due to the limited amount of computational time and memory available. Although some of the systems in this project have been considered by other authors, to date there has not been a complete study at a consistent level of theory and basis set for this extensive series.

3.1 *The HF Dimer*

The HF dimer has served as a paradigm for the study of many hydrogen bonded systems, due to its simplicity and specificity in its bonding process. There has been an extensive amount of high resolution microwave,[14,72-74] far infrared,[75-78] infrared[79-86] and matrix isolation vibrational spectroscopic studies[87-91], which have led to the determination of the vibrationally averaged structure, tunnelling dynamics, where the proton donor-acceptor roles are interchanged, dissociation energy and vibrational spectrum. From the pioneering microwave studies of Klemperer et al,[14] the dimer is known to be a planar, slightly asymmetric top with an almost linear FH...F hydrogen bond. The dimer was also shown to

execute large amplitude proton exchange motions, leading to a tunnelling splitting of 0.6578 cm^{-1} in the vibrational ground state, indicating a non-rigid structure[14]. The large amplitude motions have been observed in neon and argon matrices, however in the neon matrix, the matrix cage is much smaller than that in argon, hence there is restricted amplitude motion in the dimer.[87-91] The vibrational predissociation studies by Laush and Lisy,[84] measuring the hydrogen bond strength, were supported by the theoretical calculations of Michael et al[92] and a later study by Jensen et al.[93] Theoretical studies on the HF dimer focused mainly on the geometrical parameters, vibrational spectra and intermolecular forces.[93-110] The earliest potential energy surface of Yarkony et al,[111] which was used to study the dimerization process, has been superceded by further calculations at a higher level of sophistication.[92,94,96] The most recent theoretical calculation by Bishop et al[104] focused on the vibrational optical properties of the dimer, viz. the polarizability, hyperpolarizability and higher polarizable terms. The low vibrational frequencies have been determined by high level calculations but, due to the large amplitude motions, the harmonic predictions are only a rough estimate, therefore further calculations have been carried out using a large number of potential energy points to construct an analytical multi-dimensional potential energy surface[93,98] and a semi-empirical surface[78] both based on the *ab initio* data of Kofranek et al.[110] The results of Quack and Suhm[77] were empirically adjusted to fit the experimental data. The complexity involved in the dynamics of the non-rigid nature of the dimer rendered the calculations difficult and hence they could not predict the tunnelling quenching upon vibrational excitation,[112] but recent gas phase studies[113] suggest the monomers to be uncoupled during the tunnelling motion. Generally the high resolution microwave and infrared studies have led to an accurate determination of the vibrational frequencies and structural parameters, as well as the dissociation energy, which compare well with the high level *ab initio* calculations to date.

3.2 *The HCl Dimer*

The HCl dimer has been studied in the gas-phase, in the infrared region by Ohashi and Pine[114]. They assigned two bands, the free HCl and the bonded HCl stretching vibrations. Pine and Howard[115]found the binding energy to be 431 $\pm$ 22 cm^{-1} (5.1 $\pm$ 0.3 kJ mol^{-1}) with the tunnelling splitting estimated between 9 and 14 cm^{-1}, and they concluded the bent C_s geometry to be lower in energy than the C_{2h} transition state structure, with a barrier height of 1 kJ mol^{-1}. The first far infrared spectrum of the dimer in inert gas matrices was published by Katz et al[116]. Their finding suggested the dimer to be either collinear or cyclic in geometry, due to the lack of experimental data available for studying the intermolecular vibrational modes, hence they did not completely characterise the dimer. The matrix studies by Barnes et al[117] and Maillard et al[118-120] supported the linear C_s equilibrium configuration for the dimer in nitrogen and noble gas matrices. Furlan et al[121] refined the study of Katz et al[116], in the 13.9 -15.9 cm^{-1} spectral range using the coherent anti-Stokes Raman spectroscopic (CARS) technique, confirming the vibrationally averaged geometry inferred by Ohashi and Pine[114]. In conjunction with these gas-phase studies there have also been theoretical studies by Gomez and Bunker[122] on the potential energy surface (PES) characterising the internal dynamics in the HCl dimer. Gomez et al carried out rigid bender calculations on the PES using the minimum energy tunnelling path for the HCl dimer[123], adjusting the potential to fit the experimental intermolecular modes[124] using the adiabatic approximation, and in later studies without the adiabatic approximation[122] they obtained a dissociation energy of 336 cm^{-1} (4.02 kJ mol^{-1}), much lower than the gas-phase results[115]. Althorpe et al[125] used both *ab initio* and the electrostatic angular potential method with a three-dimensional variational calculation to predict the tunnelling dynamics and far infrared spectrum. Their prediction for the ground state tunnelling splitting was in good agreement

with that of Gomez et al[123]. Schuder et al[126] also reported an infrared study of the dimer in its excited state as well as a theoretical model for the large amplitude internal rotor dynamics of the dimer. Their findings were similar to those of Althorpe et al[125]. The early *ab initio* studies, carried out at the SCF level of theory, focused on the geometrical optimization,[58,108,109] locating a linear C_s bonded structure for the dimer. Frisch et al[127] also established a C_{2h} saddle point for the dimer, with the inclusion of correlation, having a C_s minimum energy structure.

3.3 *The H_2O Dimer*

The water dimer is probably the most important vdW dimer and accordingly has received much experimental[128-136] and theoretical[94,108,109,127,137-155] attention. The earliest matrix isolation experiments in nitrogen matrices[129] suggested a cyclic dimer configuration since the authors observed only two bands in the OH stretching and one in the HOH bending regions. Further matrix studies by Fredin et al[132] at a higher resolution located more dimer bands in the monomer stretching region, suggesting a linear bonded dimer configuration. This result was also consistent with the argon matrix spectra.[128,130,131]

There have been numerous gas-phase studies on the dimer. The earliest microwave spectra by Odutola and Dyke[135] estimated the intermolecular stretching mode from the centrifugal distortion constants. These studies also established a near linear hydrogen bond for the dimer. The tunnelling motions, however, could not be assigned at that time, but since then numerous models have been established to give assignment to the tunnelling motions of the dimer[150]. The experimental estimate[136] of the binding energy, D_e, at the equilibrium geometry was found to be 20 ± 3 kJ mol^{-1}. *Ab initio* studies by van Duijneveldt and co-workers[148] obtained a D_e value of 20 kJ mol^{-1} at the MP2 level of theory. Chakravorty and Davidson[154], also at the MP2 level, obtained a value for D_e between 16 and 18 kJ mol^{-1} using different basis

sets from those of van Duijneveldt and co-workers[148]. All theoretical calculations on the dimer[94,108,109,127,139-145] determined the linear bonded structure to be most stable at all levels of theory. Recent studies by Muguet et al[146] found the bifurcated dimer to be a local minimum at the SCF level of theory and suggest this structure to be the transition state for the proton interchange within the dimer, however Marsden and co-workers[145] could not reproduce their findings at the same level of theory and with the same basis functions, hence concluded that the bifurcated structure is not a minimum energy structure. The water dimer has also served as a model for studying the merits of the density functional theory (DFT).[137,138]

3.4 *The H_2S Dimer*

The H_2S dimer has been studied in the gas phase by Odutola et al,[156] who suggested the dimer to have C_{2v} geometry, but definite structural parameters could not be determined. The gas-phase ultraviolet photoelectron spectroscopic study by Pradeep and Rao[157] reported ionization energies from the first and second ionic states of 10.95 and 9.75 eV (1057 and 941 kJ mol^{-1}), in good agreement with the results of Sodupe et al[158]. Matrix isolation experiments were carried out in nitrogen[159], argon[160] and oxygen[161] matrices. The dimer vibrational modes in the nitrogen matrices were in closer agreement with those in the oxygen matrix than those in the argon matrix. The theoretical studies[127,162-164] predicted a C_s geometry for the dimer, which was supported by the matrix isolation results[159,161]. The most recent study on the dimer by Oliviera and Dykstra[164] using the molecular mechanics for clusters theory, concluded a linear hydrogen bonded structure for the dimer. The H_2S molecule is found to interact with molecules via dipole-quadrupole type interactions, whilst the corresponding complexes of water interact mainly through dipole-dipole type interactions.

The study by Frisch et al[127] at the SCF/6-31+G* level obtained a binding energy of 3.8 kJ mol^{-1} and of 3.4 kJ mol^{-1} at the MP4/6-31+G* level.

3.5 *The NH_3 Dimer*

The ammonia dimer has been subjected to several matrix isolation,[165-171] gas-phase,[172-180] and theoretical studies.[59,71,108,181-195] A great deal of controversy lies in the structural determination for the dimer. The suggested configurations for the dimer comprise the linear classical, the C_{2h} and the "Klemperer" structures[172]. The classical hydrogen bonded structure was supported by the early matrix isolation experiments of Pimentel et al[165] and by Ribbegard[166] who also assigned the vibrational modes. The MBERS study by Odutola et al[173] on NH_3 polymers ruled out the C_{2h} structure, due to the polar nature of the dimer, and suggested that the classical structure was more consistent with their findings. Klemperer and co-workers[172,174,175] interpreted their microwave spectra and concluded the dimer to have an asymmetric cyclic structure, which disagreed with the *ab initio* calculations[59,71,108,180-185,187-194] and matrix isolation studies[165,166,169-171] except with those of Andrews[167,168]. The only theoretical study in support of the Klemperer structure was that of Sagarik, Ahlrichs and Brode[186]. The calculations carried out by Sagarik et al[186] used the triple-zeta basis set at both the SCF and coupled pair functional (CPF) levels of theory. They found the Klemperer structure to be the minimum at the SCF and CPF levels of theory. However they varied only three of the eleven independent geometrical parameters in their work and did not use gradient techniques, so they did not locate any minima. They also fixed the hydrogen bond angle at 180°, thereby destabilising the classical bonded dimer, which led them to conclude that it was a saddle point, therefore the Sagarik[186] structure is not justified. Hasset et al[187] re-optimised the Klemperer structure using very large basis sets at high levels of theory and disproved the results of the Sagarik[186] study, and found the linear bonded dimer to be more

stable than that of Sagarik et al[186].

Suzer and Andrews[167] carried out matrix studies in Ne, Ar and nitrogen matrices, and found the dimer to be rigid, in support of the Klemperer structure. The matrix work by Barnes[170] disagreed with that of Suzer and Andrews[167], suggesting the dimer bands were due to an electron donor-acceptor complex with an open chain-type structure rather than the asymmetric cyclic structure. Klemperer assumed the dimer to be rigid in structure with no NH_3 inversion motion. The NH_3 umbrella motion in the dimer was observed to be partly quenched, since energy splittings occurred, and it is known that in most NH_3 complexes, except Ar-NH_3, inversion motions are not present[177,178]. Havenith et al[177] and Loeser et al[178] dismissed the Klemperer structure and were supported by the theoretical calculations of van Bladel and co-workers,[189] who reported the vibrational-rotational-tunnelling (VRT) dynamics of the dimer. They established the complex to be flexible, with proton acceptor interchange via a C_{2h} geometry leading to the C_s minimum. This C_s geometry was also found to be most stable by Hassett et al[187]. Thereafter Tao and Klemperer[194], using bond functions at the MP2 level, concluded the C_{2h} structure to be a minimum and not a transition state, thus contradicting the results obtained by van Bladel[189]. Similar calculations to those of Tao and Klemperer were performed by Cybulski[195], using bond functions with larger basis sets, augmented with nuclear centred basis functions. He arrived at the conclusion that the C_s linear is more stable than the C_{2h} cyclic structure. Olthof et al,[191,192] using the experimental results of Loeser[178] and Havenith[177], confirmed the energy splitting and concluded the non-rigidity of the dimer and that the vibrational averaging does effect the dipole moment. Dipole measurements by Linnartz[180] using the G_{144} point group incorporating VRT dynamics led to the conclusion that the dimer is likely to be cyclic as a consequence of vibrational averaging. Even though all the far infrared and microwave wavenumbers have been assigned there are still not enough structural data on the dimer to support or contradict the Klemperer model[172].

3.6 *The PH_3 Dimer*

Unlike the ammonia dimer the phosphine dimer has a single minimum energy structure on the HF/6-31+G* potential energy surface[127], having C_{2h} symmetry, bound by 1.2 kJ mol^{-1}. The early theoretical studies[108,109] with the 4-31G basis set at low levels of theory predicted the dimer to be bound by 3.2 kJ mol^{-1}. The dimer was found to be bound by only the van der Waals-type forces. No experimental data on this complex have been discovered.

3.7 *The CH_4 Dimer*

The methane dimer, comprising non-polar molecules, is bound by dispersive forces. The anisotropy of the methane-methane interaction[196] makes it difficult for the determination of the compressibility of gaseous methane, therefore most of the theoretical studies concentrated on the development of intermolecular potentials,[197,198] assisting the experimentalists in determining thermodynamic properties. From the crystal structure the intermolecular interaction potential near a local minimum structure can be estimated regardless of the other regions on the PES. *Ab initio* molecular orbital theory allows such anisotropy to be evaluated throughout the PES. Williams and Craycroft[199] reported the structure of the dimer to comprise an H...H interaction and established the dimer to be unbound at the SCF level of theory. Higher level theoretical calculations[197,200] predicted the face-to-face orientation of the dimer to be the most favoured structure. The authors also established that the interaction is repulsive at the SCF level due to the large exchange repulsion forces, however at the correlated level, the attractive dispersion forces are larger than the exchange repulsion, thus stabilising the dimer. The theoretical studies of Tsuzuki and Tanabe[201] were limited to two dimer orientations, one involving a CH...HC staggered interaction and a double bifurcated structure with two H...C interactions, hence their results are not conclusive. Nagy et al,[198] using MP2 theory, together with their $MP2^{(corr)}$ theory, studied 99 dimer configurations with

a medium basis set and located the global minimum structure of Szczesniak et al[200]. Further theoretical studies[202] suggested that at higher levels of theory and with larger basis sets the dispersion contribution would be improved, without commenting on the global minimum structure. Experimental gas-phase studies[203] established the dimer to be bound with a potential well depth of 1.6 kJ mol^{-1}.

3.8 *The SiH_4 Dimer*

The SiH_4 dimer has been studied in the gas phase by means of infrared photodissociation experiments[204] using CO_2 laser light in the range 880-1100 cm^{-1}. The D_e value was estimated to be about 221 cm^{-1} (2.64 kJ mol^{-1}).[205] Van Bladel and van der Avoird[205] demonstrated the mechanism by which the monomers couple using an atom-atom potential. These dimers were found to be bound by dispersion.

3.9 *The HF.HCl Complex*

The HF.HCl complex has been studied experimentally[206] and theoretically.[17,108,207,208] The microwave study by Janda et al[206] found the most stable structure with the HCl molecule proton donor to the HF molecule, having a hydrogen bond stretching force constant of 5.7 N m^{-1} and a hydrogen bond length of 212 pm. The theoretical study by Kollman et al[108] predicted the F...Cl distance correct to ± 1 pm from the experimental value using the 4-31G basis set, with the hydrogen bond angle differing by 10° from the experimental value. Later theoretical studies[17,207,208] also supported the structure with HF proton donor to the HCl molecule. The theoretical study, using intermolecular potentials, by Girardet and co-workers[207] reported the ClH.FH to be more stable than the FH.ClH complex by 0.6 kJ mol^{-1}.

3.10 *The $HSH.OH_2$ Complex*

This complex has the hydrogen sulphide molecule as the proton donor to the water molecule, since H_2S is a stronger acid than H_2O.[108] The experimental matrix isolation studies confirm the 1:1 complex in argon,[209] and in nitrogen matrices.[210] There is also evidence for the reverse structure in the argon matrix.[209] There have been several theoretical studies predicting H_2S to be the proton donor.[108,139, 211,212] The early studies by Kollman et al[108] were carried out at the SCF level. Later studies by Del Bene[139] reported the enthalpies of formation for the $HSH.OH_2$ and $HOH.SH_2$ complexes from the isolated monomers to be -6.0 and -5.2 kJ mol^{-1} respectively at the MP4/6-31+G(2d,2p) level of calculation.

3.11 *The $NH_3.PH_3$ Complex*

The ammonia-phosphine complex, with ammonia the proton donor to phosphine, has been studied by Kollman et al[108] using the 4-31G basis set at the SCF level of theory, obtaining a binding energy of approximately 9 kJ mol^{-1} and 4.4 kJ mol^{-1} for the complex with phosphine proton donor to the ammonia molecule. Del Bene[71] found that both structures were unstable at room temperature and that correlation increased the binding energies. Two minima were found, one with C_1 geometry and with NH_3 the proton donor, and the other with C_s symmetry and with PH_3 the proton donor.

3.12 *The $H_2O.HF$ Complex*

This complex was first observed in the gas phase by Bevan et al,[214] who later[215] determined the structure, establishing a $FH...OH_2$ pyramidal orientation at the oxygen atom. Gas-phase studies[216] established the dissociation energy to be 42.9 $\pm$ 8 kJ mol^{-1}. The early matrix study by Thomas[217] identified the dimer as having a C_{2v} planar geometry with a dissociation energy of 30 $\pm$ 7 kJ mol^{-1} from the intensity measurements. Further matrix studies by

Andrews and Johnson[218] were in agreement with the gas phase studies, supporting the pyramidal structure, and the inversion doubling observed in the HF librational modes confirmed the C_{2v} geometry to be a vibrationally averaged structure with a low inversion barrier. There have been numerous theoretical studies[108,139,219,220-224] which also supported the C_s minimum energy geometry in agreement with the Legon-Millen rules[21,225].

3.13 *The $H_2O.HCl$ Complex*

This complex has been characterised by the matrix studies of Ault and Pimentel[226] and Ayers and Pullin[227] in nitrogen and argon matrices. The authors agreed upon the formation of a weak hydrogen bonded structure. In the nitrogen matrix the formation of an $N_2.HCl$ complex was also observed due to the perturbation of the HCl stretching band.[226] The matrix studies, coupled with theoretical calculations, by Schriver et al,[228] confirmed the vibrationally averaged structure for the dimer to be C_{2v} and provided evidence for a 1:1 complex having a C_s equilibrium structure in argon and nitrogen matrices.[228] The microwave measurements by Legon and Willoughby[229] concluded the vibrationally averaged structure to have C_{2v} symmetry with planar orientation about the oxygen atom. Theoretical studies both at the SCF level and at correlated levels of theory predict a C_s equilibrium geometry.[139,220,230-232]

3.14 *The $H_2S.HF$ Complex*

Gas phase studies by Viswanathan and Dyke[233] and Willoughby et al[234] provided evidence for the C_s geometry, having an approximately right angled pyramidal structure. The former authors also proposed from the ground state rotational spectra that there was no evidence for proton inversion between the two equivalent sulphur lone pairs of electrons. Matrix studies by Arlinghaus and Andrews[235] supported the gas-phase studies for the predicted structure. A stable reverse structure was also observed with H_2S as proton donor to HF[235]. Theoretical

studies[108,223,236-238] also support the experimentally observed geometry. Dispersion was found to play a major role in the interaction energy[237]. The structure of the complex results partly from dipole-quadrupole interaction, unlike the water complexes which are governed by dipole-dipole interaction[236].

3.15 *The $H_2S.HCl$ Complex*

Microwave studies by Goodwin and Legon[239] supported a C_s minimum energy structure for the complex, with a high barrier to inversion. Theoretical studies[21,223,231,237] also supported this structure. The dispersion contribution was shown[237] to dominate the interaction energy as in the case of the $H_2S.HF$ complex.

3.16 *The $NH_3.HF$ Complex*

The $NH_3.HF$ complex has C_{3v} geometry, as was shown by a number of theoretical[71,107,108,181,240] and matrix isolation experiments.[241-243] The earlier calculations[107,108,181] as well as more recent ones,[71,240] including correlation, arrived at the same structure for the complex. Del Bene[71] reported a binding energy of 52 kJ mol^{-1}, whilst that of Kollman et al[108] was 65 kJ mol^{-1}. Matrix isolation experiments[241-243] support the theoretical prediction, displaying the doubly degenerate nature of the HF librational mode at 916 cm^{-1} and its overtone at 1679 cm^{-1}.

3.17 *The $NH_3.HCl$ Complex*

The reaction between ammonia and hydrogen chloride has been subjected to numerous studies, including gas-phase,[244,245] matrix isolation[246,247] and theoretical *ab initio* molecular orbital calculations.[108,248-254] The first *ab initio* SCF study by Clementi[248] showed the dimer to be hydrogen bonded. In 1968 Goldfinger and Verhaegen[244] obtained the first experimental

evidence for complex formation from mass spectroscopic studies and proposed a dissociation energy of 42 ± 12 kJ mol^{-1}. Ault and Pimentel[246] carried out matrix isolation experiments in nitrogen and confirmed the hydrogen bonded structure with an estimated disociation energy of 60 ± 20 kJ mol^{-1}. Kollman et al[108] reported a dissociation energy value of 49 kJ mol^{-1} at the SCF level of theory. The first calculation at the correlated level was that of Raffenetti and Phillips,[250] who located a C_{3v} structure for the complex, as was obtained by the earlier studies, and suggested a small degree of proton transfer from HCl to the nitrogen atom of the ammonia molecule. Latajka and Scheiner[251] found both the ionic and hydrogen bonded complexes to be minima at the SCF level, with the former being more stable energetically. At the correlated level the hydrogen bonded structure was favoured. Barnes and co-workers[247] noticed a greater degree of proton transfer than that predicted by Raffenetti and Phillips[250]. The proton transfer was also shown to be induced by the nature of the matrix. The degree of proton transfer is lowered more in argon than in nitrogen. Their[247] spectra in nitrogen agreed with those of Ault and Pimentel[246]. Most recently the study by Corongiu et al,[254] using density functional methods, predicted the dimer binding energy to be 20 ± 2.0 kJ mol^{-1}.

3.18 *The PH_3.HX Complexes (X = F,Cl)*

The PH_3.HX series has been studied in the gas-phase, by matrix isolation[255] and *ab initio* calculations.[107,108,181,256-261] The gas phase[261,262] studies detected formation of PH_3.HX complexes. The complexes have C_{3v} geometry, with a linear XH...P bond. Similar to the NH_3.HX complexes, the early theoretical studies at the SCF level of theory overestimated the binding energies of these complexes. Recent studies at the correlated level gave a better description of the interaction energy, with dispersion effects. The matrix isolation studies of Arlinghaus and Andrews[255] confirmed the C_{3v} complex geometry, by the observation of the

HF librational mode at 477.3 cm^{-1} and its overtone at 843 cm^{-1} in the PH_3.HF complex. In the PH_3.HCl complex the librational mode occurred at 336 cm^{-1} with its overtone at 587 cm^{-1}.

3.19 *The MH_4.HX Complexes (M=C, Si, X=F, Cl)*

The structures of the MH_4.HX complexes have been characterised by pulsed-nozzle Fourier transform microwave spectroscopy[263,264] and some of the bands in the infrared spectra of the MH_4.HF complex in solid argon have been assigned.[265-268] *Ab initio* calculations were also carried out for the complexes in order to predict their structures.[263,266-270] Davis and Andrews[266-268] carried out matrix experimental work as well as *ab initio* calculations on the MH_4.HF species, characterising the structures. The CH_4.HCl complex has been characterised by Oshima and Endo[264] and Legon et al[263] in the gas phase, as well as by matrix isolation by Barnes,[265] identifying it by the increase in the intensity of a band at 2855 cm^{-1}, which occurs at the same position as a HCl dimer band. To date there has been only one *ab initio* study of the SiH_4.HCl complex[270,271]

3.20 *The $NH_3.H_2O$ Complex*

The water-ammonia complex has been studied in the gas phase by Fraser and Suenram[272] who found the binding energy to be greater than 1021 cm^{-1} (12.21 kJ mol^{-1}), that of the CO_2 laser frequency used to excite the complex. Matrix isolation studies by Nelander and Nord[273] in nitrogen and argon matrices led to the conclusion that water is the proton donor to NH_3, since wavenumber shifts occurred in the water molecule stretching region and in later studies[274] of the complex in Ne and Kr they assigned the vibrational modes down to 10 cm^{-1}. The complex has also been studied both by matrix isolation and *ab initio* by Yeo and Ford[275,276]. The earlier *ab initio* studies[71,139,181] neglected correlation effects but did find the water molecule to be the proton donor to the ammonia molecule, as was observed by the

recent studies.[275-277]

3.21 *The $PH_3.H_2O$ Complex*

This complex was first studied theoretically by Kollman et al[108], having H_2O proton donor to the PH_3 molecule. A later study,[139] which included correlation effects through perturbation theory, could not locate the reverse structure, involving PH_3 as proton donor to the water molecule.

3.22 *The $NH_3.H_2S$ Complex*

The $NH_3.H_2S$ complex has been studied in the gas phase by Hilpert et al[278], and they concluded that there was proton interchange. The barriers for the proton interchange and NH_3 internal rotation were found to be 510 cm^{-1} (6.10 kJ mol^{-1}) and 5 cm^{-1} (0.06 kJ mol^{-1}) respectively. The proton interchange motion consisted of a partial internal rotation of the H_2S about its inertial axis, through a bifurcated, doubly hydrogen-bonded transition state. The authors also placed an upper bound on the zero-point bond dissociation energy of 992.5 cm^{-1} (12.0 kJ mol^{-1}).[278] The large amplitude barrier to proton interchange also suggested a stronger hydrogen bond than that in the $HOH.NH_3$ complex. The earlier study by Herbine et al[279] also found a nearly linear hydrogen bonded structure, with free NH_3 internal rotation, however they did not find any evidence of H_2S proton exchange in their microwave study. The barrier for proton exchange for $H_3N.HOH$ was found by Stockman et al[280] to be 700 cm^{-1} (8.40 kJ mol^{-1}). *Ab initio* calculations at the MP4/6-31+G(2d,2p) level by Del Bene[71] reported a C_s structure and concluded that the diffuse functions stabilised the binding energies. The enthalpy of formation for the complex from the monomers was found to be -4 kJ mol^{-1}.[71] The early calculations[108,109] on the complex at the SCF level of theory using the 4-31G basis set reported a binding energy of 18 kJ mol^{-1}, which was not corrected for BSSE

nor for correlation effects.

3.23 *The $PH_3.H_2S$ Complex*

The phosphine-hydrogen sulphide complex has been studied most recently by Sodupe et al[158] at the MP2 level of theory. The structure found to be most stable was that with H_2S donating a proton to the PH_3 lone pair electrons with a staggered conformation. With the MC-311(d,p) basis set, the binding energy was found to be 5.2 kJ mol^{-1} using modified couple pair functional theory.

3.24 *The $CH_4.H_2O$ Complex*

Water-hydrophobe interactions govern essential features of many biochemical and chemical systems. The $CH_4.H_2O$ system is the simplest hydrocarbon-water cluster and is closely related to the $Ar.H_2O$ complex since the charge distribution in methane is spherical, with the octupole moment being the lowest non-vanishing multipole moment. This system has been studied by microwave[281] and vibrational spectroscopy[282]. The microwave studies support a typical bent hydrogen bonded structure with H_2O being the proton donor to the methane molecule, with an inter-monomer stretching force constant of 1.53 N m^{-1}. The far infrared studies were incapable of providing an accurate assignment to the vibrational-rotational-tunnelling (VRT) bands because a more sophisticated *ab initio* site-site potential was required to fit the VRT energy level diagram. The authors also suggested that methane underwent hindered rotations in the complex. There have been many theoretical studies[106,283-290] on the structure of the complex, the earliest of which were either limited to inflexible basis sets or did not account for BSSE,[106,283,284,290] except for a few studies.[285,286-289] Latajka and Scheiner[289] demonstrated the importance of the BSSE, which accounted for almost half the interaction energy in the $H_3CH.OH_2$ complex. Several studies[106,283-285,287-290] found the CH_4

molecule to be the proton donor and the detailed study by Szczesniak et al[286] located two minima on the potential energy surface, one having the CH_4 molecule as the proton donor as in the case of a conventional hydrogen bond, the other having H_2O as the proton donor to the face of the methane tetrahedron. The latter structure was thought to be governed by dipole-octupole interactions but the charge penetration effects in the vdW region were found to be large due to the exchange repulsion.[286] Sennikov et al[290] established the correlation effects to account for 48% of the binding energy in the CH...O bonded complex.

3.25 *The $CH_4.H_2S$ Complex*

The $CH_4.H_2S$ complex has been studied theoretically at the SCF level, with methane being found to be the proton donor to the sulphur atom of hydrogen sulphide[108]. Recent studies at the second order level of perturbation theory by Woon et al[284] located a structure in which H_2S is the proton donor to the carbon atom of methane. This study, however, did not include a search for a minimum energy structure for the complex.

3.26 *The $SiH_4.H_2O$ Complex*

The $SiH_4.H_2O$ complex was studied by Sennikov et al[290] and this is the only theoretical work carried out to date, with no experimental studies reported either in the gas phase or in the matrix isolated state. This study did not account for BSSE,[290] but showed that correlation accounted for 36% of the binding energy. The charge transfer occurs from the water to the silane molecule, the extent of charge transfer being more than that in the methane-water complex. The attractive Si...O force balances the repulsive H...O forces.

3.27 *The $CH_4.NH_3$ Complex*

The first theoretical studies,[10,108] carried out at the SCF level, which neglected correlation effects, located the minimum energy structure corresponding to a CH...N type interaction with a staggered C_{3v} geometry. Sokalski[291] included dispersion effects via the molecular expansion terms, which are inaccurate when used with minimal basis sets. His results also supported the early studies. Orozco and Luque,[292] using the monopole-monopole model with the 6-31G** basis set at the semi-empirical level of theory, showed the electrostatic component of the interaction energy to be the major attractive force in the complex. Later Yan and co-workers[287], using perturbation theory, explored various orientations for the dimer and their minimum energy structure corresponded with the results of the earlier studies. They obtained a corrected binding energy of 2.0 kJ mol^{-1} for the complex. There have been no experimental results to date for this complex.

3.28 *The $SiH_4.NH_3$ Complex*

It is well known that the Lewis acid silane forms stable complexes with Lewis base amines.[293] Adducts involving trimethylamine with silane have been detected using vapour pressure measurements at low temperature in the gas phase[294]. The silane-ammonia adduct has been studied at room temperature in the gas phase by the mass spectroscopic technique by Rossi and Jasinski[295]. Thus far only the $SiF_4.NH_3$ adduct has been characterised under matrix isolation conditions[296]. Gordon et al[297], using semi-empirical and *ab initio* methods, obtained a C_{3v} minimum for the complex with a Si...N interaction at the MP2/6-31G* level of theory, consistent with the results obtained by Rossi and Jasinski[295] using the MP4 level of theory. They however had allowed geometrical relaxation in the dimer and observed a C_s minimum which was less stable than the C_{3v} structure.

3.29 *The $SiH_4.H_2S$, $SiH_4.PH_3$ and $CH_4.PH_3$ Complexes*

No studies, either experimental or theoretical, investigating these three complexes have been reported. The study of these complexes is the first to be undertaken and it provides an understanding of the natures of these types of molecular interaction.

Chapter Four

4.1 *Ab initio Molecular Orbital Calculations - Practical Aspects*

The Gaussian series of programs[298-306] was developed to provide fast and accurate ab initio molecular orbital calculations, using Gaussian-type functions. The first program in the GAUSSIAN series, GAUSSIAN 70[298] was introduced in 1970, and was only able to perform geometry optimizations by cyclic variation of all structural parameters. The early versions of the GAUSSIAN program[298,299] could perform only SCF calculations. With the rapid advancements in computer hardware, numerous changes were made over the years to the GAUSSIAN suite of programs[300-306], continuously upgrading the levels of calculations available, to include many post SCF methods and optimization methods, providing results which are of high accuracy in a limited amount of computational time.

The *ab initio* calculations in this study were performed using the GAUSSIAN 92[306] computer program. The program features a set of built in basis functions for each atom, representing the atomic orbitals. The input required for the computation comprises the route card, describing the level of theory and type of basis set to be used for a particular calculation, followed by the total charge and multiplicity, and finally the molecular structure, either in Cartesian or Z-matrix coordinates. The geometry optimization procedure used in this project was the Berny optimization scheme developed by Schlegel.[307] The Berny optimisation method uses analytically calculated atomic forces and a guessed force constant matrix, which is continuously updated during the optimization, to predict the position of the energy minimum. The Murtaugh-Sargent (MS)[308] optimisation was also employed in those cases where the Berny method failed to locate a minimum energy structure. The MS method does not rely on a guessed force constant matrix, and also uses analytically evaluated atomic forces, but employs a different strategy to predict the minimum energy structure. The MS method basically allows smaller stepsize increments in the determination of the minimum

energy structure of the system under study during the cyclic optimisation procedure. This aids in achieving geometry structure convergence in systems having very flat potential energy surfaces. In addition the TIGHT and VERYTIGHT convergence criteria were applied, which reduce the limits that are used to determine convergence in the optimization cycle. This process improves the accuracy of the converged structure and hence the vibrational force field. The output of any geometry optimization comprises the optimized Cartesian coordinates, given in standard orientation, the RHF and MP2 energies, the Mulliken population analysis, the dipole and higher order multipole moments and the structural parameters for the converged geometry. The calculated interaction energies have to be corrected for the BSSE, using the counterpoise technique of Boys and Bernardi[53]. This correction is carried out using the MASSAGE keyword in the route card of the input file, setting the atoms of each molecular sub-unit in turn to have zero charge. The scheme for obtaining the Mulliken charges has been criticised, since the charges are averaged among the electronegative and electropositive atoms, however it does provide qualitative information regarding the path of charge density.[309] Each minimum energy geometry was tested to ascertain whether the structure was indeed a stationary point on the potential energy surface, using the FREQ option in the route card. A set of harmonic vibrational wavenumbers, the eigenvalue matrix, the force constant matrix in both Cartesian and internal coordinate space, and the dipole moment derivatives are produced on executing the FREQ keyword.

The later Gaussian 94 program includes the density functional methods in performing geometry optimization using the Kohn-Sham type orbitals.[310]

4.1.1 *The Basis Set Superposition Error*

In the calculation of the interaction energy, $\Delta E_{AB}(r)$, for weakly bound systems, A and B, separated by a distance r, the energy difference is given by

$$\Delta E_{AB}(r) = E_{AB}(r) - E_A - E_B$$

where E_{AB} is the energy of the supermolecule AB and E_A and E_B are the energies of the separated monomers A and B. The energy of the dimer is determined with all orbitals of A and B. The basis set of each monomer is therefore extended by the presence of the other, resulting in a mathematical lowering of the monomer energies, referred to as the BSSE. The equation

$$\Delta E' = E_{AB} - (E'_A + E'_B)$$

takes BSSE into account, where

$$\text{BSSE} = (E_A + E_B) - (E'_A + E'_B)$$

$$= \Delta E' - \Delta E$$

A negative value for ΔE implies an attractive interaction. Hence a positive BSSE implies an attractive interaction. To account for the BSSE, the counterpoise method of Boys and Bernardi[53] is used. Alternative methods have been suggested[56,94,311-314], but the counterpoise method is still the most widely used. Schwenke and Truhlar[56] suggested the use of polarisation counterpoise correction, involving the use of polarisation functions on A and B. Frisch et al[94] concluded that the basis set should be increased to its maximum size possible in order to decrease the BSSE. A number of corrected counterpoise schemes using only the non-occupied functions in the individual molecules have been employed [56,313,314] to avoid the

BSSE overestimation. Davidson and Chakravorty[315] suggested an alternative description for the BSSE using the extended basis sets at the RHF and MP2 levels.

4.1.2 *Energy Decomposition Analysis*

The energy decomposition calculations, involving the partitioning of the RHF interaction energy into components,[10,316] viz. electrostatic (ES), charge transfer (CT), polarization (PL), the higher multipolar interaction (MIX) and the exchange repulsion (EX), were carried out with the MONSTERGAUSS computer program[317]. In order to perform the decomposition analysis the molecular complex first had to be optimized to a stationary point with the Gaussian 92 program. The final optimized structural parameters from the Gaussian calculation were used in the form of a Z-matrix for the energy decomposition calculation. The energy decomposition analysis does not account for the dispersion contributions, and the flaw in this analysis is that the valence electrons from one fragment can collapse into the outer shell of the other, thus violating the Pauli principle. Hence a very careful interpretation must be made for the energy decomposed terms, The decomposition terms are as follows.

4.1.2.1 **Electrostatic Term (ES)**

This type of interaction, either attractive or repulsive, occurs between the undistorted electron cloud of a monomer A and that of monomer B. This contribution includes the interaction of all permanent charges and multipoles, such as dipole-dipole, dipole-quadrupole, etc.

4.1.2.2 **Polarisation Term (PL)**

The effect of distortion of the electron cloud of monomer A by B, and vice versa, is termed the polarisation interaction. This attractive component includes interactions between all permanent charges, or multipoles and induced multipoles, viz. dipole-induced dipole, quadrupole-induced dipole, etc.

4.1.2.3 **Exchange Repulsion Term (EX)**

This short range repulsive interaction is caused by the exchange of electrons between monomer A and B due to the overlap of electron distributions.

4.1.2.4 **Charge Transfer Term (CT)**

This interaction results from the electronic delocalization from the occupied molecular orbitals of monomer A to the vacant orbitals of monomer B.

4.1.2.5 **Mixing Term (MIX)**

The difference between the total SCF interaction energy and the sum of the above four components accounts for the higher order interactions between various components.

4.1.3 *The Normal Coordinate Analysis*

All normal coordinate analysis calculations were carried out using the VIBRA 90 computer program.[318] The theoretical development is presented in Chapter 2. The Gaussian 92 program provided the force field in Cartesian coordinates, using the FREQ option. A system of internal coordinates and a U matrix were generated using the rules of Wilson et al.[70] The internal force constants were all output in units of mdyne $Å^{-1}$, which were then converted to N m^{-1}. The output also yielded the potential energy distribution and the symmetry force constant matrix.

4.1.4 Infrared Band Assignments and Nomenclature

To assist in the assignment of the calculated vibrational modes, the normal coordinate analysis calculations were carried out using the *ab initio* force field. The Cartesian displacement vectors for each mode from the FREQ calculation, summed with the equilibrium Cartesian coordinates of the atoms yielded the coordinates of the atoms of the molecule for each normal mode of vibration. This set of coordinates was represented pictorially by using the SCHAKAL-92 computer program,[319] thus generating a set of plots of the forms of the vibrational modes. The PED obtained from the VIBRA 90 computer program provided an accurate description of the nature of a particular vibrational mode.

4.1.5 *Execution of the Computer Programs*

All calculations involving the use of the GAUSSIAN 92 program, as well as the VIBRA 90 and MONSTERGAUSS programs, were carried out on a Hewlett-Packard 720 computer. The program SCHAKAL-92, used to obtain pictorial representations of the equilibrium structures and the normal modes of vibrations, was implemented on an IBM personal computer interfaced with a Hewlett-Packard Laserjet IIIP printer.

4.2 ***Matrix Isolation Infrared Spectroscopy - Practical Aspects***

4.2.1 *Matrix Isolation Equipment*

The cryogenic system comprised an Air Products Displex model CSA-202 two stage closed cycle helium refrigerator linked with a model APD-B temperature controller. Temperatures was measured with a chromel vs gold doped with 0.07 atomic per cent iron thermocouple which was internally compensated for the cold junction potential. The KBr or CsI infrared windows were held in the sample holder unit in the vacuum shroud. Two 6 mm diameter stainless steel gas inlet lines, entering the shroud through two fine nozzles, allowed for the simultaneous deposition of the separate gas mixtures onto the KBr or CsI window. The gas

flow rates were controlled by micrometer needle valves (Whitey, 22RS4), monitored by an Edwards thermocouple gauge. The vacuum in the shroud was measured by means of a Penning 8 vacuum gauge connected to a model CP25 S gauge head (Edwards), measuring in the pressure range 10^{-2} to 10^{-7} mmHg.

4.2.2 *The Infrared Spectrometer*

All spectra were recorded using a Bruker IFS 88 spectrometer, interfaced with a CS-03 infrared data station, at a resolution of 0.5 cm^{-1} in the range 4000 cm^{-1} to 400 cm^{-1}. The OPUS 2.0 software package, running under the OS/2 operating system was supplied with the data station and was used for the recording and manipulation of all spectral data.

4.2.3 *Sample Preparation*

4.2.3.1 **The Vacuum Line**

The samples used in the matrix isolation experiment were prepared in a glass vacuum line using standard manometric methods. The vacuum in the glass line was maintained by means of an Edwards two stage Diffstak (model 63) oil diffusion pump, which was protected by four liquid nitrogen traps and an Edwards E2M2 roughing pump. The pressure down to the 10^{-3} mmHg range was measured by means of a Pirani-10 vacuum gauge connected to a PR-10 S gauge head (Edwards) built into the vacuum line. Lower pressures, down to the 10^{-6} mmHg range, were measured by means of an Edwards Penning 505 gauge connected to a CP25-EX Edwards gauge head which was also built into the vacuum line. A digital pressure read-out attached to an Edwards EPS 10 gauge head was also built into the vacuum line. This was used to estimate the total gas pressure in the glass sample vessel. Ambient temperatures were measured by means of a digital read-out attached to a temperature sensor. Gases used in the sample preparation were received from the suppliers in lecture bottles which were attached to the vacuum line by a length of 6mm diameter teflon vacuum tubing. The connection of

the teflon tubing to the glass vacuum line was made by means of Cajon ultra-torr brass unions comprising an O-ring which, when finger tightened, produced a vacuum seal.

4.2.3.2 **Sample Preparation Vessels**

The sample preparation vessels were made of glass with high vacuum taps at the gas inlet and outlet points. The vessels were designed to have a short length of 6mm diameter glass tubing, containing a vacuum tap, which served as the point of attachment of the sample vessel to the vacuum line. This connection was effected using the Cajon brass unions. For all the sample gases (ammonia, hydrogen sulphide and methane) used in this project, the glass vessel consisted of a flask of 1 dm^3 capacity for the containment of the matrix gas, connected to a flask of 0.025 dm^3 capacity for the sample gas. The flasks could be isolated from each other by means of vacuum taps.

4.2.4 *Chemicals*

4.2.4.1 **Gases**

The two matrix gases, nitrogen (99.998 per cent) and argon (99.9995 per cent), were supplied by Fedgas Ltd. and were used without further purification. Ammonia, hydrogen sulphide and methane, obtained from Air Products S.A. (Pty.) Ltd., were purified by trap to trap distillation on the vacuum line before use.

4.2.5 *Sample Preparation - Ammonia, Hydrogen Sulphide and Methane/Matrix Gas Mixtures*

The sample vessel and the sample gas cylinders were connected to the vacuum line, which was evacuated until the vacuum measured 10^{-6} mmHg pressure or better. The 1 dm^3 and the 0.025 dm^3 flasks were then filled with the matrix gas and the sample gas respectively until the desired matrix gas/absorber (M/A) mole ratio was obtained by the following equation,

$$\frac{p_M V_M}{p_A V_A} = \frac{n_M}{n_A}$$

where p_M and p_A are the matrix gas and absorber pressures, respectively, V_M and V_A are the volumes of each gas and n_M and n_A are the numbers of moles of each gas. The approximate number of moles of each gas in each flask was estimated by noting the ambient temperature at the time of matrix/absorber gas preparation using the following equation

$$n = \frac{pV}{RT}$$

where the pressure, p, and volume, V, of the gas are expressed in kPa and dm^3 and T is the temperature in K, while R is the gas constant (8.314 J K^{-1} mol^{-1}). The matrix and sample gases were then allowed to mix overnight and the initial pressure of the mixture measured on the vacuum line using the EMV 251 digital read-out. After deposition of the gases onto the cold window, the final pressure of the mixture remaining in the vessel was measured. Since the initial pressure of the gas mixture, p_i, and the final pressure, p_f, as well as the total number of moles of gas initially introduced into the vessel $n_i = (n_M + n_A)$ are known, the number of moles of gas remaining in the vessel could be estimated using the equation

$$\frac{p_i}{p_f} = \frac{n_i T_i}{n_f T_f}$$

where n_f is the number of moles of gas remaining and T_i and T_f are the ambient temperatures in K when the initial and final pressures respectively were measured. The number of moles of gas introduced into the matrix isolation apparatus is then given by $(n_i - n_f)$.

4.2.6 *Matrix Deposition Techniques*

The sample glass vessel was attached to the stainless steel deposition line by means of Cajon brass unions and was evacuated until the pressure in the vacuum line reached 10^{-6} mmHg or lower. A liquid nitrogen trap, placed above the Diffstak pump assisted in trapping any impurities in the vacuum line. The cryostat was activated once the pressure in the vacuum line reached 10^{-6} mmHg pressure. At a temperature of 18 K the gas mixtures were deposited onto the cold window by adjusting the needle valves. The deposition was carried out for periods of 2 to 24 hours depending on the concentrations of the mixtures. Typical M/A/A ratios of 200/1/1 to 1000/1/1 were used in this project. Flow rates of 1 to 5 mmol h^{-1} were maintained. Annealing experiments were carried out by allowing the gas mixtures to warm to a set temperature of 35 K for 10 minutes and then reducing the temperature again to 18 K. In some cases the gas mixtures were deposited at 35 K and then cooled; this technique was used for the formation of very weak intermolecular complexes. In such cases the self-association of the more reactive species was suppressed by using M/A/A ratios of, typically, 500/5/1. Spectra of the matrix isolated samples were recorded before and after the annealing cycle. The infrared spectrometer was purged with compressed air which was dried by passing through two glass towers containing silica gel which was regenerated daily by heating to 140 °C for 10 hours. This proved effective in removing any water vapour in the sample compartment of the spectrometer thus reducing the water interferences in the 4000-3500 cm^{-1}, 1800-1300 cm^{-1} and 400-200 cm^{-1} ranges.

4.2.7 *Data Handling and Storage*

The spectra of all complexes where stored on computer disks by means of the OPUS software package supplied with the IFS 88 spectrometer. The band positions were determined by the peaking option in the OPUS package, and in some cases by locating the cursor on the peak of interest. All spectra shown have been reproduced directly from the disc without any alterations.

Chapter Five

Theoretical Predictions of the Geometries, Energies, Mulliken Charges and Vibrational Spectra of the Monomers of HF, HCl, H_2O, H_2S, NH_3, PH_3, CH_4 and SiH_4

5.1 *Geometries*

The equilibrium geometries of the monomers were optimized at the VERYTIGHT level, using the Berny optimization scheme, and use of the FREQ option established the equilibrium structure for each monomer. The structures of the monomers, HX (X=F,Cl), H_2Y (Y=O,S), AH_3 (A=N,P) and MH_4 (M=C,Si) were constrained to $C_{\infty v}$, C_{2v}, C_{3v} and T_d symmetry respectively. The geometrical parameters for the monomers are summarised in Table 5.1. From Table 5.1 it is seen that the calculated monomer geometrical parameters agree with the experimental gas phase results within 1.0 pm for the bond lengths and 1.0° for the bond angles, except for PH_3 and SiH_4. These errors are most likely to be due to the inadequate size of the basis set. Our results obtained for CH_4, H_2O and NH_3 are in reasonable agreement with those of Thomas et al,[320] who used a variety of basis sets at different levels of theory, where comparison is appropriate. A study of all the monomers except silane was undertaken by Frisch et al[127] at the Hartree Fock and Møller-Plesset levels of theory, summarising the vibrational frequencies and geometrical parameters, with which our calculated results compare well.

Table 5.1. Geometrical Parameters for the HX, H_2Y, AH_3 and MH_4 Monomers

Molecule	Parameter	Calculated	Experimental[a]	Difference[b]
HF	r(HF)/pm	92.1	91.7	0.4
HCl	r(HCl)/pm	126.8	127.5	-0.7
H_2O	r(OH)/pm	96.1	95.8	0.3
	HOH/deg	103.9	104.5	-0.6
H_2S	r(SH)/pm	132.9	133.6	-0.7
	HSH/deg	92.8	92.1	0.7
NH_3	r(NH)/pm	101.1	101.2	-0.1
	HNH/deg	106.1	106.7	-0.6
PH_3	r(PH)/pm	140.5	142.0	-1.5
	HPH/deg	94.5	93.3	1.2
CH_4	r(CH)/pm	108.4	109.2	-0.8
	HCH/deg	109.5[c]	109.5	0.0
SiH_4	r(SiH)/pm	147.1	148.1	-1.0
	HSiH/deg	109.5[c]	109.5	0.0

[a] Ref. 321.

[b] Difference = calculated - experimental value.

[c] Angles were fixed at the tetrahedral value.

The worst agreement of the calculated to experimental data occurs in the PH bond length (-1.5 pm) which could be attributed to basis set size. Generally, the poor correlation of calculated to experimental data occurs mostly in the second row hydrides. The inclusion of diffuse functions for the second row hydrides has also been stressed by several authors.[71,96,139,236]

5.2 *Energies and Mulliken Charges*

The RHF and MP2 molecular energies determined using the 6-31G** basis set, are collected in Table 5.2.

Table 5.2. Molecular RHF and MP2 Energies for the Monomers

Monomer	E(RHF)/a.u.	E(MP2)/a.u.
HF	-100.011153587	-100.1946390949
HCl	-460.066205185	-460.20544681387
H_2O	-76.0228397543	-76.21978576181
H_2S	-398.674948312	-398.81009813242
NH_3	-56.1951387238	-56.38321702127
PH_3	-342.454110433	-342.57857661677
CH_4	-40.2016949425	-40.364625909118
SiH_4	-291.230827942	-291.33899686687

The Mulliken charges are collected in Table 5.3 and the results of Tables 5.2 and 5.3 will be used for comparison with the results for the dimers and complexes later.

Table 5.3. Mulliken Atomic Charges for the Monomers

Monomer	Atom	Charge/e
HF	H	0.3972
	F	-0.3972
HCl	H	0.1924
	Cl	-0.1924
H_2O	H	0.3368
	O	-0.6739
H_2S	H	0.0660
	S	-0.1320
NH_3	H	0.2619
	N	-0.7857
PH_3	H	-0.0539
	P	0.1617
CH_4	H	0.1182
	C	-0.4729
SiH_4	H	-0.1667
	Si	0.6667

5.3 *The Vibrational Spectra*

The calculated monomer vibrational wavenumbers are reported in Table 5.4.

Table 5.4. Calculated Wavenumbers of the HX, H_2Y, AH_3 and MH_4 Monomers

Molecule	Mode	Approximate description	Calc. /cm^{-1}	Exp.[a] /cm^{-1}	Ratio[b]
HF		ν(HF)	4197	3961	1.06
HCl		ν(HCl)	3128	2886	1.08
H_2O	$\nu_1(a_1)$	$\nu_s(OH_2)$	3900	3656	1.06
	$\nu_2(a_1)$	δ(HOH)	1683	1595	1.06
	$\nu_3(b_1)$	$\nu_a(OH_2)$	4039	3756	1.08
H_2S	$\nu_1(a_1)$	$\nu_s(SH_2)$	2845	2614	1.09
	$\nu_2(a_1)$	δ(HSH)	1269	1183	1.07
	$\nu_3(b_1)$	$\nu_a(SH_2)$	2871	2626	1.09
NH_3	$\nu_1(a_1)$	$\nu_s(NH_3)$	3571	3336	1.07
	$\nu_2(a_1)$	$\delta_s(NH_3)$	1116	932	1.20
	ν_3(e)	$\nu_a(NH_3)$	3728	3443	1.08
	ν_4(e)	$\delta_a(NH_3)$	1724	1626	1.06
PH_3	$\nu_1(a_1)$	$\nu_s(PH_3)$	2531	2323	1.09
	$\nu_2(a_1)$	$\delta_s(PH_3)$	1078	992	1.09
	ν_3(e)	$\nu_a(PH_3)$	2546	2327	1.09

Table 5.4 *(continued)*

	$\nu_4(e)$	$\delta_a(PH_3)$	1184	1118	1.06
CH_4	$\nu_1(a_1)$	$\nu_s(CH_4)$	3143	2914	1.08
	$\nu_2(e)$	$\delta_s(CH_4)$	1623	1526	1.06
	$\nu_3(f_2)$	$\nu_a(CH_4)$	3289	3019	1.09
	$\nu_4(f_2)$	$\delta_a(CH_4)$	1402	1306	1.07
SiH_4	$\nu_1(a_1)$	$\nu_s(SiH_4)$	2345	2187	1.07
	$\nu_2(e)$	$\delta_s(SiH_4)$	1017	978	1.04
	$\nu_3(f_2)$	$\nu_a(SiH_4)$	2355	2191	1.07
	$\nu_4(f_2)$	$\delta_a(SiH_4)$	972	914	1.06

(a) Ref. 322.

(b) Ratio = calculated/experimental wavenumber.

The vibrational wavenumbers are consistently about 10% higher than the gas phase experimental values,[322] due to the neglect of anharmonic effects in the calculated values. Scaling factors for the vibrational wavenumbers have been investigated by Radom and Scott[66] at various levels of theory and using different basis sets. It has been suggested by these authors that a scaling factor of 1.0084 at 298.15 K should be applied to this level of calculation using the 6-31G** basis set. The intensities of the eight monomers and the reported experimentally obtained values are given in Table 5.5, which also includes the ratios of the calculated to the experimental values, showing the accuracy of the calculated intensities. The worst correlation of the calculated to experimental data occurs in $\delta_s(NH_3)$

and to date cannot be explained.

Table 5.5. Infrared Intensities of the Monomer Modes Compared with the Experimentally Obtained Values

Molecule	Mode	A/km mol^{-1}*		A_{Calc}/A_{Exp}
		Calc.	Exp.	
HF		81.7	84.6[a]	0.97
HCl		22.4	18.0[a]	1.24
H_2O	ν_1	4.2	2.2[b]	1.91
	ν_2	77.7	75.8[b]	1.03
	ν_3	33.8	42.4[b]	0.80
H_2S	ν_1	3.9	0.3[b]	13.00
	ν_2	7.6	---	---
	ν_3	6.5	---	---
NH_3	ν_1	0.2	10.4[a]	0.02
	ν_2	217.1	125.8[a]	1.73
	ν_3	0.8	3.8[a]	0.21
	ν_4	20.7	25.8[a]	0.80
PH_3	ν_1	40.6	128.1[b]	0.32
	ν_2	32.3	20.2[b]	1.60
	ν_3	98.6	128.1[b]	0.77

Table 5.5 *(continued)*

	ν_4	19.7	25.7[b]	0.77
CH_4	ν_3	21.2	65.5[b]	0.32
	ν_4	11.7	28.3[b]	0.41
SiH_4	ν_3	163.1	281.6[b]	0.58
	ν_4	186.2	381.3[b]	0.49

(a) Ref. 323.

(b) Ref. 324.

* The ν_1 and ν_2 modes of CH_4 and SiH_4 are infrared inactive.

The ratios of the calculated to the experimentally observed intensities in most cases vary over a range of 0.5 to 2 which is considered acceptable.[325] Those ratios which are outside this range result from the effect of the lack of complete account of correlation effects.[326] The symmetry coordinates of the monomers are collected in Table 5.6. The symmetry coordinate descriptions for the H_2Y, AH_3 and MH_4 monomers were obtained from Cyvin et al.[327,328]

Use of this set of symmetry coordinates for the descriptions of the various normal modes provided complete diagonalization of the force constant matrix, with no mixing of the PED terms between symmetry species for any of the molecules.

Table 5.6. Symmetry Coordinate Descriptions of the Modes of the Monomers

Monomer	Symmetry Coordinate*	Description
HX	$S_1 = \Delta r$	HX stretch
H_2Y	$S_1 = 1/\sqrt{2}(\Delta r_1 + \Delta r_2)$	YH_2 symmetric stretch
	$S_2 = \Delta\theta$	YH_2 bend
	$S_3 = 1/\sqrt{2}(\Delta r_1 - \Delta r_2)$	YH_2 antisymmetric stretch
AH_3	$S_1 = 1/\sqrt{3}(\Delta r_1 + \Delta r_2 + \Delta r_3)$	AH_3 symmetric stretch
	$S_2 = 1/\sqrt{3}(\Delta\theta_1 + \Delta\theta_2 + \Delta\theta_3)$	AH_3 symmetric bend
	$S_{3a} = 1/\sqrt{6}(2\Delta r_1 - \Delta r_2 - \Delta r_3)$	AH_3 antisymmetric stretch
	$S_{3b} = 1/\sqrt{2}(\Delta r_2 - \Delta r_3)$	AH_3 antisymmetric stretch
	$S_{4a} = 1/\sqrt{6}(2\Delta\theta_1 - \Delta\theta_2 - \Delta\theta_3)$	AH_3 antisymmetric bend
	$S_{4b} = 1/\sqrt{2}(\Delta\theta_2 - \Delta\theta_3)$	AH_3 antisymmetric bend
MH_4	$S_1 = 1/2(\Delta r_1 + \Delta r_2 + \Delta r_3 + \Delta r_4)$	MH_4 symmetric stretch
	$S_{2a} = 1/\sqrt{12}(2\theta_{23} - \theta_{13} - \theta_{12} + 2\theta_{14} - \theta_{34} - \theta_{24})$	MH_4 degenerate bend
	$S_{2b} = 1/2(\theta_{13} - \theta_{12} + \theta_{24} - \theta_{34})$	MH_4 degenerate bend
	$S_{3a} = 1/2(\Delta r_1 - \Delta r_2 + \Delta r_3 - \Delta r_4)$	MH_4 antisymmetric stretch
	$S_{3b} = 1/2(\Delta r_1 + \Delta r_2 - \Delta r_3 - \Delta r_4)$	MH_4 antisymmetric stretch
	$S_{3c} = 1/2(\Delta r_1 - \Delta r_2 - \Delta r_3 + \Delta r_4)$	MH_4 antisymmetric stretch
	$S_{4a} = 1/\sqrt{2}(\theta_{24} - \theta_{13})$	MH_4 antisymmetric bend
	$S_{4b} = 1/\sqrt{2}(\theta_{34} - \theta_{12})$	MH_4 antisymmetric bend
	$S_{4c} = 1/\sqrt{2}(\theta_{14} - \theta_{23})$	MH_4 antisymmetric bend

* θ_{ij} indicates the angle subtended by H_i and H_j to atom M

The main diagonal force constants of the monomers are reported in Table 5.7 below. The values of the calculated force constants agree fairly well with the experimentally obtained values, as shown by the ratios of the calculated to the experimental values. The major

discrepancies occur for the second row hydrides, most probably due to inadequate basis set size.

Table 5.7 Major Force Constants of the Monomers, Compared with Experimental Values

Monomer	Force Constant	Force Constant /N m^{-1}		Ratio
		Calculated	Experimental	
HF	$f_{(HF)}$	994	965[(a)]	1.03
HCl	$f_{(HCl)}$	565	481[(b)]	1.17
H_2O	$f_{(OH)}$	882	776[(c)]	1.14
	$f_{(HOH)}$	74	69[(c)]	1.05
H_2S	$f_{(SH)}$	471	414[(c)]	1.14
	$f_{(HSH)}$	46	45[(c)]	1.02
NH_3	$f_{(NH)}$	826	705[(b)]	1.18
	$f_{(HNH)}$	85	68[(b)]	1.25
PH_3	$f_{(PH)}$	371	324[(c)]	1.14
	$f_{(HPH)}$	36	33[(c)]	1.09
CH_4	$f_{(CH)}$	575	504[(c)]	1.14
	$f_{(HCH)}$	45	46[(c)]	0.98
SiH_4	$f_{(SiH)}$	316	284[(c)]	1.11
	$f_{(HSiH)}$	21	19[(c)]	1.10

(a) Ref. 329.

(b) Ref. 330.

(c) Ref. 331.

The ratios of the calculated to the experimental stretching force constants are remarkably

constant, while those of the bending force constants, scaled by dividing by the squares of the bond lengths are all slightly larger than 1.0, except that of NH_3, while that of CH_4 is actually slightly less than 1.0.

Chapter Six

Theoretical Predictions of the Structures, Energetics, Mulliken Charges and Vibrational Spectra, and Normal Coordinate Analyses of the Homodimers

6.1 *The HX Dimers (X= F,Cl)*

6.1.1 *Geometries*

The structure and the dynamics involved in the proton exchange in the HF dimer have been well studied both experimentally[14] and by VRT (vibrational-rotational tunnelling) theoretical studies.[332] The linear C_s hydrogen bonded structure was found to be the most stable conformer which is in agreement with experiment. For this dimer, three different structures were optimized. The rhomboid structure (fig 6.1) was found to be a saddle point, whilst the parallelogram (fig 6.2) and the C_s hydrogen bonded structure (fig 6.3) were minima on the PES of the dimer. The mechanism proposed[80] for the proton exchange between the two HF molecules is consistent with the results obtained in this study. On optimizing the linear C_s structure, allowing full relaxation of the geometrical parameters, the linear structure transformed to the vibrationally averaged C_{2h} structure (fig 6.2), where proton exchange occurs, leading to the equivalent hydrogen bonded structure having the proton donor-acceptor roles interchanged. A recent theoretical study by Civalleri et al[333] also reports similar findings for the HF dimer. This behaviour of the dimer is due to the use of incomplete basis sets. The tunnelling motion through the barrier separating the lowest energy states of the dimer was found to be 0.66 cm^{-1}.[73]

In the case of the HCl dimer, two structures were optimised, the parallelogram C_{2h} structure (fig 6.4) and the global minimum C_s linear hydrogen bonded structure (fig 6.5).

The linear hydrogen bonded structure agrees with that found experimentally by Pine and Ohashi[114] in the gas phase. Tunnelling splitting was found to occur in the HCl dimer, estimated to be between 9 and 14 cm^{-1}.[83] The donor-acceptor proton interchange occurs through a C_{2h} geometry with a barrier height of 1 kJ mol^{-1}.[83] The C_{2h} structure was a saddle point on the PES, consistent with the results of Frisch et al.[94]

In the case of the HCl dimer tunnelling does occur and the ab initio calculations predict ground state barriers from 150 to 50 cm^{-1} [334] in good agreement with the experimental values of Pine and Ohashi.[114] The changes in the geometrical parameters on complexation in the HX dimers are collected in Table 6.1.

Table 6.1 Geometrical Parameters for the Most Stable HX (X= F, Cl) Dimers

Complex	Parameter	Complex	Monomer	Difference
$(HF)_2$	r(F1H1)/pm	92.7	92.1	0.6
	r(F2H2)/pm	92.5	92.1	0.4
	R(F1..F2)/pm	271.0		
	H2F2..F1/deg	110.0		
	F2H1..F1/deg	180.0		
$(HCl)_2$	r(Cl1H1)/pm	127.2	126.8	0.4
	r(Cl2H2)/pm	127.0	126.8	0.2
	R(Cl2..Cl1)/pm	388.0		
	H2Cl2..Cl1/deg	101.4		
	Cl2..H1Cl1/deg	175.6		

There is a greater increase in the H1F1 bond length than in the corresponding H1Cl1 bond length, suggesting that the strength of the hydrogen bond in the HF dimer is greater than that in the HCl dimer. The theoretical parameters are in close agreement with those of Tolosa et al[335] except for the R(F1...F2) distance. They report a value of 267.6 pm at the MP2/6-31G** level of theory. The DFT calculations by Latajka and Boutellier[336] with the 6-311++G** basis also compare reasonably well with the experimental values for the HF dimer. In the case of the HCl dimer most of the theoretical studies[122-125] focused on the tunnelling dynamics and characterisation of the potential energy surface. The geometrical parameters for the HCl dimer obtained by Frisch et al[127] at the HF/6-31G* level of theory agree reasonably well with our calculated results.

The hydrogen bond angle in the case of the HF dimer was frozen at 180° due to the C_s linear hydrogen bonded structure collapsing to the vibrationally averaged structure as explained above. In the HCl dimer the hydrogen bonded angle optimized to 175.6°, resulting from a lower amplitude in the libration of the hydrogen bonded proton compared with that in the HF dimer. Gomez et al[122] used a four dimensional potential energy function to model this effect. Table 6.2 shows a comparison of the calculated geometrical parameters with the available experimental data.

The structural parameters available for both HX dimers agree well with the experimental gas phase results. On comparing the calculated X..X distances with the experimentally obtained values, the difference is much larger in the case of the HCl dimer than for the HF dimer. This could be attributed to the need to incorporate diffuse functions in the basis sets, particularly for the second row elements.

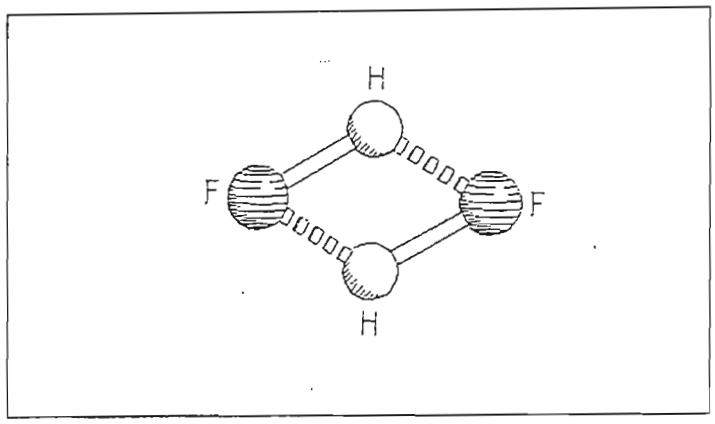

Fig 6.1 The Rhombus HF Dimer

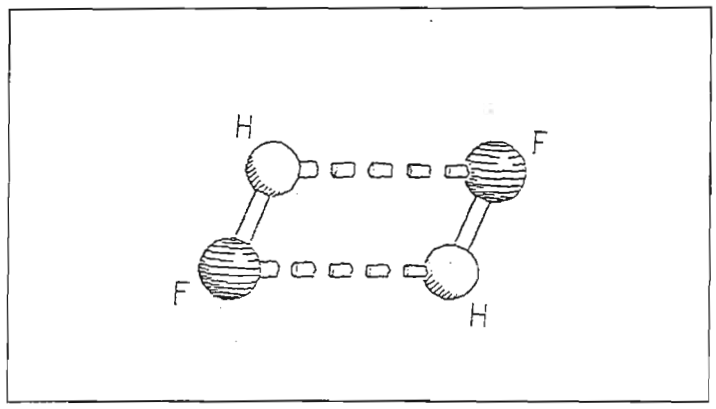

Fig 6.2 The Parallelogram HF Dimer

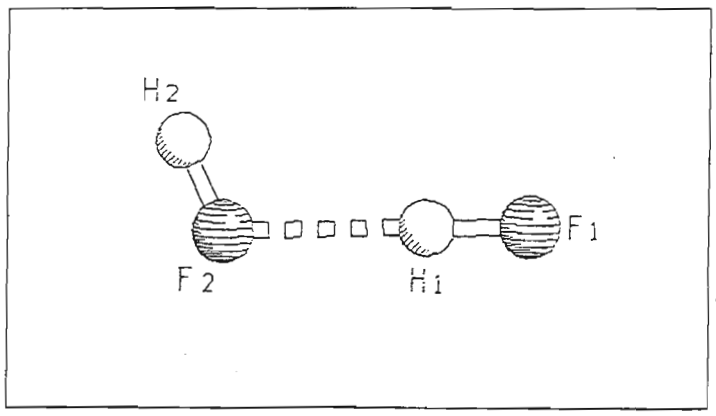

Fig 6.3 The Linear HF Dimer

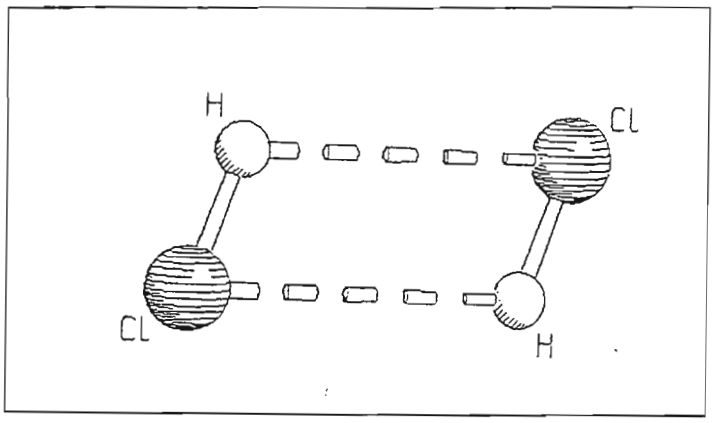

Fig 6.4 The Parallelogram HCl Dimer

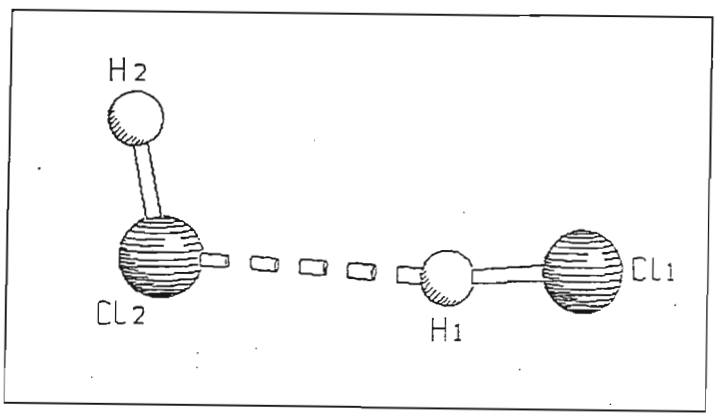

Fig 6.5 The Linear HCl Dimer

Table 6.2 Geometrical Parameters for the Most Stable HX (X= F,Cl) Dimers compared with Experiment

Complex	Parameter	Calculated	Experimental	Difference[a]
$(HF)_2$	R(F1..F2)/pm	271	272 ± 3[b]	1 ± 3
	H2F2..F1/deg	110	115 ± 5[c]	5 ± 5
$(HCl)_2$	R(H2Cl2..Cl1)/pm	388	380[d]	8.3

(a) Difference = Calculated - Experimental

(b) Ref. 73

(c) Ref. 14

(d) Ref. 114

6.1.2 *Energetics*

The binding energies, calculated at the MP2 level and corrected for the BSSE by means of the counterpoise method as described earlier in section 2.1.1 are summarised in Table 6.3. The binding energies are only reported for the most stable structures. The percentage dispersion energy contribution was also found to play a major role in the intermolecular energy and was calculated as follows

$$\%\Delta E_{Disp} = \frac{\Delta E_{(MP2)} - \Delta E_{(RHF)}}{\Delta E_{(MP2)}} x\ 100$$

The percentage dispersion contributions to the interaction energies are also collected in Table 6.3.

Table 6.3 The Binding Energies of the Most Stable HX Dimers

Complex	$\Delta E'$ /kJ mol^{-1}	ΔE /kJ mol^{-1}	BSSE /kJ mol^{-1}	$\%\Delta E_{Disp}$
$(HF)_2$	-8.0	-30.2	22.2	37.0
$(HCl)_2$	-5.6	-8.0	2.4	42.8

The HF dimer is more strongly bound than the HCl dimer, with the HCl dimer having a greater contribution due to dispersion effects. The Morokuma energy decomposition analysis of the SCF part of the interaction energy is collected in Table 6.4.

Table 6.4 Energy Decomposition Analysis of the Most Stable HX Dimers /kJ mol^{-1}

Complex	ES	EX	CT	PL	MIX	Total
$(HF)_2$	-29.5	21.3	-10.6	-2.9	4.1	-17.7
$(HCl)_2$	-10.5	10.6	-3.6	-0.8	1.2	-3.0

A detailed description of the different energy terms in Table 6.4 is provided in Chapter 4. Comparing the HF and HCl dimers, the HF dimer is governed mostly by electrostatic interactions whilst in the HCl dimer, the EX term has the largest magnitude. This is expected since the bonded proton in the HCl molecule is much closer to the chlorine atom, due to the large atomic radius of the chlorine atom compared with that of the fluorine atom. The interactions resulting from the higher order moments, described by the mixing term, are more prominent in the HF dimer than in the HCl dimer. The effects of dispersion on the interaction energy are most pronounced in the HCl dimer than in the HF dimer. On comparison of our calculated electronic interaction energies with the

experimental gas phase values[115] of 7.4 and 4.6 kJ mol^{-1} for the HF and HCl dimers, our calculated values are found to be in close agreement.

6.1.3 *Mulliken Charge Analysis*

For both the HX dimers, the direction of charge donation is through the hydrogen bonded atom to the proton acceptor. The absolute shift in charge from one sub-unit to the other in the complex is shown in Tables 6.5 and 6.6.

Table 6.5 Mulliken Charge Analysis for the Most Stable HF Dimer

Atom	Atomic Charge /e		Difference
	Complex	Monomer	/e
H1	0.402	0.397	0.005
F1	-0.439	-0.397	-0.042
			-0.037
H2	0.418	0.397	0.021
F2	-0.381	-0.397	0.016
			0.037

Table 6.6 Mulliken Charge Analysis for the Most Stable HCl Dimer

Atom	Atomic Charge /e		Difference /e
	Complex	Monomer	
H1	0.207	0.192	0.015
Cl1	-0.194	-0.192	-0.002
			0.013
H2	0.187	0.192	-0.005
Cl2	-0.200	-0.192	-0.008
			-0.013

From the Mulliken charge analysis, charge donation occurs from the proton acceptor to the proton donor in the HF dimer, whilst in the HCl dimer the charge donation occurs from the proton donor to the proton acceptor. This scenario could be explained as follows; the Cl atom has a much larger atomic radius than the F atom therefore shielding it's proton and acting as the electron donor. The chlorine atom has a greater electron affinity than the fluorine atom, thus supporting the reversal of charge donation.[181]

6.1.4 *Vibrational Properties of the Most Stable HX Dimers*

The calculated vibrational spectra, potential energy distributions and infrared intensities at the MP2/6-31G** level for the linear bonded structure are shown in Tables 6.7 - 6.13. The plots of the normal modes of vibration are also described in fig 6.6. The calculated vibrational spectrum of the HF dimer compared with experiment is reported in Table 6.7.

Table 6.7 Calculated Vibrational Spectrum of the HF Dimer Compared with Experiment

Symmetry Species	Mode	Calculated Wavenumber /cm^{-1}	Experimental Wavenumber /cm^{-1} [a]	Ratio[b]
a'	ν_1	4143	3896	1.06
	ν_2	4082	3826	1.07
	ν_3	646		
	ν_4	233	189	1.23
	ν_5	181	128	1.41
a"	ν_6	474	400	1.18

(a) ref. 90

(b) Ratio = Calculated / Experimental

The ratios of the calculated to the experimental wavenumbers are quite close to unity. The departure from unity is due to the fact that the calculated values are harmonic and simulate the gaseous state, while the experimental values were obtained by matrix isolation studies in an argon environment. The ν_3 mode was not observed experimentally hence no comparison could be made with our calculated value.

The wavenumber shifts from the monomer values are collected in Table 6.8.

Table 6.8 Calculated Wavenumber Shifts on Dimerization for the HF Dimer

Symmetry Species	Mode	Complex Wavenumber /cm^{-1}	Monomer Wavenumber /cm^{-1}	Shift[(a)] /cm^{-1}
a'	ν_1	4143	4197	-54
	ν_2	4082	4197	-115

(a) Shift = Complex - Monomer

In the infrared spectrum red shifts of 54 and 115 cm^{-1} are expected for the ν_1 and ν_2 modes from the monomer positions, characteristic of hydrogen bonded complexes. The calculated vibrational spectrum of the HCl dimer compared with experiment is collected in Table 6.9.

Table 6.9 Calculated Vibrational Spectrum of the HCl Dimer Compared with Experiment

Symmetry Species	Mode	Calculated Wavenumber /cm^{-1}	Experimental Wavenumber[(a)] /cm^{-1}	Ratio[(b)]
a'	ν_1	3110	2855	1.08
	ν_2	3085	2818	1.09

(a) ref. 120

(b) Ratio = Calculated / Experimental

The ratios of the calculated to the experimental wavenumbers are close to unity as in the case of the HF dimer. Our calculated wavenumbers compare reasonably well with the

experimental wavenumbers in argon matrices.[90.120] The difference of 10% is accounted for by the neglect of anharmonicity in the theoretical determination of the wavenumbers. The wavenumber shifts on complexation for the HCl dimer are collected in Table 6.10.

Table 6.10 Calculated Wavenumber Shifts on Dimerization for the HCl Dimer

Symmetry Species	Mode	Complex Wavenumber /cm^{-1}	Monomer Wavenumber /cm^{-1}	Shift[(a)] /cm^{-1}
a'	ν_1	3110	3128	-18
	ν_2	3085	3128	-43

(a) Shift = Complex - Monomer

The red shifts on forming the hydrogen bonds are clearly shown in the tables above for the HX dimers. The ratios of the calculated to the experimentally observed wavenumbers are close to unity except for the intermolecular vibrational modes. The experimental spectra of the HCl dimer in argon matrices agree well with the predicted shifts of -18 and -43 cm^{-1} obtained from the calculations, as shown later in the collected tables of matrix infrared spectra. In Table 6.11 are collected the local symmetry coordinates, S_i, describing the various vibrational modes.

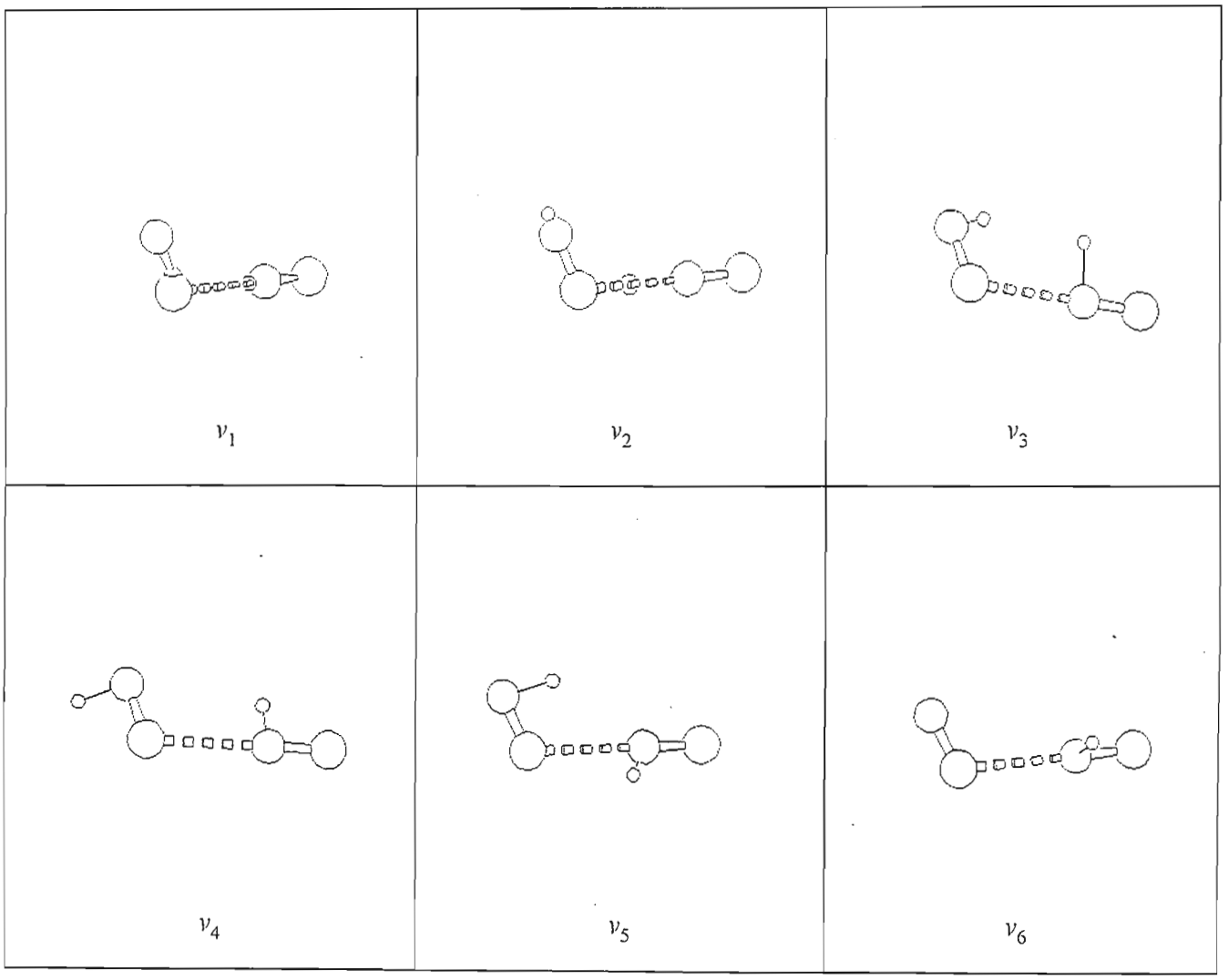

Fig 6.6 Graphical Representation of the HX Dimer Vibration modes

Table 6.11 Symmetry Coordinates for the HX Dimers

Symmetry Coordinate	Description
$S_1 = \Delta r_1$	HX stretch (proton acceptor)
$S_2 = \Delta r_2$	HX stretch (proton donor)
$S_3 = \Delta R$	H..X stretch
$S_4 = \Delta\delta$	HX..H bend
$S_5 = \Delta\pi_1$	X..HX in plane bend
$S_6 = \Delta\pi_2$	X..HX out of plane bend

The symmetry coordinates for the intermolecular modes were generated following the rules of Wilson et al.[70] The percentage PEDs for the HX dimers are reported in Tables 6.12 and 6.13.

The trend in the percentage PED contributions to the ν_1 and ν_2 modes are similar in both HX dimer series. The H..X stretching wavenumbers of the dimers correspond fairly poorly with each other in respect of the percentage PEDs, due to the large amplitude librational motion of the hydrogen bond in the HF dimer compared with that in the HCl dimer. In the HX dimers the ν_5 mode has a 93% and 39% PED contribution from the S_3 symmetry coordinate, for the HCl and HF dimers respectively. This also indicates the ease with which proton tunnelling occurs in the HF dimer compared with that in the HCl dimer, whereby proton donor-acceptor roles are interchanged.

Table 6.12 Wavenumbers and %PEDs in the HF Dimer

Symmetry Species	Wavenumber /cm^{-1}	%PED
a'	4143	$90S_1 + 10S_2$
	4082	$11S_1 + 89S_2$
	646	$48S_4 + 52S_5$
	233	$22S_3 + 41S_4 + 37S_5$
	181	$39S_3 + 29S_4 + 32S_5$
a"	474	$100S_6$

Table 6.13 Wavenumbers and %PEDs in the HCl dimer

Symmetry Species	Wavenumber /cm^{-1}	%PED
a'	3111	$98S_1 + 2S_2$
	3086	$2S_1 + 98S_2$
	308	$22S_3 + 37S_4 + 41S_5$
	125	$29S_3 + 51S_4 + 20S_5$
	75	$91S_3 + 4S_4 + 4S_5$
a"	231	$100S_6$

The intensities of the various vibrational modes are collected in Table 6.14 and the ratios of complex to monomer intensities are compared for both the HX dimers.

Table 6.14 The Ratios of Complex to Monomer Intensities in the HX Dimers

Complex	Symmetry Species	Mode	Complex A_c/km mol^{-1}	A_c/A_m
$(HF)_2$	a'	ν_1	94.3	1.15
		ν_2	442.1	5.41
$(HCl)_2$	a'	ν_1	30.0	1.34
		ν_2	135.8	6.06

The ratios of the complex to the monomer intensity values are similar for both the HF and HCl dimers with greater enhancement being observed in the ν_2 mode for both dimers. This ratio is greater in the case of the HCl dimer, despite the hydrogen bond formed in the HF dimer being stronger than that in the HCl dimer.

6.2 *The H_2Y Dimers (Y= O,S)*

6.2.1 *Geometries*

The structures considered for these complexes comprised the linear C_s hydrogen bonded conformers shown in figs 6.7 and 6.8. The geometrical parameters for these complexes are presented in Table 6.15 below. The C_{2h} bifurcated water dimer structure was found to be a transition state; similar findings was also reported by Radom et al[145] and hence this structure will not be mentioned in this project. In the H_2O dimer the hydrogen bond angle deviates more from linearity compared with that in the H_2S dimer.

This is characteristic of the hybridisation of the heavy atom in both the dimers. The H_2S dimer has been shown experimentally[156] to exist as either a linear C_s or a bifurcated C_{2v} structure. The recent theoretical studies by Bertran et al[158] suggest the linear C_s structure

to be the global minimum, while the C_{2v} structure could not even be identified as being a local minimum on the potential energy surface of the H_2S dimer.

The HY bond length of the proton donor increases by 0.6 pm and 0.3 pm in the H_2O and H_2S dimers respectively. Similar findings were also observed by Bertran et al[158] at the MP2/6-311G** level, reporting values of the increment in the HY bond length of 0.6 and 0.1 pm. Our calculated values of the geometrical parameters of the H_2S dimer were found to compare well with the previous theoretical studies[211,230] at both the SCF and MP2 levels of theory.

The major change in the geometrical parameters in Table 6.15 occurs in the lengthening of the O1H1 bond. Studies by Del Bene et al[139] and Dill and co-workers[107] at the HF/6-31G* level of theory also reported an increase in the O1H1 bond length. Further extensive studies[137,147,148] involving the effects of levels of theory and basis set were carried out. The study by van Duijeneveldt et al[148] reported an O1..O2 separation of 294.9 pm at the MP2 level using a large basis set; this result is close to our value of 291.2 pm. However the value obtained experimentally by Dyke et al[135] yielded a R_e value of 295.2 pm.

Table 6.15 Geometrical Parameters for the Most Stable H_2Y (Y= O,S) Dimers

Complex	Parameter	Calculated	Monomer	Difference
$(H_2O)_2$	r(O1H1)/pm	96.7	96.1	0.6
	r(O1H2)/pm	96.0	96.1	-0.1
	r(O2H3), r(O2H4)/pm	96.3	96.1	0.2
	R(O2..O1)/pm	291.2		
	H1O2H2/deg	104.1		
	H3O1H4/deg	104.1		
	O2..H1O1/deg	170.2		
	O1..O2H1/deg	9.8		
$(H_2S)_2$	r(S1H1)/pm	133.2	132.9	0.3
	r(S1H2)/pm	133.0	132.9	0.1
	r(S2H3), r(S2H4)/pm	133.0	132.9	0.1
	R(S2..S1)/pm	417.2		
	H2S1H1/deg	93.1		
	H3S2H4/deg	93.1		
	S2..H1S1/deg	178.2		

Table 6.16 Geometrical Parameters for the Most Stable H_2O Dimer compared with Experiment

Complex	Parameter	Calculated	Experimental[(a)]	Difference
$(H_2O)_2$	R(O2..O1)/pm	291.2	298.0	6.8
	O1..O2H1/deg	9.8	2 ± 10	8 ± 10

(a) Ref. 135

The calculated values obtained for the water dimer are in agreement with the experimental gas phase values.[135] There were no experimental data for comparison of the H_2S dimer.

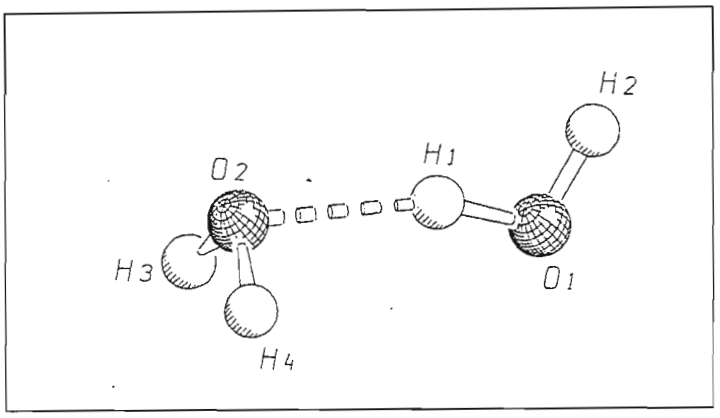

Fig 6.7 The Linear H_2O Dimer

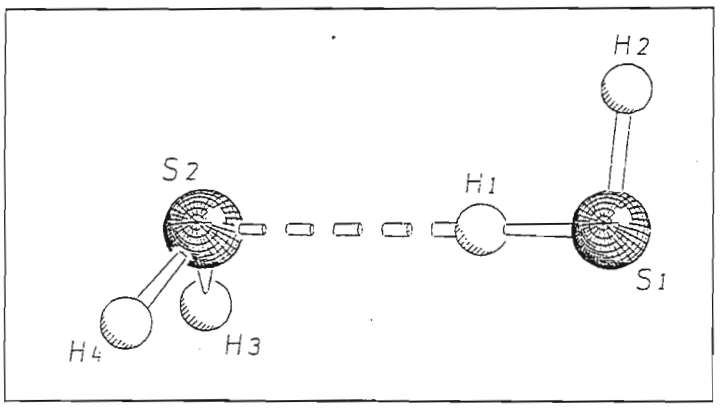

Fig 6.8 The Linear H_2S Dimer

6.2.3 *Energetics*

The corrected and uncorrected binding energies together with the BSSEs are reported in Table 6.17. The percentage dispersion contributions to the MP2 corrected binding energies obtained are also shown.

Table 6.17 The Binding Energies of the Linear H_2Y Dimers

Complex	$\Delta E'$ /kJ mol^{-1}	ΔE /kJ mol^{-1}	BSSE /kJ mol^{-1}	$\%\Delta E_{Disp}$
$(H_2O)_2$	-19.6	-29.5	9.9	9.4
$(H_2S)_2$	-4.3	-6.9	2.6	57.4

$(H_2O)_2$ is more strongly bound than $(H_2S)_2$, but the dispersion contribution to the binding energy plays a larger role in the case of the hydrogen sulphide dimer (57.4%). A similar trend was also observed in the case of the HX dimers; as one descends the group on the periodic table, the dimer tends to be bonded more by the forces of dispersion. The binding energies determined experimentally for the water and hydrogen sulphide dimers were; 22.6 $\pm$ 3 kJ mol^{-1} [136] and 7.1 $\pm$ 1.3 kJ mol^{-1} [337] respectively which are in agreement with our calculated results. The Morokuma energy decomposition analysis is reported in Table 6.18 for the H_2Y dimers.

Table 6.18 Energy Decomposition Analysis of the Linear H_2Y Dimers /kJ mol^{-1}

Complex	ES	EX	CT	PL	MIX	Total
$(H_2O)_2$	-35.6	24.3	-6.4	-3.0	1.7	-19.0
$(H_2S)_2$	-10.2	10.8	-2.9	-0.6	1.0	1.9

The H_2S dimer interaction is mainly governed by dispersion interactions, since 57% of the interaction energy is due to dispersion, an expected trend for molecules containing sulphur atoms.[236] From the decomposition analysis the water dimer is a conventional electrostatically hydrogen bonded dimer, whilst in the case of the H_2S dimer the exchange repulsion term dominates the uncorrelated interaction energy, thus emphasising the importance of correlation of the level of theory used. Similar results were obtained by the earlier energy decomposition calculations by Morokuma and Umeyama.[316]

6.2.3 *Mulliken Charge Analysis*

The Mulliken charge analyses are reported in Tables 6.19 and 6.20 for the H_2O and H_2S dimers respectively.

In the H_2O dimer negative charge donation occurs from the proton donor to the proton acceptor, whilst in the case of the H_2S dimer, negative charge donation occurs from the proton acceptor to the proton donor. This reversal of charge donation could be explained as follows; the sulphur lone pair electrons have more d-orbital character than p-orbital character as in the oxygen lone pair electrons, resulting in a larger radial extent of the lone pair electrons in the H_2S, enabling it to accept charge from the proton acceptor more readily. The magnitude of charge transfer from the proton donor to the acceptor in each of the H_2Y dimers is almost the same.

Table 6.19 Mulliken Charge Analysis for the Linear H_2O Dimer

Atom	Atomic Charge /e		Difference /e
	Complex	Monomer	
O1	-0.716	-0.674	-0.042
H1	0.364	0.337	0.027
H2	0.364	0.337	0.027
			0.012
O2	-0.726	-0.674	-0.052
H3	0.357	0.337	0.020
H4	0.357	0.337	0.020
			-0.012

Table 6.20 Mulliken Charge Analysis for the Linear H_2S Dimer

Atom	Atomic Charge /e		Difference /e
	Complex	Monomer	
S1	-0.151	-0.132	-0.019
H1	0.079	0.066	0.013
H2	0.063	0.066	-0.003
			-0.009
S2	-0.143	-0.132	-0.011
H3	0.076	0.066	0.010
H4	0.076	0.066	0.010
			0.009

6.2.4 *Vibrational Properties of the Most Stable H_2Y Dimers*

The calculated vibrational spectra compared with the experimental vibrational spectra for the H_2O and H_2S dimers are collected in Tables 6.21 and Tables 6.22. The plots of the vibrational modes for the H_2Y dimers are shown in fig 6.9.

Table 6.21 Calculated Vibrational Spectrum of the H_2O Dimer Compared with Experiment

Symmetry Species	Mode	Calculated Wavenumber /cm^{-1}	Experimental Wavenumber /cm^{-1} [(a)]	Ratio[(b)]
a'	ν_1	3998	3881	1.03
	ν_2	3876	3797	1.02
	ν_3	3818	3718	1.03
	ν_4	1714	1669	1.03
	ν_5	1680	1653	1.02
a"	ν_9	4006	3899	1.03

(a) Ref. 132

(b) Ratio = Calculated / Experimental

The experimental values obtained for the H_2O dimer in a nitrogen matrix compare well with our calculated spectrum of the dimer. The hydrogen bonded OH stretching band was assigned by Dyke et al[135] at 150 cm^{-1} in the gas phase, whilst in argon and nitrogen matrices[128] this band was assigned at 145 and 155 cm^{-1} respectively. The calculated hydrogen bond stretch at 206 cm^{-1} in the water dimer gives a ratio of 1.4 and 1.3 when compared with those bands in argon and nitrogen matrices respectively.

Table 6.22 Calculated Vibrational Spectrum of the H_2S Dimer Compared with Experiment

Symmetry Species	Mode	Calculated /cm^{-1}	Experimental[(a)] /cm^{-1}	Ratio[(b)]
a'	ν_1	2857	2624	1.09
	ν_2	2839	2617	1.08
	ν_3	2822	2579	1.09
	ν_4	1277	1181	1.08
	ν_5	1266	1178	1.07
a"	ν_9	2865	2631	1.09

(a) Ref. 159

(b) Ratio = Calculated / Experimental

Our calculated vibrational spectrum of the H_2S dimer is in excellent agreement with that of Nelander et al[159] in a nitrogen matrix. The spectrum obtained by Barnes et al[338] in an argon matrix report the band at 2582.5 cm^{-1} as the ν_1 of the monomer band, which in fact was closer to the dimer bands at 2579 and 2585.3 cm^{-1} in N_2 [159] and O_2 [161] matrices. The ratios obtained for the H_2S dimer are consistent with each other as in the case of the water dimer. Tables 6.23 and 6.24 collect the vibrational wavenumber shifts on dimerization in the H_2O and H_2S dimers.

Table 6.23 Calculated Wavenumber Shifts on Dimerization in the H_2O Dimer

Symmetry Species	Mode	Complex Wavenumber /cm^{-1}	Monomer Wavenumber /cm^{-1}	Shift[(a)] /cm^{-1}
a'	ν_1	3998	4039	-41
	ν_2	3876	3900	-24
	ν_3	3818	3900	-82
	ν_4	1714	1683	31
	ν_5	1680	1683	-3
a"	ν_9	4006	4039	-33

(a) Shift = Complex - Monomer

In both the H_2Y dimers there is a shift of the ν_1 mode and a red shift of the ν_3 mode from the monomer wavenumbers; this trend is characteristic of hydrogen bonds as observed in Tables 6.23 and 6.24. These shifts are more pronounced in the H_2O dimer than the H_2S dimer, suggesting the H_2O dimer to be more strongly bound than the H_2S dimer.

Table 6.24 Calculated Wavenumber Shifts on Dimerization in the H_2S Dimer

Symmetry Species	Mode	Complex Wavenumber /cm^{-1}	Monomer Wavenumber /cm^{-1}	Shift[(a)] /cm^{-1}
a`	ν_1	2857	2871	-14
	ν_2	2839	2845	-6
	ν_3	2822	2845	-23
	ν_4	1277	1269	8
	ν_5	1266	1269	-3
a"	ν_9	2856	2871	-15

(a) Shift = Complex - Monomer

The symmetry coordinate description for the different vibrational modes in the H_2Y dimers are shown in Table 6.25.

The set of symmetry coordinates described in Table 6.25 was used in the descriptions of the vibrational modes for the H_2Y dimers. The symmetry coordinates were generated using the rules of Wilson et al.[70]

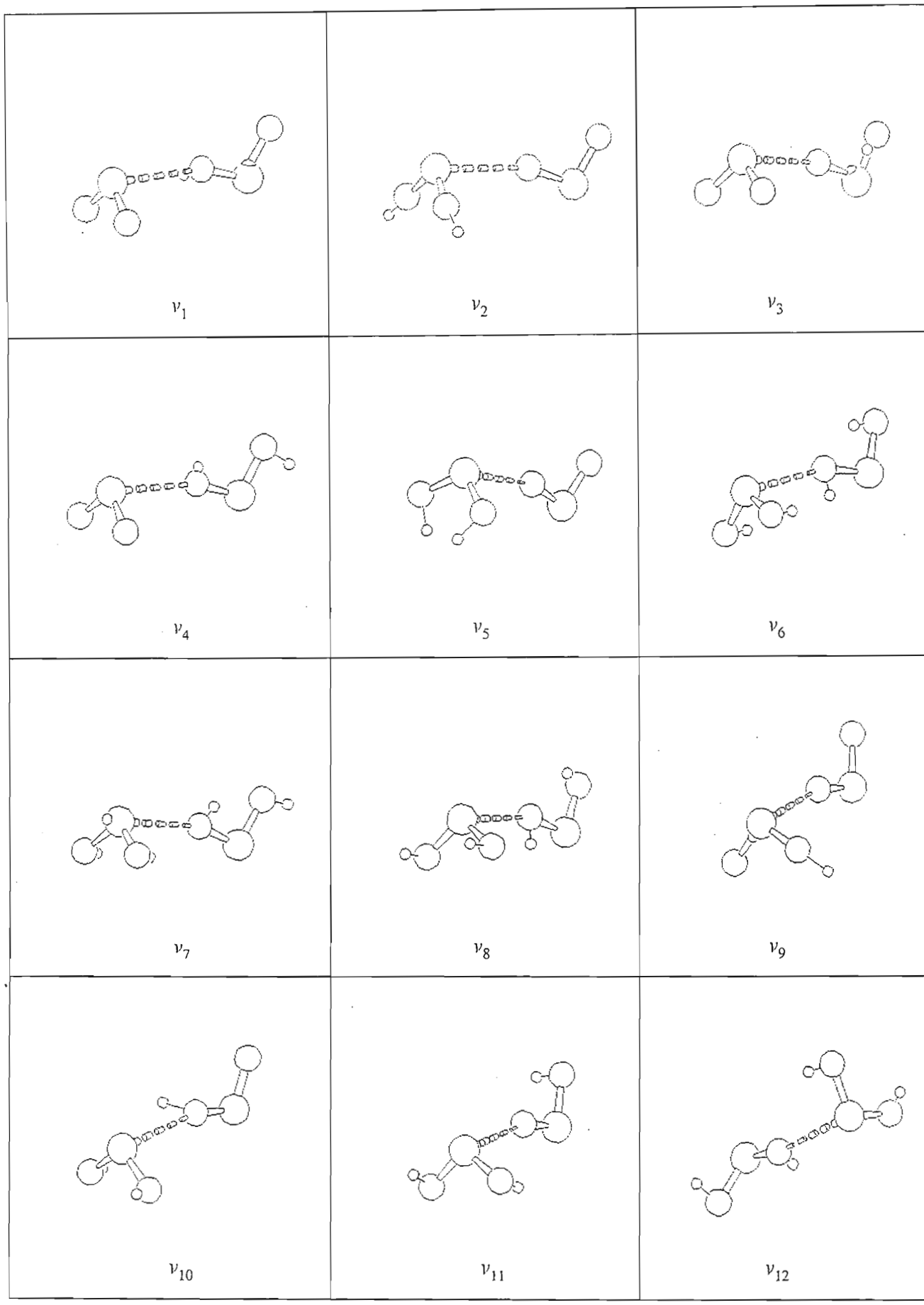

Fig 6.9 Graphical Representation of the H_2Y Dimer Vibration modes

Table 6.25 Symmetry Coordinates for the H_2Y Dimers

Symmetry Coordinate	Description
$S_1 = 1/\sqrt{2}\ (\Delta r_1 + \Delta r_2)$	H_2Y symmetric stretch
$S_2 = \Delta r_3$	HY stretch (proton donor)
$S_3 = \Delta r_4$	HY stretch (proton acceptor)
$S_4 = \Delta\beta$	HYH bend (proton donor)
$S_5 = \Delta\gamma$	H_2Y bend (proton acceptor)
$S_6 = \Delta R$	Y..H stretch
$S_7 = 1/\sqrt{2}\ (\Delta\gamma_1 + \Delta\gamma_2)$	H_2Y wag (proton acceptor)
$S_8 = \Delta\pi_1$	HY..H in plane bend
$S_9 = 1/\sqrt{2}\ (\Delta r_1 - \Delta r_2)$	H_2Y antisymmetric stretch
$S_{10} = 1/\sqrt{2}\ (\Delta\gamma_1 - \Delta\gamma_2)$	H_2Y twist (proton acceptor)
$S_{11} = \Delta\pi_2$	HY..H out of plane bend
$S_{12} = \Delta\tau$	HY..HY torsion

The percentage potential energy distributions amongst the various vibrational modes in the H_2O and H_2S dimers are reported in Tables 6.26 and 6.27 respectively.

Table 6.26 Wavenumbers and %PED's in the H_2O Dimer

Symmetry Species	Wavenumber /cm^{-1}	%PED
a'	3998	$15S_2 + 85S_3$
	3876	$96S_1 + 4S_2$
	3818	$4S_1 + 81S_2 + 14S_3$
	1714	$1S_2 + 95S_4 + 4S_8 + 1S_3$
	1680	$2S_1 + 98S_5$
	429	$56S_7 + 30S_8 + 13S_4$
	205	$66S_6 + 22S_7 + 11S_8$
	142	$2S_4 + 3S_6 + 40S_7 + 54S_8$
a"	4007	$100S_9$
	660	$63S_{11} + 38S_{12}$
	162	$33S_{11} + 18S_{10} + 49S_{12}$
	87	$47S_{11} + 16S_{10} + 37S_{12}$

From Table 6.26 which shows the symmetry coordinates and PED contributions, it can be seen that the ν_1 mode is due to the free OH stretch in the proton donor species. This indicates the strength of the hydrogen bond in the water dimer is much larger than that in the H_2S dimer, since the bonded proton is being attracted much more strongly by the oxygen atom in the proton acceptor than the sulphur atom in H_2S. This trend is characteristic since water exists as a liquid due to the strong hydrogen bonding between

the molecules and H_2S is a gas at room temperature.

Table 6.27 Wavenumbers and %PED in the H_2S Dimer

Symmetry Species	Wavenumber /cm^{-1}	%PED
a'	2857	$16S_2 + 84S_3$
	2839	$100S_1$
	2822	$82S_2 + 17S_3$
	1277	$98S_4 + 2S_5$
	1267	$99S_5 + 1S_4$
	158	$4S_4 + 63S_7 + 33S_8$
	88	$2S_4 + 40S_7 + 58S_8$
	66	$99S_6 + 1S_7$
a"	2865	$100S_9$
	273	$32S_{10} + 68S_{12}$
	78	$54S_{10} + 46S_{12}$
	50	$94S_{11} + 4S_{10} + 3S_{12}$

The ν_1 and ν_3 modes in the H_2Y dimers have contributions from S_2 and S_3 suggesting that neither mode is independent of the other thus implying that there is a slight perturbation in the inherent individual vibrational modes of the monomers on hydrogen bond formation.

The PED's amongst the vibrational modes are consistent per symmetry species in both dimers except for the wagging mode of the proton acceptor and the in-plane hydrogen bond bending mode represented by ν_7 and ν_8 respectively, while the twisting (ν_{10}), out-of-plane hydrogen bond bending (ν_{11}) and torsional modes (ν_{12}) have their symmetry coordinate contribution to the PED's reversed in the case of the H_2S dimer. This anomaly is due to the hydrogen bond being stronger in the former than in the latter dimer, resulting in the hydrogen bond stretching coordinate playing a minor role in the H_2S dimer. The changes in the intensities on complexation are reported in Tables 6.28 and 6.29 and the complex / monomer intensity ratios are compared for both the H_2Y dimers.

The major intensity enhancements occur in the ν_1 and ν_3 modes of the H_2O dimer, which involve the H_2O symmetric stretch and the hydrogen bonded OH stretch. The ν_3 mode in the water dimer shows an intensity enhancement of 47.9 characteristic of the strength of the hydrogen bond in the dimer. The ν_4 and ν_5 mode intensities in the water dimer, corresponding to the bending vibrations, are almost unchanged compared with the monomers. In the case of the H_2S dimer the major intensity enhancement occurs in ν_3 and ν_9 modes by 4.35 and 6.71 respectively; being the symmetric and antisymmetric stretching modes of the proton acceptor.

Table 6.28 Ratio of the Complex to Monomer Intensity Values for the H_2O Dimer

Complex	Symmetry Species	Mode	Complex A/km mol^{-1}	A_c/A_m
$(H_2O)_2$	a'	ν_1	78.8	18.76
		ν_2	13.5	3.21
		ν_3	201.2	47.90
		ν_4	76.4	0.98
		ν_5	76.1	0.97
		ν_6	32.9	
		ν_7	163.9	
		ν_8	254.2	
	a"	ν_9	60.3	1.78
		ν_{10}	139.4	1.79
		ν_{11}	170.5	
		ν_{12}	53.1	

Table 6.29 Ratio of the Complex to Monomer Intensity Values for the H_2S Dimer

Complex	Symmetry Species	Mode	Complex A/km mol^{-1}	A_c/A_m
$(H_2S)_2$	a'	ν_1	5.8	1.48
		ν_2	1.9	0.48
		ν_3	17.0	4.35
		ν_4	9.7	1.27
		ν_5	6.5	0.85
		ν_6	18.0	
		ν_7	52.0	
		ν_8	0.5	
	a"	ν_9	44.0	6.71
		ν_{10}	3.2	0.42
		ν_{11}	24.0	
		ν_{12}	44.0	

6.3 *The AH_3 Dimers (A= N,P)*

6.3.1 *Geometries*

The AH_3 dimers have been characterised theoretically by numerous studies, however most attention has focused on the ammonia dimer. The early theoretical studies[108,127] on the phosphine dimer predicted a linear C_s structure, however later studies by Del Bene et al[71] located a doubly bifurcated structure of C_{2h} symmetry. There have been no experimental studies on the phosphine dimer to our knowledge. Two structures were optimized for the phosphine dimer, comprising the linear C_s hydrogen bonded structure (fig 6.10) and the C_{2h} doubly bifurcated structure (fig 6.11). The doubly bifurcated structure was found to be the global minimum energy structure for this dimer and hence the properties of this structure only will be reported. The ammonia dimer on the other hand has attracted a lot more attention, resulting in diverse structural findings by different studies. The microwave studies[172,174,175] by the Klemperer group proposed a C_s geometrical arrangement, having a bifurcated type interaction with a dipole moment of 0.7 D. Infrared matrix isolation studies by Barnes[170] favour the linear C_s arrangement for the dimer, while similar studies by Suzer and Andrews[167] support the "Klemperer" type structure. Most of the theoretical studies support the linear C_s geometry, with some studies focusing on the C_{2h} geometry. To date there is only one study in favouring of the Klemperer structure, that of Sagarik et al.[186] The studies by Sagarik et al[186] were controversial, since the technique employed in geometry optimization was fairly rigid in the assumptions which were made. Our studies focused on different possible structures for the ammonia dimer; these comprised the "Klemperer" structure (fig. 6.12), C_{2h} bifurcated (fig 6.13) and the C_s linear hydrogen bonded (fig 6.14) geometries. We located the C_{2h} geometry as the only local minimum energy structure, however this was energetically less favoured than the C_s linear hydrogen bonded structure, clearly a larger basis set and higher level of theory are required for a more detailed geometry optimization of this dimer, which was beyond the scope of this

study. The "Klemperer" structure was also optimized by imposing symmetry constraints, since the structure always collapsed to the C_s linear hydrogen bonded structure. The "Klemperer" structure was found to be a saddle point on the PES of the ammonia dimer. The mode corresponding to the negative eigenvalue for the C_s linear structure suggests that the linear dimer structure is undergoing some torsion about the NH..N bond. Tables 6.30 collect the geometrical parameters for the C_{2h} ammonia dimer structure.

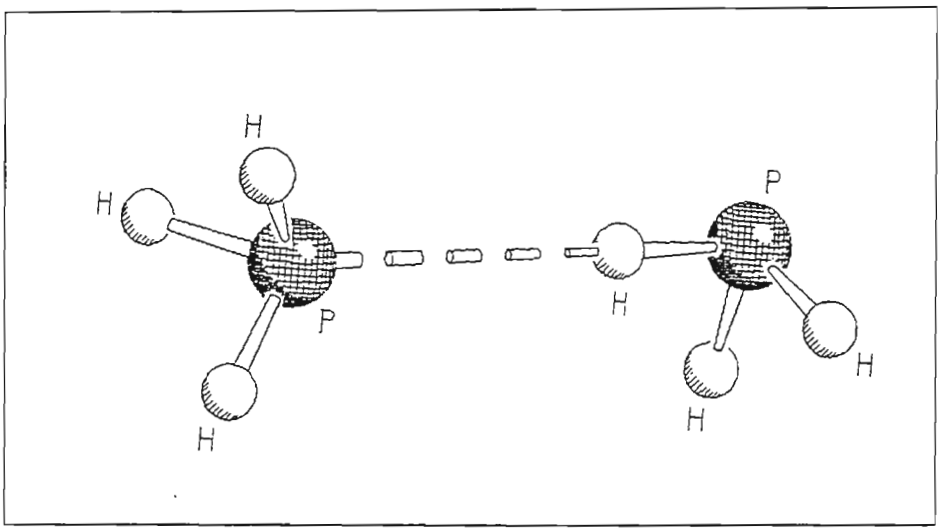

Fig 6.10 The Linear PH_3 Dimer

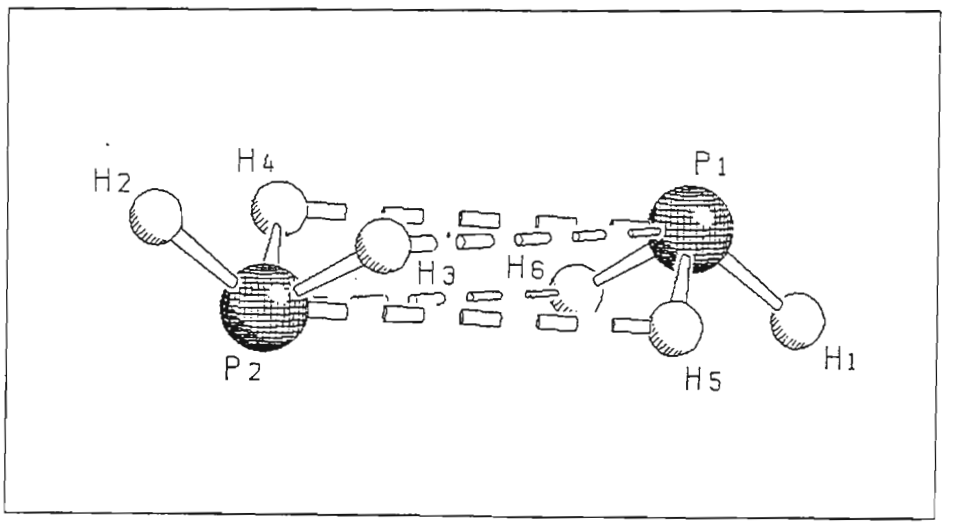

Fig 6.11 The Doubly Bifurcated PH_3 Dimer

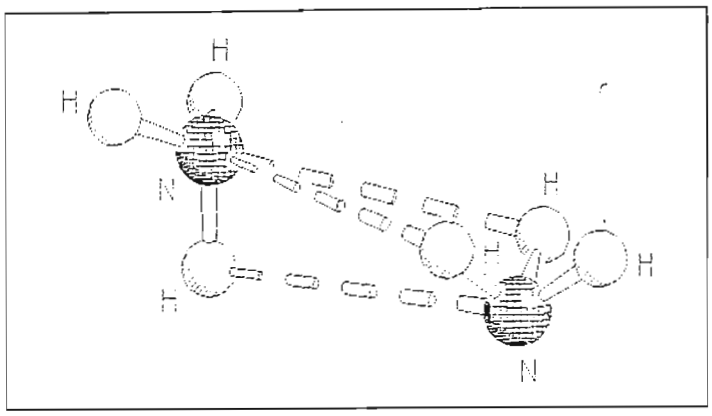

Fig 6.12 The "Klemperer" NH_3 Dimer

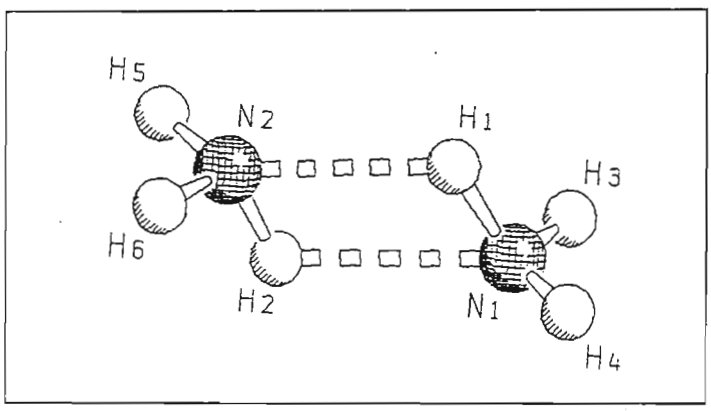

Fig 6.13 The C_{2h} NH_3 Dimer

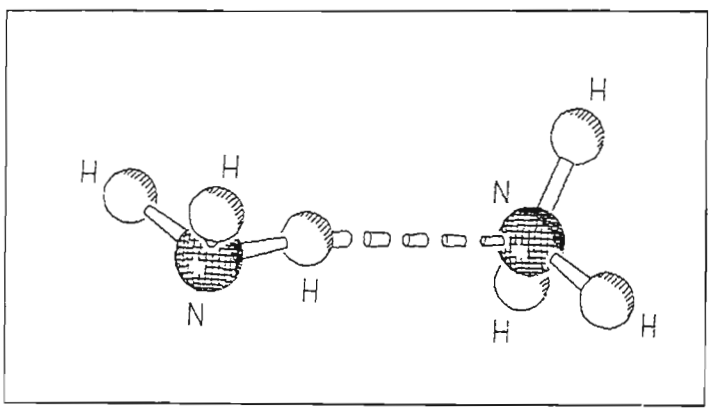

Fig 6.14 The Linear NH_3 Dimer

Table 6.30 Geometrical Parameters for the Most Stable (C_{2h}) NH_3 Dimer

Parameter	Complex	Monomer	Difference
r(N1H1)/pm	101.4	101.2	0.2
r(N1H3)/pm	101.3	101.2	0.1
R(N1..H2)/pm	245.5		
H4N1H3/deg	106.1	106.1	0.0
H3N1..H1/deg	106.5		
N1H1..N2/deg	123.7		

The major change that occurred in the geometrical parameters of the linear dimer was the increased proton donor NH bond length (by 0.5 pm), while the remaining parameters retain almost the monomer parameter values. The hydrogen bond angle was found to be close to linear. The increase in bond length and the hydrogen bond angle being close to linear are indicative of a typical hydrogen bond. However in the C_{2h} dimer the major change in the geometrical parameters occurs in the N1H1 and N2H2 bond lengths of 0.2 pm while the remaining geometrical parameters are close to the monomer parameter values. The changes in the geometrical parameters of the phosphine dimer on complexation are collected in Table 6.31.

Table 6.31 Geometrical Parameters of the Doubly Bifurcated (C_{2h}) PH_3 Dimer

Parameter	Complex	Monomer	Difference
r(P1H1)/pm	140.7	140.5	0.2
r(P1H2), r(P1H3)/pm	140.5	140.5	0.0
r(P2H4)/pm	140.7	140.5	0.2
r(P2H5), r(P2H6)/pm	140.5	140.5	0.0
R(P1..P2)/pm	383.0		
P2..P2H1/deg	179.9		
H1P1H3, H1P1H2/deg	94.8	94.5	0.3
H4P2H5, H4P2H6/deg	94.8	94.5	0.3

On examining the changes in geometrical parameters in the phosphine dimer, the major changes are seen to occur in the bond angles in contrast with the bond length increases in the ammonia dimer. The major changes occur in the H1P1H3 and H1P1H2 bond angles by 0.3°. The PH..P bond angle in the linear dimer was found to be 165.3°, suggesting that this bond is not characteristic of a strongly hydrogen bonded complex since there is a large deviation from linearity. The transformation from the C_{2h} to the C_s structure involves the rocking motion of one PH_3 monomer in the PH..P plane coupled with a rotation of the other unit about its three-fold axis. The identification of the C_s dimer as a local minimum on the PES, with a P1H1..P2 angle of 165.3° suggests that the curvature of the PES around the C_{2h} doubly bifurcated global minimum structure is irregular as opposed to that in the ammonia dimer.

6.3.2 *Energetics*

The corrected and uncorrected binding energies together with the BSSEs are reported in Table 6.32 below for the AH_3 dimers. The percentage dispersion contributions to the MP2 corrected binding energies obtained are also shown.

Table 6.32 The MP2 Binding Energies for the Most Stable (C_{2h}) AH_3 Dimers

Complex	$\Delta E'$ /kJ mol^{-1}	ΔE /kJ mol^{-1}	BSSE /kJ mol^{-1}	$\%\Delta E_{Disp}$
$(NH_3)_2$	-10.5	-18.4	7.9	26.8
$(PH_3)_2$	-10.6	-18.7	8.1	99.3

Both the AH_3 dimers have comparable binding energies, the phosphine interaction energy, however, is dominated by the dispersion energy, 99% of the interaction energy being due to dispersion effects. The dispersion energy tends to play a larger role in the second row hydrides, as in the case of the HCl and H_2S dimers. This is expected since the orbitals involved in bonding are now more diffuse, containing greater d-orbital character, unlike the first row hydrides which contain a large percentage of p-orbital character. The early studies by Frisch et al[94] found the linear dimer to be the most stable structure while a later study by Latajka and Scheiner[185] using a similar approach to that of Frisch et al[94] found the C_{2h} structure to be the local minimum energy structure. The Morokuma energy decomposition analysis is reported in Table 6.33 for the NH_3 dimer.

Table 6.33 Energy Decomposition Analysis of the NH_3 Dimer/kJ mol^{-1}

Complex	ES	EX	CT	PL	MIX	Total
C_{2h}	-55.8	82.3	-14.3	-4.3	4.8	12.7

The major contribution in the C_{2h} dimer results from the exchange repulsion term, followed by the electrostatic term, hence this complex may be seen to be an exchange repulsion-electrostatic type complex. Steric considerations would most likely result in the dominance of the exchange repulsion term. The other attractive components of the SCF part of the interaction energy play a small role in overcoming the strong repulsive force of the exchange repulsion term. The NH_3 dimer can thus be classed as being repulsive and non-bonded in the gas phase. The decomposition analysis of the PH_3 dimer is shown in Table 6.34.

Table 6.34 Energy Decomposition Analysis of the Doubly Bifurcated PH_3 Dimer/kJ mol^{-1}

Complex	ES	EX	CT	PL	MIX	Total
C_{2h}	-1.88	2.98	-0.61	-0.23	0.28	0.54

As in the case of the NH_3 dimer, the PH_3 dimer has also the exchange repulsion term (2.98 kJ mol^{-1}) as the dominating force, followed by the attractive electrostatic term (-1.88 kJ mol^{-1}). At the SCF level this dimer is unbound and governed by repulsive forces.

6.3.3 *Mulliken Charge Analysis*

The Mulliken charge analyses for the NH_3 and PH_3 dimers are recorded in Tables 6.35 and 6.36 respectively.

Table 6.35 Mulliken Charge Analysis for the Most Stable (C_{2h}) NH_3 Dimer

Atom	Atomic Charge /e		Difference /e
	Complex	Monomer	
N1	-0.842	-0.786	-0.056
H2	0.316	0.262	0.054
H3	0.263	0.262	0.001
H4	0.263	0.262	0.001
			0.000
N2	-0.842	-0.786	-0.056
H1	0.316	0.262	0.054
H5	0.263	0.262	0.001
H6	0.263	0.262	0.001
			0.000

From the Mulliken charge analysis, being a symmetrical structure there is no nett charge transfer in the C_{2h} ammonia dimer and the monomers retain their inherent atomic charges. The nitrogen atoms do gain negative charge (-0.056 e) in both NH_3 units at the expense of the hydrogen bonded protons (0.054 e) in the dimer. The non bonded hydrogens also

suffer a small loss of negative charge (0.001 e) on complexation. The Mulliken charge analysis of the C_{2h} phosphine dimer is shown in Table 6.36.

Table 6.36 Mulliken Charge Analysis of the Doubly Bifurcated (C_{2h}) PH_3 Dimer

Atom	Atomic Charge /e		Difference /e
	Complex	Monomer	
P1	0.155	0.162	-0.007
H1	-0.061	-0.054	-0.007
H2	-0.047	-0.054	0.007
H3	-0.047	-0.054	0.007
			0.000
P2	0.155	0.162	-0.007
H4	-0.061	-0.054	-0.007
H5	-0.047	-0.054	0.007
H6	-0.047	-0.054	0.007
			0.000

From Table 6.36 it can be seen that there is no nett charge transfer because both monomer units are equivalent as in the case of the NH_3 dimer. The sign of the atomic charge on the phosphorus atom in the PH_3 monomer is positive, since the hydrogen atoms are more electronegative than the phosphorus atom. The phosphorus atoms and the non-hydrogen bonded hydrogen atoms both gain negative charge (-0.007 e) at the expense of the

hydrogen bonded hydrogen atoms, as in the case of the ammonia dimer.

6.3.4 *Vibrational Properties of the Most Stable AH_3 Dimers*

The calculated vibrational spectrum of the ammonia dimer compared with the calculated monomer vibrational spectrum is collected in Table 6.37. The vibrational modes for the ammonia and phosphine dimers are collected in figs. 6.15 and 6.16 respectively. The red and blue shifts of ν_2 and ν_4 are characteristic of a hydrogen bonded complex. The major shift occurring on dimerization occurs in ν_4 (45 cm^{-1}); the magnitudes of the remaining wavenumber shifts are all less than 30 cm^{-1}. These small shifts are typical of weak hydrogen bonded complexes. In this C_{2h} dimer, having no proton donor nor acceptor, the task of determining whether the dimer is hydrogen bonded from it's infrared spectrum, as in the case of linear hydrogen bonded systems, becomes impossible since all the modes become coupled in the two sub-units.

Table 6.37 Calculated Wavenumber Shifts on Dimerization for the (C_{2h}) Ammonia Dimer

Symmetry Species	Mode	Calculated Wavenumber /cm^{-1}	Monomer Wavenumber /cm^{-1}	Shift[(a)] / cm^{-1}
a_g	ν_1	3703	3728	-25
	ν_2	3548	3571	-23
	ν_3	1733	1724	9
	ν_4	1161	1116	45
a_u	ν_7	3714	3728	-14
	ν_8	1747	1724	23

Table 6.37 Continued

b_g	ν_{11}	3713	3728	-15
	ν_{12}	1736	1724	12
b_u	ν_{14}	3704	3728	-24
	ν_{15}	3553	3571	-18
	ν_{16}	1707	1724	-17
	ν_{17}	1138	1116	22

(a) Shift = Complex - Monomer

The symmetry coordinate descriptions for the C_{2h} NH_3 dimer are collected in Table 6.36.

Table 6.38 Symmetry Coordinates for the (C_{2h}) NH_3 Dimer

Symmetry Coordinate	Description
$S_1 = 1/\sqrt{2}\ (\Delta r_1 + \Delta r_2)$	NH_2 symmetric stretch
$S_2 = 1/\sqrt{12}\ (2\Delta r_1 - \Delta r_3 - \Delta r_4 + 2\Delta r_2 - \Delta r_5 - \Delta r_6)$	NH_3 symmetric stretch
$S_3 = 1/\sqrt{12}\ (2\Delta r_1 - \Delta r_3 - \Delta r_4 - 2\Delta r_2 + \Delta r_5 + \Delta r_6)$	NH_3 antisymmetric stretch
$S_4 = 1/2\ (-\Delta r_3 + \Delta r_4 + \Delta r_5 - \Delta r_6)$	NH_3 antisymmetric stretch
$S_5 = 1/2\ (-\Delta r_3 + \Delta r_4 - \Delta r_5 + \Delta r_6)$	NH_3 symmetric stretch
$S_6 = 1/\sqrt{6}\ (\Delta r_1 + \Delta r_3 + \Delta r_4 - \Delta r_2 - \Delta r_5 - \Delta r_6)$	NH_3 antisymmetric stretch

Table 6.38 Continued

$S_7 = 1/\sqrt{12}\ (2\Delta\alpha_1 - \Delta\alpha_2 - \Delta\alpha_3 - 2\Delta\theta_1 + \Delta\theta_2 + \Delta\theta_3)$	NH_2 symmetric bend
$S_8 = 1/2\ (\Delta\alpha_2 - \Delta\alpha_3 + \Delta\beta_2 - \Delta\beta_3)$	NH_2 twist
$S_9 = 1/\sqrt{6}\ (\Delta\alpha_1 + \Delta\alpha_2 + \Delta\alpha_3 + \Delta\beta_1 + \Delta\beta_2 + \Delta\beta_3)$	NH_3 symmetric bend
$S_{10} = 1/\sqrt{12}\ (2\Delta\alpha_1 - \Delta\alpha_2 - \Delta\alpha_3 - 2\Delta\beta_1 + \Delta\beta_2 + \Delta\beta_3)$	NH_3 symmetric bend
$S_{11} = 1/2\ (\Delta\alpha_2 - \Delta\alpha_3 + \Delta\beta_2 - \Delta\beta_3)$	NH_2 twist
$S_{12} = 1/\sqrt{2}\ (\Delta\theta_1 + \Delta\theta_4)$	out of plane shearing motion
$S_{13} = 1/\sqrt{2}\ (\Delta\delta_1 + \Delta\delta_2)$	in plane geared rotation
$S_{14} = 1/\sqrt{2}\ (\Delta R_1 + \Delta R_2)$	N..H symmetric stretch
$S_{15} = 1/\sqrt{2}\ (\Delta\delta_1 - \Delta\delta_4)$	out of plane geared rotation
$S_{16} = 1/\sqrt{6}\ (\Delta\alpha_1 + \Delta\alpha_2 + \Delta\alpha_3 - \Delta\beta_1 - \Delta\beta_2 - \Delta\beta_3)$	NH_3 antisymmetric bend
$S_{17} = 1/\sqrt{6}\ (\Delta\alpha_1 + \Delta\alpha_2 + \Delta\alpha_3 + \Delta\beta_1 + \Delta\beta_2 + \Delta\beta_3)$	NH_3 symmetric bend
$S_{18} = \Delta\tau_3$	anti-geared rotation

The symmetry coordinates for the NH_3 dimer intramolecular modes were generated using those modes localised to the individual monomers and coupling them, thus accounting for the motion of both NH_3 units together. The symmetry coordinates for the intermolecular

modes were generated using the cyclic ring as the sub group, for the definition of the torsional and rotational modes of the NH_3 units. The remaining symmetry coordinates for the intermolecular modes were generated using the first order rules of Wilson et al.[70] The contribution of the different symmetry coordinates to the PEDs are collected in Table 6.39 for the ammonia dimer.

Table 6.39 Wavenumbers and %PEDs in the (C_{2h}) NH_3 Dimer

Symmetry Species	Wavenumber /cm^{-1}	%PED
a_g	3703	$100S_2$
	3548	$100S_1$
	1733	$100S_{10}$
	1161	$100S_9$
	473	$50S_{10} + 50S_{13}$
	151	$100S_{14}$
a_u	3714	$100S_5$
	1747	$64S_8 + 36S_{16}$
	254	$67S_{18} + 22S_{16} + 10S_8$
	100	$100S_{18}$
b_g	3713	$100S_4$
	1736	$100S_{11}$
	1733	$76S_7 + 11S_{17} + 9S_{12} + 9S_{13}$

Table 6.39 Continued

b_u	3704	$100S_3$
	3553	$100S_6$
	1707	$100S_{10}$
	1138	$100S_{16}$
	107	$50S_{16} + 50S_{17}$

In the C_{2h} dimer the vibrational modes transform as $6_{ag} + 4_{au} + 3_{bg} + 5_{bu}$. The vibrational modes for the cyclic dimer are shown in fig 6.15. Since the cyclic dimer had no negative eigenvalues the complete vibrational analysis was performed only on this dimer. The early studies by Latajka and Scheiner[185] at the MP2 level of theory with the 6-31G** and 4-31G* basis sets also found the C_{2h} dimer structure to be a local minimum on the PES; these studies were also supported by the recent studies of Cybulski et al[195] incorporating mid-bond functions into the basis sets.

Hence we are justified in carrying out a thorough analysis on the C_{2h} dimer structure only. Most of the intramolecular modes have symmetry coordinate contributions to their PEDs exclusively from the resulting modes in the parent monomers, except for the bending modes ν_8 and ν_{13}. The ν_8 mode has its major symmetry coordinate contribution from the twisting of the non-bonded hydrogens and a minor contribution from the bending mode of the bonded NH groups, while in the case of ν_{13}, the major symmetry coordinate contribution is from the bending mode of the bonded hydrogen atoms. The intermolecular modes on the other hand have symmetry coordinate distributions from various species since each intermolecular mode causes a perturbation of another mode in the ring of the dimer.

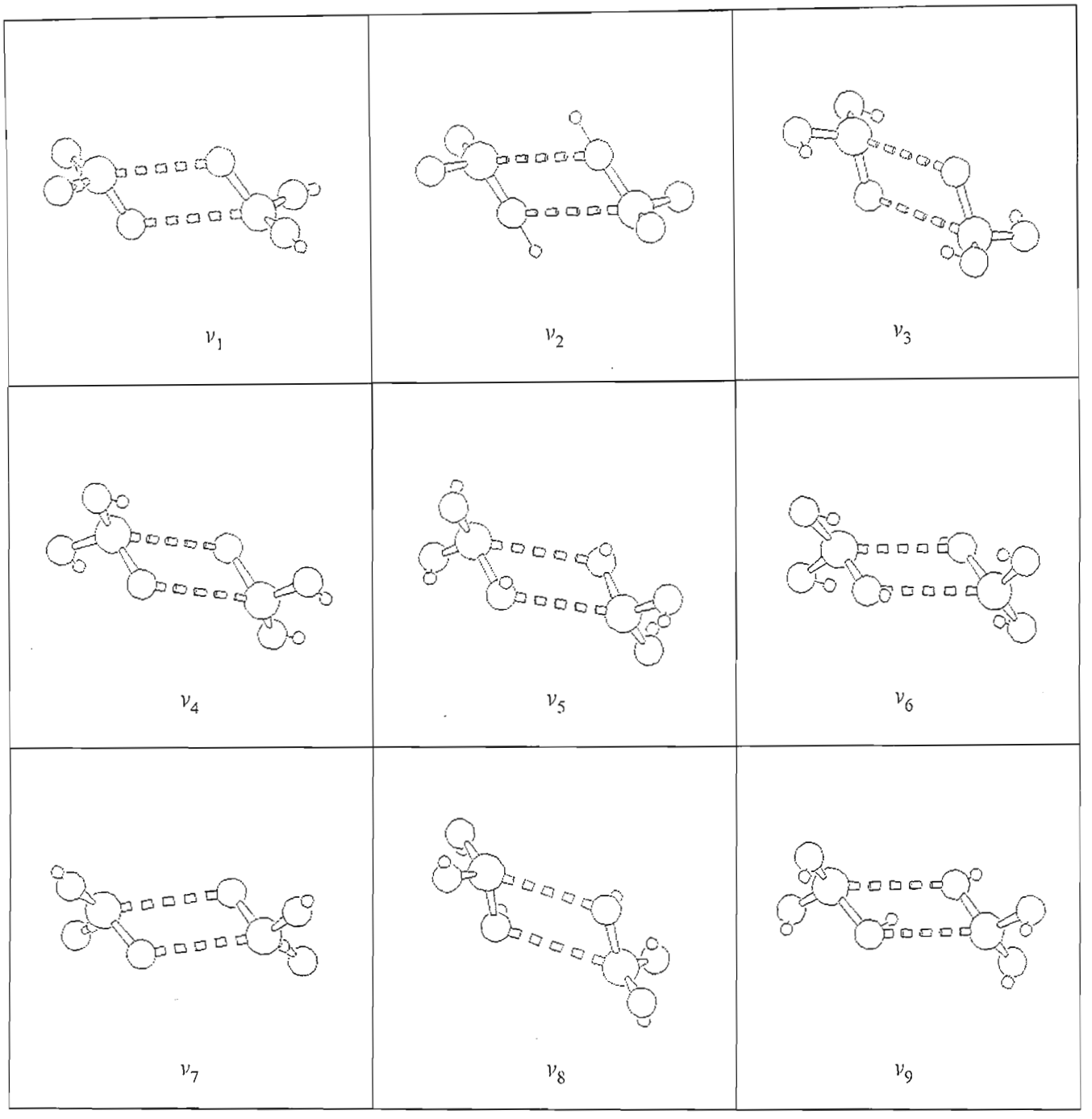

Fig 6.15 Graphical Representation of the NH_3 Dimer Vibration modes

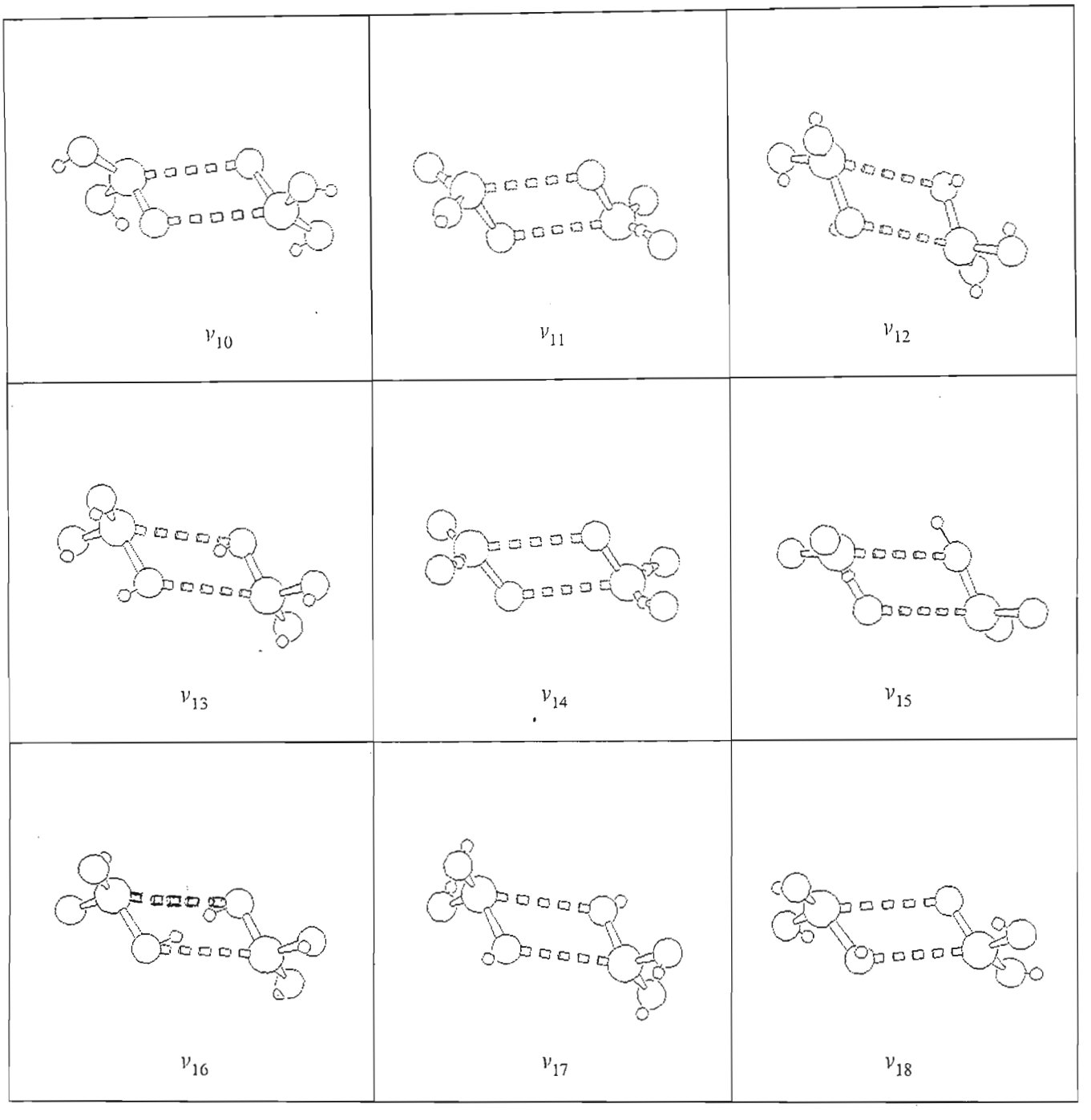

Fig 6.15 Graphical Representation of the NH_3 Dimer Vibration modes

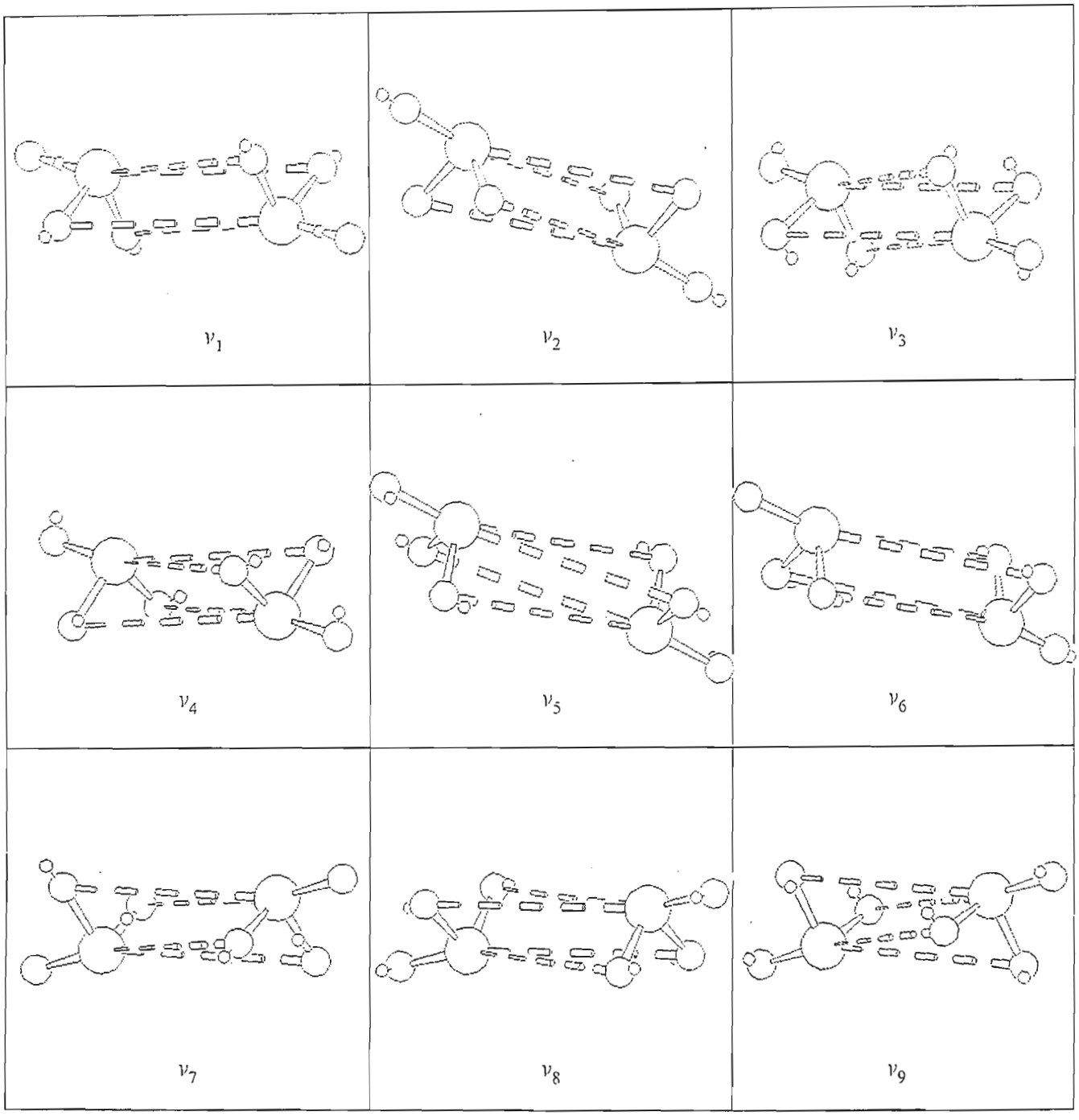

Fig 6.16 Graphical Representation of the PH_3 Dimer Vibration modes

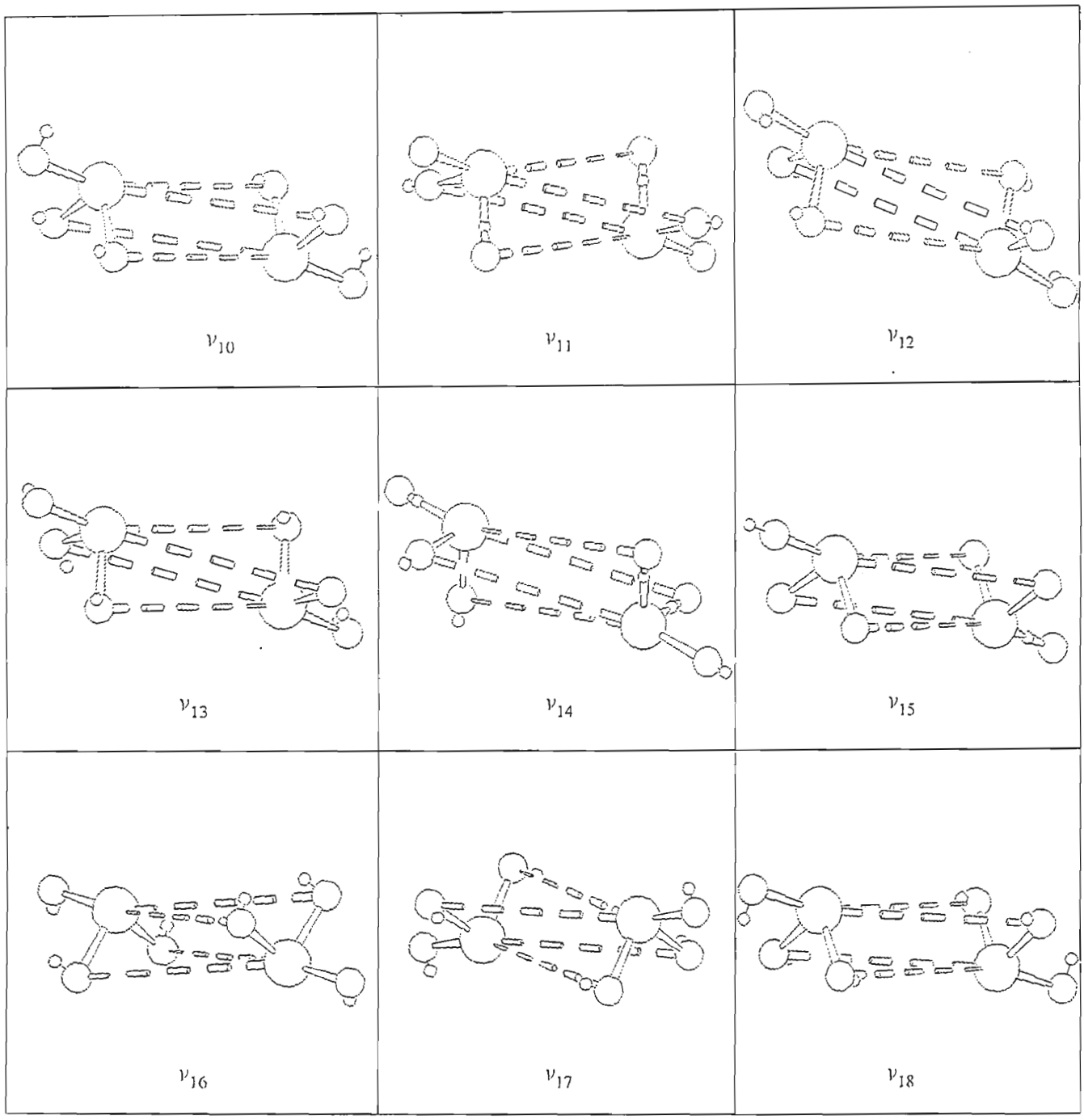

Fig 6.16 Graphical Representation of the PH_3 Dimer Vibration modes

The changes in the intensities of the vibrational modes in the C_{2h} NH_3 dimer are reported in Table 6.40.

Table 6.40 Ratio of the Complex to Monomer Intensities in the NH_3 Dimer

Complex	Symmetry Species	Mode	Complex A_c/km mol^{-1}	A_c/A_m
$(NH_3)_2$	a_g	ν_1	0.0	-
		ν_2	0.0	-
		ν_3	0.0	-
		ν_4	0.0	-
		ν_5	0.0	-
		ν_6	0.0	-
	a_u	ν_7	0.9	1.12
		ν_8	29.1	1.41
		ν_9	122.4	
		ν_{10}	27.8	
	b_g	ν_{11}	0.0	-
		ν_{12}	0.0	-
		ν_{13}	0.0	-
	b_u	ν_{14}	25.3	31.62
		ν_{15}	15.3	19.12

Table 6.40 Continued

		ν_{16}	17.1	0.82
		ν_{17}	365.4	1.68
		ν_{18}	301.4	

The major intensity enhancement occurs in ν_{14}, being the antisymmetric stretching mode, comprising 100%S_3, followed by ν_{15}, comprising 100%S_6. The intensity enhancements of ν_{14} and ν_{15} by 31.62 and 19.12 respectively, are due to the inherent low intensities of the corresponding monomer modes. The minimal wavenumber shifts coupled with the low intensity enhancements on dimerization confirms the weakness of the NH..N bonds. The calculated vibrational spectrum of the doubly bifurcated PH_3 dimer is reported in Table 6.41.

From Table 6.41, the major wavenumber shifts occur in ν_7 and ν_{11}. The magnitudes of the wavenumber shifts are smaller than those in the ammonia dimer, suggesting this dimer to be even more weakly bound. The changes in the intensities on complexation are collected in Table 6.42, which would provide further evidence regarding the strength of binding of this dimer.

Table 6.41 Calculated Wavenumber Shifts in the Doubly Bifurcated PH_3 Dimer

Symmetry Species	Mode	Calculated Wavenumber /cm^{-1}	Monomer Wavenumber /cm^{-1}	Shift[(a)] /cm^{-1}
a_g	ν_1	2548	2546	2
	ν_2	2532	2531	1
	ν_3	1182	1183	-1
	ν_4	1073	1078	-5
a_u	ν_7	2555	2546	9
	ν_8	1185	1183	2
b_g	ν_{11}	2552	2546	6
	ν_{12}	1180	1183	3
b_u	ν_{14}	2548	2546	2
	ν_{15}	2531	2531	0
	ν_{16}	1180	1183	-3

(a) Shift = Complex - Monomer

Table 6.42 Ratio of the Complex to Monomer Intensities in the PH_3 Dimer

Complex	Symmetry Species	Mode	Complex A/km mol^{-1}	A_c/A_m
$(PH_3)_2$	a_g	ν_1	0.0	-
		ν_2	0.0	-
		ν_3	0.0	-
		ν_4	0.0	-
		ν_5	0.0	-
		ν_6	0.0	-
	a_u	ν_7	163.7	1.6
		ν_8	32.8	1.7
		ν_9	0.0	
		ν_{10}	15.0	
	b_g	ν_{11}	0.0	-
		ν_{12}	0.0	-
		ν_{13}	0.0	-
	b_u	ν_{14}	184.6	1.9
		ν_{15}	126.6	1.3
		ν_{16}	44.0	2.2

Table 6.42 Continued

		ν_{17}	63.0	-
		ν_{18}	26.4	-

The major changes in the intensities on dimerization occur in ν_{16} and ν_{14} by 2.2 and 1.9 respectively. In conventional hydrogen bond type complexes the major intensity enhancements always occur in the bonded stretching modes, while in this dimer the bending mode tends to dominate the intensity enhancement. These changes occur since the intensities of the corresponding monomer modes are very low, thus magnifying the ratios obtained on dimerization. In general the intensity ratios are close to unity. Hence this dimer is fairly weak and the monomers are held together solely by forces of dispersion.

6.4 *The MH_4 Dimers (M= C,Si)*

6.4.1 *Geometries*

The methane dimer has been subjected to numerous theoretical studies. The structures optimized for this dimer include the linear electron donor-acceptor type complex having $HCH_3..H_3CH$ (fig 6.17) and $H_3CH..H_3CH$ (fig 6.18) interactions. The first structure was found to be a saddle point, while the second was found to be a minimum energy structure on the potential energy surface. Complexes of this type are mostly dispersive in nature and hence require a large basis set coupled with a high level of theory for a proper study of the most feasible global minimum structure. Tsuzuki and Tanabe[201] showed, in their studies of the methane dimer at the Møller-Plesset level of theory, that as the basis set is increased in size the dispersion contribution also increases, hence stabilizing the dimer at the expense of the exchange repulsion term, resulting from the steric repulsion of the hydrogens of both methane monomers. Therefore one would expect that using the 6-

31G** basis set the $HCH_3..H_3CH$ structure would be found to be destabilized energetically. Studies by Williams et al[199] at the SCF level showed the dimer to be unbound and governed largely by the exchange repulsion term. Szczesniak et al[200] and Nagy et al[198] found the $HCH_3..H_3CH$ structure to be the minimum energy structure using a larger basis set than that used in this study. The approach used by Szczesniak et al and Nagy et al included the use of $MP2^{corr}$ theory, whereby the MP2 energies are approximated to be those energies obtained using an infinite basis set. In this study the data for the linear hydrogen bonded dimer only will be presented, since this structure was found to be a minimum energy structure. In the case of the SiH_4 dimer, the structures optimized comprise the $H_3SiH..HSiH_3$ (fig 6.19) with the non-bonded hydrogen atoms in both silane molecules staggered with respect to one another, the $HSiH_3..H_3SiH$ eclipsed (fig 6.20), and the $H_3SiH..H_3SiH$ staggered (fig 6.21), with one unit being the proton donor to the other as in the case of the linear methane dimer. The structures optimised for this dimer were analogous to those found in the SiF_4 dimer by Dixon et al[339] and Urban et al.[340] The failure to locate a local minimum energy structure for this dimer could be attributed once more to the inadequate basis set size and perhaps the level of theory used in this study. Hence no further discussion on the silane dimer will be reported in this study. The geometrical parameters of the linear bonded methane dimer are tabulated in Table 6.43

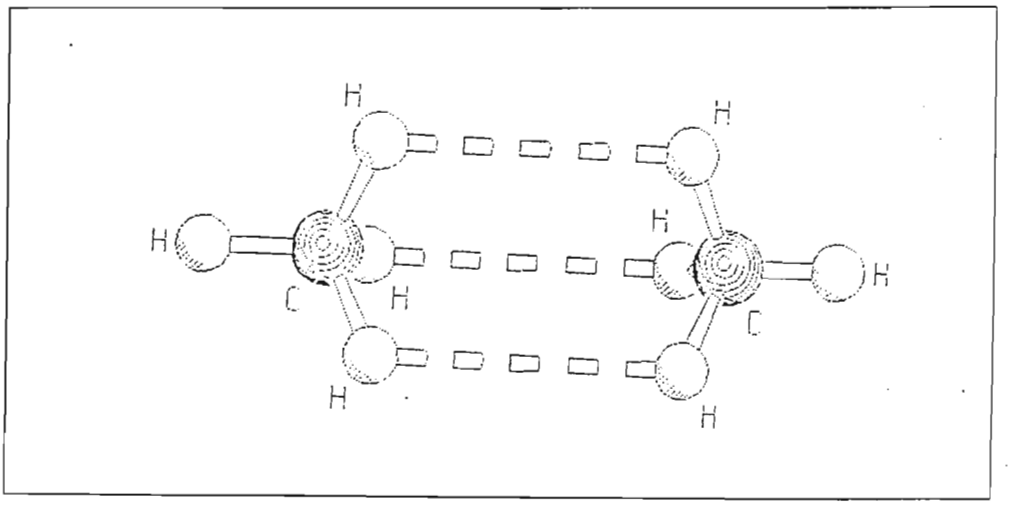

Fig 6.17 The CH_4 Trifurcated Dimer

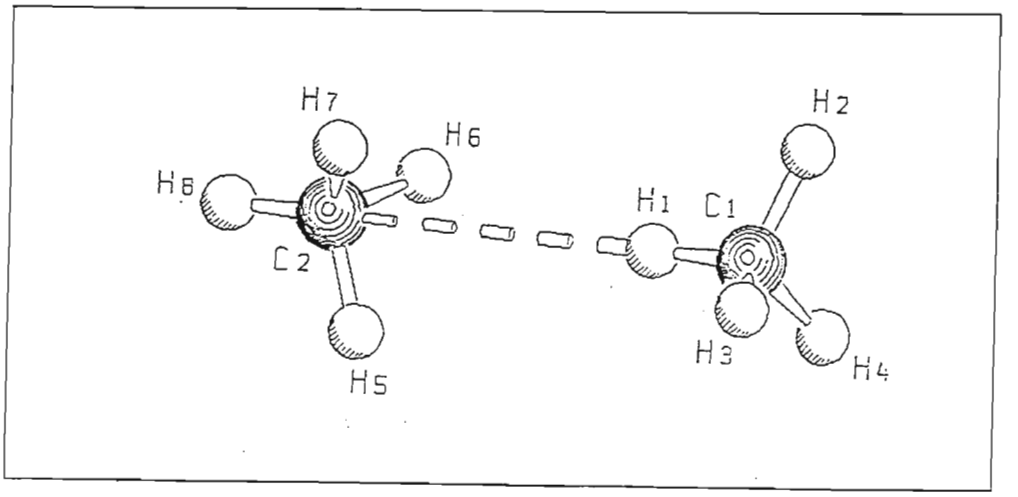

Fig 6.18 The Linear Staggered CH_4 Dimer

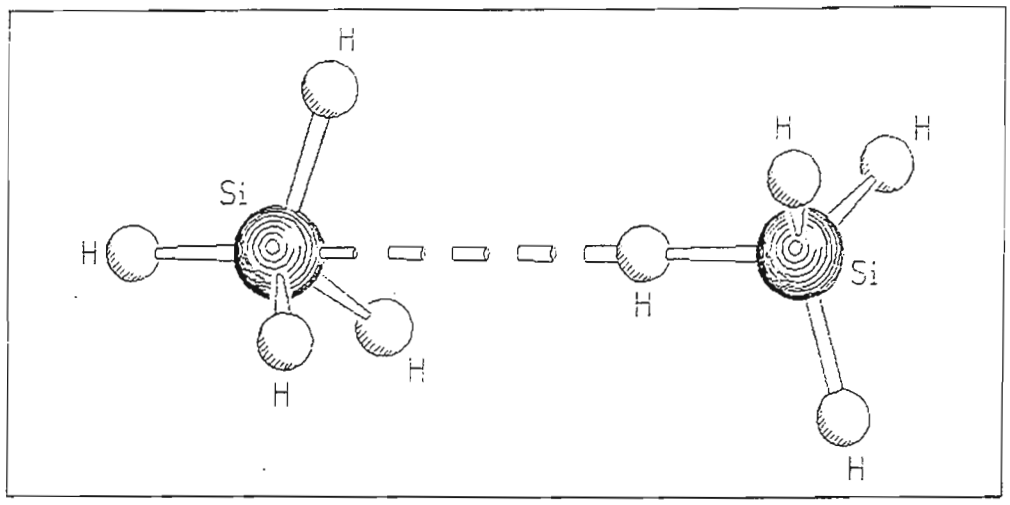

Fig 6.19 The Linear Staggered SiH_4 Dimer

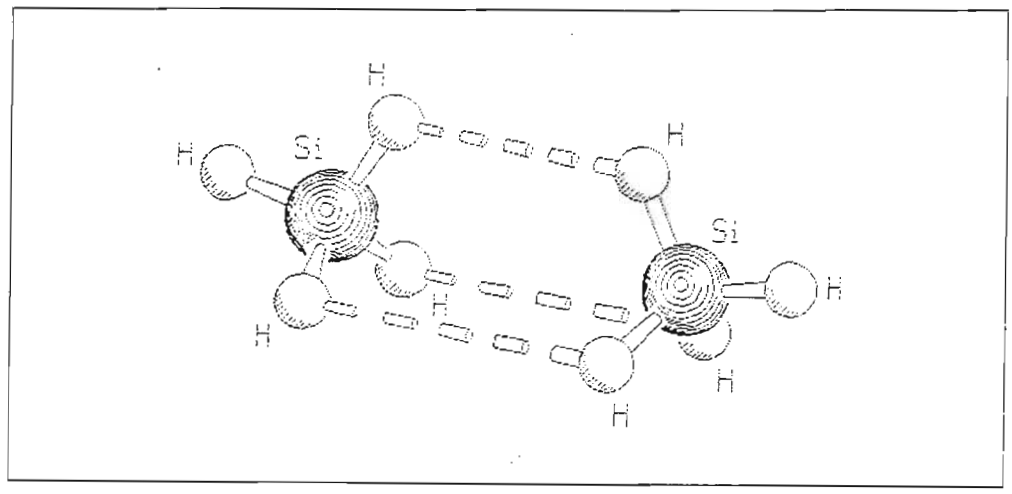

Fig 6.20 The SiH_4 Trifurcated Dimer

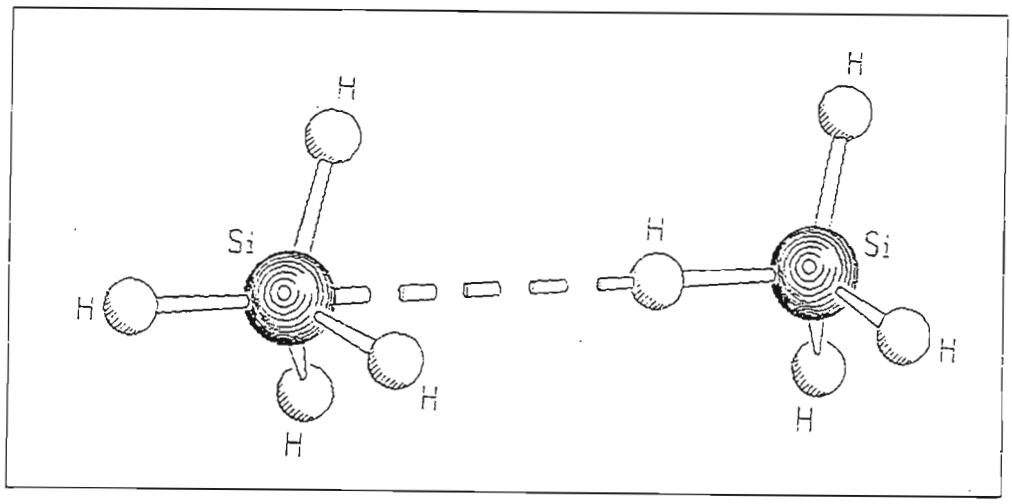

Fig 6.21 The Linear Eclipsed SiH_4 Dimer

Table 6.43 Geometrical Parameters For the Linear CH_4 Dimer

Parameter	Complex	Monomer	Difference
r(C1H1)/pm	108.5	108.4	0.1
r(C1H2), r(C1H3), r(C1H4)/pm	108.6	108.4	0.2
r(C2H8)/pm	108.6	108.4	0.2
r(C2H5), r(C2H6), r(C2H7)/pm	108.6	108.4	0.2
R(C2..H1)/pm	317.8		
C1H1..C2/deg	180.0		
H2C1H1, H3C1H1, H4C1H1/deg	109.4	109.5	-0.1
H5C2H8, H6C2H8, H7C2H8/deg	109.4	109.5	-0.1

The major changes in the geometrical parameters occur in the CH bond lengths. The C..H bond length was found to be 317.8 pm, which is much longer than that in a conventional hydrogen bonded complex. The intramolecular bond angles decreased by 0.1°. Even though the geometrical parameters are barely perturbed one could conclude that this dimer is indeed of a hydrogen bonded type. The analysis to follow on the energetics, Mulliken charge analysis and the vibrational spectrum will provide more information on the bonding in the dimer.

6.4.2 *Energetics*

The corrected and uncorrected binding energies together with the BSSEs are reported in Table 6.44 below for the linear hydrogen bonded CH_4 dimer. The percentage dispersion contributions to the MP2 corrected binding energies obtained are also shown.

Table 6.44 Binding Energy of the Most Stable CH_4 Dimer

Complex	$\Delta E'$ /kJ mol^{-1}	ΔE /kJ mol^{-1}	BSSE /kJ mol^{-1}	$\%\Delta E_{Disp}$
$(CH_4)_2$	-0.74	0.36	-1.10	95.5

From Table 6.44 it can be seen that the methane dimer is almost totally bonded by the forces of dispersion (95.5%), with the MP2 corrected energy being 0.36 kJ mol^{-1}, showing this complex to be very weak. Hence using a larger basis set should result in a better description of the forces of dispersion and would probably lead to convergence to the $HCH_3..H_3CH$ dimer structure. The Morokuma energy decomposition analysis is reported in Table 6.45, depicting the nature of the SCF interaction energy of the CH_4 dimer.

Table 6.45 Energy Decomposition Analysis of the Most Stable CH_4 Dimer /kJ mol^{-1}

Complex	ES	EX	CT	PL	MIX	Total
$(CH_4)_2$	-0.3	1.0	-0.2	0.0	0.1	0.6

The largest term in the decomposition analysis is the EX term followed by the ES term. The large contribution of the EX term to the SCF binding energy implies that the complex

is unbound at the SCF level of theory. A similar finding was reported by Williams et al.[199]

6.4.3 *Mulliken Charge Analysis*

The Mulliken charge analyses for the linear hydrogen bonded CH_4 dimer is recorded in Table 6.46.

It can be seen from Table 6.46, the proton donor gains negative charge from the acceptor, which is accepted solely by the carbon atom. In the process the hydrogen atoms in the proton donor also lose negative charge. Most of this negative charge in the proton acceptor comes from the hydrogen atoms as well, while the charge on the carbon atom remains unchanged on complexation. The negative charge accepted by the proton donor most likely occupies the antibonding orbitals, thus accounting for the increase in the CH bond length of the proton donor.

Table 6.46 Mulliken Charge Analysis for the Linear CH_4 Dimer

Atom	Atomic Charge /e		Difference /e
	Complex	Monomer	
C1	-0.477	-0.473	-0.004
H1	0.123	0.118	0.005
H2	0.117	0.118	-0.001
H3	0.117	0.118	-0.001
H4	0.117	0.118	-0.001
			-0.002
C2	-0.473	-0.473	0.000
H5	0.119	0.118	0.001
H6	0.119	0.118	0.001
H7	0.119	0.118	0.001
H8	0.118	0.118	0.000
			0.003

6.4.4 *Vibrational Properties of the Most Stable CH_4 Dimer*

The calculated wavenumber shifts on complexation for the CH_4 dimer are collected in Table 6.47, with the plot of the vibrational modes shown in fig 6.22.

Table 6.47 Calculated Wavenumber Shifts on Dimerization in the CH_4 Dimer

Symmetry Species	Mode	Calculated Wavenumber /cm^{-1}	Monomer Wavenumber /cm^{-1}	Shift[(a)] /cm^{-1}
a_1	ν_1	3281	3278	3
	ν_2	3276	3278	-2
	ν_3	3132	3143	-11
	ν_4	3130	3143	-13
	ν_5	1405	1404	1
	ν_6	1401	1404	-3
e	ν_9	3278	3278	0
	ν_{10}	3277	3278	-1
	ν_{11}	1626	1624	2
	ν_{12}	1620	1624	-4
	ν_{13}	1406	1404	2
	ν_{14}	1403	1404	-1

(a) Shift = Complex - Monomer

The major changes in the vibrational wavenumbers of the dimer occur in the ν_3 (-11 cm^{-1}) and ν_4 (-13 cm^{-1}) modes. The remaining vibrational modes are all shifted to a small extent from their monomer wavenumbers. This small shift on dimerization is an indication of a weakly hydrogen bonded dimer as shown in Table 6.44. The minor perturbations in the

wavenumbers could also be attributed to the distortion of the methane tetrahedrons on dimerization to the lower C_{3v} subgroup in the dimer. The symmetry coordinate description for the vibrational modes in the linear CH_4 dimer is reported in Table 6.48 in order to assist with the vibrational mode assignments.

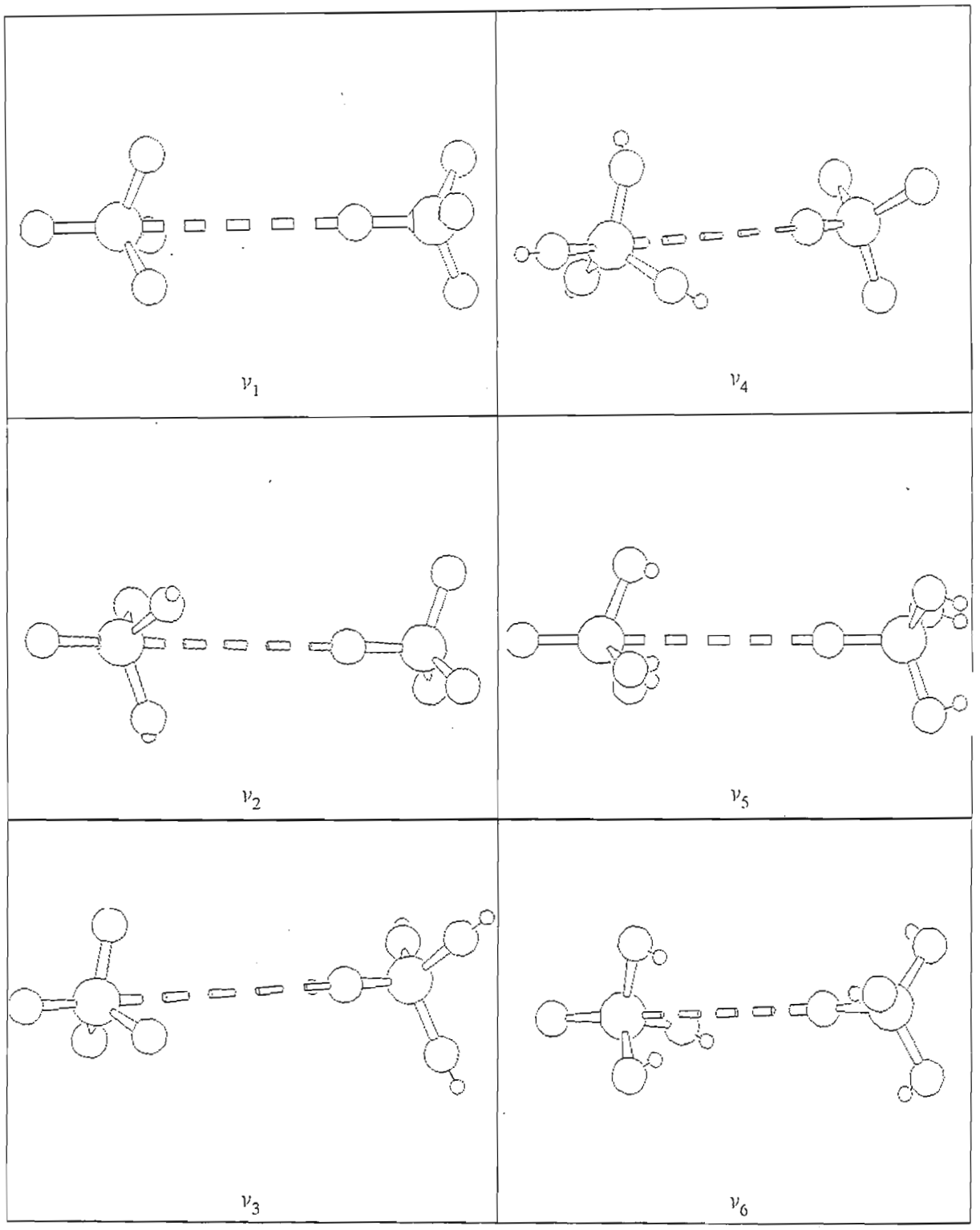

Fig 6.22 Graphical Representation of the CH_4 Dimer Vibration modes

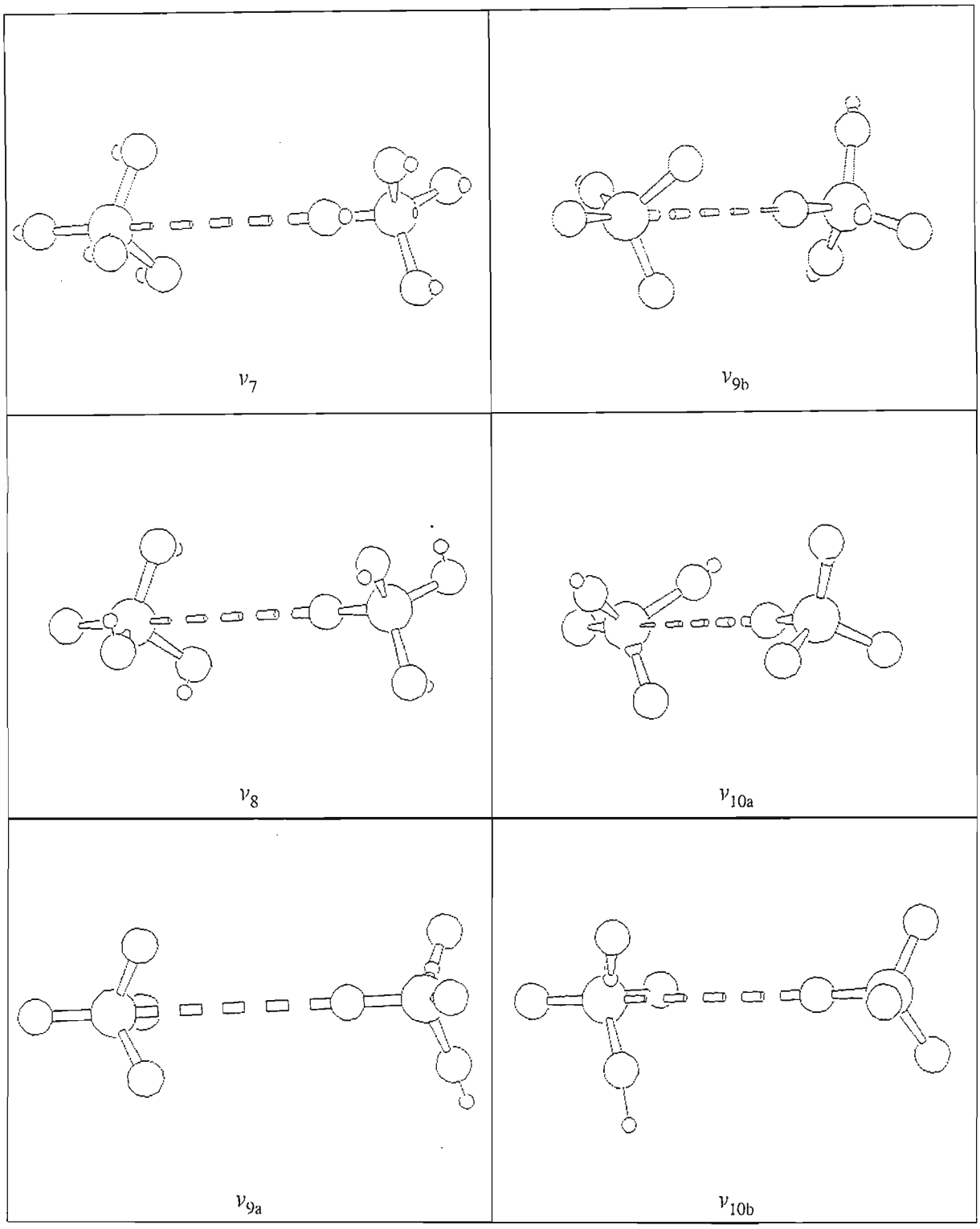

Fig 6.22 Graphical Representation of the CH_4 Dimer Vibration modes

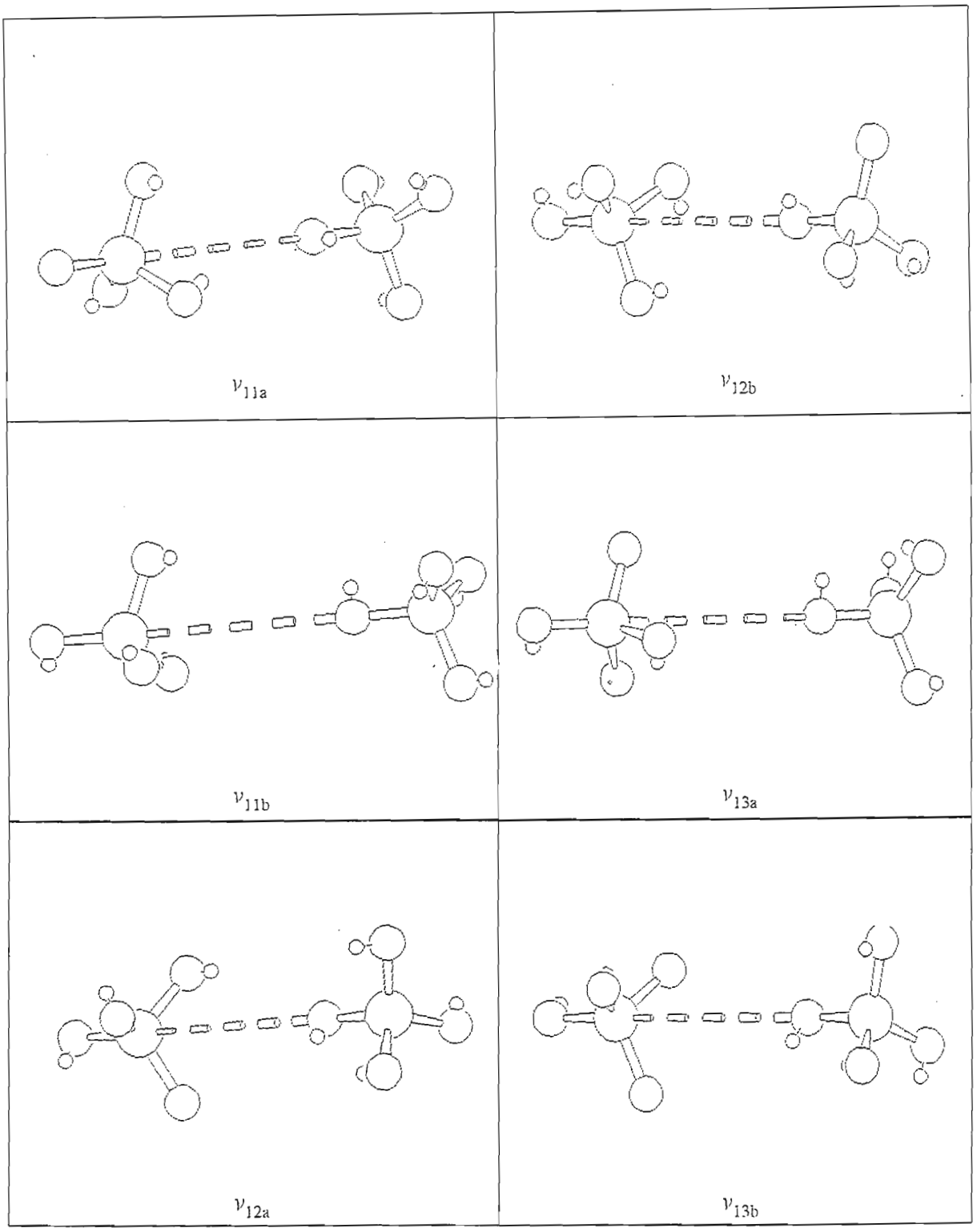

Fig 6.22 Graphical Representation of the CH_4 Dimer Vibration modes

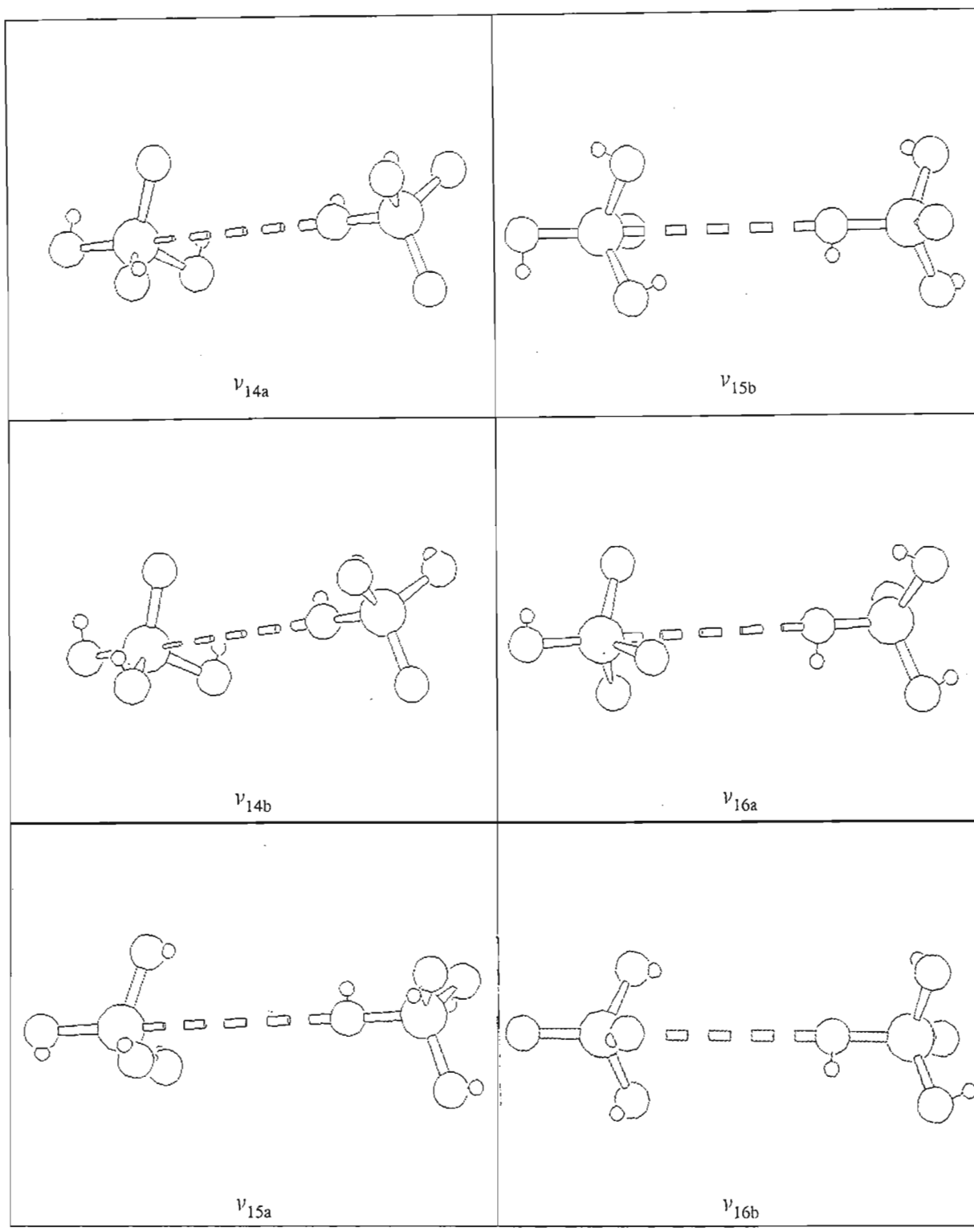

Fig 6.22 Graphical Representation of the CH_4 Dimer Vibration modes

Table 6.48 Symmetry Coordinates for the Linear CH_4 Dimer

Symmetry Coordinate	Description
$S_1 = \Delta r_1$	CH stretch (proton donor)
$S_2 = 1/\sqrt{3}\ (\Delta r_2 + \Delta r_3 + \Delta r_4)$	CH_3 symmetric stretch (proton donor)
$S_3 = \Delta r_5$	CH stretch (proton acceptor)
$S_4 = 1/\sqrt{3}\ (\Delta r_6 + \Delta r_7 + \Delta r_8)$	CH_3 symmetric stretch (proton acceptor)
$S_5 = \Delta R$	C..H stretch
$S_6 = 1/\sqrt{12}\ (\Delta\alpha_1 + \Delta\alpha_2 + \Delta\alpha_3 - \Delta\beta_1 - \Delta\beta_2 - \Delta\beta_3 + \Delta\theta_1 + \Delta\theta_2 + \Delta\theta_3 - \Delta\gamma_1 - \Delta\gamma_2 - \Delta\gamma_3)$	CH_4 symmetric bend (proton donor)
$S_7 = 1/\sqrt{12}\ (\Delta\alpha_1 + \Delta\alpha_2 + \Delta\alpha_3 - \Delta\beta_1 - \Delta\beta_2 - \Delta\beta_3 + \Delta\theta_1 - \Delta\theta_2 - \Delta\theta_3 + \Delta\gamma_1 + \Delta\gamma_2 + \Delta\gamma_3)$	CH_4 symmetric bend (proton acceptor)
$S_8 = \Delta\tau_1$	in phase rock of both CH_4 units
$S_9 = 1/\sqrt{6}\ (2\Delta r_2 - \Delta r_3 - \Delta r_4)$	CH_3 symmetric stretch (proton donor)
$S_{10} = 1/\sqrt{6}\ (2\Delta r_6 - \Delta r_7 - \Delta r_8)$	CH_3 symmetric stretch (proton acceptor)
$S_{11} = 1/\sqrt{6}\ (2\Delta\alpha_1 - \Delta\alpha_2 - \Delta\alpha_3)$	CH_3 symmetric bend (proton donor)

Table 6.48 Continued

$S_{12} = 1/\sqrt{6}\ (2\Delta\beta_1 - \Delta\beta_2 - \Delta\beta_3)$	CH_3 symmetric bend (proton donor)
$S_{13} = 1/\sqrt{6}\ (2\Delta\theta_1 - \Delta\theta_2 - \Delta\theta_3)$	CH_3 symmetric bend (proton acceptor)
$S_{14} = 1/\sqrt{6}\ (2\Delta\gamma_1 - \Delta\gamma_2 - \Delta\gamma_3)$	CH_3 symmetric bend (proton acceptor)
$S_{15} = 1/\sqrt{2}\ (\Delta r_3 - \Delta r_4)$	CH_2 antisymmetric stretch (proton donor)
$S_{16} = 1/\sqrt{2}\ (\Delta r_7 - \Delta r_8)$	CH_2 antisymmetric stretch (proton acceptor)
$S_{17} = 1/\sqrt{2}\ (\Delta\alpha_2 - \Delta\alpha_3)$	CH_2 twist (proton donor)
$S_{18} = 1/\sqrt{2}\ (\Delta\beta_2 - \Delta\beta_3)$	CH_2 twist (proton donor)
$S_{19} = 1/\sqrt{2}\ (\Delta\theta_2 + \Delta\theta_3)$	CH_2 twist (proton acceptor)
$S_{20} = 1/\sqrt{2}\ (\Delta\gamma_2 - \Delta\gamma_3)$	CH_2 twist (proton acceptor)
$S_{21} = \Delta\tau_2$	out of phase rock of both CH_4 units
$S_{22} = \Delta\delta_1$	in phase rotation of CH_4 units
$S_{23} = \Delta\delta_2$	out of phase rotation of CH_4 units

The intramolecular symmetry coordinates for the CH_4 dimer were generated using the

corresponding modes from the monomer species except for the axial CH bonds which had a different symmetry coordinate from the other species. In the case of the bending modes both methane units executed simultaneous in- and out- of phase bending vibrations, hence they were represented by a combination of their symmetry coordinates, similar to the intermolecular rocking and rotational modes. The stretching modes were localised in each methane unit separately, thus their symmetry coordinates were captured from the monomer symmetry coordinates of a molecule with C_{3v} symmetry. The intermolecular modes were generated using the rules of Wilson et al.[70] The computed wavenumbers and %PED contributions to the vibrational modes are collected in Table 6.49.

Table 6.49 Wavenumbers and %PEDs in the Linear CH_4 Dimer

Symmetry Species	Wavenumber /cm^{-1}	%PED
a_1	3281	$100S_1$
	3276	$100S_3$
	3132	$90S_2 + 10S_1$
	3130	$90S_4 + 10S_3$
	1405	$100S_6$
	1401	$100S_7$
	42	$100S_5$
	2	$100S_{22}$
e	3278	$100S_9$

Table 6.49 Continued

	3278	$100S_{15}$
	3277	$100S_{10}$
	3277	$100S_{16}$
	1626	$68S_{14} + 14S_{13} + 14S_{12}$
	1626	$68S_{15} + 14S_{13} + 14S_{12}$
	1620	$68S_{20} + 14S_{18} + 14S_{19}$
	1620	$68S_{21} + 14S_{18} + 14S_{19}$
	1406	$68S_{12} + 14S_{14} + 14S_{15}$
	1406	$68S_{13} + 14S_{14} + 14S_{15}$
	1403	$68S_{18} + 14S_{20} + 14S_{21}$
	1403	$68S_{19} + 14S_{20} + 14S_{21}$
	38	$100S_{8}$
	38	$100S_{21}$
	26	-[a]
	26	-[a]

(a) The percentage PED could not be obtained due to the computer program limitation.

The stretching modes of vibration are localised in either the proton donor or acceptor while the bending modes are delocalised in both the proton acceptor and donor. The ν_1

and ν_2 modes are due to the stretching mode of the bonded CH of the proton donor and that of the axial CH bond in the proton acceptor. The ν_3 and ν_4 modes, being the symmetric stretching of the CH_3 units also have some contribution from the S_1 and S_3 symmetry coordinates. The ν_5 and ν_6 modes are the symmetric bending modes of the CH_3 units in the proton donor and acceptor, while ν_8 is the CH..C stretching mode and ν_9 the in phase rotation of both the CH_3 units. In the case of the e modes, ν_9 results from the stretching modes in the proton donor, while ν_{10} results from those in the proton acceptor. The bending motion occurs symmetrically in both methane units. The intermolecular modes ν_{15} and ν_{16}, being the rocking and rotational motion of both methane units, are delocalised in both the proton donor and acceptor as in the bending modes. The changes in the intensities in the methane dimer are reported in Table 6.50.

Table 6.50 Ratio of the Complex to Monomer Intensities in the CH_4 Dimer

Complex	Symmetry Species	Mode	Complex A/km mol^{-1}	A_c/A_m
$(CH_4)_2$	a_1	ν_1	13.8	0.65
		ν_2	30.5	1.44
		ν_3	0.1	-
		ν_4	0.1	-
		ν_5	24.4	2.08
		ν_6	2.8	0.24
	e	ν_9	6.9	0.32
		ν_{10}	0.1	0.00

Table 6.50 Continued

		ν_{11}	0.0	-
		ν_{12}	0.9	-
		ν_{13}	20.6	1.76
		ν_{14}	0.0	0.0

It can be seen from Table 6.50 that the major intensity enhancements occur for ν_2, ν_5 and ν_{13}. The magnitude of the enhancement reaches a maximum in ν_5; had this complex been a strongly hydrogen bonded complex the intensity enhancement would have been large, as was observed in the other hydrogen bonded dimers. The ν_1 and ν_2 modes in the CH_4 monomer are infrared inactive, hence no intensity ratios are listed for ν_3, ν_4, ν_{11} and ν_{12}; the intensity ratios for the complex were obtained by mapping the complex vibrational intensities on those of the monomer.

Chapter Seven

Theoretical Predictions of the Structures, Energetics, Mulliken Charges, Vibrational Spectra and Normal Coordinate Analyses of the Heterodimers

7.1 *The HF.HCl Complex*

7.1.1 *Geometries*

HF.HCl, being one of the simplest hydrogen bonded complexes, has HCl as the proton donor to the HF molecule. The experimental gas phase studies by Janda et al[206] support the linear C_s hydrogen bonded structure for this complex. Our study involved the optimization of two structures (fig 7.1 and fig 7.2) for this complex having the proton donor-acceptor roles interchanged. The most stable structure (fig 7.1) optimized was the structure having HCl as the proton donor. A similar result was obtained in the theoretical studies by Kollman et al[181] and Girardet et al.[207] The geometrical parameters for the most stable structure are collected in Table 7.1. From Table 7.1 both the HF and HCl bond lengths increase on forming the hydrogen bond. The values of the hydrogen bond length and the bond angle are consistent with this complex being a hydrogen bonded complex. Since the electronegativity of fluorine is greater than that of chlorine, the hydrogen of HF has a greater affinity for electrons than the hydrogen of HCl, therefore one would expect HF to be the proton acceptor.

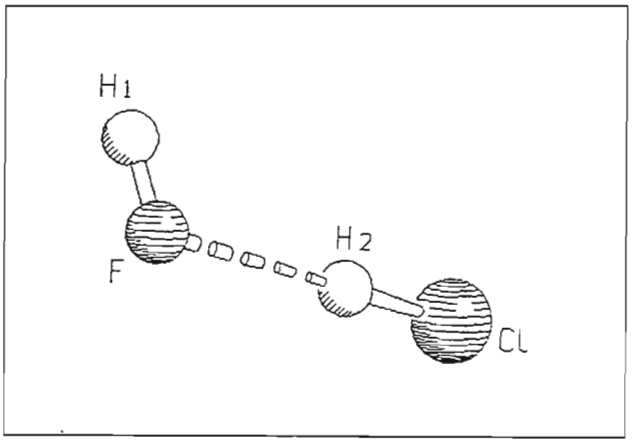

Fig 7.1 The Linear HF.HCl Complex

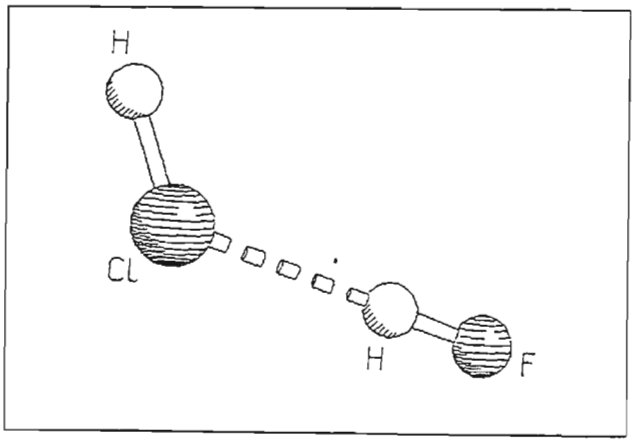

Fig 7.2 The Linear HCl.HF Complex

Table 7.1 Geometrical Parameters for the Most Stable HF.HCl Complex

Complex	Parameter	Complex	Monomer	Difference
HF.HCl	r(H1F)/pm	92.5	92.1	0.4
	r(H2Cl)/pm	127.5	126.8	0.7
	R(F..H2)/pm	195.6		
	R(F..Cl)	323.1		
	F..H2Cl/deg	180[a]		

(a) The angle of 180° was fixed due to convergence failure on performing full optimization

The comparison of the calculated with the experimental geometrical parameters is recorded in Table 7.2. The hydrogen bond angle measured for this complex experimentally was 144.5°. The large deviation of the computed from the experimental value can be explained as follows. The structure determined experimentally is most likely a position-averaged structure of the complex in its ground vibrational state, due to the large amplitude vibration of the hydrogen atom of the proton donor. Janda et al[206] also emphasised that the linear equilibrium structure can have a hydrogen bond angle of 180° ± 5°. The linear hydrogen bonded complex is an indication that the accepting orbital of HF has mostly fluorine 2s character while the donor HCl has mostly chlorine $2p_z$ character. Thus the resulting bond in the complex would be more directional, thus leading to a weak hydrogen bond in this complex as confirmed in the energy analysis.

Table 7.2 Comparison of the Calculated with the Experimental Geometrical Parameters for the HF.HCl Complex

Complex	Parameter	Calculated	Experimental[(a)]	Difference
HF.HCl	r(F..H)/pm	196	224 ± 20	28 ± 20
	r(F..Cl)/pm	323	336 ± 5	13 ± 5
	F..HCl/deg	180	144.5	35.5

(a) Ref. 206

7.1.2 *Energetics*

The energies for the HF.HCl complex are reported in Table 7.3. This complex can be considered to be a weakly hydrogen bonded complex. The complex however has a large dispersion energy contribution to its interaction energy as seen in Table 7.3.

Table 7.3 The Binding Energies of the Most Stable HF.HCl Complex

Complex	$\Delta E'$ /kJ mol^{-1}	ΔE /kJ mol^{-1}	BSSE /kJ mol^{-1}	$\%\Delta E_{Disp}$
HF.HCl	-11.1	-18.0	6.9	50.1

The complex has a binding energy of 11.1 kJ mol^{-1}, of which a 50.1% contribution comes from the effects of dispersion. This complex is however more strongly bound than either of the HX homodimers.

7.1.3 *Mulliken Charge Analysis*

From the Mulliken charge analyses shown in Table 7.4, the proton donor gains the larger amount of negative charge due to the high electronegativity of fluorine. This flux of negative charge has its origin mostly from the hydrogen of the proton donor. On analyzing the Mulliken charge redistribution, overall there is a delocalisation of negative charge throughout the molecule, suggesting stability in the complex.

Table 7.4 Mulliken Charge Analysis for the Most Stable HF.HCl Complex

Atom	Atomic Charge /e		Difference
	Complex	Monomer	/e
H1	0.413	0.397	0.016
F	-0.377	-0.397	0.020
			0.036
H2	0.196	0.192	0.004
Cl	-0.232	-0.192	-0.040
			-0.036

From the Mulliken charge analysis the HCl molecule gains negative charge (-0.036 e) from the proton acceptor. This charge donation has most of its origin from the fluorine atom, to the antibonding orbital of the proton donor, resulting in an increase in the HCl bond length on complexation as was shown in Table 7.1.

7.1.4 *Vibrational Properties of the Most Stable HF.HCl Complex*

The calculated vibrational spectra, potential energy distributions and infrared intensities at the MP2/6-31G** level for the linear bonded structure are shown in the Tables 7.5 - 7.8 respectively. The plots of the normal modes of vibrations are also collected in fig 7.3.

Table 7.5 Calculated Wavenumber Shifts in the HF.HCl Complex

Symmetry Species	Mode	Complex Wavenumber /cm^{-1}	Monomer Wavenumber /cm^{-1}	Shift[(a)] /cm^{-1}
a'	ν_1(HF)	4147	4197	-50
	ν_2(HCl)	3054	3128	-74

(a) Complex - Monomer

The ν_1 and ν_2 modes are both red shifted, by 50 and 74 cm^{-1} respectively. The HCl stretching mode is more strongly perturbed on complexation with the HF molecule, thus suggesting that the proton of the HCl is attracted to the HF molecule, but not as strongly as in the HX homodimers.

The wavenumber of the ν_6 (359 cm^{-1}) vibrational mode is large, emphasising the large amplitude of vibration in the proton of the proton donor, thus supporting the conclusion reached earlier about the geometry of this complex being different from the experimental structure. The symmetry coordinates for the HF.HCl complex are reported in Table 7.6. The descriptions of the symmetry coordinates are similar to those used in the case of the HX dimers. The S_4 coordinate involves the bending motion about the fluorine atom while the S_5 and S_6 coordinates involve the bending motion about the hydrogen atom of the proton donor.

Table 7.6 Symmetry Coordinates of the HF.HCl Complex

Complex	Symmetry Coordinate	Description
HF.HCl	$S_1 = \Delta r_1$	HF stretch
	$S_2 = \Delta r_2$	HCl stretch
	$S_3 = \Delta R$	F..H stretch
	$S_4 = \Delta\delta$	HF..H bend
	$S_5 = \Delta\pi_1$	F..HCl in plane bend
	$S_6 = \Delta\pi_2$	F..HCl out of plane bend

The wavenumbers and percentage PEDs are collected in Table 7.7. From Table 7.7, it is seen that there is no mixing of the symmetry coordinates for the intermolecular modes.

Table 7.7 Wavenumbers and %PEDs in the HF.HCl Complex

Complex	Symmetry Species	Wavenumber /cm^{-1}	%PED
HF.HCl	a'	4147	$100S_1$
		3053	$100S_2$
		482	$100S_3$
		218	$100S_4$
		141	$100S_5$
	a"	359	$100S_6$

The intramolecular stretching modes retain their parent symmetry coordinate descriptions. The hydrogen bond stretching motion is uncoupled from the other vibrational modes as was found in the case of the HX dimers. The difference between the librational mode wavenumbers is quite large, suggesting that the potential energy surface of this complex is not as flat as those in conventional hydrogen bonded complexes.

The changes in the intensities of the intramolecular modes on complexation are collected in Table 7.8.

Table 7.8 The Ratios of the Complex to Monomer Intensity values in the HF.HCl Complex

Complex	Symmetry Species	Mode	Complex A_c/km mol^{-1}	A_c/A_m
HF.HCl	a'	ν_1	128.1	1.56
		ν_2	268.3	11.97
		ν_3	117.2	
		ν_4	122.9	
		ν_5	0.01	
	a"	ν_6	55.7	

The intensity of the ν_2 mode is enhanced by a factor of 11.9, suggesting the hydrogen in the HCl to be strongly attracted to the fluorine atom in HF. This effect can be seen in the large magnitudes of ν_3 and ν_6 in Table 7.7. This intensity enhancement, coupled with the large wavenumber shifts on complexation, are indicative of hydrogen bond formation in this complex.

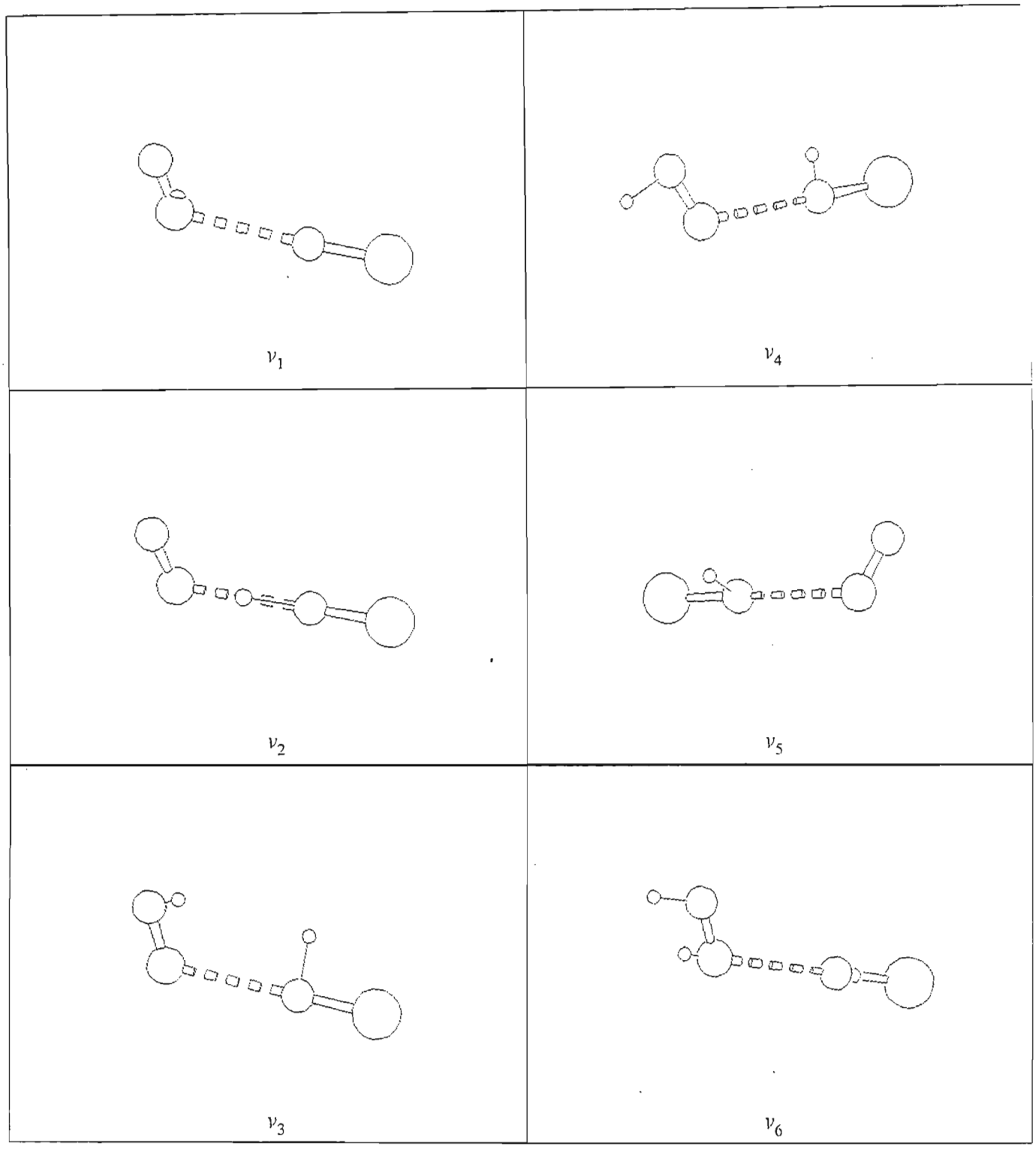

Fig 7.3 Graphical Representation of the HF.HCl Vibration modes

7.2 *The $H_2O.HX$ Complexes (X= F,Cl)*

7.2.1 *Geometries*

The structures optimized for this system all had C_s geometries with HX the proton donor to H_2O (fig 7.4 and fig 7.5). The reverse structures were also optimized having water as the proton donor to HX; these structures were found to be saddle points on the potential energy surface. The geometries of the local minimum energy structures were found to be directional in that generally the hydrogen of the proton donor was directed towards the lone pair electrons of the oxygen in water. The geometrical parameters for the most stable $H_2O.HF$ complex are reported in Table 7.9.

From an analysis of the geometrical parameters in Table 7.9, the HF bond length has increased by 1.4 pm on complexation, suggesting that the hydrogen bond is quite strong, the other large change in the geometrical parameters on complexation is the increase in the H2OH3 angle by 1.0°. The angle formed between the H2OH3 angle bisector and the HF axis was found to be 108.6°, suggesting a near tetrahedral orientation around the oxygen of water.

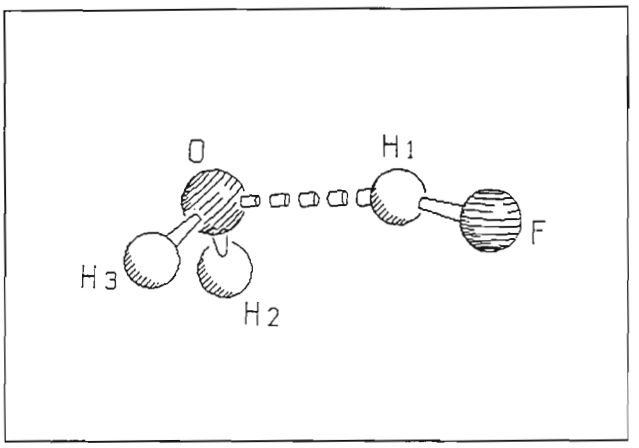

Fig 7.4 The Linear $H_2O.HF$ Complex

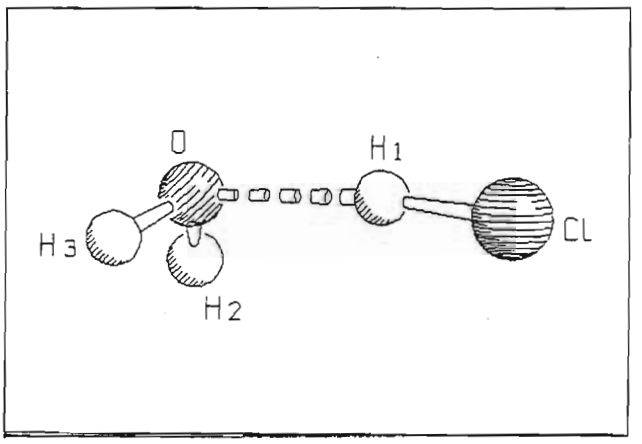

Fig 7.5 The Linear $H_2O.HCl$ Complex

Table 7.9 Geometrical Parameters for the Most Stable $H_2O.HF$ Complex

Complex	Parameter	Complex	Monomer	Difference
$H_2O.HF$	r(H1F)/pm	93.5	92.1	1.4
	r(OH2)/pm	96.3	96.1	0.2
	r(OH3)/pm	96.3	96.1	0.2
	R(O..H1)/pm	174.9		
	FH..O/deg	170.3		
	H2OH3/deg	104.8	103.8	1.0

The comparison of the calculated with the experimental gas phase geometrical parameters is shown in Table 7.10.

Table 7.10 Comparison of the Calculated with the Experimental Geometrical Parameters in the $H_2O.HF$ Complex

Complex	Parameter	Calculated	Exp[(a)]	Difference
$H_2O.HF$	r(O..F)/pm	263.8	266.4	-2.6
	bisector (HOH..HF)/deg	108.6	134.0	-25.4

(a) Ref. 20

The O..F calculated distance (263.8 pm) compares well with the experimental gas phase value (266.4 pm), while the angle formed between the H2OH3 angle bisector and the HF axis differs by 25.4°. This large deviation in the angle could be due to the experimental

gas phase structure being a vibrationally averaged state, having structural characteristics intermediate between the C_{2v} and C_s structures. The calculated geometrical parameters for the $H_2O.HCl$ complex are reported in Table 7.11.

On analyzing the changes in geometrical parameters in the $H_2O.HCl$ complex, the largest changes occur in the HCl bond length and the H_2O bond angle. The increase in bond length of HCl suggests that the hydrogen bond formed is indeed quite strong since the hydrogen of the HCl is being strongly attracted to the oxygen of the proton acceptor. The water bond angle increases due to a decrease in the lone pair - bonded electron pair repulsive force in the proton acceptor, thus allowing the bond angle to increase. This decrease in the electron repulsion is due to the delocalisation of the lone pair electrons of the oxygen towards the hydrogen bond.

Table 7.11 Geometrical Parameters for the Most Stable $H_2O.HCl$ Complex

Complex	Parameter	Complex	Monomer	Difference
$H_2O.HCl$	r(H1Cl)/pm	128.8	127.0	1.8
	r(OH2)/pm	96.3	96.1	0.2
	r(OH3)/pm	96.3	96.1	0.2
	R(O..H1)/pm	186.3		
	ClH..O/deg	175.4		
	H2OH3/deg	104.7	103.8	0.9

On comparing the calculated geometries with the available experimental values for the $H_2O.HCl$ complex, the calculated O..Cl distance of 304.2 pm was found to be in agreement with the experimental value of 321.0 pm obtained by Legon and

Willoughby.[341] It should also be remembered that the experimentally obtained bond distance was obtained by approximating the complex to having a vibrationally averaged structure of C_{2v} symmetry, hence the deviation of the calculated from the experimental O..Cl distance is acceptable.

The hydrogen bond angle in the HCl complex was found to be closer to linearity than that in the HF complex; this could be rationalised on the basis that due to the large electronegativity of fluorine, it could perhaps be involved in a secondary interaction with the hydrogen atoms in the water molecule, thus resulting in a slightly bent hydrogen bonded structure.

7.2.2 *Energetics*

The binding energies of the $H_2O.HF$ and $H_2O.HCl$ complexes are tabulated in Table 7.12.

Table 7.12 The Binding Energies of the Most Stable $H_2O.HX$ Complexes

Complex	$\Delta E'$ /kJ mol^{-1}	ΔE /kJ mol^{-1}	BSSE /kJ mol^{-1}	$\%\Delta E_{Disp}$
$H_2O.HF$	-33.7	-36.9	3.2	1.8
$H_2O.HCl$	-19.7	-24.2	4.5	18.3

From Table 7.12, the binding energy of the HF complex (-33.7 kJ mol^{-1}) was found to be larger than that of the HCl complex (-19.7 kJ mol^{-1}) by 14 kJ mol^{-1}. This follows since HF is a better proton donor than HCl due to the greater electronegativity of fluorine compared with that of chlorine. The experimental binding energy of the $H_2O.HF$ complex was found by North et al[216] to be 42.9 kJ mol^{-1}, using the absolute intensities of the rotational lines. The smaller contribution of the dispersion term to the binding energy in

the HF complex is due to its low polarizability compared with that of HCl. The Morokuma decomposition analysis is presented in Table 7.13, with the electrostatic term dominating the SCF interaction energy in both complexes.

Table 7.13 Energy Decomposition Analysis of the most Stable $H_2O.HX$ Complexes /kJ mol^{-1}

Complex	ES	EX	CT	PL	MIX	Total
$H_2O.HF$	-60.6	41.5	-11.4	-6.2	2.9	-33.8
$H_2O.HCl$	-50.2	46.6	-16.2	-4.2	4.2	-19.8

From the decomposition analysis the $H_2O.HX$ complexes can be characterised as being mainly electrostatic in nature while in the case of the $H_2O.HCl$ complex the dispersion effects also play a major role in the interaction energy. The exchange repulsion term also dominates the SCF interaction energy; this could arise from back donation of negative charge from the proton donor to the acceptor. The directionality of the hydrogen bond formed was shown by Scheiner and Szczesniak et al [237] to be a function of the interplay between the electrostatic and exchange repulsion terms. Thus from the difference in the magnitudes of the ES and EX terms, the $H_2O.HCl$ complex has a smaller difference (-3.6 kJ mol^{-1}) than the $H_2O.HF$ complex (-19.1 kJ mol^{-1}) hence the linearity of the hydrogen bond in the $H_2O.HCl$ complex would be expected to be more pronounced than in the $H_2O.HF$ complex.

7.2.3 *Mulliken Charge Analysis*

The Mulliken charge analyses in the $H_2O.HF$ and $H_2O.HCl$ complexes is given in Tables 7.14 and 7.15 respectively, depicting the flow of negative charge on complexation. From

the Mulliken charge analysis, the HF molecule can be seen to be the acceptor of negative charge from the water molecule. This would therefore result in a decrease of charge density in the OH bonds of the water molecule thus accounting for the increase in the H2OH3 angle.

Table 7.14 Mulliken Charge Analysis for the Most Stable $H_2O.HF$ Complex

Atom	Atomic Charge /e		Difference
	Complex	Monomer	/e
H1	0.427	0.397	0.030
F	-0.466	-0.397	-0.069
			-0.039
O	-0.687	-0.674	-0.013
H2	0.363	0.337	0.026
H3	0.363	0.337	0.026
			0.039

A similar scenario is observed for the direction of negative charge donation in the $H_2O.HCl$ complex, as was found in the case of the $H_2O.HF$ complex. The amount of charge gained by the proton donor was however much larger in the case of the HCl than the HF complex.

The increase in the HCl bond length is indicative of the gain of negative charge from the water molecule into its antibonding orbitals. Even though the amount of negative charge gained by the HCl molecule is greater than that acquired by the HF molecule, the HF

complex is still more stabilised as seen in Table 7.12; the rationale behind this lies in the dipole moment of HF being much larger than that of HCl, therefore stabilising the complex electrostatically to a greater extent.

Table 7.15 Mulliken Charge Analysis for the Most Stable $H_2O.HCl$ Complex

Atom	Atomic Charge /e		Difference /e
	Complex	Monomer	
H1	0.218	0.193	0.035
Cl	-0.264	-0.193	-0.071
			-0.046
O	-0.672	-0.674	0.002
H2	0.359	0.337	0.022
H3	0.359	0.337	0.022
			0.046

7.2.4 *Vibrational Properties of the Most Stable $H_2O.HX$ Complexes*

The calculated vibrational spectra, potential energy distributions and infrared intensities at the MP2/6-31G** level for the linear hydrogen bonded $H_2O.HX$ complexes are shown in Tables 7.16 - 7.24. The plots of the normal modes of vibrations are depicted in fig 7.6.

Table 7.16 Calculated Wavenumber Shifts in the Most Stable $H_2O.HF$ Complex

Symmetry Species	Mode	Complex Wavenumber /cm^{-1}	Monomer Wavenumber /cm^{-1}	Shift[(a)] /cm^{-1}
a'	ν_1	3905	4197	-292
	ν_2	3867	3901	-34
	ν_3	1675	1680	-5
a"	ν_7	4010	4039	-29

(a) Complex - Monomer

From Table 7.16 the major changes in the calculated vibrational spectrum on complexation occur in ν_1, ν_2 and ν_7, the HF stretching, H_2O symmetric and antisymmetric stretching modes, which are red shifted by 292, 34 and 29 cm^{-1} respectively. The closeness of the librational modes of 823 cm^{-1} and 705 cm^{-1} led Thomas et al[217] in their early matrix isolation studies to conclude that this complex had C_{2v} symmetry since they could not resolve these two modes accurately resulting from the low barrier to inversion of 126 $\pm$ 70 cm^{-1} between the C_s and C_{2v} structures. The comparison of the experimental to the calculated vibrational spectrum in an argon matrix is reported in Table 7.17. The ratios of the calculated to the experimental wavenumbers are within reasonable agreement with each other. The sharp librational modes (ν_4 and ν_8) and the HF stretching mode (ν_1) in the argon spectrum provided evidence for the inversion doubling occurring in the complex.[218] The ν_1 mode was observed at 3586 cm^{-1} in Ne and 3543 cm^{-1} in Kr matrices by Bowers et al.[343] The shift of 31 cm^{-1} of the ν_1 mode obtained in the argon matrix compared with that in the Ne matrix is a consequence of Ne being less polarizable than

argon. No comparison of the vibrational spectra could be made in the water stretching and bending regions due to overlapping with the water dimer bands.

Table 7.17 Comparison of the Calculated with the Experimental Vibrational Spectrum of the Most Stable $H_2O.HF$ Complex

Symmetry Species	Mode	Calculated Wavenumber /cm^{-1}	Experimental Wavenumber[(a)] /cm^{-1}	Ratio[(b)]
a'	ν_1	3905	3555	1.10
	ν_4	705	753	0.94
	ν_8	823	636	1.29

(a) Ref. 218

(b) Ratio = Calculated / Experimental

The librational modes on the other hand were quite distinct in both the Ne and Kr matrices. The calculated wavenumber shifts observed on complexation in the $H_2O.HCl$ complex are reported in Table 7.18. In the $H_2O.HCl$ complex the ν_1 mode (HCl stretching vibration) is red shifted by 270 cm^{-1} similar to the shift in the $H_2O.HF$ complex, with librational modes at 542 and 655 cm^{-1}. The difference in the librational modes is much greater in this complex compared with that in the $H_2O.HF$ complex, suggesting that the barrier to inversion between the C_{2v} and C_s geometries is greater than that in the $H_2O.HF$ complex.

Table 7.18 Calculated Wavenumber Shifts in the Most Stable $H_2O.HCl$ Complex

Symmetry Species	Mode	Complex Wavenumber /cm^{-1}	Monomer Wavenumber /cm^{-1}	Shift[(a)] /cm^{-1}
a'	ν_1	3876	3901	-25
	ν_2	2858	3128	-270
	ν_3	1673	1680	-5
a"	ν_7	4011	4039	-28

(a) Complex - Monomer

The comparison of the calculated and the experimental vibrational spectra of the $H_2O.HCl$ complex is shown in Table 7.19. The calculated complex wavenumbers agree well with the experimental bands observed in an argon matrix by Ayers and Pullin.[227] The bands observed in a nitrogen matrix by Ault and Pimentel[226] were located at 3712, 3622 and 1594 cm^{-1} respectively for the ν_7, ν_1 and ν_3 modes, being the antisymmetric and symmetric stretching, and the bending vibrations of the proton acceptor in the complex. These values are also in reasonable agreement with our calculated frequencies. The large shift in the HCl stretching mode observed in the nitrogen matrix due to the $N_2.HCl$ complex complicated the assignment of the HCl stretching mode as observed by Ault and Pimental.[226]

Table 7.19 Comparison of the Calculated to the Experimental Vibrational Spectrum of the Most Stable $H_2O.HCl$ Complex

Symmetry Species	Mode	Calculated Wavenumber /cm^{-1}	Experimental Wavenumber /cm^{-1} [(a)]	Ratio[(b)]
a'	ν_1	3876	3630	1.06
	ν_2	2858	2663	1.07
	ν_3	1673	1590	1.05
a"	ν_7	4011	3722	1.08

(a) Ref. 227

(b) Ratio = Calculated / Experimental

The symmetry coordinates for the $H_2O.HX$ complexes are collected in Table 7.20. The symmetry coordinates used for describing the intramolecular modes were similar to those used for the parent monomers. In the case of the intermolecular modes, symmetry coordinates were generated according to the rules of Wilson et al.[70]

Table 7.20 Symmetry Coordinates for the $H_2O.HX$ Complexes

Complex	Symmetry Coordinate	Description
$H_2O.HX$	$S_1 = \Delta r_1$	HX stretch
	$S_2 = \Delta R$	O..H stretch
	$S_3 = 1/\sqrt{2}(\Delta r_3 + \Delta r_4)$	H_2O symmetric stretch
	$S_4 = \Delta\pi_1$	O..HX in plane bend
	$S_5 = \Delta\alpha$	HOH bend
	$S_6 = 1/\sqrt{2}(\Delta\theta_1 + \Delta\theta_2)$	HOH wag
	$S_7 = 1/\sqrt{2}(\Delta r_3 - \Delta r_4)$	H_2O antisymmetric stretch
	$S_8 = 1/\sqrt{2}(\Delta\theta_1 - \Delta\theta_2)$	HOH twist
	$S_9 = \Delta\pi_2$	O..HX out of plane bend

The percentage symmetry coordinate distributions over the PEDs are shown in Table 7.21 for the $H_2O.HF$ complex. From an analysis of the percentage potential energy distributions over the intramolecular modes all these modes contain a majority contribution from their parent symmetry coordinates, for example the ν_1, HF stretching vibration, has 71% PED contribution from the HF stretching coordinate and 27% from the water symmetric stretching mode. This scenario is reversed in the ν_2 mode (the symmetric stretching mode of the proton acceptor), with 69%S_3 and 29%S_1. The effect of mixed contribution to the PED would suggest stabilisation of the complex due to electronic delocalisation. The intermolecular modes also experience similar mixing of the symmetry coordinates in the PED; the in plane hydrogen bond bending coordinate has a 20% contribution from the wagging mode of the water molecule. The out of plane hydrogen bond bending mode also

has a contribution to its PED from the twisting mode (38%) of the water molecule. The hydrogen bond stretching mode has a large contribution to its PED from the wagging mode of the proton acceptor and the in plane hydrogen bond bending mode. The hydrogen bond bending mode also suffers similar mixing of symmetry coordinates from the hydrogen bond stretching and the water wagging modes. In the case of the a" intermolecular modes the water twisting and out of plane modes are integrated together in their symmetry coordinate distributions.

Table 7.21 Wavenumbers and %PEDs in the $H_2O.HF$ Complex

Complex	Symmetry Species	Wavenumber /cm^{-1}	%PED
$H_2O.HF$	a'	3905	$71S_1 + 27S_3$
		3867	$69S_3 + 29S_1$
		1675	$100S_5$
		705	$78S_4 + 20S_6$
		272	$45S_2 + 34S_6 + 18S_4$
		215	$44S_6 + 32S_4 + 21S_2$
	a"	4010	$100S_7$
		823	$61S_9 + 38S_8$
		212	$52S_8 + 47S_9$

The trends of the symmetry coordinate distributions amongst the PEDs in the $H_2O.HCl$ complex are reported in Table 7.22.

From Table 7.22 the amount of different symmetry coordinate contributions to the PED for the intra- and intermolecular modes is not as large as was the case for the $H_2O.HF$ complex. This could be attributed to the stability of this complex being lower than that of the HF complex. The other trend observable for the HCl complex is the magnitude of the HCl stretching mode being lower than the symmetric water stretching mode, while in the HF complex the opposite occurs. The hydrogen bond stretching mode (175 cm^{-1}) occurs at a lower wavenumber than in the $H_2O.HF$ complex (272 cm^{-1}), further implying the former bond to be weaker than the latter.

Table 7.22 Wavenumbers and PEDs for the $H_2O.HCl$ Complex

Complex	Symmetry Species	Wavenumber /cm^{-1}	%PED
$H_2O.HCl$	a'	3876	$100S_3$
		2858	$95S_1 + 5S_2$
		1673	$100S_5$
		542	$80S_4 + 19S_6$
		244	$61S_6 + 27S_4 + 9S_2$
		175	$89S_2 + 6S_6 + 2S_4$
	a"	4011	$100S_7$
		655	$59S_9 + 40S_8$
		239	$54S_8 + 45S_9$

It is also worth noting that the librational modes have slightly smaller contributions from

the other symmetry coordinates in the case of the HCl complex, suggesting the degree of libration in the HCl complex is somewhat less than that in the HF complex. The changes in intensities on complexation in the $H_2O.HF$ complex are reported in Table 7.23.

Table 7.23 The Ratios of the Complex to Monomer Intensity values for the $H_2O.HF$ Complex.

Complex	Symmetry Species	Mode	Complex A_c/km mol^{-1}	A_c/A_m
$H_2O.HF$	a'	ν_1	405.8	4.96
		ν_2	278.9	64.80
		ν_3	84.2	1.08
		ν_4	210.7	
		ν_5	175.4	
		ν_6	85.2	
	a"	ν_7	77.7	2.29
		ν_8	155.0	
		ν_9	5.8	

From Table 7.23 the major intensity enhancement occurs in the water symmetric stretching band by a factor of 64.80 with the other intensity enhancements all being minimal. The experimental argon matrix spectrum observed by Andrews and Johnson[243] also suggests the appearance of the strong, highly intensified ν_2 band as being the major product band in the matrix spectrum. The ratios of the calculated complex to monomer

intensities for the $H_2O.HCl$ complex are tabulated in Table 7.24.

Table 7.24 The Ratios of the Complex to Monomer Intensity values in the $H_2O.HCl$ Complex

Complex	Symmetry Species	Mode	Complex A_c/km mol^{-1}	A_c/A_m
$H_2O.HCl$	a'	ν_1	22.5	5.35
		ν_2	673.3	30.05
		ν_3	75.3	0.96
		ν_4	114.9	
		ν_5	244.6	
		ν_6	1.8	
	a"	ν_7	70.0	2.07
		ν_8	72.9	
		ν_9	0.2	

From Table 7.24 the major changes in intensity occur in the HCl stretching mode as opposed to that of the water stretching mode in the HF complex. This results due to the greater amount of charge donation to the HCl than the HF thus increasing the magnitude of the displacement of the dipole moment vector in the proton donor on executing the stretching vibration. The ν_1 and ν_7 modes also experience intensity enhancements on complexation of magnitudes 5.35 and 2.07 respectively.

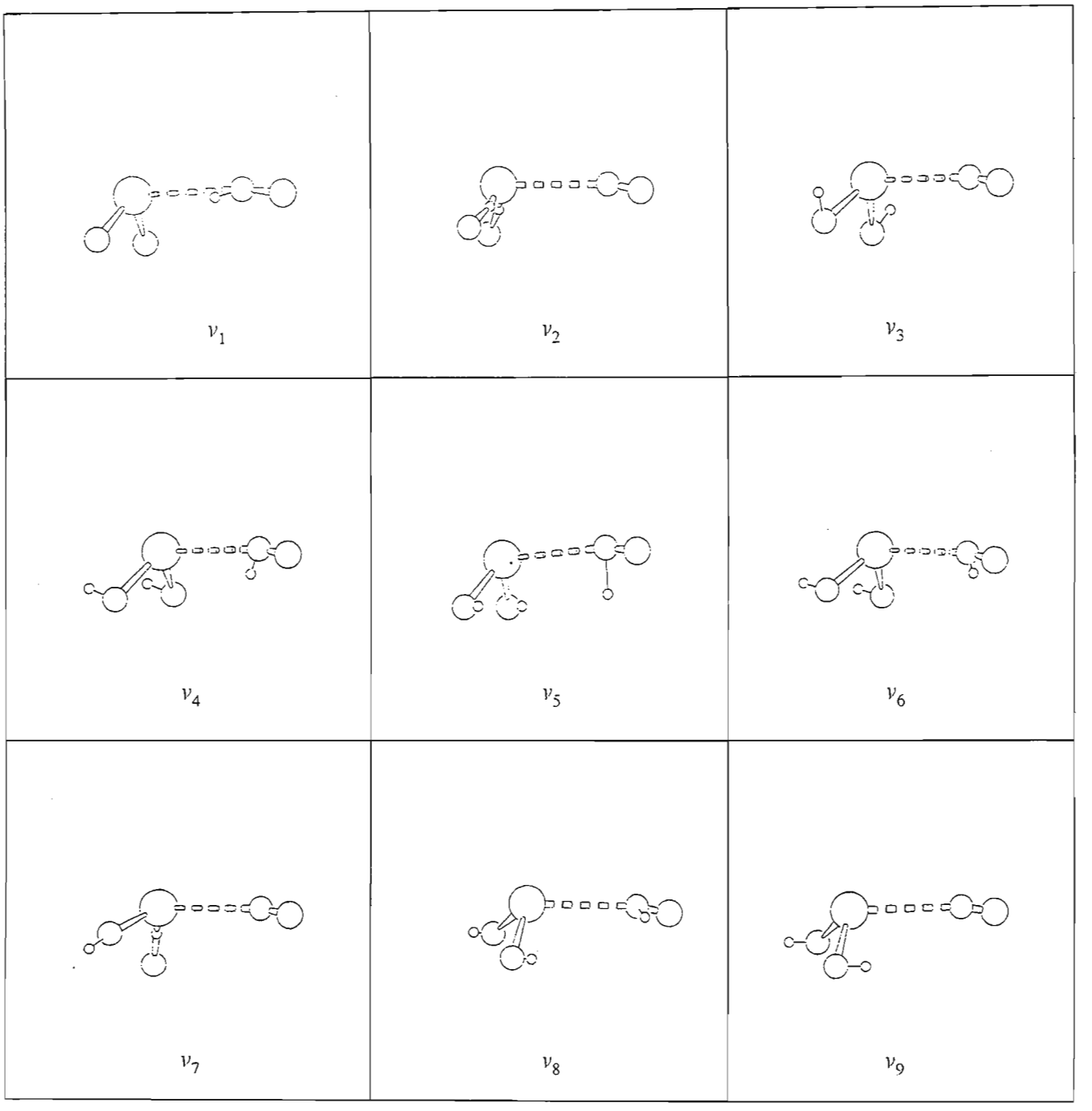

Fig 7.6 Graphical Representation of the $H_2O.HX$ Vibration modes

7.3 *The $H_2S.HX$ Complexes (X= F,Cl)*

7.3.1 *Geometries*

The geometries optimized for the $H_2S.HX$ structures have similar structures to those of the water counterparts with the HX as proton donor to the hydrogen sulphide molecule. The global minimum energy structures found for these complexes were C_s in structure with a nearly linear hydrogen bond (figs 7.7 and 7.8). The reverse structures, with the hydrogen sulphide molecule the proton donor to the fluorine atom of HF or to the chlorine atom of HCl, were also optimized but were found to be saddle points on the potential energy surfaces. The major difference that was found geometrically in the hydrogen sulphide complexes compared with those of the water complexes was in the angular orientation of the hydrogen bond at the Y atom. In the case of the water molecule there was a tendency towards tetrahedral orientation at the lone-pair electrons of oxygen, while in the case of the H_2S complexes there was a tendency towards a more perpendicular orientation at the lone-pair electrons of the sulphur. The experimental gas phase studies by Viswanathan and Dyke[233] also concluded that the angle between the bisector of the H_2S bond angle and the HF axis was almost 90°. The ab initio studies by Scheiner[236] with the inclusion d-orbital functions in their calculation also observed near 90° orientation at the sulphur; without d-orbital functions the orientation at the sulphur was found to collapse to that of a tetrahedral arrangement. Our studies have found that the angle subtended by the HSH bisector and the HF axis was 92.5°, while in the case of the $H_2O.HF$ complex this angle was 108.6°. Further geometrical data relating to the $H_2S.HF$ complex are collected in Table 7.25.

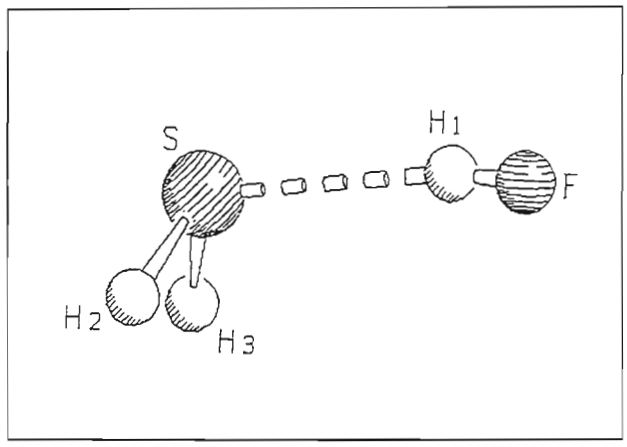

Fig 7.7 The Linear $H_2S.HF$ Complex

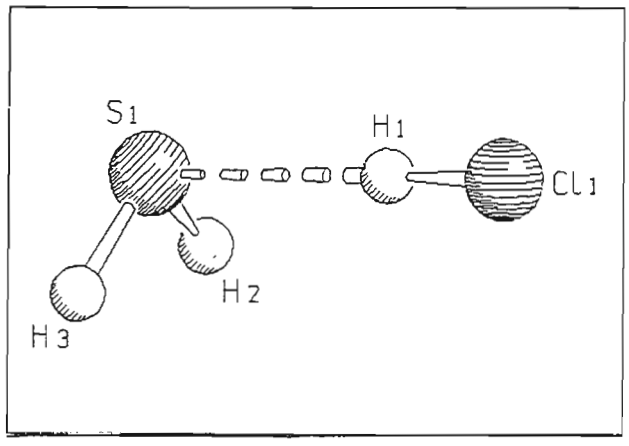

Fig 7.8 The Linear $H_2S.HCl$ Complex

Table 7.25 Geometrical Parameters for the Most Stable $H_2S.HF$ Complex

Complex	Parameter	Complex	Monomer	Difference
$H_2S.HF$	r(H1F)/pm	92.7	92.1	0.6
	r(SH2,SH3)/pm	133.0	132.9	0.1
	R(S..H1)/pm	239.6		
	H2SH3/deg	93.2	92.8	0.4
	FH1..S/deg	172.0		

From Table 7.25 the major changes in the geometrical parameters are those in the H1F bond length and the H2SH3 angle. The H1F bond distance increases due to the attraction of the proton of HF to the sulphur lone-pair electrons. As was the case in the $H_2O.HX$ complexes, the H2SH3 bond angle increases due to the decrease in the lone pair - bonding pair electronic repulsion in the proton acceptor. This effect arises from the delocalisation of the lone-pair electronic density towards the vicinity of the HF molecule. The hydrogen bond length (239.6 pm) is much longer suggesting a weaker hydrogen bond compared with the $H_2O.HX$ complexes. The hydrogen bond angle is close to those of the water complexes. The comparison of the calculated with the experimental geometrical parameters is presented in Table 7.26.

Our calculated values are found to be in good agreement with the gas phase experimental results of Viswanathan and Dyke.[233] The early ab initio studies without d-functions on the sulphur atom led to dubious results regarding the angular orientation around the sulphur; these calculations led to a more tetrahedral than right angled structure of the complex, in conflict with the experimental observations of Viswanathan and Dyke.

Table 7.26 Comparison of the Calculated and the Experimental Geometrical Parameters in the $H_2S.HF$ Complex

Complex	Parameter	Calculated	Exp[(a)]	Difference
$H_2S.HF$	R(S..F)/pm	332	325 ± 3	7 ± 3
	HS..F/deg	93	91 ± 10	2 ± 10
	S..FH/deg	8	0 ± 10	8 ± 10

(a) Ref. 233

The ab initio study by Scheiner et al[236] incorporating d-orbital functions on the sulphur led to the correct structure of this complex, consistent with experiment. The calculated geometrical parameters for the $H_2S.HCl$ complex are presented in Table 7.27. From Table 7.27 the major changes occurring in the geometrical parameters on complexation are the lengthening of the HCl bond, and the increase in the H2SH3 angle. This observation is similar to that found in the case of the $H_2S.HF$ complex and can be attributed to the same reasoning. The hydrogen bond length has also increased in this complex compared with that in the $H_2S.HF$ complex; the hydrogen bond angle, on the other hand, tends more towards linearity than in the HF complex. This trend is due to the contribution of the dispersion energy to the angular orientation of the complex which plays a larger role in the $H_2S.HCl$ complex as observed in Table 7.29.

Table 7.27 Geometrical Parameters for the Most Stable $H_2S.HCl$ Complex

Complex	Parameter	Complex	Monomer	Difference
$H_2S.HCl$	r(H1Cl)/pm	127.7	127.0	0.7
	r(SH2,SH3)/pm	133.0	132.9	0.1
	R(S..H1)/pm	253.0		
	H2SH3/deg	93.2	92.8	0.4
	S..H1Cl/deg	178.4		

The comparison of the calculated to the experimental geometrical parameters for the $H_2S.HCl$ complex is shown in Table 7.28.

Table 7.28 Comparison of the Calculated to Experimental Geometrical Parameters in the $H_2S.HCl$ Complex

Complex	Parameter	Calculated	Exp[a]	Difference
$H_2S.HCl$	r(S..Cl)/pm	381	381	0
	bisect(H2SH3..H1Cl axis)/deg	90	94	-4
	R(S..H1Cl)/deg	178	180	-2

(a) Ref. 239

The calculated values agree well with the gas phase experimental values of Goodwin et al.[239] The angle at the sulphur atom is close to 90°, which implies that in the sulphur atom, the 3s orbital is not involved in the bonding process and thus the non bonded pair

electrons can be described as occupying a 3p orbital.

7.3.2 *Energetics*

The binding energies of the $H_2S.HX$ complexes, together with the percentage dispersion effects and the BSSEs are collected in Table 7.29.

Table 7.29 The Binding Energies of the Most Stable $H_2S.HX$ Complexes

Complex	$\Delta E'$ /kJ mol^{-1}	ΔE /kJ mol^{-1}	BSSE /kJ mol^{-1}	$\%\Delta E_{Disp}$
$H_2S.HF$	-12.8	-13.9	1.1	9.2
$H_2S.HCl$	-6.4	-8.2	1.8	35.1

The $H_2S.HF$ complex is more strongly bound than the HCl complex by 6.4 kJ mol^{-1}, with the HCl complex having a large dispersion energy contribution to its binding energy, as observed by Scheiner et al.[236] This trend is also seen in the $H_2O.HX$ complexes with dispersion becoming more dominant as one descends the periodic table. The energy decomposition analysis is collected in Table 7.30.

From Table 7.30 it can be established that the HF complex is more electrostatic in nature than the HCl complex. The exchange repulsion term dominates the SCF part of the interaction energy, hence one may conclude that in the HCl complex energy stabilisation is achieved mostly by the dispersive forces.

Table 7.30 Energy Decomposition Analysis of the Most Stable $H_2S.HX$ Complexes /kJ mol^{-1}

Complex	ES	EX	CT	PL	MIX	Total
$H_2S.HF$	-28.6	24.2	-7.0	-3.5	2.2	-12.7
$H_2S.HCl$	-22.9	24.2	-8.0	-2.1	2.4	-6.4

7.3.3 *Mulliken Charge Analysis*

The Mulliken charge analyses for the $H_2S.HX$ complexes are presented in Table 7.31 and Table 7.32 respectively.

Table 7.31 Mulliken Charge Analysis for the Most Stable $H_2S.HF$ Complex

Atom	Atomic Charge /e		Difference /e
	Complex	Monomer	
H1	0.414	0.397	0.017
F	-0.429	-0.397	-0.032
			-0.015
S	-0.167	-0.132	-0.035
H2	0.091	0.066	0.025
H3	0.091	0.066	0.025
			0.015

From Table 7.31, the HF molecule gains negative charge (-0.015 e) which essentially occupies the antibonding orbital of the HF thus increasing its bond distance. This negative charge has its origin primarily from the protons in the complex. The sulphur also gains negative charge (-0.035 e); this charge also occupies the antibonding orbitals in the hydrogen sulphide sub-unit thus creating a two pronged effect, viz., the increase in the HS bond lengths and secondly the increase in the H2SH3 bond angle. The increase in the H2SH3 bond angle occurs through the bonding pair - bonding pair electron repulsive force being greater than that of the sulphur lone pair - bonding pair electron repulsive force. The changes in the Mulliken charge analysis for the $H_2S.HCl$ complex are collected in Table 7.32.

Table 7.32 Mulliken Charge Analysis for the Most Stable $H_2S.HCl$ Complex

Atom	Atomic Charge /e		Difference
	Complex	Monomer	/e
H1	0.187	0.193	-0.006
Cl	-0.212	-0.193	-0.019
			-0.025
S	-0.145	-0.132	-0.013
H2	0.085	0.066	-0.019
H3	0.085	0.066	-0.019
			0.025

From Table 7.32, the HCl molecule gains negative charge (-0.025 e), which has its origin in the protons of the H_2S molecule. The proton of HCl also gains negative charge (-0.006 e) like the chlorine (-0.019 e) and sulphur atoms (-0.013 e). The explanation for the lengthening of the HCl bond and the increase in the H2SH3 angle follows from that in the corresponding HF complex.

7.3.4 *Vibrational Properties of the Most Stable $H_2S.HX$ Complexes*

The calculated vibrational spectra, potential energy distributions and infrared intensities at the MP2/6-31G** level for the linear hydrogen bonded $H_2S.HX$ complexes are shown in Tables 7.33 - 7.39. The plots of the normal modes of vibrations for the $H_2S.HX$ complexes are depicted in fig 7.9.

Table 7.33 Calculated Wavenumber Shifts in the Most Stable $H_2S.HF$ Complex

Symmetry Species	Mode	Complex Wavenumber /cm^{-1}	Monomer Wavenumber /cm^{-1}	Shift[(a)] /cm^{-1}
a'	ν_1	4058	4197	-139
	ν_2	2840	2846	-6
	ν_3	1264	1268	-4
a"	ν_7	2866	2872	-6

(a) Complex - Monomer

The major change occurring in the calculated vibrational spectrum of $H_2S.HF$ on complexation is the large red shift of ν_1 by 139 cm^{-1}. The stretching modes and the

bending mode of the H_2S molecule are also slightly red shifted by 6, 6 and 4 cm^{-1} respectively. The HF stretching mode is red shifted to a large extent mainly because of the strong affinity of the HF proton for the sulphur of the proton acceptor. The librational modes (474 cm^{-1} and 499 cm^{-1}) are also quite close to one other with a difference of 25 cm^{-1}, suggesting that the structure of this complex could easily undergo vibrational averaging, resulting in a C_{2v} structure.

Table 7.34 Comparison of the Calculated and the Experimental Vibrational Spectrum of the Most Stable $H_2S.HF$ Complex

Symmetry Species	Mode	Complex Wavenumber /cm^{-1}	Experimental Wavenumber /cm^{-1} [(a)]	Ratio[(b)]
a'	ν_1	4058	3799	1.07
	ν_4	474	481	0.98
a"	ν_8	499	508	0.98

(a) Ref. 235

(b) Ratio = Calculated / Experimental

The experimental matrix spectrum in an argon matrix reported by Arlinghaus et al[235] located ν(HF) at 3652 cm^{-1} with a low frequency doublet, and with strong bands at 481 cm^{-1} and 508.5 cm^{-1} assigned to the librational modes. Our calculated vibrational spectrum is found to be in good agreement with the matrix isolated argon spectrum. The wavenumbers of the H_2S fundamental modes were not given hence no comparison could be made. The reverse complex having ν(HF) at 3799 cm^{-1} was also observed in the argon matrix. The decrease in the magnitude of the librational modes further reinforces the

presumption that there is a decrease in the rigidity of this complex as in the case of the corresponding water complex. The calculated vibrational spectrum of the $H_2S.HCl$ complex is collected in Table 7.35. The major change in the vibrational spectrum on complexation occurs in ν_1, the HCl stretching mode, being red shifted by 127 cm^{-1}.

Table 7.35 Calculated Wavenumber Shifts in the Most Stable $H_2S.HCl$ Complex

Symmetry Species	Mode	Complex Wavenumber /cm^{-1}	Monomer Wavenumber /cm^{-1}	Shift[(a)] /cm^{-1}
a'	ν_1	3001	3128	-127
	ν_2	2838	2864	-26
	ν_3	1264	1268	-4
a"	ν_7	2864	2872	-8

(a) Complex - Monomer

As in the case of the corresponding HF complex a similar trend is observed for the changes in complex vibrational properties. The large red shift of 127 cm^{-1} in ν_1, the HCl stretching mode is indicative of a strong hydrogen bond. On comparison of the librational modes (388 and 407 cm^{-1}) with those of the HF complex (474 and 499 cm^{-1}), the magnitude has decreased, implying even less rigidity in this complex to undergo vibrational averaging.

The symmetry coordinate descriptions of the $H_2S.HX$ modes are collected in Table 7.36, which are similar to those used in the case of the $H_2O.HX$ complexes. The derivation of the symmetry coordinates follows from those used in the $H_2O.HX$ complexes.

Table 7.36 Symmetry Coordinates for the $H_2S.HX$ Complexes

Complex	Symmetry Coordinate	Description
$H_2S.HX$	$S_1 = \Delta r_1$	HX stretch
	$S_2 = \Delta R$	H..X stretch
	$S_3 = 1/\sqrt{2}(\Delta r_3 + \Delta r_4)$	H_2S symmetric stretch
	$S_4 = \Delta\pi_1$	S..HX in plane bend
	$S_5 = \Delta\alpha$	H_2S bend
	$S_6 = 1/\sqrt{2}(\Delta\theta_1 + \Delta\theta_2)$	H_2S wag
	$S_7 = 1/\sqrt{2}(\Delta r_3 - \Delta r_4)$	H_2S antisymmetric stretch
	$S_8 = 1/\sqrt{2}(\Delta\theta_1 - \Delta\theta_2)$	H_2S twist
	$S_9 = \Delta\pi_2$	S..HX out of plane bend

The contribution of the symmetry coordinates to the PED are collected in Tables 7.37 and 7.38 for the $H_2S.HF$ and $H_2S.HCl$ complexes respectively. On analyzing the results in Table 7.37, the intramolecular modes all retain their parent symmetry coordinate distributions as in the case of the water-hydrogen halide complexes. The intermolecular modes however have contributions from different symmetry coordinates. The H_2S twist and out of plane hydrogen bending modes both have almost equal proportions of symmetry coordinate distributions from S_8 and S_9. The hydrogen bond stretching mode is coupled

quite extensively with the in plane hydrogen bond bending mode and the H_2S wagging mode.

Table 7.37 Wavenumbers and %PEDs in the $H_2S.HF$ Complex

Complex	Symmetry Species	Wavenumber /cm^{-1}	%PED
$H_2S.HF$	a'	4057	$100S_1$
		2840	$100S_3$
		1264	$100S_5$
		474	$55S_4 + 43S_6$
		147	$40S_2 + 34S_4 + 24S_6$
		117	$37S_4 + 33S_6 + 29S_2$
	a"	2866	$100S_7$
		499	$50S_8 + 49S_9$
		119	$50S_9 + 49S_8$

The symmetry coordinate distribution among the PEDs for the $H_2S.HCl$ complex are collected in Table 7.38. On analyzing the results in Table 7.38, the intramolecular modes retain the symmetry coordinates of the parent monomers, as was the case for the $H_2S.HF$ complex. The librational modes are not as close to one another as in the $H_2S.HF$ complex. The hydrogen bond stretching mode is due to one symmetry coordinate alone and not a contribution from the other symmetry coordinates as was observed for the HF complex.

Table 7.38 Wavenumbers and %PEDs in the $H_2S.HCl$ Complex

Complex	Symmetry Species	Wavenumber /cm^{-1}	%PED
$H_2S.HCl$	a'	3001	$100S_1$
		2838	$100S_3$
		1264	$100S_5$
		388	$70S_4 + 30S_6$
		167	$58S_6 + 39S_4$
		94	$100S_2$
	a"	2864	$100S_7$
		407	$63S_9 + 36S_8$
		148	$55S_8 + 44S_9$

The changes of the intensity values on complexation are collected in Table 7.39 for the $H_2S.HF$ complex. The major intensity enhancement occurs in the HF stretching mode, characteristic of a hydrogen bond. The ν_3 mode, H_2S angle bending mode is also enhanced; this could result from the charge donation to the HF molecule and the increase in the HSH bond angle on complexation, as was shown earlier. The intensities of the symmetric and antisymmetric stretching modes of the H_2S molecule in the complex are reduced on complexation.

Table 7.39 The Ratios of the Complex to Monomer Intensity values for the $H_2S.HF$ Complex

Complex	Symmetry Species	Mode	Complex A_c/km mol^{-1}	A_c/A_m
$H_2S.HF$	a'	ν_1	444.3	5.43
		ν_2	0.3	0.07
		ν_3	5.5	0.72
		ν_4	121.3	
		ν_5	53.4	
		ν_6	17.0	
	a"	ν_7	1.1	0.17
		ν_8	109.4	
		ν_9	28.7	

The ratios of the complex to monomer intensity values for the $H_2S.HCl$ complex are collected in Table 7.40 below. From an analysis of Table 7.40 a similar trend of intensity enhancement is observed for the $H_2S.HCl$ complex, however the magnitude of the intensity enhancement for the HCl stretching mode is much greater than that of the HF in the former complex. The remaining intensity changes occurring in the H_2S molecule are similar to those occurring in the $H_2S.HF$ complex.

Table 7.40 The Ratios of the Complex to Monomer Intensity values for the $H_2S.HCl$ Complex

Complex	Symmetry Species	Mode	Complex A_c/km mol^{-1}	A_c/A_m
$H_2S.HCl$	a'	ν_1	346.7	15.47
		ν_2	0.4	0.10
		ν_3	5.7	0.75
		ν_4	49.6	
		ν_5	35.2	
		ν_6	0.8	
	a"	ν_7	1.7	0.26
		ν_8	40.3	
		ν_9	4.2	

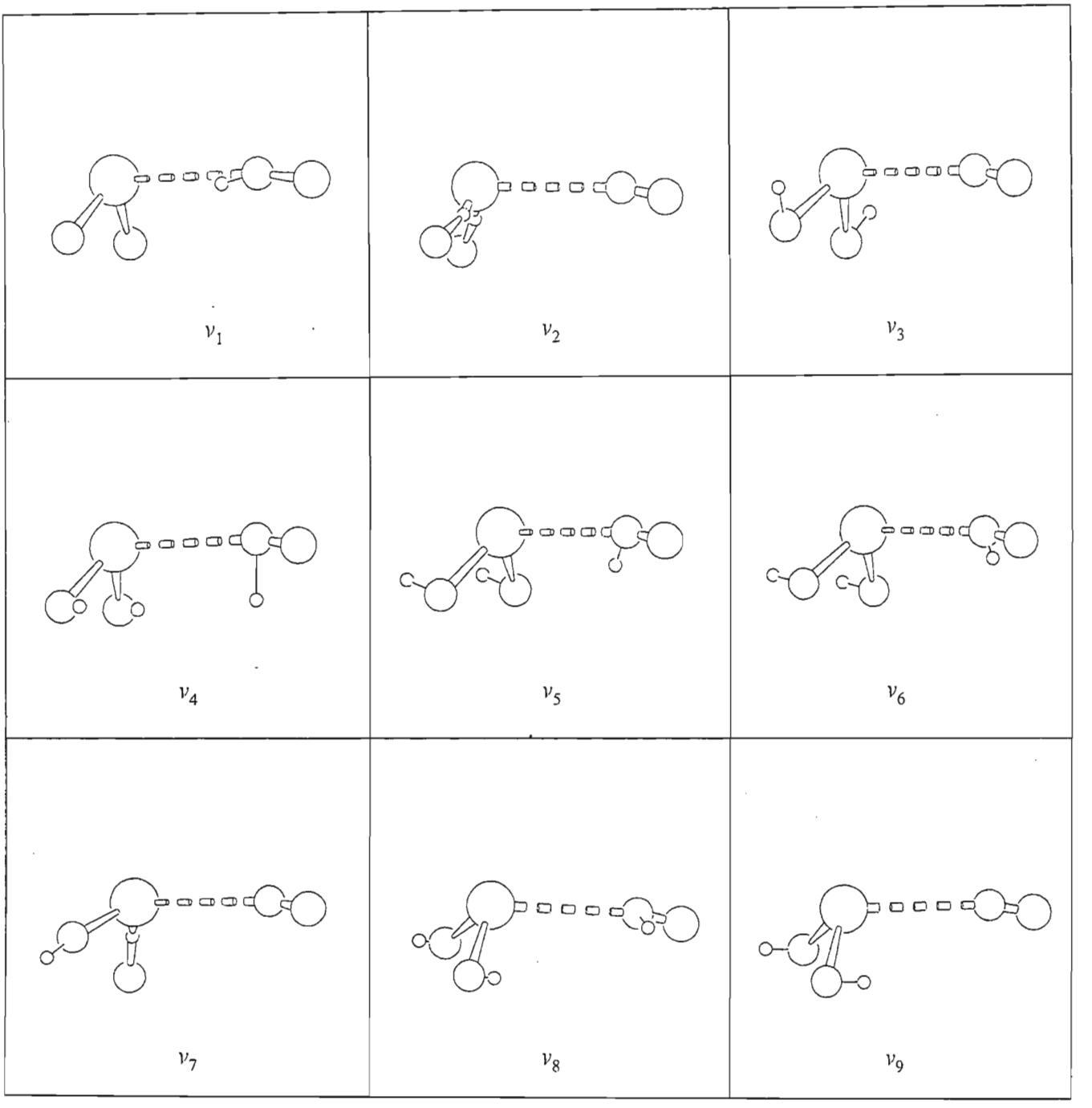

Fig 7.9 Graphical Representation of the $H_2S.HX$ Vibration modes

7.4 *The AH_3.HX Complexes (A=N,P X=F,Cl)*

7.4.1 *Geometries*

This system of complexes comprises HX being the proton donor to the lone-pair electrons on the Y atom of AH_3. The geometries of the AH_3.HX complexes were all found to have C_{3v} symmetry (figs 7.10 to fig 7.13). The NH_3 complexes will be discussed first, followed by the phosphine complexes. The major difference noted in the AH_3.HX complexes is the charge on the Y atom; the phosphorus carries a positive Mulliken charge while the nitrogen carries a negative Mulliken charge. Hence one would expect a AH_3.HX complex containing phosphine to be more repulsive since the proton of HX also carries a positive Mulliken charge. The calculated geometrical parameters for the NH_3.HF complex are collected in Table 7.41.

On examining the changes in the geometrical parameters on complexation, the major change occurs in the HF bond distance, by 2.4 pm. This large increase in the HF bond length is indicative of a strong hydrogen bond between the HF and the NH_3. The experimental microwave studies[344] report a value for the N..F distance of 266 pm, also suggesting that the hydrogen bond is relatively strong. Our calculated N..F distance of 269.3 pm compares well with the experimental value of 266 pm. The other changes in the geometrical parameters were in the ammonia bond lengths and bond angles by 0.2 pm and 0.7°. The changes in the geometrical parameters observed coupled with the linearity and length of the N..H separation suggest this complex to be strongly hydrogen bonded.

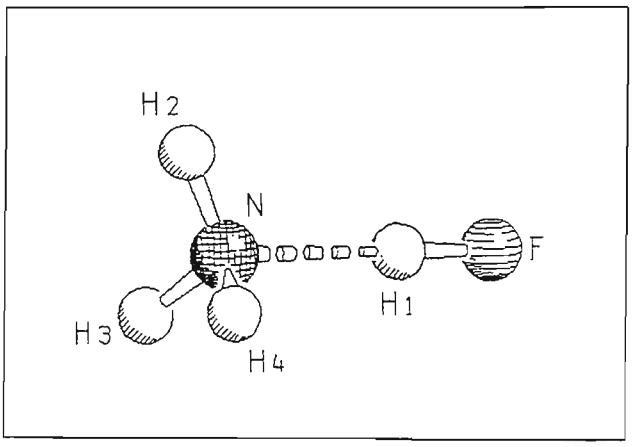

Fig 7.10 The Linear NH_3.HF Complex

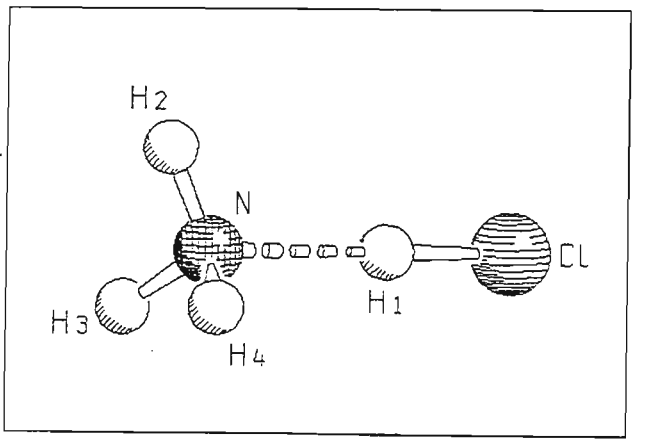

Fig 7.11 The Linear NH_3.HCl Complex

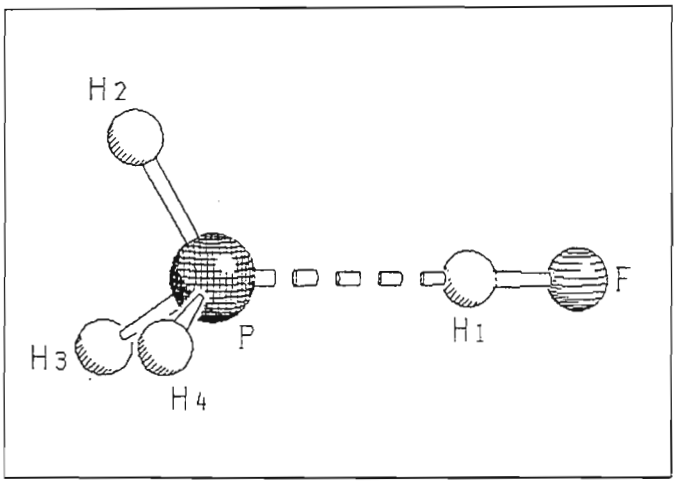

Fig 7.12 The Linear PH_3.HF Complex

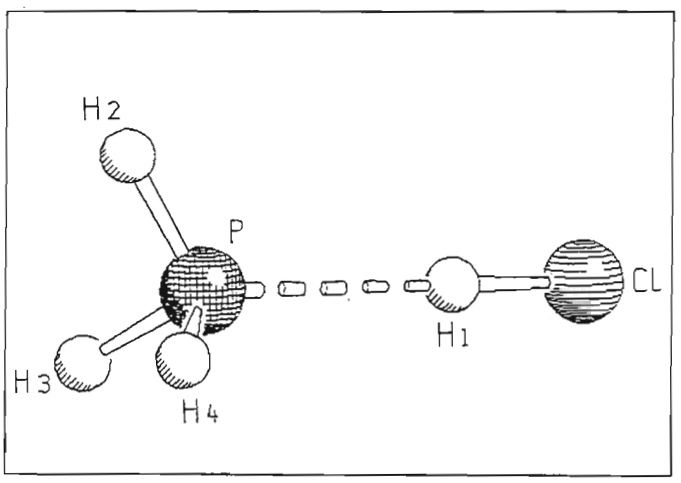

Fig 7.13 The Linear PH_3.HCl Complex

Table 7.41 Geometrical Parameters for the Most Stable NH_3.HF Complex

Complex	Parameter	Complex	Monomer	Difference
NH_3.HF	r(H1F)/pm	94.5	92.1	2.4
	r(NH2), r(NH3), r(NH4)/pm	101.3	101.1	0.2
	R(N..H1)/pm	174.8		
	H2NH3/deg	106.8	106.1	0.7
	N..HF/deg	180.0		

The changes in the geometrical parameters in the NH_3.HCl complex are collected in Table 7.42.

Table 7.42 Geometrical Parameters for the Most Stable NH_3.HCl Complex

Complex	Parameter	Complex	Monomer	Difference
NH_3.HCl	r(H1Cl)/pm	131.6	126.8	4.8
	r(NH2), r(NH3), r(NH4)/pm	101.3	101.1	0.2
	R(N..H1)/pm	177.5		
	H2NH3/deg	107.0	106.1	0.9
	N..H1Cl/deg	180.0		

The studies involving the geometrical parameters of the NH_3.HCl complexes have played

a big role in understanding the bonding process involved. The strength of the hydrogen bond and the close proximity of the hydrogen in HF to the nitrogen in ammonia suggested that this complex may be ionic in nature. Latajka and Scheiner[251] showed that at the SCF level the ionic structure is more stable than the hydrogen bonded structure. However with the inclusion of correlation effects the stabilities of the complexes are reversed. Our calculations predict a N..Cl separation of 309.1 pm, showing that this complex definitely cannot be ionic in nature since this would require a much shorter N..Cl bond length. The N..Cl distance of 309.1 pm is in excellent agreement with that of 313.64 pm observed by Howard and Legon.[245] The major changes in the geometrical parameters on complexation were those of the HCl bond length and the H2NH3 bond angle, which increased by 4.8 pm and 0.9° respectively, similar to what was observed in the HF complex of ammonia. These changes are in excellent agreement with those of Latajka and Scheiner.[251]

7.4.2 *Energetics*

The binding energies of the NH_3.HX complexes, together with the percentage dispersion effects and the BSSEs are collected in Table 7.43

Table 7.43 The Binding Energies of the Most Stable NH_3.HX Complexes

Complex	$\Delta E'$ /kJ mol^{-1}	ΔE /kJ mol^{-1}	BSSE /kJ mol^{-1}	$\%\Delta E_{Disp}$
NH_3.HF	-50.5	-57.7	7.2	2.2
NH_3.HCl	-39.9	-46.7	6.8	19.4

From Table 7.43 the NH_3.HF and NH_3.HCl complexes have binding energies of 50.5 and 39.9 kJ mol^{-1} respectively. The contribution of the dispersion term to the binding energy

is significantly larger in the case of the HCl complex, being 19.4%. A similar trend for the dispersion energies was also observed by Latajka and Scheiner.[251] The experimental binding energy for the NH_3.HCl complex was reported as 33.4 ± 11.7 kJ mol^{-1} by Goldfinger and Verhaegen[244] from their mass spectroscopic studies. The Morokuma decomposition analysis for the NH_3.HX complexes is collected in Table 7.44.

Table 7.44 Energy Decomposition Analysis of the most Stable NH_3.HX complexes /kJ mol^{-1}

Complex	ES	EX	CT	PL	MIX	Total
NH_3.HF	-93.9	68.9	-16.6	-10.0	2.2	-49.5
NH_3.HCl	-93.7	97.4	-31.2	-10.1	5.4	-32.2

The electrostatic term (-93.9 kJ mol^{-1}) dominates the SCF interaction energy in the NH_3.HF complex, followed by the exchange repulsion term (68.9 kJ mol^{-1}), while in the case of the NH_3.HCl complex, the exchange repulsion term (97.4 kJ mol^{-1}) is larger than the electrostatic term (-93.7 kJ mol^{-1}). As was observed in Table 7.43, the dispersion contribution did indeed play an important role in the interaction energy of the NH_3.HCl complex. Therefore the NH_3.HCl complex can be classified as being bound by dispersive as well as by electrostatic forces. The magnitude of the other decomposition energy terms are quite negligible when compared with the major terms, hence their roles would be negligible in the interaction energies of the NH_3.HX complexes.

7.4.3 *Mulliken Charge Analysis*

From the Mulliken charge analyses collected in Table 7.45 for the NH_3.HF complex, the proton donor was found to be the acceptor of negative charge (-0.040 e) as was the case

for the $H_2Y.HX$ complexes.

The hydrogen atoms of both NH_3 and HF are the contributors of negative charge. The negative charge (-0.040 e) gained by the HF molecule explains the increase in the HF bond length due to the residence of this negative charge in the HF antibonding orbital of the proton donor as was the case in the $H_2Y.HX$ complexes. The increase in the H2NH3 angle on complexation could also be explained by the same line of reasoning; with the loss of negative charge in the hydrogens of ammonia, the repulsion between the bonding electrons in the proton acceptor bonds and the lone-pair electrons of the nitrogen decreases, allowing for a greater repulsion between the electrons in the proton acceptor bonds and hence resulting in an increase in the proton acceptor bond angles.

Table 7.45 Mulliken Charge Analysis for the Most Stable NH_3.HF Complex

Atom	Atomic Charge /e		Difference
	Complex	Monomer	/e
H1	0.452	0.397	0.055
F	-0.492	-0.397	-0.095
			-0.040
N	-0.845	-0.785	-0.060
H2	0.295	0.262	0.033
H3	0.295	0.262	0.033
H4	0.295	0.262	0.033
			0.040

In the case of the NH_3.HCl complex, the Mulliken charge analysis is collected in Table 7.46. For the NH_3.HCl complex a similar trend in the charge migration is observed as in the case of the NH_3.HF complex. The HCl gains negative charge (-0.064 e) from the proton acceptor, which primarily has its origin from the hydrogens of both proton donor and acceptor. Similar reasoning for the increase in the HCl bond length and NH_3 bond angles is applicable as was the case in the NH_3.HF complex. The magnitude of the increase in the HX bond length and NH_3 bond angle is much greater in this complex than in the NH_3.HF complex. This is expected since fluorine is more electronegative than chlorine, hence exerting a stronger attractive force on its hydrogen.

Table 7.46 Mulliken Charge Analysis for the Most Stable NH_3.HCl Complex

Atom	Atomic Charge /e		Difference /e
	Complex	Monomer	
H1	0.241	0.192	0.049
Cl	-0.305	-0.192	-0.113
			-0.064
N	-0.824	-0.785	-0.039
H2	0.296	0.262	0.034
H3	0.296	0.262	0.034
H4	0.296	0.262	0.034
			0.064

7.4.4 *Vibrational Properties of the Most Stable NH_3.HX Complexes*

The calculated vibrational spectra, potential energy distributions and infrared intensities at the MP2/6-31G** level for the linear hydrogen bonded NH_3.HX complexes are shown in the Tables 7.47 - 7.55. The plots of the normal modes of vibration for the NH_3.HX complexes are depicted in fig 7.14. The calculated vibrational spectrum of the NH_3.HF complex is presented in Table 7.47.

Table 7.47 Calculated Wavenumber Shifts in the Most Stable NH_3.HF Complex

Symmetry Species	Mode	Complex Wavenumber /cm^{-1}	Monomer Wavenumber /cm^{-1}	Shift[(a)] /cm^{-1}
a_1	ν_1	3653	4197	-544
	ν_2	3564	3881	-317
	ν_3	1193	1653	-460
e_a	ν_5	3718	3899	-181
	ν_6	1717	1784	-67
e_b	ν_5	3718	3899	-181
	ν_6	1717	1784	-67

(a) Complex - Monomer

From Table 7.47, all of the intramolecular vibrational modes are red shifted to a large extent from the monomer band positions, with HF stretching mode shifted by -544 cm^{-1} and the proton donor symmetric stretching and bending modes by -317 and -460 cm^{-1} respectively. These large red shifts were also observed in the calculations performed by

Kurnig et al.[258] The large red shift of 317 cm^{-1} in the stretching and 460 cm^{-1} in the symmetric bending modes of ammonia coupled to the red-shifted antisymmetric stretch of 181 cm^{-1} is indicative of the strongly basic nature of ammonia, essentially sharing the proton of HF in the complex. These large red shifts could also be the result of using the harmonic approximation, since hydrogen bonding interactions tend to increase the anharmonicity in the XH bond thereby allowing the XH bond to dissociate more readily. The final outcome of this is a lowering of the ν_1 wavenumber to a large extent.[223] A comparison of our calculated vibrational spectrum to the experimental matrix isolation spectrum in an argon matrix is collected in Table 7.48.

Table 7.48 Comparison of the Calculated to Experimental Vibrational Spectrum of the Most Stable NH_3.HF Complex

Symmetry Species	Mode	Calculated Wavenumber /cm^{-1}	Experiment Wavenumber /cm^{-1} [a]	Ratio[b]
a_1	ν_1	3653	3041	1.21
	ν_3	1193	1094	1.09
e	ν_7	918	916	1.00

(a) Ref. 243

(b) Ratio = Calculated / Experimental

Our calculated vibrational spectrum of the NH_3.HF complex was found to be in agreement with the experimental matrix isolated spectrum. The ν_1 band was red shifted by 848 cm^{-1} from its monomer band position,[243] suggesting the bond between the NH_3 and HF to be extremely strong. A single sharp band at 916 cm^{-1} was assigned to the librational mode

by Andrews and Johnson,[243] hence suggesting no vibrational splitting in the complex, therefore supporting the C_{3v} geometry of the complex. The calculated vibrational spectrum of the NH_3.HCl complex is collected in Table 7.49.

Table 7.49 Calculated Wavenumber Shifts in the Most Stable NH_3.HCl Complex

Symmetry Species	Mode	Complex Wavenumber /cm^{-1}	Monomer Wavenumber /cm^{-1}	Shift[a] /cm^{-1}
a_1	ν_1	3561	3881	-320
	ν_2	2454	3001	-547
	ν_3	1184	1653	-469
e	ν_5	3716	3899	-183
	ν_6	1714	1784	-70

(a) Complex - Monomer

From Table 7.49, the intramolecular modes are all red shifted to a large extent as was the case in the NH_3.HF complex. A similar trend was also observed by Szczesniak and co-workers.[252] They found that ν_1 was red shifted by 424 cm^{-1} at the SCF level and by 898 cm^{-1} at the MP2 level. This further supports the nature of the complex being ionic at the SCF level of theory and strongly hydrogen bonded at the MP2 level. Boutellier et al[240] also support the conclusions reached by Szczesniak and co-workers;[252] their calculations reveal ν_1 to be red shifted by 445 cm^{-1} at the SCF and 700 cm^{-1} at the MP2 level of theory. The symmetric and antisymmetric NH_3 stretching modes are both red-shifted to a large extent but in the case of the bending modes, the ν_3 symmetric bending

mode of the proton acceptor is red-shifted more than the antisymmetric bending mode ν_6. The experimental matrix isolated spectrum of the NH_3.HCl complex in argon matrix is collected in Table 7.50.

From Table 7.50, our calculated vibrational spectrum of the NH_3.HCl complex was found to agree with the matrix isolated argon spectrum of Barnes et al,[247] except for ν_1. The explanation for the low value obtained by Barnes et al[247] follows from the explanation given for the large red shift in the NH_3.HF complex. Matrix isolation studies by Ault and Pimentel[246] located ν_1 at 720 cm^{-1} in a nitrogen matrix for the NH_3.HCl complex. They attributed the occurrence of ν_1 at 720 cm^{-1} to matrix cage effects, which resulted in a lower degree of proton transfer in an argon rather than a nitrogen matrix.

Table 7.50 Comparison of the Calculated and the Experimental Vibrational Spectrum of the Most Stable NH_3.HCl Complex

Symmetry Species	Mode	Calculated Wavenumber /cm^{-1}	Experiment Wavenumber /cm^{-1} [(a)]	Ratio[(b)]
a_1	ν_1	3561	1371	2.59
	ν_3	1184	1072	1.10
	ν_4	200	166	1.20
e	ν_5	3716	3420	1.08
	ν_7	825	733	1.12

(a) Ref. 247

(b) Ratio = Calculated / Experimental

Our calculated value of the intermolecular mode at 200 cm^{-1} was found to be in excellent agreement with experiment; a similar observation was also made by Szczesniak et al.[252] The difficulty in observing ν_6, the antisymmetric NH_3 bending mode is expected based on the small red shifts this mode undergoes relative to the ν_3 mode, as seen in Table 7.49. The symmetry coordinates used in the descriptions of the vibrational modes in the NH_3.HX complexes are collected in Table 7.51.

Table 7.51 Symmetry Coordinates for the NH_3.HX Complexes

Complex	Symmetry Coordinate	Description
NH_3.HX	$S_1 = \Delta r_1$	HX stretch
	$S_2 = 1/\sqrt{3}(\Delta r_2 + \Delta r_3 + \Delta r_4)$	NH_3 symmetric stretch
	$S_3 = 1/\sqrt{6}(\Delta\alpha_1 + \Delta\alpha_2 + \Delta\alpha_3 - \Delta\beta_1 - \Delta\beta_2 - \Delta\beta_3)$	NH_3 symmetric bend
	$S_4 = \Delta R$	N..H stretch
	$S_{5a} = 1/\sqrt{2}(\Delta r_3 - \Delta r_4)$	NH_3 antisymmetric stretch
	$S_{6a} = 1/\sqrt{2}(\Delta\alpha_2 - \Delta\alpha_3)$	NH_3 antisymmetric bend
	$S_{7a} = 1/\sqrt{2}(\Delta\beta_2 - \Delta\beta_3)$	NH_3 rock
	$S_{8a} = \Delta\delta_1$	libration
	$S_{5b} = 1/\sqrt{6}(2\Delta r_2 - \Delta r_3 - \Delta r_4)$	NH_3 antisymmetric stretch
	$S_{6b} = 1/\sqrt{6}(2\Delta\alpha_1 - \Delta\alpha_2 - \Delta\alpha_3)$	NH_3 antisymmetric bend
	$S_{7b} = 1/\sqrt{6}(2\Delta\beta_1 - \Delta\beta_2 - \Delta\beta_3)$	NH_3 rock
	$S_{8b} = \Delta\delta_2$	libration

The symmetry coordinates used to describe the intramolecular vibrational modes were those used earlier in the descriptions of the monomer modes. The intermolecular modes, hydrogen bond stretching, rocking and libration modes were generated according to the rules of Wilson et al.[70] The percentage PEDs amongst the various symmetry coordinates are collected in Table 7.52 for the NH_3.HF complex.

Table 7.52 Wavenumbers and %PEDs in the NH_3.HF Complex

Complex	Symmetry Species	Wavenumbers /cm^{-1}	%PED
NH_3.HF	a_1	3654	$95S_1 + 4S_4 + 2S_2$
		3564	$97S_2 + 3S_1$
		1193	$96S_3 + 5S_2$
		262	$97S_4 + 2S_1$
	e_a	3718	$100S_5$
		1717	$100S_6$
		918	$70S_8 + 30S_7$
		221	$55S_7 + 45S_8$
	e_b	3718	$100S_9$
		1717	$100S_{10}$
		918	$70S_{12} + 30S_{11}$
		221	$55S_{11} + 45S_{12}$

From Table 7.52, the a_1 vibrational modes tend to retain their monomer vibrational mode natures with little contribution from the other symmetry coordinates. The ν_1, ν_2 and ν_5 stretching modes are minimally perturbed by the other vibrational modes, further supporting the fact that this complex is strongly bonded. The hydrogen bond stretching mode also shows little mixing of the other vibrational modes. On examining the symmetry

coordinate distribution in the %PEDs amongst the degenerate vibrational modes, the mixing of symmetry coordinates occurs mostly in the intermolecular modes. There is coupling between the rocking and libration modes of the NH_3 molecule. The contributions of the symmetry coordinates to the PEDs for the NH_3.HCl complex are collected in Table 7.53.

A similar trend is observed in the case of the symmetry coordinate mixing as was the case in the NH_3.HF complex. The intramolecular stretching and bending modes all have majority contributions from the monomer symmetry coordinates describing their particular vibrations. The intermolecular modes on the other hand exhibit symmetry coordinate mixing from the different vibrational modes; this effect is more pronounced in the e-symmetry species. The hydrogen bond stretching mode has a larger contribution from the HCl stretching mode compared with that in the HF complex; this could be attributed to the proton being more or less equally shared between the nitrogen and the chlorine of the proton acceptor and the donor.

Table 7.53. Wavenumbers and %PEDs in the NH_3.HCl Complex

Complex	Symmetry Species	Wavenumber /cm^{-1}	%PED
NH_3.HCl	a_1	3560	$100S_2$
		2453	$94S_1 + 6S_4$
		1183	$96S_3 + 4S_2$
		200	$90S_4 + 10S_1$
	e_a	3715	$100S_5$
		1714	$100S_6$
		824	$70S_8 + 30S_7$
		263	$58S_7 + 42S_8$
	e_b	3715	$100S_9$
		1714	$100S_{10}$
		824	$70S_{12} + 30S_{11}$
		263	$58S_{11} + 42S_{12}$

The changes in the intensities in the NH_3.HF complex are collected in Table 7.54. While the intensity of the HF stretching vibration increases on complexation, the intensity of the NH_3 symmetric and antisymmetric stretches undergo even more drastic changes. The increase in the intensity of the HF stretching mode is expected, since the bond formed between the HF and NH_3 molecule is strong, thus creating a large amount of charge

distribution in the N..HF region, hence allowing for displacement of the proton in HF which in turn is responsible for the intensity enhancement.

Table 7.54 The Ratios of the Complex to Monomer Intensity values for the NH_3.HF Complex

Complex	Symmetry Species	Mode	Complex A_c/km mol^{-1}	A_c/A_m
NH_3.HF	a_1	ν_1	1001.3	12.25
		ν_2	46.6	233.00
		ν_3	160.0	0.74
		ν_4	3.7	
	e	ν_5	12.0	15.00
		ν_6	20.9	1.01
		ν_7	173.6	
		ν_8	11.9	

In the case of the ammonia molecule, the monomer stretching intensities are quite weak, being 0.2 and 0.8 km mol^{-1} for the symmetric and antisymmetric stretching modes, thus leading to a large magnification factor on complexation. Alternatively this enhancement of the intensities on complexation can be explained as follows. In the monomer NH_3 molecule, the intensities are low because of the cancellation of two opposite effects. On executing the stretching motion, the hydrogens in NH_3 move further away from the nitrogen, thus creating a positive pole at the hydrogen atoms, but this displacement also

causes a build-up of negative charge at the nitrogen, hence resulting in only a small change in the dipole moment. On complexation with the HF molecule, the NH_3 acts as an electron donor thus increasing the electropositivity of the hydrogens in ammonia, therefore increasing the dipole moment during the NH_3 stretching vibration in the complex.[259] The ratios of the complex to monomer intensity values in the NH_3.HCl complex are collected in Table 7.55.

Table 7.55 The Ratios of the Complex to Monomer Intensity values for the NH_3.HCl Complex

Complex	Symmetry Species	Mode	Complex A_c/km mol^{-1}	A_c/A_m
NH_3.HCl	a_1	ν_1	3.4	17.00
		ν_2	1700.1	75.89
		ν_3	124.7	0.57
		ν_4	24.3	
	e	ν_5	13.3	16.62
		ν_6	23.4	1.13
		ν_7	82.9	
		ν_8	22.9	

An intensity enhancement of ν_2 also occurs in this complex, as was the case in the NH_3.HF complex. This occurs due to the flux of negative charge from the electron donor to HCl bond, which when executing its stretching motion results in an increase in the

dipole moment of the HCl molecule, therefore resulting in an intensity enhancement. The intensification of the NH_3 intramolecular modes can also be explained on the basis of the charge flux as in the case of the NH_3.HF complex.

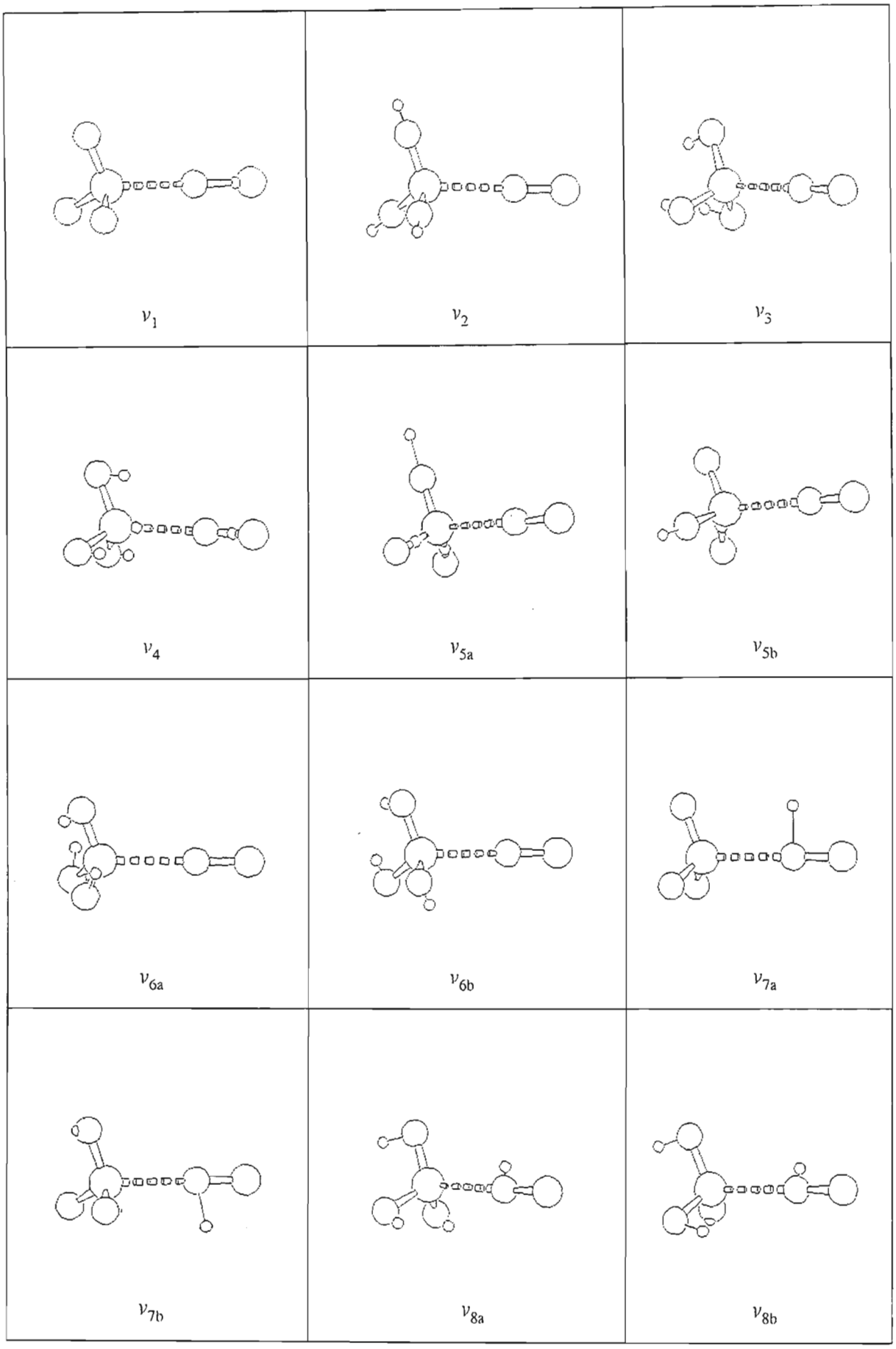

Fig 7.14 Graphical Representation of the $NH_3.HX$ Complex Vibration modes

7.5 *The PH_3.HX Complexes (X= F,Cl)*

7.5.1 *Geometries*

The geometries optimized for these complexes were found to have C_{3v} symmetry with HX the proton donor to the phosphorus lone-pair electrons (figs 7.12 and 7.13). The ab initio[224,257,260], experimental gas[261,262] and matrix isolation studies[255] also support the C_{3v} geometry for these PH_3.HX complexes. The major difference between the NH_3.HX and the PH_3.HX complexes is in the sign of the Mulliken charge on the phosphorus and the nitrogen atoms. The phosphorus carries a positive atomic charge while the nitrogen a negative atomic charge. This is due to the phosphorus atom being less electronegative than the hydrogen atoms in the phosphine molecule.

The changes in the geometrical parameters in the PH_3.HF complex are collected in Table 7.56. The major changes occurring on complexation are the lengthening of the HF bond by 0.7 pm, the decrease in the PH_3 bond distances by 0.3 pm and the increase in the PH_3 bond angles by 1.5°. The changes are fairly minimal, emphasising the weakness of this complex. The explanation for the changes in the geometrical parameters on complexation is similar to that in the NH_3.HX complexes. Our calculated P..F separation of 336.8 pm agrees well with the gas phase experimental value of 331 pm obtained by Legon and Willoughby.[262]

Table 7.56 Geometrical Parameters for the Most Stable PH_3.HF complex

Complex	Parameter	Complex	Monomer	Difference
PH_3.HF	r(H1F)/pm	92.8	92.1	0.7
	r(PH2), r(PH3), r(PH4)/pm	140.2	140.5	-0.3
	H2PH3/deg	96.0	94.5	1.5
	R(P..H1)/pm	244.0		
	P..HF/deg	180.0		

The geometrical parameters of the PH_3.HCl complex are collected in Table 7.57.

Table 7.57 Geometrical Parameters for the Most Stable PH_3.HCl Complex

Complex	Parameter	Complex	Monomer	Difference
PH_3.HCl	r(H1Cl)/pm	127.8	126.8	1.0
	r(PH2), r(PH3), r(PH4)/pm	140.3	140.5	-0.2
	H2PH3/deg	95.6	94.5	1.1
	R(P..H1)/pm	258.2		
	P..HCl/deg	180.0		

The major changes occurring in the monomer geometrical parameters are the increase in the HCl bond length by 1.0 pm, the increase in the PH_3 bond angles by 1.1° and the

decrease in the PH_3 bond lengths by 0.2 pm.

The magnitudes of the changes in the geometrical parameters for the HCl complex are a little larger than those in the corresponding HF complex.

7.5.2 *Energetics*

The binding energies, together with the percentage dispersion energy contributions in the PH_3.HX complexes are collected in Table 7.58.

Table 7.58 The Binding Energies of the Most Stable PH_3.HX Complexes

Complex	$\Delta E'$ /kJ mol^{-1}	ΔE /kJ mol^{-1}	BSSE /kJ mol^{-1}	$\%\Delta E_{Disp}$
PH_3.HF	-14.9	-20.8	5.9	3.9
PH_3.HCl	-10.6	-15.5	4.9	32.8

From Table 7.58, the HF complex is observed to be stronger than the HCl complex as one would expect, due to the greater electronegativity of fluorine, resulting in a tendency to form stronger hydrogen bonds. Our calculated binding energy for the PH_3.HF complex agrees well with the estimated experimental binding energy of 11.7 kJ mol^{-1} obtained from the rotational spectrum by Legon and Willoughby.[262] No experimental binding energy value was available for comparison with the PH_3.HCl complex. The dispersion contribution to the interaction energy was found to play a large role in the case of the PH_3.HCl complex, as was shown by Latajka and Scheiner[257] and Alabart and Caballol.[260] The energy decomposition analyses of the PH_3.HX complexes are collected in Table 7.59.

Table 7.59 Energy Decomposition Analysis of the PH_3.HX Complexes /kJ mol^{-1}

Complex	ES	EX	CT	PL	MIX	Total
PH_3.HF	-32.4	28.8	-8.5	-3.7	2.0	-13.8
PH_3.HCl	-25.7	28.3	-2.5	-9.9	2.7	-7.1

The electrostatic term (32.4 kJ mol^{-1}) dominates the attractive energy component in the HF complex, while in the HCl complex the exchange repulsion term (28.3 kJ mol^{-1}) is found to be the major contributor to the binding energy. The polarization term is also found to be larger in the HCl complex than in the HF complex. The charge transfer term on the other hand is found to be larger in the HF complex. The EX term most probably arises from the repulsion between the phosphorus and the HX hydrogens, since they are similarly charged.

7.5.3 *Mulliken Charge Analysis*

The amount of charge transfer occurring on complexation in the PH_3.HF complex is collected in Table 7.60.

The HF molecule gains -0.024 e charge from the phosphine molecule on complexation, thus decreasing the negative charges on the hydrogen atoms of the phosphine molecule. The gain of negative charge by the HF molecule into the HF antibonding orbital leads to the increase in the HF bond length. The loss of negative charge in the phosphine molecule leads to the decrease in the PH bond lengths and the increase in the phosphine HPH bond angle.

Table 7.60 Mulliken Charge Analysis for the Most Stable PH_3.HF Complex

Atom	Atomic Charge /e		Difference /e
	Complex	Monomer	
H1	0.406	0.192	0.214
F	-0.430	-0.192	0.238
			-0.024
P	0.126	0.161	0.035
H2	-0.034	-0.054	0.020
H3	-0.034	-0.054	0.020
H4	-0.034	-0.054	0.020
			0.024

In the PH_3.HCl complex a similar trend is also observed with the directionality of the charge distribution as shown in Table 7.61. The HCl gains -0.033 e charge from the phosphine on complexation, greater than that gained by the HF molecule, thus accounting for the larger change in the geometrical parameters in the case of the PH_3.HCl complex. Once again the loss of negative charge by the hydrogen atoms results in the increase in the HCl bond length coupled with the increase in the phosphine internal bond angle.

Table 7.61 Mulliken Charge Analysis for the PH_3.HCl Complex

Atom	Atomic Charge /e		Difference /e
	Complex	Monomer	
H1	0.183	0.192	-0.009
Cl	-0.216	-0.192	-0.024
			-0.033
P	0.145	0.161	0.016
H2	-0.037	-0.054	0.017
H3	-0.037	-0.054	0.017
H4	-0.037	-0.054	0.017
			0.035

7.5.4 *Vibrational Properties of the Most Stable PH_3.HX Dimers*

The calculated vibrational spectra, potential energy distributions and infrared intensities at the MP2/6-31G** level for the linear hydrogen bonded PH_3.HX complexes are shown in Tables 7.62 - 7.70. The plots of the normal modes of vibrations for the PH_3.HX complexes are depicted in fig 7.15. The calculated vibrational spectrum of the PH_3.HF complex is collected in Table 7.62.

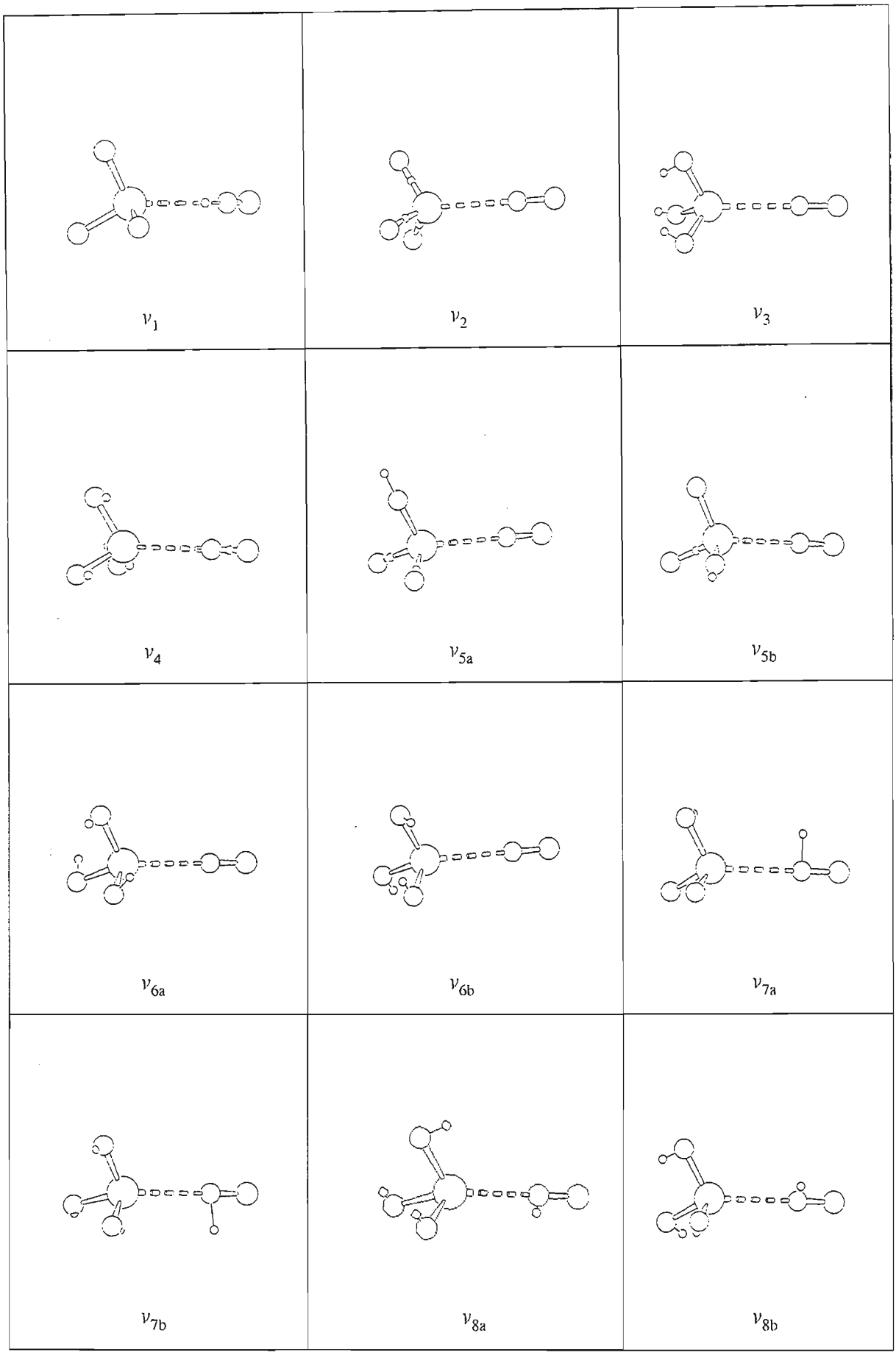

Fig 7.15 Graphical Representation of the $PH_3.HX$ Complex Vibration modes

Table 7.62 Calculated Wavenumber Shifts in the Most Stable PH_3.HF Complex

Symmetry Species	Mode	Complex Wavenumber /cm^{-1}	Monomer Wavenumber /cm^{-1}	Shift[(a)] /cm^{-1}
a_1	ν_1	4037	4197	-160
	ν_2	2557	2531	26
	ν_3	1079	1078	1
e	ν_5	2574	2546	28
	ν_6	1180	1184	-4

(a) Complex - Monomer

On analyzing the monomer to complex wavenumber differences, a marked difference is observed from trend of red shifting of the monomer vibrational modes on complexation. The HF stretching mode is red shifted by 160 cm^{-1} from the monomer, as was the case with the NH_3.HX series. This red shift of the HF stretch is characteristic of a strong bond being formed. The phosphine stretching modes are all blue shifted. The blue shifting on complexation indicates that the nature of the bonding in the phosphine molecule has changed; this suggests an increase in the polarization of the phosphorus lone-pair electrons, with a corresponding increase in the s-character in the bonding pair electrons. The phosphine bending mode wavenumbers are slightly perturbed from the monomer modes with the librational modes decreasing considerably in magnitude from the NH_3.HX to the PH_3.HX complexes, thus indicating a decrease in the rigidity of these complexes. On comparing the ν_2 mode in the NH_3.HF with that in the PH_3.HF complex, the ν_2 in the NH_3 complex occurs at a higher wavenumber than in the monomer while in the PH_3

complex it occurs at a lower wavenumber than in the monomer. This probably arises from the greater electrostatic repulsions between the base and acid hydrogens which are closer in the stronger NH_3 complex than in the weaker PH_3 complex. These repulsions are further weakened in PH_3.HCl, as shown by the lower wavenumber of the ν_2 mode in Table 7.64. The comparison of the calculated to the experimental matrix isolation vibrational spectrum is shown in Table 7.63 for the PH_3.HF complex.

Our calculated vibrational spectrum for the PH_3.HF complex agrees well with the matrix isolated argon spectrum of Arlinghaus and Andrews.[255] The experimental observation of sharp doubly degenerate librational modes for the HF molecule confirm that the three-fold symmetry is preserved in the complex.

Table 7.63 Comparison of the Calculated to Experimental Vibrational Spectrum of the Most Stable PH_3.HF Complex

Symmetry Species	Mode	Calculated Wavenumber /cm^{-1}	Experimental Wavenumber /cm^{-1} [a]	Ratio[b]
a_1	ν_1	4037	3627	1.11
	ν_2	2557	2365	1.08
	ν_3	1079	986	1.09
e	ν_5	2574	2372	1.08
	ν_7	483	477	1.01

(a) Ref. 255

(b) Ratio = Calculated / Experimental

The changes in the calculated vibrational spectrum in the PH_3.HCl complex are collected in Table 7.64.

As in the case of the PH_3.HF complex a similar trend is observed for the PH_3.HCl complex, with the HCl being red shifted by 145 cm^{-1}, and the PH_3 stretching modes blue shifted by 18 and 21 cm^{-1} for the symmetric and antisymmetric vibrations respectively.

Table 7.64 Calculated Wavenumber Shifts in the Most Stable PH_3.HCl Complex

Symmetry Species	Mode	Complex Wavenumber /cm^{-1}	Monomer Wavenumber /cm^{-1}	Shift[(a)] /cm^{-1}
a_1	ν_1	2983	3128	-145
	ν_2	2549	2531	18
	ν_3	1077	1078	-1
e	ν_5	2567	2546	21
	ν_6	1181	1184	-3

(a) Complex - Monomer

The matrix isolated vibrational spectrum of the PH_3.HCl complex is reported in Table 7.65. As in case of the PH_3.HF complex, our calculated vibrational spectrum is once again in excellent agreement with the matrix isolated vibrational spectrum. The symmetry of the complex is also preserved in the argon matrix cage as was the case in the PH_3.HF complex. The librational mode in the PH_3.HCl complex is much lower in wavenumber than in the HF complex, suggesting once again a decrease in rigidity in the former complex is observed.

It should also be noted that in the $YH_3.HX$ complexes, the worst correlation of the calculated to experimental data occurs in the ν_1 mode suggesting that larger basis sets are required on the fluorine and chlorine atoms.

Table 7.65 Comparison of the Calculated to Experimental Vibrational Spectrum of the Most Stable $PH_3.HCl$ Complex

Symmetry Species	Mode	Calculated Wavenumber /cm^{-1}	Experimental Wavenumber /cm^{-1} [a]	Ratio[b]
a_1	ν_1	2983	2646	1.13
	ν_2	2549	2360	1.08
	ν_3	1077	983	1.09
e	ν_5	2567	2368	1.08
	ν_7	401	336	1.19

(a) Ref. 255

(b) Ratio = Calculated / Experimental

The descriptions of the various symmetry coordinates describing the vibrational modes in the $PH_3.HX$ complexes are collected in Table 7.66. The symmetry coordinates shown in Table 7.66 were generated using the monomer symmetry coordinates for the intramolecular vibrational modes and those used in the description of the intermolecular vibrational modes according to the rules of Wilson et al.[70]

Table 7.66 Symmetry Coordinates for the PH_3.HX Complexes

Complex	Symmetry Coordinate	Description
PH_3.HX	$S_1 = \Delta r_1$	HX stretch
	$S_2 = 1/\sqrt{3}(\Delta r_2 + \Delta r_3 + \Delta r_4)$	PH_3 symmetric stretch
	$S_3 = 1/\sqrt{6}(\Delta\alpha_1 + \Delta\alpha_2 + \Delta\alpha_3 - \Delta\beta_1 - \Delta\beta_2 - \Delta\beta_3)$	PH_3 symmetric bend
	$S_4 = \Delta R$	P..H stretch
	$S_{5a} = 1/\sqrt{2}(\Delta r_3 - \Delta r_4)$	PH_3 antisymmetric stretch
	$S_{6a} = 1/\sqrt{2}(\Delta\alpha_2 - \Delta\alpha_3)$	PH_3 antisymmetric bend
	$S_{7a} = 1/\sqrt{2}(\Delta\beta_2 - \Delta\beta_3)$	PH_3 rock
	$S_{8a} = \Delta\delta_1$	libration
	$S_{5b} = 1/\sqrt{6}(2\Delta r_2 - \Delta r_3 - \Delta r_4)$	PH_3 antisymmetric stretch
	$S_{6b} = 1/\sqrt{6}(2\Delta\alpha_1 - \Delta\alpha_2 - \Delta\alpha_3)$	PH_3 antisymmetric bend
	$S_{7b} = 1/\sqrt{6}(2\Delta\beta_1 - \Delta\beta_2 - \Delta\beta_3)$	PH_3 rock
	$S_{8b} = \Delta\delta_2$	libration

The percentage contributions of the symmetry coordinates among the different vibrational modes are collected in Table 7.67 for the PH_3.HF complex. The a_1 symmetry vibrational modes exhibit no mixing with the other symmetry coordinates. In the case of the e symmetry type vibrational modes, mixing occurs only in the intermolecular modes, in the ν_7 and ν_8 modes. These modes involve the coupling of the libration mode with the PH_3 rocking mode.

Table 7.67 Wavenumbers and %PEDs in the PH_3.HF Complex

Complex	Symmetry Species	Wavenumbers /cm^{-1}	%PED
PH_3.HF	a_1	4637	$100S_1$
		2558	$100S_2$
		1079	$100S_3$
		128	$100S_4$
	e_a	2575	$100S_{5a}$
		1184	$100S_{6a}$
		483	$37S_{7a} + 63S_{8a}$
		93	$52S_{7a} + 48S_{8a}$
	e_b	2575	$100S_{5b}$
		1184	$100S_{6b}$
		483	$62S_{8b} + 38S_{7b}$
		93	$53S_{7b} + 47S_{8b}$

The percentage contributions of the symmetry coordinates among the vibrational modes for the PH_3.HCl complex are collected in Table 7.68.

Table 7.68 Wavenumbers and %PEDs in the PH_3.HCl Complex

Complex	Symmetry Species	Wavenumbers /cm^{-1}	%PED
PH_3.HCl	a_1	2983	$100S_1$
		2550	$100S_2$
		1078	$100S_3$
		95	$100S_4$
	e_a	2567	$100S_{5a}$
		1181	$100S_{6a}$
		401	$22S_{7a} + 77S_{8a}$
		117	$62S_{7a} + 38S_{8a}$
	e_b	2567	$100S_{9b}$
		1181	$100S_{10b}$
		401	$76S_{12b} + 23S_{11b}$
		117	$61S_{11b} + 39S_{12b}$

The symmetry coordinate distributions amongst the different vibrational modes follow the same trend as in the HF complex. The intermolecular rocking mode of PH_3 has 22% contribution from the librational mode, as in the case of the HF complex. The librational modes in the HCl complex occur at magnitudes lower than those in the HF complex, suggesting a lower degree of rigidity in the complex, as one would expect based on the hydrogen bond strengths of the HF and HCl complexes. The changes in the intensities of

the various vibrational modes on complexation are reported in Table 7.69.

Table 7.69 The Ratios of the Complex to Monomer Intensity values for the PH_3.HF Complex

Symmetry Species	Mode	Complex A_c/km mol^{-1}	A_c/A_m
a_1	ν_1	510.7	6.25
	ν_2	27.4	0.67
	ν_3	38.6	1.19
e	ν_5	62.8	0.63
	ν_6	17.9	0.91

The intensity of the ν_1 mode increases by a factor of 6.25 on complexation, as also observed by Kurnig et al.[259] In the case of the phosphine stretching vibrational modes, the intensities have been reduced on complexation. The lowering occurs since the phosphorus atom carries a positive atomic charge and the HF withdraws negative charge from the hydrogen atoms of phosphine on complexation, thereby reducing the dipole moment of the phosphine molecule, which on executing the stretching vibrational mode results in a reduction of the intensities of the stretching bands. The antisymmetric bending mode also suffers an intensity decrease and the symmetric counterpart an increase. The ratios of the complex to monomer intensities in the PH_3.HCl complex are reported in Table 7.70.

Table 7.70 The Ratios of the Complex to Monomer Intensities for the PH_3.HCl Complex

Symmetry Species	Mode	Complex A_c/km mol^{-1}	A_c/A_m
a_1	ν_1	402.6	17.97
	ν_2	37.7	0.92
	ν_3	53.8	1.66
e	ν_5	67.2	0.68
	ν_6	15.5	0.78

The HCl stretching mode is enhanced by 17.97 times that of the monomer value on complexation, with the proton acceptor stretching modes being reduced in intensity as in the case of the PH_3.HF complex. The symmetric bending mode intensity in the proton acceptor is enhanced on complexation similar to the case of the PH_3.HF complex. The ν_1 is enhanced to a larger degree than in the PH_3.HF complex, since it accepts a greater amount of negative charge, as seen in Table 7.61, therefore increasing the magnitude of the dipole moment in the HCl molecule in the complex, which on executing the stretching vibrational mode results in a greater enhancement of the intensity in the HCl stretching mode.

7.6 *The CH_4.HX Complexes (X= F,Cl)*

7.6.1 *Geometries*

For this series of complexes a number of starting geometrical models were optimized, with the HF molecule approaching an apex, an edge and a face of the CH_4 tetrahedron, both through the hydrogen and the fluorine atom. A total of six stationary points were located on the PES through optimization as shown in fig 7.16. In structures III and V, hydrogen fluoride is the proton donor to the carbon of the methane molecule, acting perpendicularly to an edge and a face of the tetrahedron respectively, while in structure VI the methane is the proton donor to the HF molecule, with the HF oriented towards the apex of the tetrahedron. On relaxing the constraint that HF should be parallel to a C_3 or C_2 axis of the methane tetrahedron, three further stable structures were produced, two derived from VI, in which the proton of HF approached the carbon atom in either a staggered (I) or eclipsed (II) configuration with respect to the hydrogen atoms of methane, and one derived from III in which the fluorine atom interacts weakly with one of the in-plane methane hydrogen atoms (IV). Structure I was found to be the minimum energy species. In the case of the CH_4.HCl complex, three structures were optimized as shown in fig 7.17, one having a C..H interaction with C_{3v} and C_{2v} symmetry whilst the third structure had an H..Cl interaction. Structure I was found to be the most stable. The changes in the geometrical parameters on complexation of the most stable CH_4.HF complex are collected in Table 7.71.

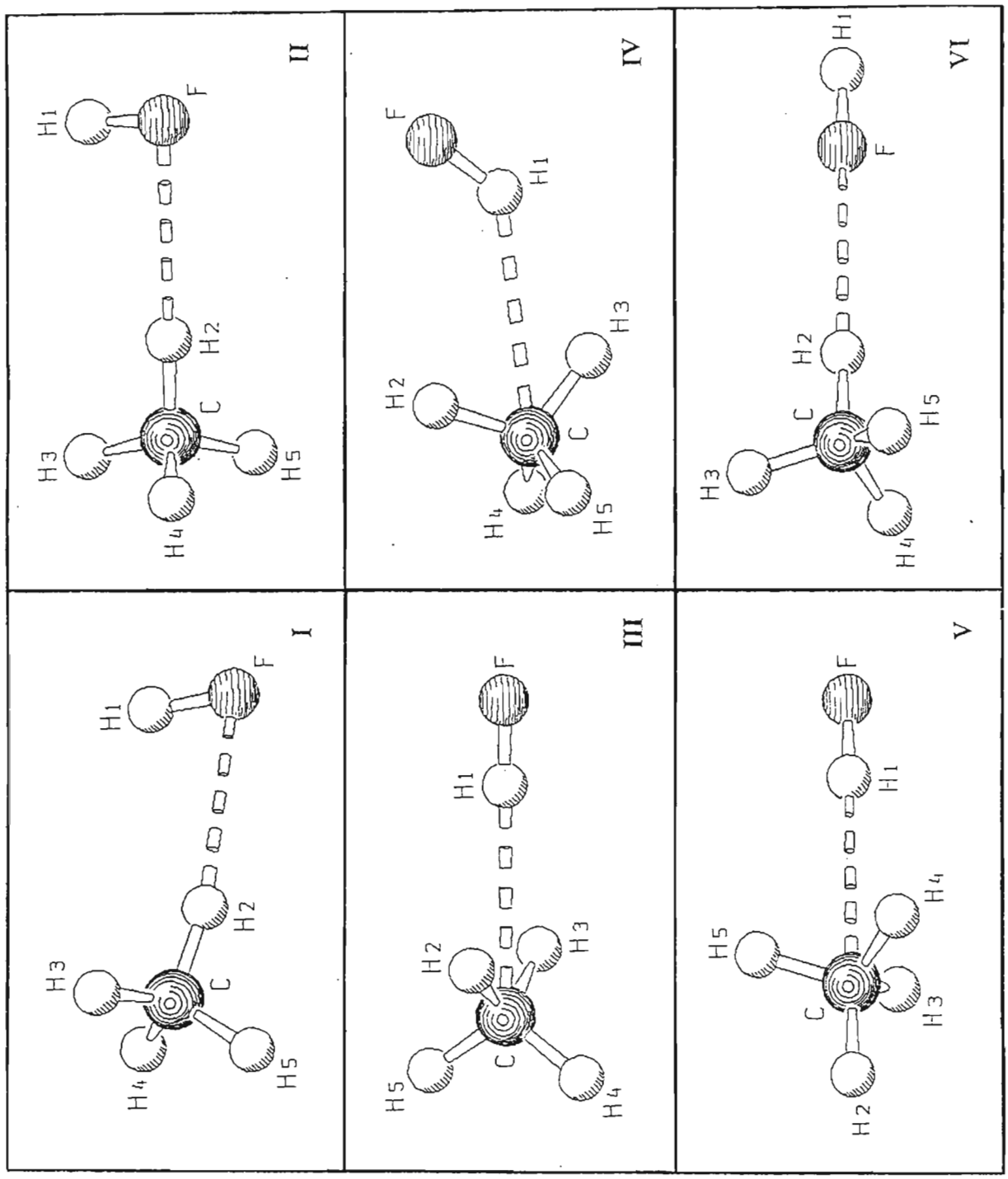

Fig 7.16 The Local Minimum Energy Structures for the CH_4.HF Complexes

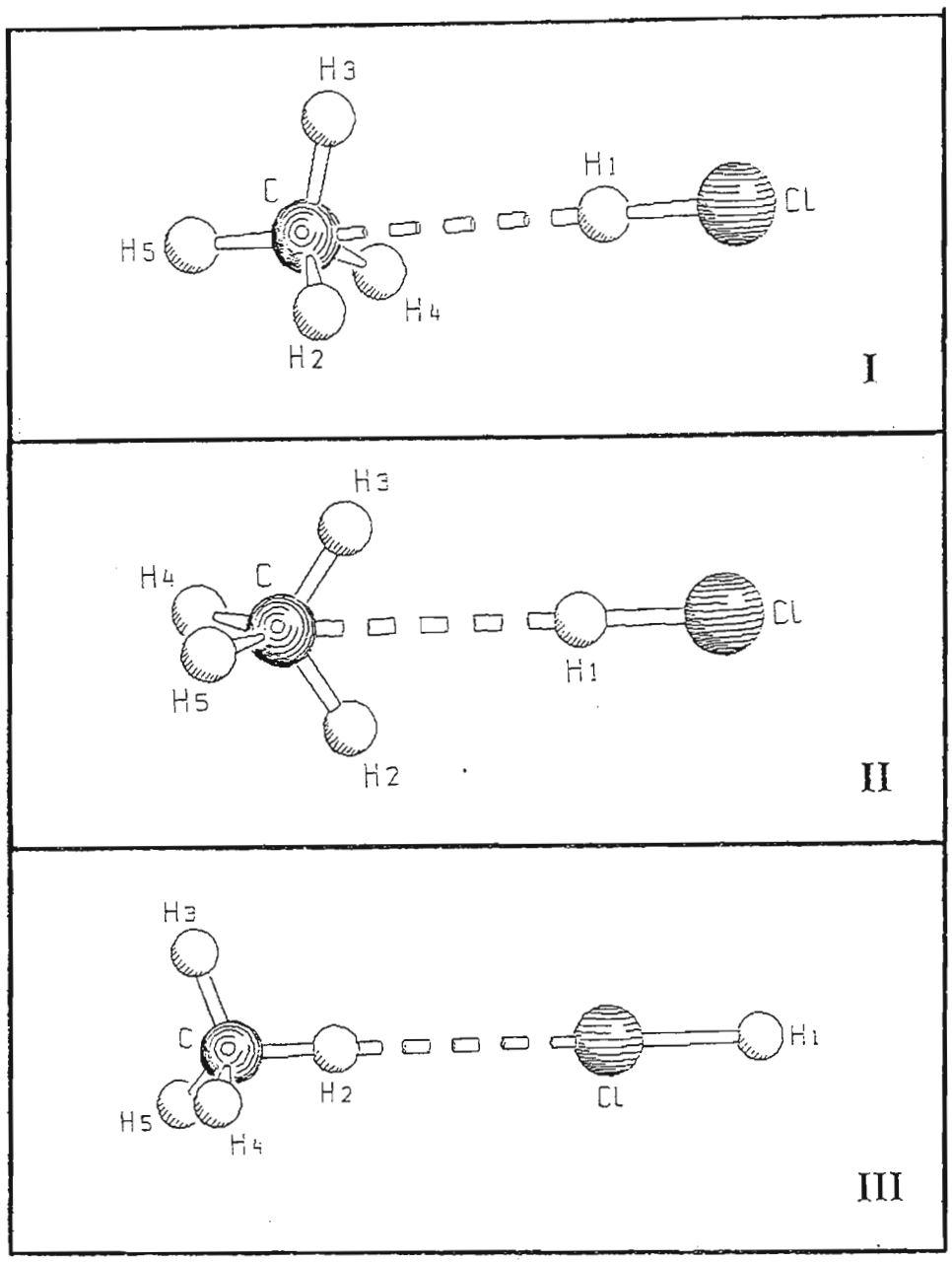

Fig 7.17 The Local Minimum Energy Structures for the CH_4.HCl Complexes

I – face-bonded; II – edge-bonded; III – apex-bonded

Table 7.71 Geometrical Parameters for the Most Stable CH_4.HF Complex

Complex	Parameter	Complex	Monomer	Difference
CH_4.HF	r(H1F)/pm	92.3	92.1	0.2
	r(CH2)/pm	108.5	108.4	0.1
	R(C..H1)/pm	336.3		
	R(H..F)/pm	241.5		
	r(CH3), r(CH4), r(CH5)/pm	108.5	108.4	0.1
	H2..FH1/deg	100.8		
	CH2..F/deg	169.2		

The changes in the geometrical parameters on complexation are marginal in that the monomers still retain their basic geometrical structures. This is typical of weak van der Waals type complexes. Our calculated values compare well with the values calculated by Legon et al[263] and those of Davis and Andrews.[266,268] The H..F separation agrees almost exactly with Legon's while our calculated C..H distance is only marginally shorter. Calculations by Davis and Andrews[266] report a H..F distance of 258.7 pm, which is significantly larger than our calculated value, likewise their HF..H angle of 83.4° is substantially smaller than ours. The geometrical parameters for the most stable CH_4.HCl complex are collected in Table 7.72.

Table 7.72 Geometrical Parameters for the Most Stable CH_4.HCl Complex

Complex	Parameter	Complex	Monomer	Difference
CH_4.HCl	r(H1Cl)/pm	127.0	126.9	0.2
	r(CH2)/pm	108.6	108.4	0.1
	R(C..H1)/pm	264.1		
	r(CH3), r(CH4), r(CH5)/pm	108.5	108.5	0.0
	C..HCl/deg	180.0		
	H3CH4, H4CH5, H5CH3/deg	109.9	109.5	0.4

The major changes occurring in the geometrical parameters are in the HCl bond length by 0.2 pm and methane internal bond angles by 0.4°. On optimizing all the geometrical parameters structure I was still found to be the minimum, with a linear C..HCl bond angle as in the case of a conventional hydrogen bonded complex. Our finding that the complex has C_{3v} symmetry is consistent with the gas-phase results of Legon et al[263] and Oshima and Endo.[264] Our calculated C..Cl separation of 391.1 pm was found to be very close to the experimentally determined values of 393.76 pm by Legon and 393.71 pm by Oshima and Endo. The C..H distance of 264.1 pm was also found to be close to the experimental value of 265 pm obtained by Oshima and Endo. Our calculated structure for the CH_4.HCl complex having C_{3v} symmetry is contrary to the results of Craw et al.[269] The main difference in the complexes of the HF and HCl complexes with methane lie in the electronegativity of the halogen atom. HF is a better proton donor than HCl, thus resulting in a closer C..F distance, hence favouring a secondary interaction.

7.6.2 *Energetics*

The computed interaction energies, BSSEs and the percentage dispersion energy contributions for the most probable CH_4.HX complexes are collected in Table 7.73.

Table 7.73 The Binding Energies of the Most Stable CH_4.HX Complexes

Complex	$\Delta E'$ /kJ mol^{-1}	ΔE /kJ mol^{-1}	BSSE /kJ mol^{-1}	$\%\Delta E_{Disp}$
CH_4.HF	-3.1	-8.7	5.6	74.8
CH_4.HCl	-4.6	-3.7	-1.9	82.1

From Table 7.73, the CH_4.HF complex is more strongly bound than the HCl complex; this is because the HF molecule has two sites of interaction in the methane complex whilst the HCl complex has just one site of interaction. Our uncorrected binding energy for the CH_4.HF complex is very close to that of Legon et al[263] of 8.8 kJ mol^{-1} but the corrected and uncorrected values for the CH_4.HCl complex differ from that of Craw et al[269] being -4.5 and -3.4 kJ mol^{-1}, mainly due to the use of different basis sets. The percentage dispersion contribution to the binding energy is greater in the HCl complex than in the HF complex by 7.3%.

The contributions to the total interaction energies via the Morokuma decomposition analysis are collected in Table 7.74.

The charge transfer term dominates the attractive forces in the CH_4.HF complex, while in the CH_4.HCl complex the electrostatic term is the major attractive term. The exchange repulsion term is larger in the HF than in the HCl complex and offsets the attractive energy terms by about 5 kJ mol^{-1}. The polarisation term is larger for the more polarisable HCl-containing complex.

Table 7.74 Energy Decomposition Analysis of the CH_4.HX Complexes /kJ mol^{-1}

Complex	ES	EX	CT	PL	MIX	Total
CH_4.HF	-2.4	5.3	-6.3	-0.2	-0.3	-3.9
CH_4.HCl	-3.3	5.0	-1.9	-0.7	0.3	-0.6

The mixing term due to the effects of higher multipole moments is attractive for CH_4.HF but repulsive for CH_4.HCl complex.

7.6.4 *Mulliken Charge Analysis*

The Mulliken charge analyses in the CH_4.HF and CH_4.HCl complexes are reported in Tables 7.75 and 7.76 respectively.

The CH_4 molecule accepts negative charge (-0.016 e) from the HF molecule, of which most of the charge originates from the proton of HF. The changes in the charges in the protons of methane are relatively slight compared with H1. The fluorine and the carbon both become more negative on complexation, accounting for the secondary interaction. The net charge transfer from HF to CH_4 is -0.016 e which compares well with the estimate of -0.01 e obtained by Davis and Andrews.[266]

Table 7.75 Mulliken Charge Analysis for the Most Stable CH_4.HF Complex

Atom	Atomic Charge /e		Difference /e
	Complex	Monomer	
H1	0.400	0.192	0.208
F	-0.384	-0.192	-0.192
			0.016
C	-0.492	-0.473	-0.019
H2	0.127	0.118	0.019
H3	0.123	0.118	0.005
H4, H5	0:114	0.118	-0.008
			-0.016

In the CH_4.HCl complex the HCl gains negative charge from the methane molecule of -0.006 e; this charge has most of its origin at the H2 atom of methane. The net charge transfer from the methane to the HCl, -0.006 e, is about one third of that in the CH_4.HF complex, despite the CH_4.HF complex having a secondary interaction.

Table 7.76 Mulliken Charge Analysis for the Most Stable CH_4.HCl Complex

Atom	Atomic Charge /e		Difference /e
	Complex	Monomer	
H1	0.181	0.192	-0.011
Cl	-0.187	-0.192	0.005
			-0.006
C	-0.499	-0.473	-0.026
H2	0.136	0.118	0.018
H3, H4, H5	0.123	0.118	0.015
			0.006

7.6.4 *Vibrational Properties of the Most Stable CH_4.HX Complexes*

The calculated vibrational spectra, potential energy distributions and infrared intensities at the MP2/6-31G** level for the CH_4.HX complexes are shown in Tables 7.77 - 7.84. The plots of the normal modes of vibrations for the CH_4.HX complexes are depicted in figs 7.18 and 7.19. The calculated vibrational spectrum for the CH_4.HF complex is reported in Table 7.77.

Table 7.77 Calculated Wavenumber Shifts in the Most Stable CH_4.HF Complex

Symmetry Species	Mode	Complex Wavenumber /cm^{-1}	Monomer Wavenumber /cm^{-1}	Shift[(a)] /cm^{-1}
a'	ν_1	4175	4197	-22
	ν_2	3299	3289	10
	ν_3	3275	3289	-14
	ν_4	3134	3143	-9
	ν_5	1633	1623	10
	ν_6	1417	1402	15
	ν_7	1404	1402	2
a"	ν_{11}	3273	3289	-16
	ν_{12}	1632	1623	9
	ν_{13}	1415	1402	13

(a) Complex - Monomer

The ν_1 mode undergoes a red shift of 22 cm^{-1} on complexation, consistent with the formation of a weak hydrogen bond. This calculated shift compares with -23 cm^{-1} observed for CH_4.HF by Andrews and Davis.[266] The CH_4 stretching modes ν_3, ν_4 and ν_{11} also undergo red shifts on complexation, while the remaining intramolecular modes are all blue shifted. Davis and Andrews[266] reported absorptions at 130 and 165 cm^{-1} assigned to the HF librational modes in an argon matrix. The agreement between our results and those of the experimental librational modes is remarkable. The calculated vibrational

spectrum of the CH_4.HCl complex is collected in Table 7.78.

Table 7.78 Calculated Wavenumber Shifts in the Most Stable CH_4.HCl Complex

Symmetry Species	Mode	Complex Wavenumber /cm^{-1}	Monomer Wavenumber /cm^{-1}	Shift[(a)] /cm^{-1}
a_1	ν_1	3277	3289	-12
	ν_2	3127	3143	-16
	ν_3	3112	3128	-16
	ν_4	1400	1402	-2
	ν_5	74		
e	ν_6	3270	3289	-19
	ν_7	1624	1623	1
	ν_8	1407	1402	5
	ν_9	124		
	ν_{10}	78		

(a) Complex - Monomer

The ν_3 mode is red shifted by 16 cm^{-1}, identical to the shift observed by Barnes et al[265] in an argon matrix. The CH stretching modes all show red shifts in the 10 - 20 cm^{-1} region. The bending mode shifts from the monomer band positions of methane are negligible and of the order of 1 - 5 cm^{-1}, showing the bending modes in the methane tetrahedron to be insensitive to hydrogen bonding, at least in complexes with such low

interaction energies. The hydrogen bond stretching mode occurs at 74 cm^{-1}, significantly lower than that in the CH_4.HF complex, even though the CH_4.HF complex has two interaction sites. The degenerate hydrogen bond bending mode occurs at 124 cm^{-1}. The symmetry coordinate descriptions for the CH_4.HF complex are collected in Table 7.79. The symmetry coordinates for the intramolecular modes were derived from those of the monomers with slight modifications. The symmetry of the methane molecule on complexation is reduced from T_d to C_s, however on examining the geometrical parameters the C_3 axis of the methane molecule was found to be only slightly perturbed, hence the symmetry coordinates used in the description of the CH_4 intramolecular modes were close to that of a molecule with C_{3v} symmetry. The intermolecular modes were less easy to describe due to the ring-like structure of the complex.

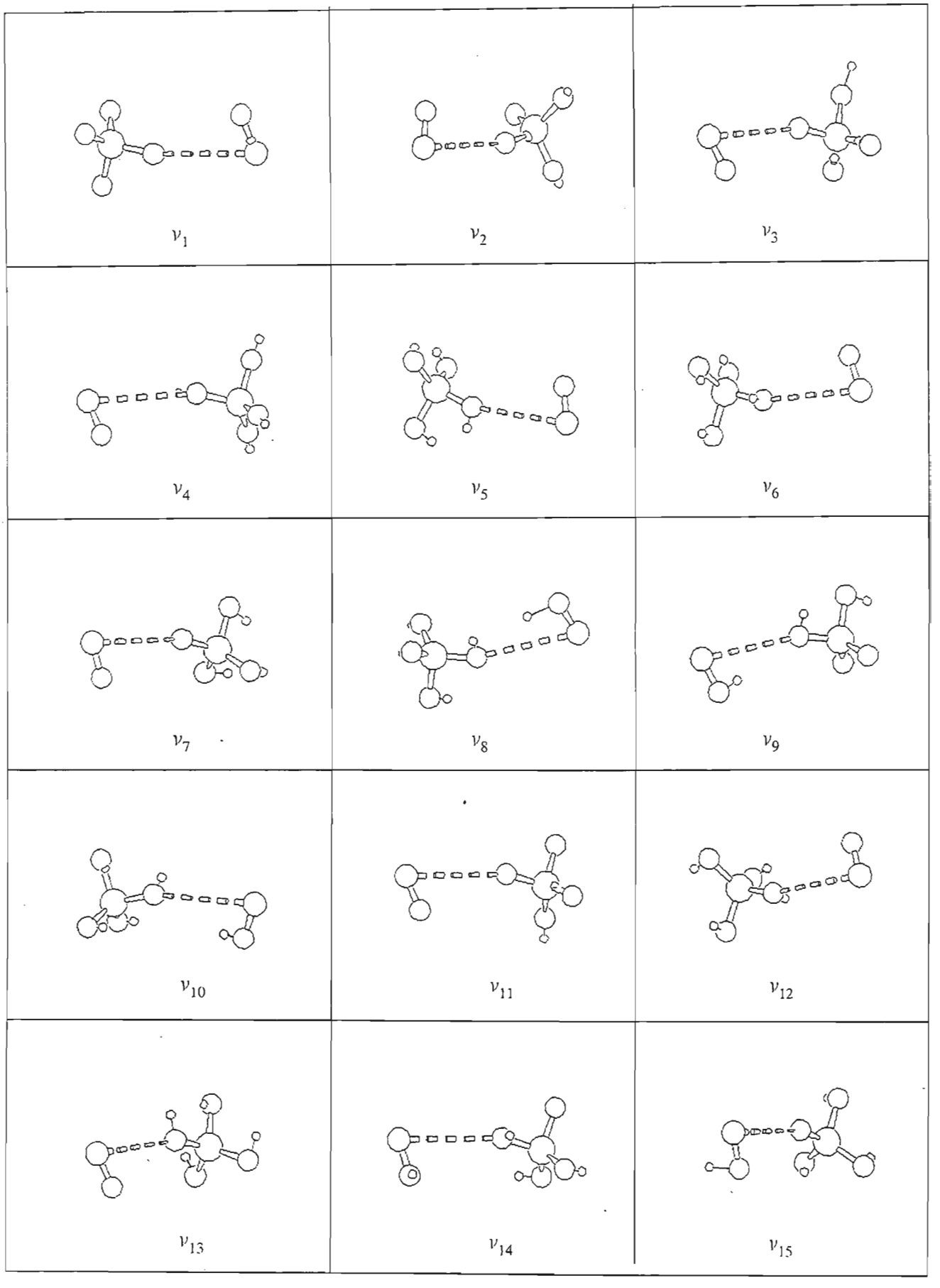

Fig 7.18 Graphical Representation of the CH_4.HF Complex Vibration modes

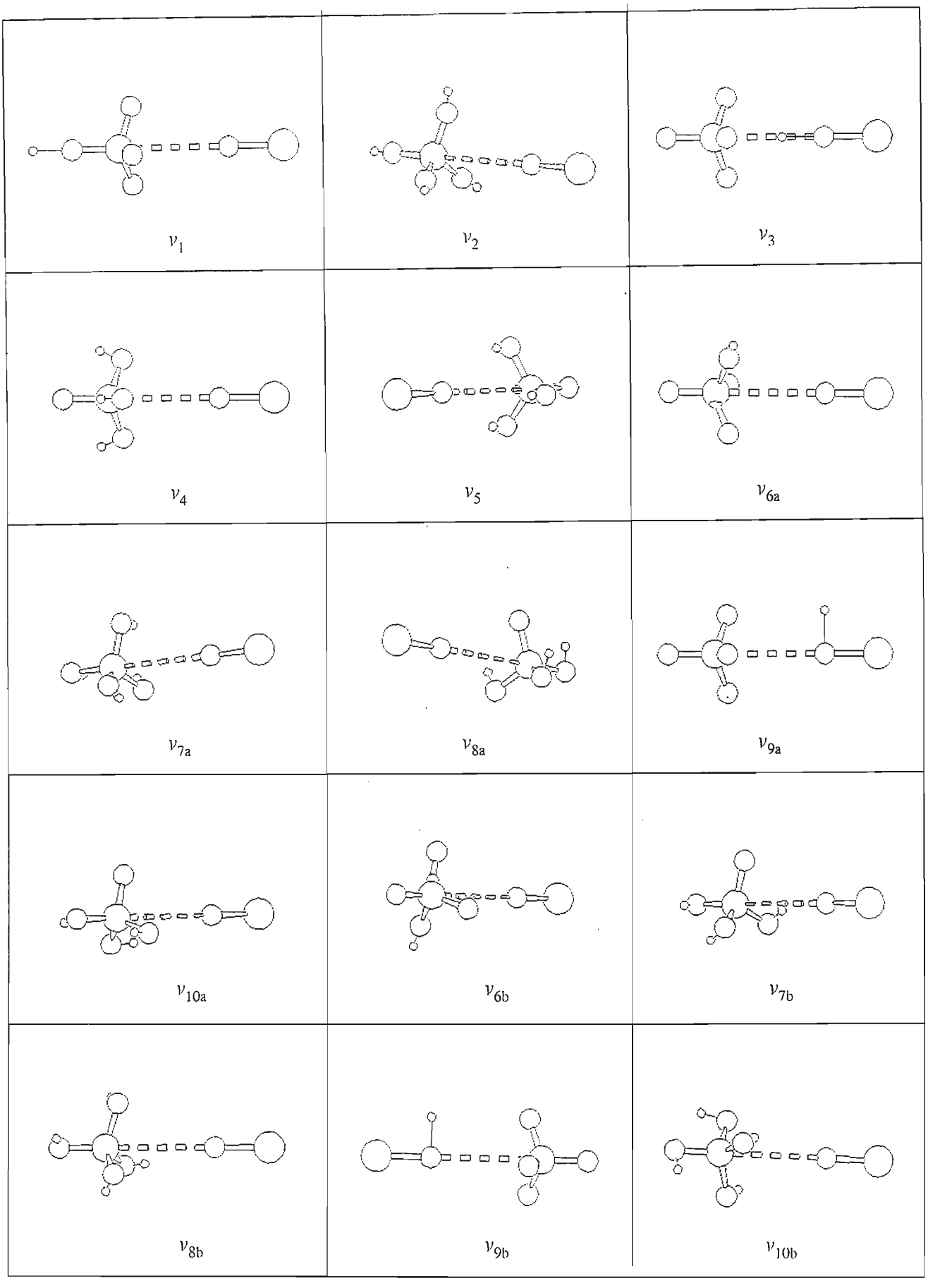

Fig 7.19 Graphical Representation of the CH_4.HCl Complex Vibration modes

Table 7.79 Symmetry Coordinates for the CH_4.HF Complex

Complex	Symmetry Coordinate	Description
CH_4.HF	$S_1 = \Delta r_1$	HF stretch
	$S_2 = \Delta r_2$	CH stretch
	$S_3 = 1/\sqrt{3}(\Delta r_3 + \Delta r_4 + \Delta r_5)$	CH_3 symmetric stretch
	$S_4 = 1/\sqrt{6}(2\Delta r_3 - \Delta r_4 - \Delta r_5)$	CH_3 antisymmetric stretch
	$S_5 = 1/\sqrt{6}(2\Delta\alpha_1 - \Delta\alpha_2 - \Delta\alpha_3)$	CH_3 antisymmetric bend
	$S_6 = 1/\sqrt{6}(2\Delta\beta_1 - \Delta\beta_2 - \Delta\beta_3)$	CH_3 antisymmetric bend
	$S_7 = 1/\sqrt{6}(\Delta\alpha_1 + \Delta\alpha_2 + \Delta\alpha_3 - \Delta\beta_1 - \Delta\beta_2 - \Delta\beta_3)$	CH_4 symmetric bend
	$S_8 = \Delta R$	H..F stretch
	$S_9 = \Delta\theta$	CH..F bend
	$S_{10} = \Delta\pi_1$	H..HF in plane bend
	$S_{11} = 1/\sqrt{2}(\Delta r_4 - \Delta r_5)$	CH_2 antisymmetric stretch
	$S_{12} = 1/\sqrt{2}(\Delta\alpha_2 - \Delta\alpha_3)$	CH_2 antisymmetric bend
	$S_{13} = 1/\sqrt{2}(\Delta\beta_2 - \Delta\beta_3)$	CH_2 antisymmetric bend
	$S_{14} = \Delta\pi_2$	H..HF out of plane bend

The symmetry coordinate distributions amongst the various vibrational modes are collected in Table 7.80 for the CH_4.HF complex.

Table 7.80 Wavenumbers and %PEDs in the CH_4.HF Complex

Complex	Symmetry Species	Wavenumber /cm^{-1}	%PED
CH_4.HF	a'	4175	$100S_1$
		3299	$80S_2 + 20S_3$
		3275	$100S_4$
		3134	$80S_3 + 20S_2$
		1633	$45S_5 + 54S_6$
		1417	$55S_5 + 44S_6$
		1404	$100S_7$
		242	$77S_9 + 17S_{10} + 5S_6$
		144	$36S_8 + 29S_9 + 37S_{10}$
		109	$50S_8 + 41S_{10} + 8S_9$
	a"	3272	$100S_{11}$
		1632	$53S_{12} + 47S_{13}$
		1415	$48S_{12} + 54S_{13}$
		152	$100S_{14}$
		14	

The HF stretching mode is unperturbed on complexation with the methane molecule since it has no contribution from the other symmetry coordinates of the complex. The ν_2 mode

has a contribution from ν_3. This occurs mostly likely due to the charge gained from the HF molecule on complexation being redistributed in the methane molecule. As in the case of the methane stretching modes, the bending modes also have contributions from the axial and equatorial methane bond angle bends, however the symmetric bending mode of the methane molecule is still unperturbed on complexation. The antisymmetric stretching mode, ν_{11}, is also unperturbed on complexation, as in the case of ν_3. The a" bending modes exhibit the same trend as the a' bending modes on complexation. We have managed to provide a reasonable description for the symmetry coordinates of the intermolecular modes, of which all have contributions from other symmetry coordinates as well. The ν_8 mode has contributions from both the H..FH bending mode and the CH..F in-plane bending modes. The out of plane bending mode at 152 cm^{-1} has no contribution from the other symmetry coordinates. The remaining intermolecular modes have a spread of symmetry coordinate contributions except for ν_{15}, which our set of symmetry coordinates could not reproduce. The symmetry coordinates used in the description of the CH_4.HCl complex are shown in Table 7.81.

The symmetry coordinates for the CH_4.HCl complex were generated using the parent monomer symmetry coordinates since in the case of the methane molecule there was little change in the geometrical parameters on complexation. For the intermolecular symmetry coordinates, viz., the hydrogen bond stretch, the hydrogen bond bending mode and the rocking motion of the CH_3 group, symmetry coordinates were defined according to the rules of Wilson et al.[70]

Table 7.81 Symmetry Coordinates for the CH_4.HCl Complex

Complex	Symmetry Coordinate	Description
CH_4.HCl	$S_1 = \Delta r_1$	CH stretch
	$S_2 = 1/\sqrt{3}(\Delta r_2 + \Delta r_3 + \Delta r_4)$	CH_3 symmetric stretch
	$S_3 = \Delta r_5$	HCl stretch
	$S_4 = \Delta R$	C..H stretch
	$S_5 = 1/\sqrt{6}(\Delta\alpha_1 + \Delta\alpha_2 + \Delta\alpha_3 - \Delta\beta_1 - \Delta\beta_2 - \Delta\beta_3)$	CH_3 symmetric bend
	$S_{6a} = 1/\sqrt{6}(2\Delta r_2 - \Delta r_3 - \Delta r_4)$	CH_2 antisymmetric bend
	$S_{7a} = 1/\sqrt{6}(2\Delta\alpha_1 - \Delta\alpha_2 - \Delta\alpha_3)$	CH_2 twist
	$S_{8a} = 1/\sqrt{6}(2\Delta\beta_1 - \Delta\beta_2 - \Delta\beta_3)$	CH_2 twist
	$S_{9a} = \Delta\pi_1$	C..HCl in plane bend
	$S_{10a} = \Delta\rho_1$	CH_3 rock
	$S_{6b} = 1/\sqrt{2}(\Delta r_3 - \Delta r_4)$	CH_3 antisymmetric stretch
	$S_{7b} = 1/\sqrt{2}(\Delta\alpha_2 - \Delta\alpha_3)$	CH_3 antisymmetric bend
	$S_{8b} = 1/\sqrt{2}(\Delta\beta_2 - \Delta\beta_3)$	CH_3 antisymmetric bend
	$S_{9b} = \Delta\pi_2$	C..HCl out of plane bend
	$S_{10b} = \Delta\rho_2$	CH_3 rock

The symmetry coordinate distributions amongst the different vibrational species are shown in Table 7.82.

Table 7.82 Wavenumbers and %PEDs in the CH_4.HCl Complex

Complex	Symmetry Species	Wavenumber /cm^{-1}	%PED
CH_4.HCl	a_1	3277	$78S_1 + 22S_2$
		3126	$75S_2 + 20S_1$
		3111	$94S_3 + 5S_2$
		1400	$100S_5$
		74	$99S_4$
	e_a	3270	$100S_{6a}$
		1624	$100S_{7a}$
		1407	$100S_{8a}$
		124	$63S_{10a} + 26S_{9a}$
		76	$89S_{9a} + 10S_{7a}$
	e_b	3270	$100S_{6b}$
		1624	$100S_{7b}$
		1407	$100S_{8b}$
		124	$63S_{10b} + 26S_{9b}$
		76	$89S_{9b} + 10S_{7b}$

In the case of the a_1 symmetry species, the HCl stretching mode has minor contribution from the CH_3 stretching mode. In the case of the methane molecule, the ν_1 mode has a

22% contribution from S_2. This occurs since on complexation, there is charge donation from the methane molecule to the HCl thus affecting the force constants of the CH bonds and hence the vibrational modes. The a_1 bending mode is unperturbed on complexation and has 100% PED from the symmetry coordinate describing the "breathing" motion of the methane molecule. The hydrogen bond stretching mode has a 99% PED from the S_5 symmetry coordinate. The degenerate intramolecular modes are also unperturbed on complexation, but the intermolecular modes show contributions from the other symmetry coordinates in their subgroup; this is expected since the complex is fairly weakly bound and the librational motion involves the rocking of the methane coupled with the bending mode of the C..HCl hydrogen bond angle.

The intensity changes on complexation of the CH_4.HF complex are collected in Table 7.83. The HF stretching intensity remains almost unchanged from the monomer value, the CH stretching intensities corresponding to the f_2 monomer vibration consistently decrease, except for that of ν_{11}, where an increase takes place. The complex bending vibrations related to the f_2 monomer mode undergo practically no change of intensity. In the a' species the ν_6 and ν_7 intensities decrease while the intensity of the ν_{13} mode experiences a minor increase, thus in these two cases the pattern of the intensity profile on hydrogen bond formation is well ordered.

Table 7.83 The Ratios of the Complex to Monomer Intensity values for the CH_4.HF Complex

Symmetry Species	Mode	Complex A_c/km mol^{-1}	A_c/A_m
a'	ν_1	79.7	0.97
	ν_2	4.1	0.19
	ν_3	20.3	0.96
	ν_4	3.1	-
	ν_5	0.06	-
	ν_6	9.4	0.80
	ν_7	11.5	0.98
a"	ν_{11}	24.3	1.14
	ν_{12}	0.0	-
	ν_{13}	11.9	1.02

The intensity changes on complexation in the CH_4.HCl complex are collected in Table 7.84. The HCl stretching vibration intensity increases by a factor of 3.3 as expected in a hydrogen bonded complex. The intensities of the CH stretching bands correlating with the f_2 monomer mode decrease consistently. The CH bending mode intensities derived from the f_2 mode increase on complexation.

Table 7.84 The Ratios of the Complex to Monomer Intensity values for the CH_4.HCl Complex

Symmetry Species	Mode	Complex A_c/km mol^{-1}	A_c/A_m
a_1	ν_1	18.0	0.85
	ν_2	0.4	-
	ν_3	73.3	3.27
	ν_4	22.7	1.94
	ν_5	0.3	-
e	ν_6	16.8	0.79
	ν_7	0.4	-
	ν_8	13.4	1.14

7.7. *The SiH_4.HX Complexes (X= F,Cl)*

7.7.1 *Geometries*

In the case of the SiH_4.HF complex, six stationary point structures were optimized as shown in fig 7.20. The prediction of the tendency of silicon to form penta-coordinate species by re-hybridization from sp^3 to dsp^3 would result in the HF interacting with SiH_4 at the face of the tetrahedron along the C_3 axis, thus distorting the tetrahedral structure of the silane molecule. On relaxing the symmetry conditions we optimized structure II having C_s symmetry, where the proton of HF approached either the two out of plane hydrogen atoms in the silane or closer to the two in plane hydrogens as in structure I. This structure was found to be the most probable structure with no negative eigenvalues and with the lowest binding energy. The other structures optimized for this complex include one in which the HF molecule approaching the C_2 axis of SiH_4 (V) or in which the H..H interaction is the dominant one (IV and VI). These are significantly higher in energy. Structure I has an Si..F interaction coupled with a secondary H..H interaction. Our optimized geometry agrees with that of Andrews and Davis[267] who had initially proposed structure VI to be the minimum energy complex, but later revised their interpretation of this geometry to propose a complex with geometry similar to structure I. In the case of the SiH_4.HCl complex no previous data were available. Our calculated structures (fig 7.21) comprise three stationary points; two of C_{3v} symmetry having a H..H and a Si..Cl interaction, and one of C_{2v} symmetry also involving the Si..Cl attraction. Allowing the intermolecular bonds to deviate did not result in any further structures of lower energy. The structure involving a single attraction of the hydrogen of silane to the hydrogen of HCl was found to be the most favourable. The geometrical parameters of the SiH_4.HF complex are collected in Table 7.85.

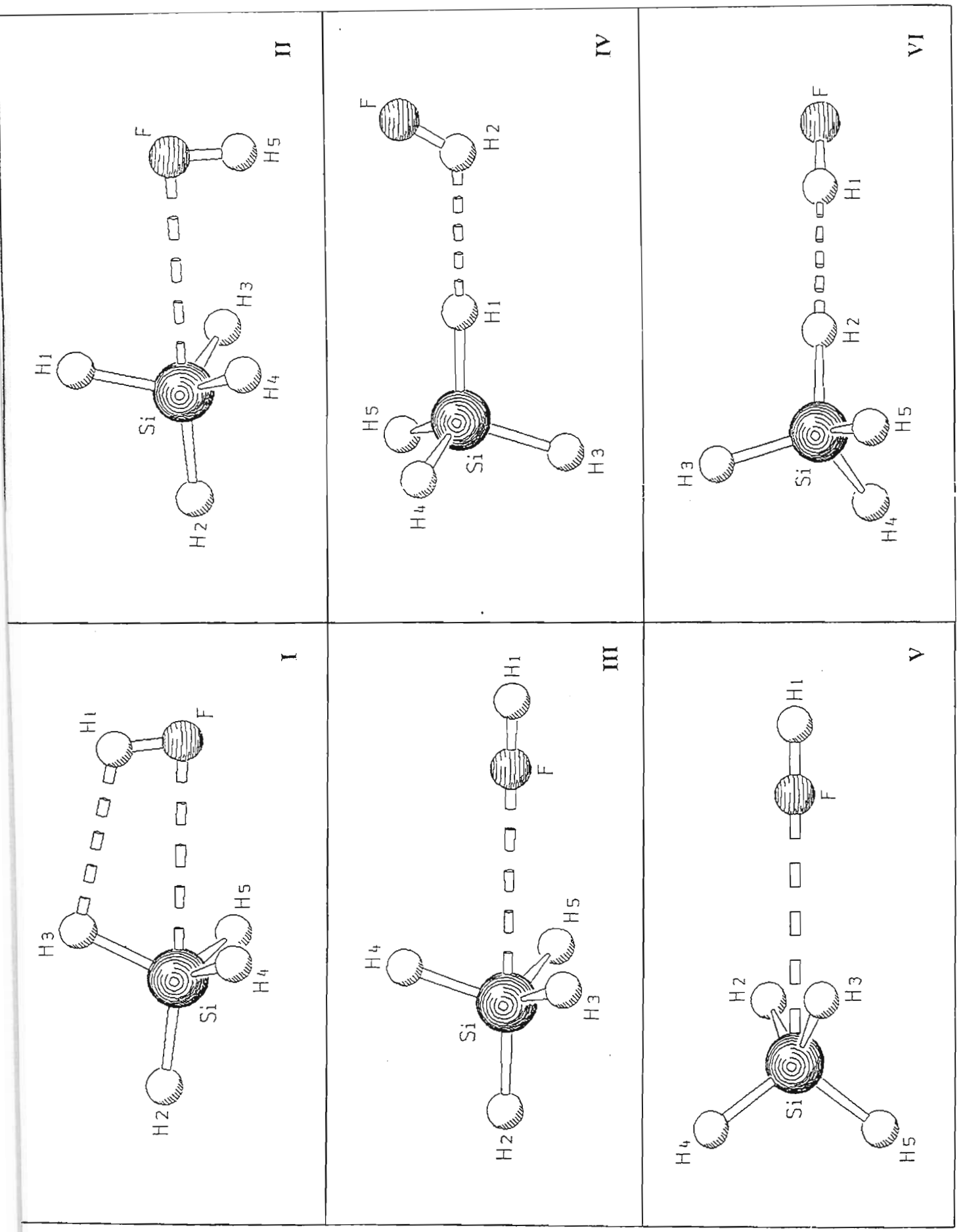

Fig 7.20 The Local Minimum Energy Structures for the SiH_4.HF Complexes

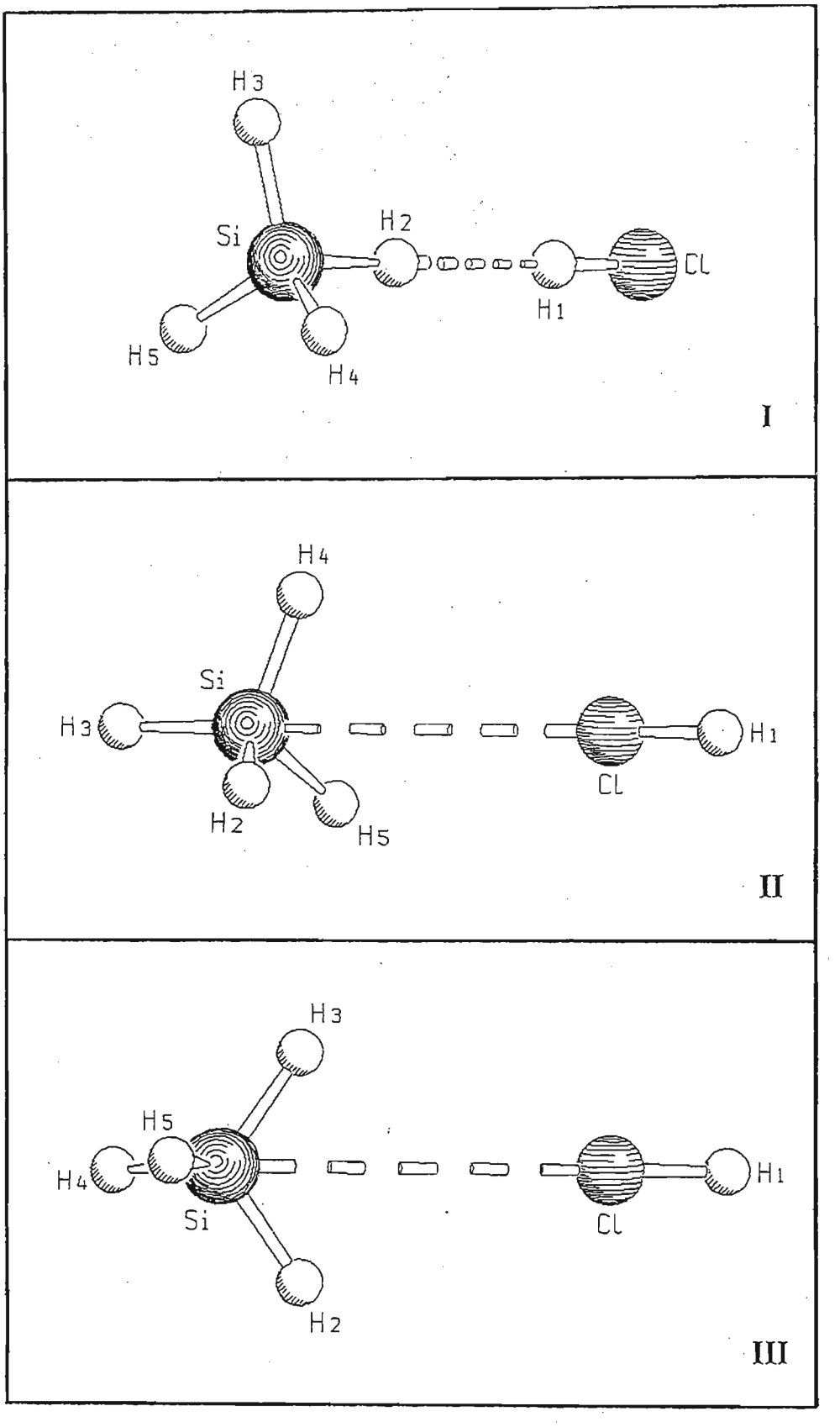

Fig 7.21 The Local Minimum Energy Structures for the $SiH_4.HCl$ Complexes

I – apex-bonded; II – face-bonded; III – edge-bonded

Table 7.85 Geometrical Parameters for the Most Stable SiH_4.HF Complex

Complex	Parameter	Complex	Monomer	Difference
SiH_4.HF	r(H1F)/pm	92.3	92.1	0.2
	R(Si..F)/pm	322.9		
	R(H1..H3)/pm	253.1		
	r(SiH2)/pm	147.7	147.4	0.3
	r(SiH4), r(SiH5)/pm	147.1	147.4	-0.3
	r(SiH3)/pm	147.5	147.4	0.1
	H1F..Si/deg	82.4		
	H3Si..F/deg	65.6		
	H2SiH3/deg	108.1	109.5	-1.4
	H4SiH5/deg	110.6	109.5	1.1
	H2SiH4, H2SiH5/deg	109.4	109.5	-0.1
	H3SiH4, H3SiH5/deg	109.6	109.5	0.1

The major changes occurring in the geometrical parameters on complexation are in the silane bond angles. The bond angles are perturbed due to the close proximity of the hydrogen atom of HF with those of the silane molecule. The bond lengths are not perturbed as much from the monomer values on complexation. Our estimate of the H..H distance was found to be shorter than the estimate of Davis and Andrews[267] of 274.3 pm. On considering the covalent HF bond lengths and those of the SiH_4 bonds, the computed bond lengths are shorter than the sums of the covalent radii. In the case of the Si..F

interaction the interatomic separation exceeds the sum of the covalent radii by 133.9 pm, while for the H1..H3 interaction the difference is 179.1 pm. The greater deviation indicates that the H1..H3 interaction is relatively weaker than the Si..F interaction. The changes in the geometrical parameters in the SiH_4.HCl complex are similar to those in the SiH_4.HF complex. The geometrical parameters of the SiH_4.HCl complex are collected in Table 7.86.

Table 7.86 Geometrical Parameters for the Most Stable SiH_4.HCl Complex

Complex	Parameter	Complex	Monomer	Difference
SiH_4.HCl	r(H1Cl)/pm	127.1	126.9	0.2
	R(H1..H3)/pm	213.0		
	r(SiH2)/pm	147.7	147.4	0.3
	r(SiH3), r(SiH4), r(SiH5)/pm	147.2	147.4	-0.2
	SiH2..H1/deg	180.0°		
	H2..H1Cl/deg	180.0°		
	H2SiH3, H2SiH4, H2SiH5/deg	108.9	109.5°	-0.6°
	H3SiH4, H4SiH3, H3SiH5/deg	110.0	109.5°	0.5°

The changes occurring in the bond angles of both SiH_4.HX complexes could be attributed to the charge transfer from the HX to the SiH_4 molecule along the Si..F axis and along the SiH..H axis into the antibonding orbitals of the SiH2 in the SiH_4.HX complexes, thus

resulting in increases in their bond lengths as well. This charge density further exerts a repulsive force on the hydrogens of the silane molecule thus causing the bond angles to change.

7.7.2 *Energetics*

The computed interaction energies, BSSEs and the percentage dispersion energy contribution for the most probable SiH_4.HX complexes are collected in Table 7.87.

Table 7.87 The Binding Energies of the Most Stable SiH_4.HX Complexes

Complex	$\Delta E'$ /kJ mol^{-1}	ΔE /kJ mol^{-1}	BSSE /kJ mol^{-1}	$\%\Delta E_{Disp}$
SiH_4.HF	-0.1	-13.4	13.3	100.0
SiH_4.HCl	-2.2	-3.4	1.2	81.8

In the case of the SiH_4.HF complex the interaction energy is exaggerated by the BSSE, although the BSSE can be minimised by the use of extensive basis sets, as was noted by Del Bene et al.[71] The dispersion energy was found to play a larger role in the SiH_4.HF complex even though it has a Si..F interaction which one would expected to be due to charge transfer effects. The percentage dispersion contribution in the SiH_4.HX complexes are similar to those in the CH_4.HX complexes. The binding energies for these complexes are very low when compared with those of the strong hydrogen bonded complexes. The Morokuma energy decomposition analysis is collected in Table 7.88.

Table 7.88 Energy Decomposition Analyses of the SiH_4.HX Complexes /kJ mol^{-1}

Complex	ES	EX	CT	PL	MIX	Total
SiH_4.HF	-4.0	4.7	-7.0	-0.6	-0.9	-7.8
SiH_4.HCl	-3.5	5.3	-2.3	-1.0	0.5	-0.8

Of the attractive components of the decomposition analysis the charge transfer term is largest in the SiH_4.HF complex, while the electrostatic term dominates in the SiH_4.HCl complex. The charge transfer term is larger in the former complex since the silicon is directly bonded to the fluorine atom thus gaining electron density from the highly electronegative fluorine atom. The electrostatic term dominates in the SiH_4.HCl complex since the interaction involves a negative hydrogen atom of silane and a positive hydrogen atom of HCl. The polarisation term is larger in the HCl complex, since chlorine is more polarisable than fluorine. The exchange repulsion term partly offsets the net attractive term in each complex by about 5 kJ mol^{-1}. Once again the mixing term is attractive for the SiH_4.HF complex and repulsive for the SiH_4.HCl complex, as was seen in the methane complexes.

7.7.3 *Mulliken Charge Analysis*

The Mulliken charge analysis depicting the direction of negative charge donation in the SiH_4.HF complex is presented in Table 7.89.

The HF molecule donates negative charge to the silane through the silicon atom, and this negative charge further migrates to atom H3 of silane. The H3 atom also receives charge from the H1 atom of HF. The major source of charge donation occurs through the Si..F interaction from the fluorine to the silicon atom, as proposed by Davis and Andrews.[268]

Table 7.89 Mulliken Charge Analysis for the Most Stable SiH_4.HF Complex

Atom	Atomic Charge /e		Difference /e
	Complex	Monomer	
H1	0.401	0.397	0.004
F	-0.379	-0.397	0.018
			0.022
Si	0.685	0.667	0.018
H2	-0.174	-0.167	-0.007
H3	-0.209	-0.167	-0.042
H4, H5	-0.162	-0.167	0.010
			-0.022

In the case of the SiH_4.HCl complex we see a reverse trend in the migration of charge which is collected in Table 7.90.

The net charge donation in the case of the SiH_4.HCl complex is from the SiH_4 to the HCl molecule as in the CH_4.HCl complex. The H2 atom gains a large amount of negative charge (-0.052 e), of which most originates from the silane subunit.

Table 7.90 Mulliken Charge Analysis for the Most Stable SiH_4.HCl Complex

Atom	Atomic Charge /e		Difference /e
	Complex	Monomer	
H1	0.183	0.192	-0.009
Cl	-0.189	-0.192	0.002
			-0.007
Si	0.703	0.667	0.035
H2	-0.219	-0.167	-0.052
H3,H4,H5	-0.159	-0.167	0.024
			0.007

7.7.4 *Vibrational Properties of the Most Stable SiH_4.HX Complexes*

The calculated vibrational spectra, potential energy distributions and infrared intensities at the MP2/6-31G** level for the SiH_4.HX complexes are shown in the Tables 7.91 - 7.94. The plots of the normal modes of vibrations for the SiH_4.HX complexes are depicted in figs 7.22 and 7.23. The calculated vibrational spectrum for the SiH_4.HF complex is reported in Table 7.91.

The HF stretching mode is red shifted (30 cm^{-1}) on complexation, consistent with a weak hydrogen bond. This calculated shift corresponds with that observed by Davis and Andrews[266] at -65 cm^{-1}. The ν_4 mode, involving the SiH stretch, is shifted by -19 cm^{-1}. The ν_2 and ν_3 modes are blue and red-shifted by 6 and 14 cm^{-1} respectively. Davis and

Andrews report a single band for ν_3 shifted 51 cm^{-1} from the monomer position.

Table 7.91 Calculated Wavenumber Shifts in the Most Stable SiH_4.HF Complex

Symmetry Species	Mode	Complex Wavenumber /cm^{-1}	Monomer Wavenumber /cm^{-1}	Shift[(a)] /cm^{-1}
a'	ν_1	4167	4197	-30
	ν_2	2361	2355	6
	ν_3	2341	2355	-14
	ν_4	2326	2345	-19
	ν_5	1029	1017	12
	ν_6	983	972	11
	ν_7	977	972	5
a"	ν_{11}	2369	2355	14
	ν_{12}	1021	1017	4
	ν_{13}	981	972	9

(a) Complex - Monomer

The silane bending modes are blue shifted similar to those in the CH_4.HF complex. The stretching vibrations follow a similar trend to those in the CH_4.HF complex except for ν_{11}, which is red shifted in the CH_4.HF complex but blue shifted in the SiH_4.HF complex. The ν_8 librational mode due to the hydrogen in HF occurs slightly higher than in the CH_4.HF complex at 243 cm^{-1}. The ν_9 modes in both complexes occur relatively close to one

another at 161 and 144 cm^{-1}. Davis and Andrews assign the ν_9 mode at 165 cm^{-1} in an argon matrix, remarkably close to our calculated value. The a" mode at 175 cm^{-1} corresponds well with the HF librational mode in the CH_4.HF complex at 156 cm^{-1}.

The wavenumber shifts on complexation in the SiH_4.HCl complex are collected in Table 7.92. From an analysis of the wavenumber shifts in the SiH_4.HCl complex, the ν_1 vibration undergoes a 31 cm^{-1} red shift on complexation, typical of a hydrogen bonded type complex. The a_1 modes of silane also undergo red shifts on complexation. The red shifts of ν_2 and ν_4 are small in magnitude indicating a lower sensitivity of the f_2 modes of silane to hydrogen bonding.

In the case of the e species the shifts from the monomer modes are negligible. Likewise, the f_2 mode also suffers small changes on complexation, indicating that the e modes are insensitive to hydrogen bonding in those complexes which have low energies of interaction, as was the case in the a_1 modes. The intermolecular mode wavenumbers are extremely low as in the case of the CH_4.HCl complex. The hydrogen bond stretching mode (SiH..HCl) occurs at 54 cm^{-1}, indicating the weakness of the hydrogen bond in these complexes. The ν_{10} mode is the degenerate hydrogen bond bending mode, which corresponds to the librational mode in the CH_4.HCl complex.

Table 7.92 Calculated Wavenumber Shifts in the Most Stable SiH_4.HCl Complex

Symmetry Species	Mode	Complex Wavenumber /cm^{-1}	Monomer Wavenumber /cm^{-1}	Shift[(a)] /cm^{-1}
a_1	ν_1	3097	3128	-31
	ν_2	2349	2355	-6
	ν_3	2325	2345	-20
	ν_4	969	972	-3
e	ν_6	2360	2355	5
	ν_7	1014	1017	-3
	ν_8	974	972	2

(a) Complex - Monomer

The symmetry coordinate description for the SiH_4.HF complex collected in Table 7.93 were derived for the intramolecular modes by treating the SiH_4 molecule in the complex as having C_{3v} symmetry. The intermolecular modes were defined within the Si..FH..H ring for the rocking modes, the Si..F stretch and the librational mode of the hydrogen of HF.

Table 7.93 Symmetry Coordinates for the SiH_4.HF Complex

Complex	Symmetry Coordinate	Description
SiH_4.HF	$S_1 = \Delta r_1$	HF stretch
	$S_2 = \Delta r_2$	Si..F stretch
	$S_3 = \Delta r_3$	SiH stretch
	$S_4 = 1/\sqrt{3}(\Delta r_4 + \Delta r_5 + \Delta r_6)$	SiH_3 symmetric stretch
	$S_5 = 1/\sqrt{6}(\Delta\alpha_1 + \Delta\alpha_2 + \Delta\alpha_3 - \Delta\beta_1 - \Delta\beta_2 - \Delta\beta_3)$	SiH_3 symmetric bend
	$S_6 = 1/\sqrt{6}(2\Delta r_4 - \Delta r_5 - \Delta r_6)$	SiH_3 symmetric stretch
	$S_7 = \Delta\rho$	in phase rock
	$S_8 = 1/\sqrt{6}(2\Delta\alpha_1 - \Delta\alpha_2 - \Delta\alpha_3)$	SiH_3 antisymmetric bend
	$S_9 = 1/\sqrt{6}(2\Delta\beta_1 - \Delta\beta_2 - \Delta\beta_3)$	SiH_3 rock
	$S_{10} = \Delta\pi_1$	in plane H-bend
	$S_{11} = \Delta\theta_2$	out of phase rock
	$S_{12} = \Delta\pi_2$	out of plane H-bend
	$S_{13} = 1/\sqrt{2}(\Delta r_6 - \Delta r_5)$	SiH_2 antisymmetric stretch
	$S_{14} = 1/\sqrt{2}(\Delta\alpha_2 - \Delta\alpha_3)$	SiH_2 deformation
	$S_{15} = 1/\sqrt{2}(\Delta\beta_2 - \Delta\beta_3)$	SiH_2 deformation

The percentage symmetry coordinate distributions amongst the vibrational modes are collected in Table 7.94 for the SiH_4.HF complex.

Table 7.94 Wavenumbers and %PEDs in the SiH_4.HF Complex

Complex	Symmetry Species	Wavenumber /cm^{-1}	%PED
SiH_4.HF	a'	4167	$100S_1$
		2360	$48S_4 + 50S_6$
		2341	$49S_4 + 49S_6$
		2325	$100S_3$
		1029	$57S_8 + 17S_9 + 22S_7$
		982	$84S_5 + 8S_7 + 6S_9$
		976	$64S_9 + 29S_8 + 4S_5$
		271	$72S_{10} + 19S_7 + 5S_5$
		161	$53S_7 + 44S_{10}$
		90	$78S_2 + 11S_7 + 9S_{10}$
	a"	2368	$100S_{13}$
		1020	$59S_{14} + 38S_{15}$
		980	$57S_{15} + 40S_{14}$
		173	$100S_{12}$
		99	$90S_{11} + 6S_{12} + 3S_{15}$

In the case of the intramolecular a' modes, the silane stretching modes have contributions from symmetry coordinates S_4 and S_6 in the case of ν_2 and ν_3. The ν_4 mode, involving the

stretching of the SiH bond involved in the H..H interaction, is unperturbed by the other symmetry coordinates, suggesting this interaction to be weak compared with the Si..F interaction. The Si..F interaction, arising from the flux of negative charge to the silicon, results in the perturbation in the ν_2 and ν_3 modes. The bending modes are all perturbed on complexation as in the case of the stretching modes, having contributions from the other symmetry coordinates carrying similar bond angle deformation descriptions. In the case of the a' intermolecular mode, ν_8, the major contribution to the PED results from the rocking of the HF. The ν_9 mode involving the Si..F stretching mode also has a large contribution from the rocking mode of the HF. This occurs because of the weak secondary H..H interaction. Lastly ν_{10}, the Si..F stretching mode has contributions from the rocking of both the silane and HF molecules. In the case of the a" modes the antisymmetric stretching mode has no contributions from any other symmetry coordinates as in the a' species. The bending modes however do show the same trend of symmetry coordinate mixing as for the a' bending modes. The ν_{14} mode comprises major contributions from the out of plane hydrogen bond bending mode, while ν_{15} results from the out of plane hydrogen bond bending mode coupled with minor contributions from the silane bending modes. The symmetry coordinate descriptions for the SiH_4.HCl complex are given in Table 7.95.

Table 7.95 Symmetry Coordinates for the SiH_4.HCl Complex

Complex	Symmetry Coordinate	Description
SiH_4.HCl	$S_1 = \Delta r_1$	HCl stretch
	$S_2 = 1/\sqrt{3}(\Delta r_2 + \Delta r_3 + \Delta r_4)$	SiH_3 symmetric stretch
	$S_3 = \Delta r_5$	SiH stretch
	$S_4 = 1/\sqrt{6}(\Delta\alpha_1 + \Delta\alpha_2 + \Delta\alpha_3 - \Delta\beta_1 - \Delta\beta_2 - \Delta\beta_3)$	SiH_3 symmetric bend
	$S_5 = \Delta r_6$	H..H stretch
	$S_{6a} = 1/\sqrt{6}(2\Delta r_3 - \Delta r_4 - \Delta r_5)$	SiH_3 antisymmetric stretch
	$S_{7a} = 1/\sqrt{6}(2\Delta\alpha_1 - \Delta\alpha_2 - \Delta\alpha_3)$	SiH_3 antisymmetric bend
	$S_{8a} = 1/\sqrt{6}(2\Delta\beta_1 - \Delta\beta_2 - \Delta\beta_3)$	SiH_3 rock
	$S_{9a} = \Delta\tau_1$	SiH_4 libration
	$S_{10a} = \Delta\rho$	HCl libration
	$S_{6b} = 1/\sqrt{2}(\Delta r_4 - \Delta r_5)$	SiH_3 antisymmetric stretch
	$S_{7b} = 1/\sqrt{2}(\Delta\alpha_2 - \Delta\alpha_3)$	SiH_3 antisymmetric bend
	$S_{8b} = 1/\sqrt{2}(\Delta\beta_2 - \Delta\beta_3)$	SiH_3 rock
	$S_{9b} = \Delta\tau_2$	SiH_4 libration
	$S_{10b} = \Delta\rho_2$	HCl libration

The symmetry coordinates for the SiH_4.HCl complex were generated using the base C_{3v} symmetry for the silane molecule to generate the intramolecular modes. The contribution

of the symmetry coordinates to the PEDs for the SiH_4.HCl complex are collected in Table 7.96.

In the case of the a_1 modes, all the vibrational modes have symmetry coordinate distributions exclusively due to their particular symmetry coordinate, with no contribution from the other symmetry coordinates, which is quite different compared with the CH_4.HCl complex. The e symmetry species on the other hand show such behaviour for the stretching modes only, with the bending vibrations having almost equal symmetry coordinate contributions from S_7 and S_8.

The intermolecular e species have contributions from both the hydrogen bond bending mode and the rocking modes. The ν_9 mode has a major contribution from the hydrogen bond bending mode, while in ν_{10} the rocking modes have major contributions.

Table 7.96 Wavenumbers and %PEDs in the SiH_4.HCl Complex

Complex	Symmetry Species	Wavenumber /cm^{-1}	%PED
SiH_4.HCl	a_1	3097	$100S_1$
		2348	$100S_2$
		2324	$100S_3$
		968	$100S_4$
		54	$100S_5$
	e_a	2360	$100S_{6a}$
		1014	$45S_{7a} + 50S_{8a}$
		973	$50S_{7a} + 46S_{8a}$
		179	$36S_{9a} + 63S_{10a}$
		13	$63S_{9a} + 36S_{10a}$
	e_b	2360	$100S_{6b}$
		1014	$45S_{7b} + 50S_{8b}$
		973	$50S_{7b} + 46S_{8b}$
		179	$63S_{10b} + 36S_{9b}$
		13	$63S_{9b} + 36S_{10b}$

The changes in the intensities on complexation in the SiH_4.HF complex are collected in Table 7.97.

Table 7.97 The Ratios of the Complex to Monomer Intensity values in the SiH_4.HF Complex

Symmetry Species	Mode	Complex A_c/km mol^{-1}	A_c/A_m
a'	ν_1	78.4	0.95
	ν_2	103.9	0.64
	ν_3	126.4	0.77
	ν_4	142.3	-
	ν_5	21.8	-
	ν_6	176.7	0.95
	ν_7	169.0	0.91
a"	ν_{11}	152.7	0.94
	ν_{12}	2.0	-
	ν_{13}	201.1	1.08

The ν_4 mode which correlates with the stretching vibration of the SiH_4 monomer has a high intensity because of the lowering of symmetry in silane on complexation. The same phenomenon is observed for ν_5 which is derived from the bending mode of the silane monomer. The HF stretching intensity remains almost unchanged from the monomer values, decreasing by a factor 0.95. The SiH stretching mode intensities corresponding to the f_2 monomer vibrations consistently decrease. The two a' modes ν_6 and ν_7 decrease in intensity while the intensity of mode ν_{13} increases by a small amount. Thus in these two cases the pattern of intensity behaviour on hydrogen bond formation is well ordered. The

ratios of the complex to monomer intensity values for the SiH_4.HCl complex are collected in Table 7.98.

Table 7.98 The Ratios of the Complex to Monomer Intensity values in the SiH_4.HCl Complex

Symmetry Species	Mode	Complex A_c/km mol^{-1}	A_c/A_m
a_1	ν_1	94.7	4.22
	ν_2	62.4	0.38
	ν_3	225.4	-
	ν_4	219.9	1.34
	ν_5	0.4	-
e	ν_6	149.3	0.92
	ν_7	0.2	-
	ν_8	190.8	1.02
	ν_9	40.0	
	ν_{10}	2.8	

The ν_1 intensity value increases by a factor 4.2 on complexation as expected for a proton engaged in a hydrogen bond. The intensities of the SiH stretching bands correlating with the f_2 monomer mode decrease consistently. The SiH bending mode intensities correlating with the f_2 monomer mode increase on complexation.

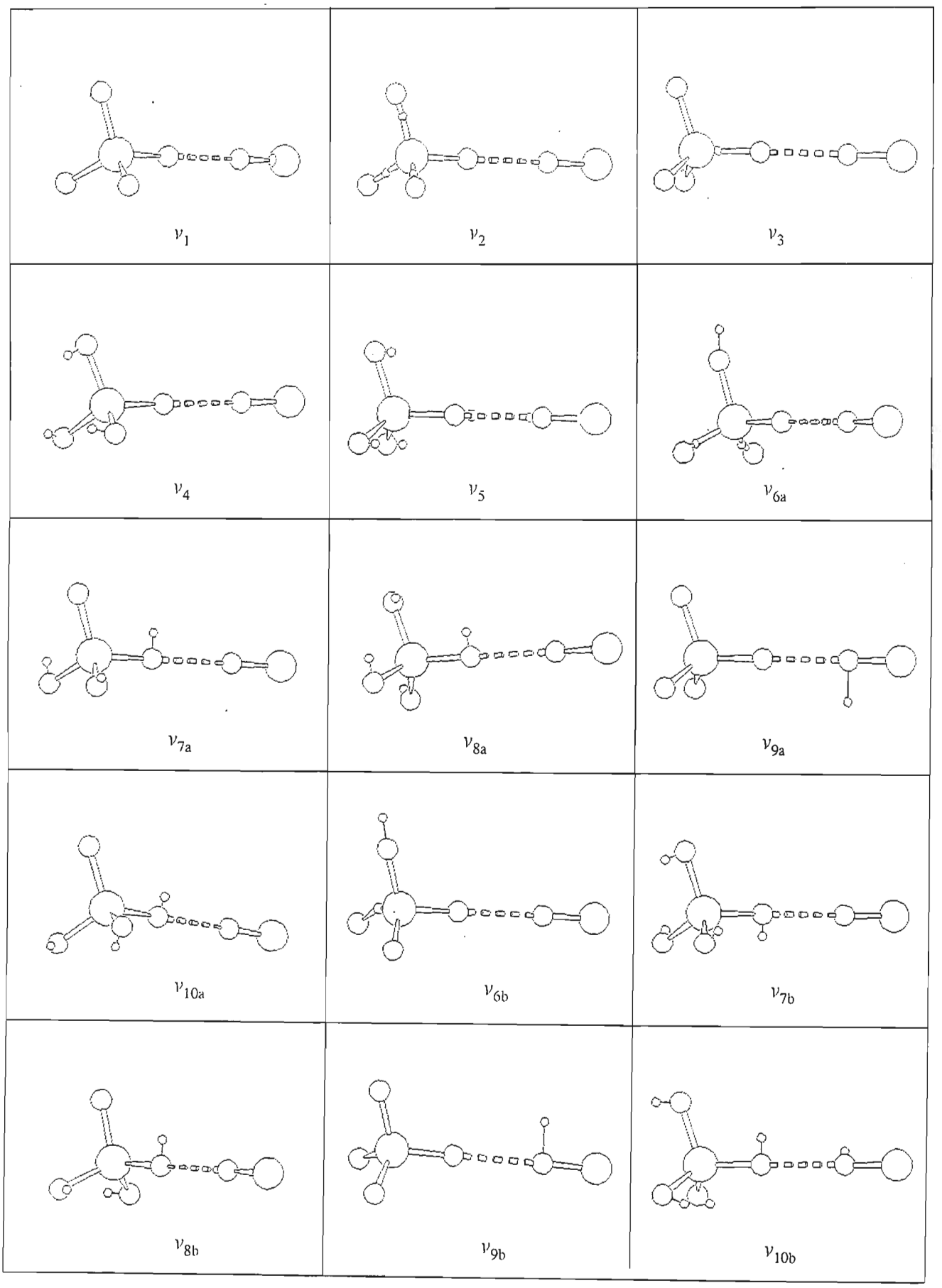

Fig 7.22 Graphical Representation of the SiH_4.HCl Complex Vibration modes

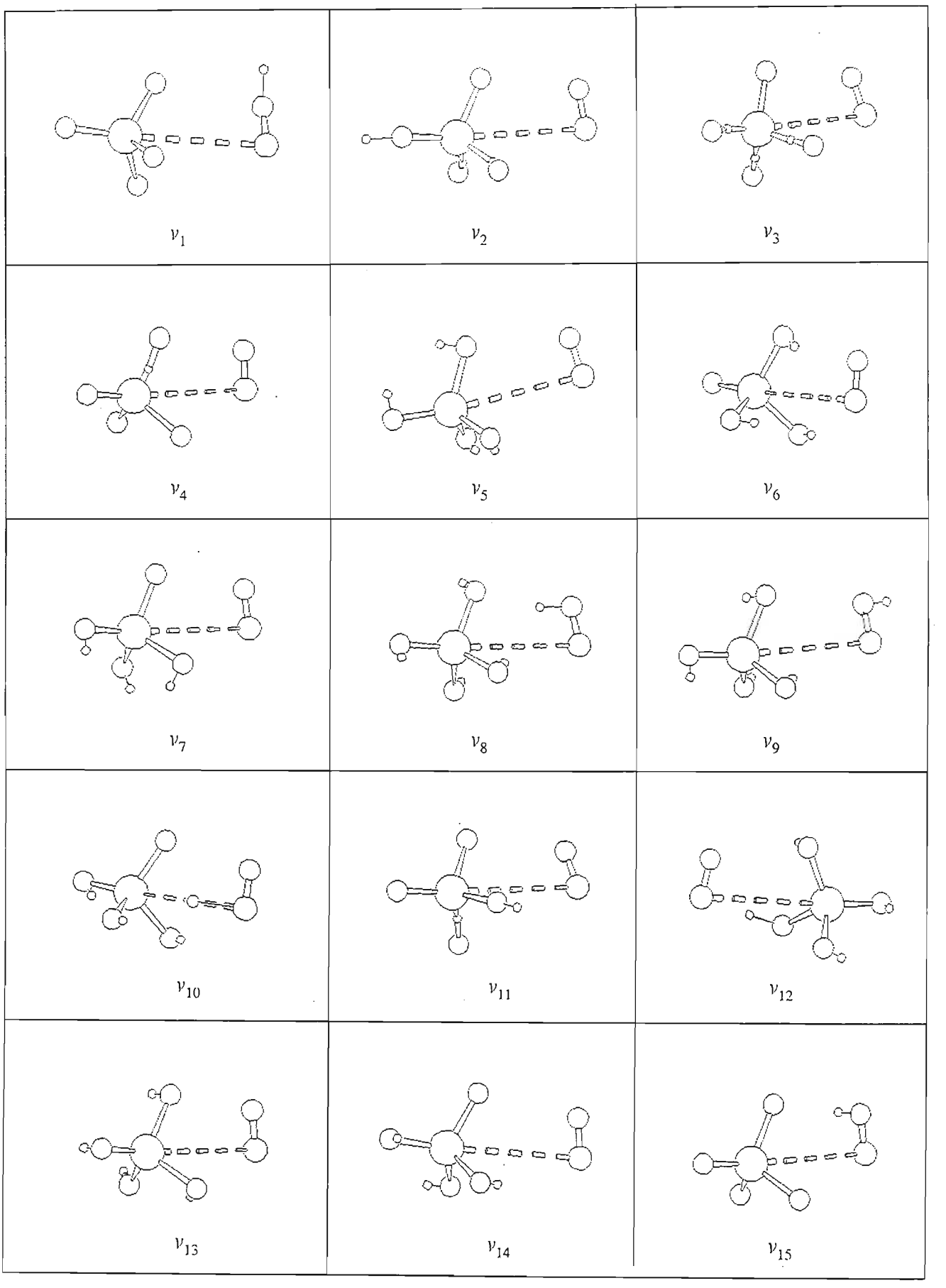

Fig 7. 23 Graphical Representation of the SiH_4.HF Complex Vibration modes

Chapter Eight

Theoretical Predictions of the Structures, Energetics, Mulliken Charges, Vibrational Spectra and Normal Coordinate Analysis of the Heterodimers

8.1 *The $H_2S.H_2O$ Complex*

8.1.1 *Geometries*

For this complex two structures were optimized, one having H_2S as proton donor to H_2O (fig 8.1) and the other H_2O as proton donor to H_2S (fig 8.2). Our calculations support the previous experimental[209,210] and theoretical studies[212,213] reporting the structure of this complex having H_2S as proton donor to H_2O. A recent study involving the use of the Laplacian of the wavefunction by Platts et al[343] also predicted the above type of interaction, which is supported by the electrostatic model of Buckingham and Fowler.[17] Hence the structure having H_2O as the proton donor to H_2S will not be mentioned in this project. The geometrical parameters for the $H_2S.H_2O$ complex are collected in Table 8.1. The major changes in the geometrical parameters of the $H_2S.H_2O$ complex occur in the H3OH4 and H1SH2 angles and the SH1 bond length by 17.2°, 0.6° and 0.6 pm respectively. Our calculated S..O separation of 347.0 pm is shorter than the value of 361.9 pm reported by Del Bene et al[139] using the 6-31G* basis set at the MP2 level of theory. The hydrogen bond angle is essentially linear (175.7°) and together with the SH1..O distance (213.5 pm) classifies the complex as hydrogen-bonded.

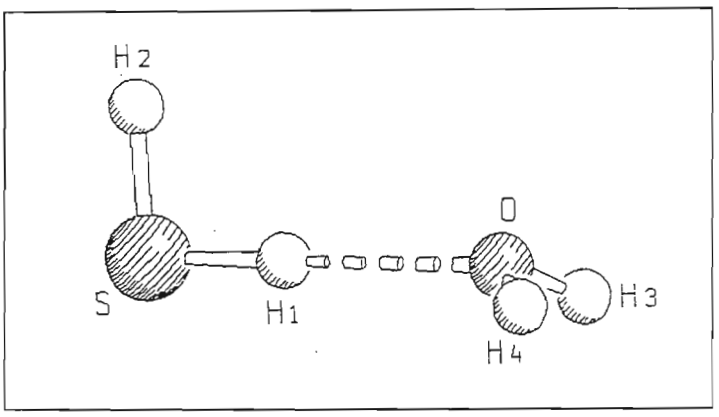

Fig 8.1 The Linear $H_2O.H_2S$ Complex

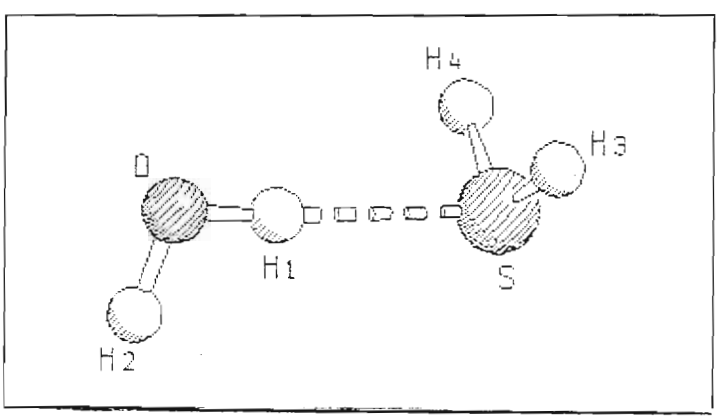

Fig 8.2 The Linear $H_2S.H_2O$ Complex

Table 8.1 Geometrical Parameters for the Most Stable $H_2S.H_2O$ Complex

Complex	Parameter	Complex	Monomer	Difference
$H_2S.H_2O$	r(SH1)/pm	133.5	132.9	0.6
	r(SH2)/pm	132.9	132.9	0.0
	r(OH3), r(OH4)/pm	96.2	96.1	0.1
	R(H1..O)/pm	213.5		
	H1SH2/deg	93.4	92.8	0.6
	H3OH4/deg	121.1	103.9	17.2
	SH1..O/deg	175.7		

8.1.2 *Energetics*

The binding energy calculated at the MP2/6-31G** level of theory and corrected for the BSSE by means of the counterpoise method as described in section 2.1.1 is summarised in Table 8.2.

Table 8.2 The Binding Energy of the Most Stable $H_2S.H_2O$ Complex

Complex	$\Delta E'$ /kJ mol^{-1}	ΔE /kJ mol^{-1}	BSSE /kJ mol^{-1}	$\%\Delta E_{Disp}$
$H_2S.H_2O$	-16.0	-17.1	1.1	13.2

The binding energy of this complex has a low dispersion energy contribution of 13.2%. Our calculated interaction energy is in good agreement with the pseudopotential results of Les et al [212] (-16.37 kJ mol^{-1}) and the MP2/6-31G** calculation of Del Bene et al[139] (-15.89 kJ mol^{-1}). The Morokuma energy decomposition analysis is collected in Table 8.3.

Table 8.3 Energy Decomposition Analysis of the Most Stable $H_2S.H_2O$ Complex /kJ mol^{-1}

Complex	ES	EX	CT	PL	MIX	Total
$H_2S.H_2O$	-22.6	22.3	-8.2	-1.7	2.8	-7.4

The ES term dominates the attractive energy component (-22.6 kJ mol^{-1}) of this complex followed by the CT term (-8.2 kJ mol^{-1}). The exchange repulsion term also plays a large role but is compensated by the attractive components. Hence this complex may be classed as an electrostatically bound complex, whose structure was also accurately predicted by the electrostatic Buckingham and Fowler model.[19] The earlier studies by Morokuma et al[10] also show the ES term to be dominating in the decomposition analysis.

8.1.3 *Mulliken Charge Analysis*

The Mulliken charge analysis depicting the direction of charge flow in the $H_2S.H_2O$ complex is collected in Table 8.4.

The charge donation (-0.024 e) occurs from the proton acceptor to the proton donor in the $H_2S.H_2O$ complex. The sulphur atom gains negative charge (-0.058 e) which has its origin from the hydrogens of the proton acceptor. This influx of charge extends to the non-bonded proton in the proton donor.

Table 8.4 Mulliken Charge Analysis for the Most Stable $H_2S.H_2O$ Complex

Atom	Atomic Charge /e		Difference /e
	Complex	Monomer	
H1	0.104	0.066	0.038
S	-0.190	-0.132	-0.058
H2	0.062	0.066	-0.004
			-0.024
O	-0.672	-0.673	0.001
H3	0.348	0.336	0.012
H4	0.348	0.336	0.012
			0.025

The loss of charge from the hydrogen bonded proton results in the increase of the SH1 bond length, and also the increase in the H3OH4 bond angle. The increase in the HOH bond angle arises from the decrease in the lone pair - bonded pair electron repulsive force, thus allowing the bonded pair - bonded pair repulsion in the OH bonds of the proton acceptor to increase.

8.1.4 *Vibrational Properties of the Most Stable $H_2S.H_2O$ Complex*

The calculated vibrational spectra, potential energy distributions and infrared intensities at the MP2/6-31G** level of theory for the $H_2S.H_2O$ complex are shown in Tables 8.5 - 8.9. The plots of the normal modes of vibration are also shown in fig 8.3. The calculated

vibrational spectrum of the $H_2S.H_2O$ complex compared with experiment is reported in Table 8.5.

Table 8.5 Calculated Vibrational Spectrum of the $H_2S.H_2O$ Complex Compared with Experiment

Symmetry Species	Mode	Calculated Wavenumber /cm^{-1}	Experimental Wavenumber[(a)] /cm^{-1}	Ratio[(b)]
a'	ν_1	3885	3628	1.1
	ν_2	2855	2574	1.1
	ν_4	1675	1598	1.0
a"	ν_9	4023	3719	1.1

(a) Ref. 210

(b) Ratio = Calculated / Experimental

Our calculated vibrational spectrum of the $H_2S.H_2O$ complex is in good agreement with the experimental nitrogen matrix spectrum.[210] The matrix spectrum obtained by Barnes et al,[209] in an argon matrix contained new bands at 3703 and 3590 cm^{-1} corresponding to our calculated OH stretching modes (4023 and 3885 cm^{-1}). In the SH stretching region a strong band at 2587 cm^{-1} due to H_2S acting as the proton donor in the argon matrix compares with the band at 2574 cm^{-1} in the nitrogen matrix. In the bending regions, the band at 1598 cm^{-1} was assigned to the water bending mode in both argon and nitrogen matrices. In the less polarizable argon matrix there was also evidence supporting the existence of the $HOH.SH_2$ complex. This complex was assigned on the basis of the OH

stretching band occurring on the low frequency side (3536 cm^{-1}) compared with that in the water dimer (3574 cm^{-1}), since H_2S is a better proton acceptor than is H_2O in the water dimer. The calculated wavenumber shifts for the $H_2S.H_2O$ complex are collected in Table 8.6.

Table 8.6 Calculated Wavenumber Shifts in $H_2S.H_2O$ Complex

Symmetry Species	Mode	Complex Wavenumber /cm^{-1}	Monomer Wavenumber /cm^{-1}	Shift[(a)] /cm^{-1}
a'	ν_1	3885	3900	-15
	ν_2	2855	2871	-16
	ν_3	2785	2845	-60
	ν_4	1675	1683	-8
	ν_5	1285	1269	16
a"	ν_9	4023	4039	-16

(a) Complex - Monomer

In the proton donor, the SH stretching bands are red shifted, while the bending mode (ν_5) is blue shifted, typical of a hydrogen bonded complex. The major wavenumber shift occurring in the $H_2S.H_2O$ complex occurs in ν_3 (-60 cm^{-1}). The magnitudes of the remaining wavenumber shifts are less than 20 cm^{-1}. These small wavenumber shifts are characteristic of weakly hydrogen bonded complexes.

The symmetry coordinate descriptions for the intra- and intermolecular modes are collected in Table 8.7.

Table 8.7 Symmetry Coordinates of the $H_2S.H_2O$ Complex

Complex	Symmetry Coordinate	Description
$H_2S.H_2O$	$S_1 = 1/\sqrt{2}(\Delta r_1 + \Delta r_2)$	H_2O symmetric stretch
	$S_2 = \Delta r_3$	HS stretch (free)
	$S_3 = \Delta r_4$	HS stretch (bonded)
	$S_4 = \Delta\beta_1$	HSH bend
	$S_5 = \Delta\gamma_1$	HOH bend
	$S_6 = \Delta R$	H..O stretch
	$S_7 = 1/\sqrt{2}(\Delta\gamma_2 + \Delta\gamma_3)$	HOH wag
	$S_8 = \Delta\pi_1$	SH..O in plane bend
	$S_9 = 1/\sqrt{2}(\Delta r_1 - \Delta r_2)$	H_2O antisymmetric stretch
	$S_{10} = 1/\sqrt{2}(\Delta\gamma_2 - \Delta\gamma_3)$	HOH twist
	$S_{11} = \Delta\pi_2$	SH..O out of plane bend
	$S_{12} = \Delta\tau$	SH..OH torsion

The symmetry coordinates for the intramolecular modes in the case of the proton acceptor have been captured from the corresponding coordinates in the monomer. In the case of the proton donor the symmetry coordinates are slightly different from those of the parent

monomer due to the inequivalence of the SH bonds. The intermolecular modes were generated using the rules of Wilson et al.[70] The percentage potential energy distribution amongst the various vibrational modes in the $H_2S.H_2O$ complex are reported in Table 8.8. From Table 8.8, the intramolecular modes have symmetry coordinates unperturbed from those of the monomer. On complexation the local symmetry of the H_2S unit is reduced from C_{2v} to C_s, resulting in two non-equivalent SH bonds. In the case of the proton acceptor the C_{2v} symmetry is essentially retained, as seen in the distinct appearance of the ν_1 and ν_9 modes. When comparing the intramolecular modes of this complex with those of the individual H_2Y dimers, little perturbation is observed from their monomer modes. The intermolecular modes however tend naturally to have contributions from both the monomer units.

Table 8.8 Wavenumbers and %PEDs in the $H_2S.H_2O$ Complex

Symmetry Species	Wavenumbers /cm^{-1}	%PED
a'	3885	$100S_1$
	2855	$100S_2$
	2785	$100S_3$
	1675	$100S_5$
	1285	$100S_4$
	207	$60S_7 + 40S_8$
	131	$60S_6 + 30S_7 + 9S_8$
	111	$60S_8 + 40S_7$
a"	4023	$100S_9$
	438	$53S_{11} + 47S_{12}$
	149	$48S_{12} + 36S_{10} + 16S_{11}$
	84	$71S_{11} + 19S_{12} + 10S_{10}$

The changes in the intensities in the $H_2S.H_2O$ complex are collected in Table 8.9. The intensity of ν_3 has been enhanced 16.8 fold on complexation. The ν_3 mode, being the hydrogen bonded SH stretching mode, undergoes this large intensity enhancement on complexation because of the net charge influx to this bond along the hydrogen bonded axis thus resulting in an intensity enhancement on executing the SH stretching mode. The intensity enhancements of the stretching modes in this complex are in support of the

results observed by Barnes et al.[209] The ratios of the complex / monomer intensities for the bending modes were observed to be close to unity.

Table 8.9 Ratios of the Complex to Monomer Intensity values for the $H_2S.H_2O$ Complex

Symmetry Species	Mode	Complex A_c/km mol^{-1}	A_c/A_m
a'	ν_1	14.3	3.40
	ν_2	8.0	2.05
	ν_3	109.2	16.80
	ν_4	73.8	0.94
	ν_5	7.8	1.02
a"	ν_9	52.4	1.55

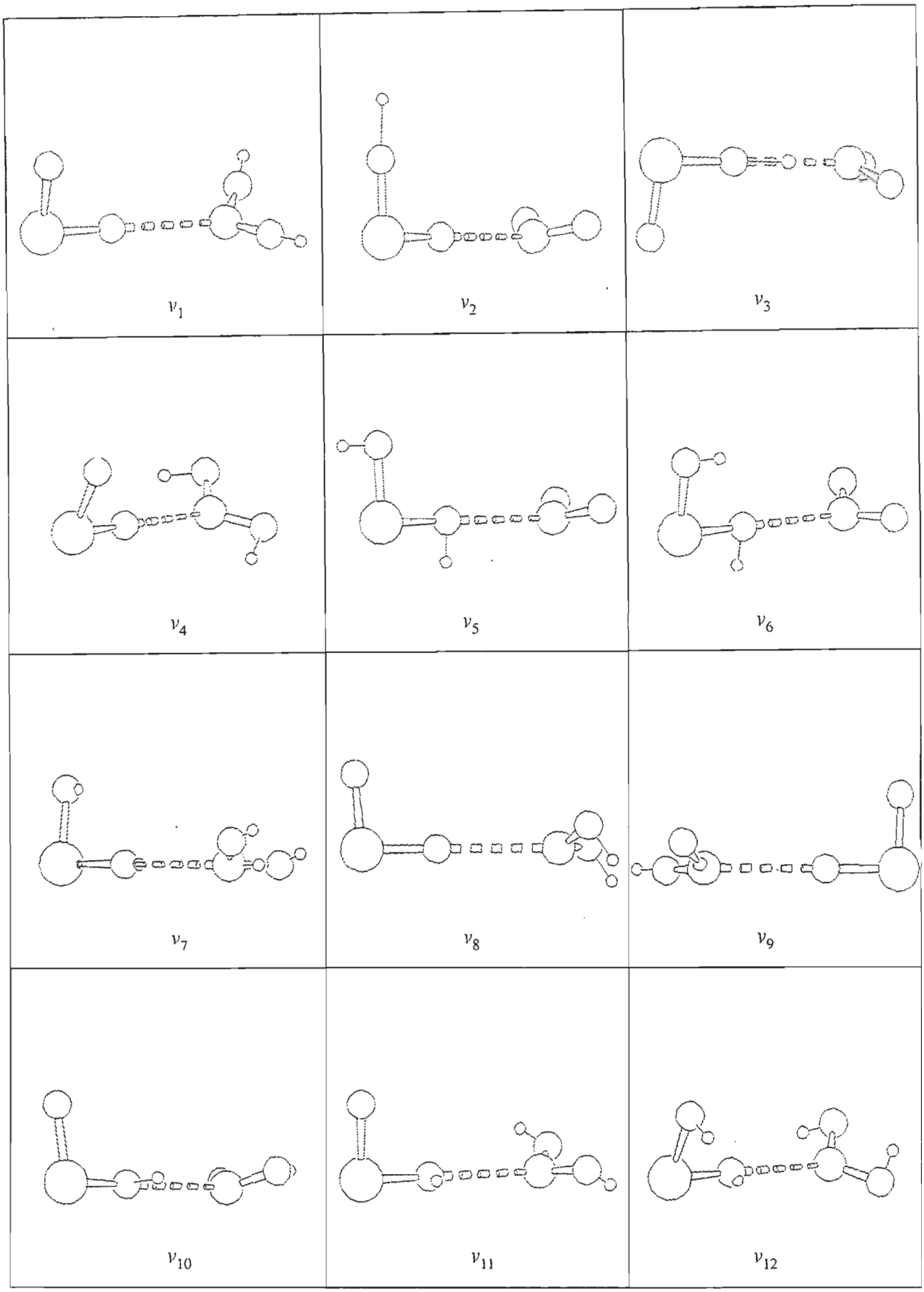

Fig 8.3 Graphical Representation of the $H_2O.H_2S$ Complex Vibration modes

8.2 *The $NH_3.H_2Y$ (Y= O,S) Complexes*

8.2.1 *Geometries*

The geometry optimized for the $NH_3.H_2O$ complex (fig 8.4) had C_s symmetry with H_2O proton donor to the nitrogen of NH_3 along its C_3 axis, having a nearly linear hydrogen bond. The geometry of this complex was also obtained by Del Bene et al[139] at the HF/6-31G* level of theory, who had studied the complexes of H_2O with the hydrides of the first and second row elements of the periodic table. Coitino et al[344] using the ab initio and semi-empirical approaches also arrived at the same conclusion regarding the geometry of this complex. Experimental matrix isolation studies[273-276] and gas phase studies [279] also support the linear hydrogen bonded geometry (OH..N) of the complex to be the global minimum energy structure. In the case of the $NH_3.H_2S$ complex a structure similar to that of the $NH_3.H_2O$ complex was optimized since this structure was found to be most probable by the gas phase studies of Hilpert et al.[278] The C_s linear hydrogen bonded structure having H_2S as proton donor to the nitrogen of NH_3 was found to be a local minimum on the PES at the SCF level of theory. The inclusion of correlation effects rendered this complex unstable, being a saddle point on the PES with a negative eigenvalue of 14.5 cm^{-1}, possibly suggesting torsional strain about the hydrogen bond. The negative wavenumber (-14.5 cm^{-1}) obtained at the MP2/6-31G** level corresponds to 235.7 cm^{-1} at the RHF/6-31G** level of theory. This effect is typical of SCF wave functions leading to an overestimation of the calculated dissociation properties relating to a steeper potential gradient around the equilibrium structure thus giving rise to much higher harmonic wavenumbers.[346] As was seen in the case of the $H_2S.HX$ series, correlation effects play a large role in complexes having sulphur atoms.The ab initio calculations by Del Bene et al[71] located the linear hydrogen bonded structure for the $NH_3.H_2S$ complex at the HF level of theory to be a local minimum energy structure.

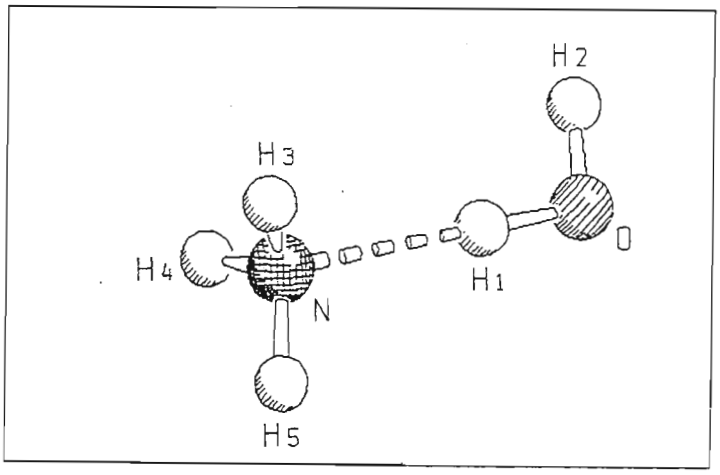

Fig 8.4 The Linear $H_2O.NH_3$ Complex

our calculations at the MP2 level of theory yielded no local minimum energy structure for the $NH_3.H_2S$ complex, this complex will not be further discussed in this project. The geometrical parameters of the $NH_3.H_2O$ complex are reported in Table 8.10.

Table 8.10 Geometrical Parameters for the Most Stable $NH_3.H_2O$ Complex

Complex	Parameter	Complex	Monomer	Difference
$NH_3.H_2O$	r(NH3), r(NH4), r(NH5)/pm	101.3	101.1	0.2
	r(OH1)/pm	97.3	96.1	1.2
	r(OH2)/pm	96.0	96.1	0.1
	R(N..H1)/pm	199.7		
	H1OH2/deg	103.9	103.9	0.0
	H3NH4, H3NH5, H4NH5/deg	106.6	106.1	0.5
	N..H1O/deg	175.7		

On complexation the geometrical parameters in the complex are slightly changed from their corresponding monomer values. The major change in the geometrical parameters occurs in the OH1 bond length by 1.2 pm and in the internal bond angles of the proton acceptor. The hydrogen bond angle is nearly linear with a hydrogen bond length of 199.7 pm. Our calculated geometrical parameters are in perfect agreement with the ab initio study of Latajka and Scheiner [275] and that of Ford and Yeo[276.277] who had reported an increase of the OH1 bond distance by 1.3 pm and a hydrogen bond angle of near linearity

at the same level of theory and with the same basis set. Our calculated structure for the $NH_3.H_2O$ complex also supports the experimental gas phase results of Herbine and co-workers.[279] The far IR study by Fraser and Suenram[272] reported tunnelling of the proton donor coupled with the rotation of the proton acceptor about its C_3 axis, whereby the other hydrogen of the proton donor is involved in the hydrogen bond.

8.2.2 *Energetics*

The binding energy together with the percentage dispersion energy contribution calculated at the MP2/6-31G** level of theory and basis set is collected in Table 8.11 for the most stable $NH_3.H_2O$ complex.

Table 8.11 The Binding Energy of the $NH_3.H_2O$ Complex

Complex	$\Delta E'$ /kJ mol^{-1}	ΔE /kJ mol^{-1}	BSSE /kJ mol^{-1}	$\%\Delta E_{Disp}$
$NH_3.H_2O$	-26.6	-33.3	6.7	16.7

Using basis sets augmented with diffuse functions, Latajka and Scheiner[277] report a 22% dispersion energy contribution to the binding energy for the $NH_3.H_2O$ complex. This discrepancy from our calculated dispersion energy contribution is attributed to the difference in the basis set sizes. This complex is more strongly bonded than most of the complexes under study in this project; this could be attributed to the existence of NH_4OH in the liquid state which could be responsible for the stability of the $NH_3.H_2O$ complex. The energy decomposition analysis for the $NH_3.H_2O$ complex is collected in Table 8.12. The SCF component of the interaction energy in the $NH_3.H_2O$ complex is dominated by the attractive electrostatic force (-58.6 kJ mol^{-1}) which completely masks the effects of the

exchange repulsion term (37.7 kJ mol^{-1}). Hence this complex may be classed as being an ES type complex.

Table 8.12 Energy Decomposition Analysis of the $NH_3.H_2O$ Complex /kJ mol^{-1}

Complex	ES	EX	CT	PL	MIX	Total
$NH_3.H_2O$	-58.6	37.7	-10.0	-4.6	1.7	-33.8

8.2.3 *Mulliken Charge Analysis*

The Mulliken charge analysis for the $NH_3.H_2O$ complex is reported in Table 8.13.

Table 8.13 Mulliken Charge Analysis for the $NH_3.H_2O$ Complex

Atom	Atomic Charge /e		Difference /e
	Complex	Monomer	
H1	0.395	0.337	0.058
O	-0.735	-0.674	-0.061
H2	0.314	0.337	-0.023
			-0.026
N	-0.819	-0.786	-0.033
H3	0.280	0.262	0.018
H4	0.280	0.262	0.018
H5	0.285	0.262	0.023
			0.026

The negative charge (-0.026 e) donation occurs from the proton acceptor to the donor, most of this negative charge originates from the hydrogens of the proton acceptor and from H1 in proton donor. The net delocalisation of negative charge occurs in the N..H1OH2 fragment of the complex, further emphasising the great stability of the hydrogen bond in this complex. Even though NH_3 is the electron donor, the nitrogen atom also gains negative charge (-0.033 e) on complexation; this reinforces the amount of stability present in the vicinity of the hydrogen bond.

8.2.4 *Vibrational Properties of the Linear $NH_3.H_2O$ Complex*

The calculated vibrational spectrum and infrared intensities at the MP2/6-31G** level of theory for the $NH_3.H_2O$ complex are shown in Tables 8.14 - 8.16. The plots of the normal modes of vibrations are shown in fig 8.5.

The calculated vibrational spectrum of the $NH_3.H_2O$ complex compared with experiment is reported in Table 8.14. The spectrum is in good agreement with the experimental matrix isolated spectrum of Engdahl et al[274] obtained in a neon matrix. In the case of the intramolecular modes, ν_1 and ν_2 in argon and nitrogen matrices[273] occur at 3702, 3697 and 3434, 3414 cm^{-1} respectively. The lack of identification of the ν_3, ν_4 and ν_{11} bands experimentally is due to their being too close to the parent monomer bands, however the weak ν_4 band was identifiable in the less interacting neon matrix.[274] The ν_5 mode was observed weakly in the neon matrix but was masked by the monomer bands of water in N_2 and Ar matrices. The ν_7 mode in the N_2, Ar and Ne matrices was identified as being the symmetric bending mode of the proton acceptor. The intermolecular modes are also in good agreement with experiment except for ν_{15}. This discrepancy could be attributed to the anharmonicity of this mode and matrix cage effects.

Table 8.14 Calculated Vibrational Spectrum of the $NH_3.H_2O$ Complex compared with Experiment

Symmetry Species	Mode	Calculated Wavenumber /cm^{-1}	Experimental Wavenumber[(a)] /cm^{-1}	Ratio[(b)]
a'	ν_1	3987	3727	1.07
	ν_2	3727	3456	1.08
	ν_4	3567	3329	1.07
	ν_5	1742	1626	1.07
	ν_7	1156	1032	1.12
	ν_8	456	430	1.06
	ν_9	200	202	0.99
	ν_{10}	170	180	0.94
a"	ν_{13}	709	662	1.07
	ν_{15}	28	20	1.40

(a) Ref. 274

(b) Ratio = Calculated / Experimental

The calculated vibrational spectrum of the $NH_3.H_2O$ complex compared with the calculated monomer vibrational spectrum is shown in Table 8.15.

Table 8.15. Calculated Wavenumber Shifts on Complexation in the $NH_3.H_2O$ Complex

Symmetry Species	Mode	Complex Wavenumbers /cm^{-1}	Monomer Wavenumbers /cm^{-1}	Shift[(a)] /cm^{-1}
a'	ν_1	3987	4039	-52
	ν_2	3727	3900	-173
	ν_3	3719	3728	-9
	ν_4	3567	3571	-4
	ν_5	1742	1683	59
	ν_6	1713	1724	-11
	ν_7	1156	1116	40
a"	ν_{11}	3720	3728	-8
	ν_{12}	1720	1724	-4

(a) Shift = Complex - Monomer

The major shift occurring on complexation occurs in ν_2 (-173 cm^{-1}), the stretching mode of the bonded hydrogen in the proton donor. The large red shift of ν_2 coupled with the blue shift (59 cm^{-1}) of ν_5 in the proton donor is indicative of a strongly hydrogen bonded complex. The symmetric stretching mode of NH_3 is slightly perturbed on complexation in comparison with its symmetric bending mode. The relative insensitivity of the stretching modes of the proton acceptor on complexation is characteristic of hydrogen bonded complexes, as was found in the case of the $H_2O.HCl$ complex. The ν_8, ν_9 and ν_{13} intermolecular modes occur within the general range of 80 - 200 cm^{-1} normally associated

with hydrogen bonded complexes.[277] The appearance of the intermolecular bands at higher frequency than the other conventional hydrogen bonded complexes, e.g. H_2O and HF dimers, enables one to conclude that this complex is indeed strongly bonded. The examination of the changes in the intensities on complexation is collected in Table 8.16.

Table 8.16 Ratios of the Complex to Monomer Intensity values in the $NH_3.H_2O$ Complex

Symmetry Species	Mode	Complex A_c/km mol^{-1}	A_c/A_m
a'	ν_1	44.6	1.32
	ν_2	390.4	92.95
	ν_3	10.2	12.75
	ν_4	3.3	16.50
	ν_5	30.2	0.42
	ν_6	42.2	2.03
	ν_7	168.8	0.77
a"	ν_{11}	5.8	7.25
	ν_{12}	21.7	1.04

The 92-fold intensity enhancement coupled with the large red shift of ν_2 further supports our conclusion regarding the strength of this hydrogen bonded complex. Our results for the wavenumber shifts and the intensity changes on complexation are in excellent agreement with those of Yeo and Ford.[275,276] The other major intensity enhancements occur in ν_3, ν_4 and ν_{11} by 12.75, 16.5 and 7.25-fold respectively. Latajka and Scheiner[277]

report a decrease in the intensity of the ν_4 mode, contrary to our calculations. This probably results from the inclusion of diffuse functions in their basis set. The intensities of ν_5 and ν_7 are both diminished on complexation. The large intensity values of the ν_8 and ν_{13} modes are also in agreement with those obtained by Latajka and Scheiner.[277]

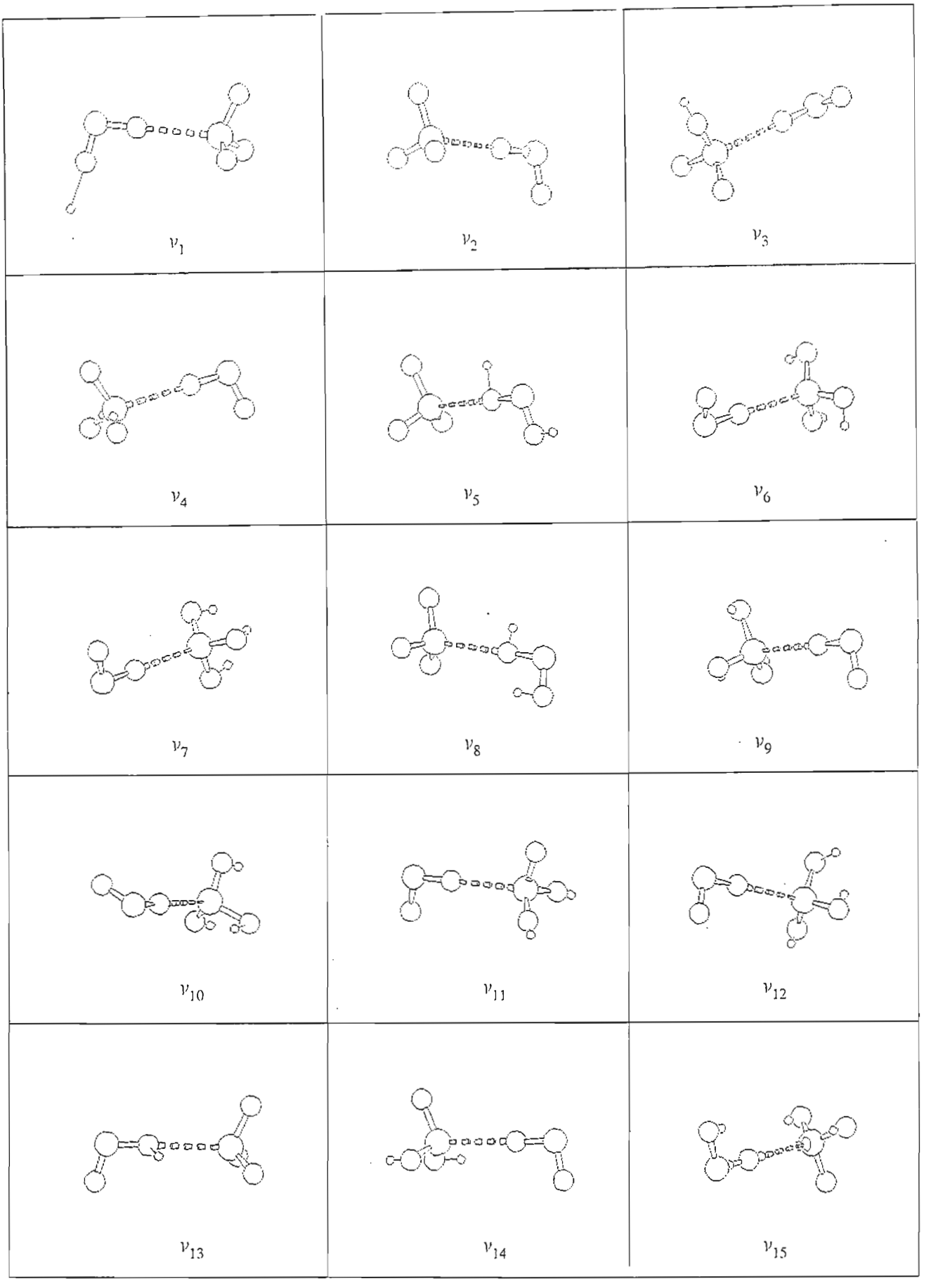

Fig 8.5 Graphical Representation of the $NH_3.H_2O$ Complex Vibration modes

8.3 *The $PH_3.H_2S$ Complex*

8.3.1 *Geometries*

Since H_2S is a better proton donor than PH_3, the most favourable structure investigated for this complex comprised H_2S being the proton donor to phosphorus of phosphine along its C_3 axis. This structure (fig 8.6) was found to be the local minimum energy structure on the PES in support of the structure optimized by Sodupe et al.[158] The geometrical parameters for the $PH_3.H_2S$ complex are collected in Table 8.17.

On complexation the major changes in the geometrical parameters occur in the H3PH5, H4PH3 and H4PH5 angles by 0.6°, 0.6° and 0.3° respectively, with the bond lengths remaining unchanged. In the case of the proton donor, the major change occurring in the geometrical parameters occurs in the SH1 bond distance and the H1SH2 bond angle by 0.3 pm and 0.2° respectively. This complex has a hydrogen bond angle and bond length of 177.5° and 292.8 pm respectively. This complex can thus be classed as being a weak hydrogen bonded complex. Our calculated values for the hydrogen bond length and angle are in good agreement with those of Sodupe[158] and co-workers who report values of 297.7 pm and 175.4° calculated at the MP2/MC-311(d,p) level of theory and basis set.

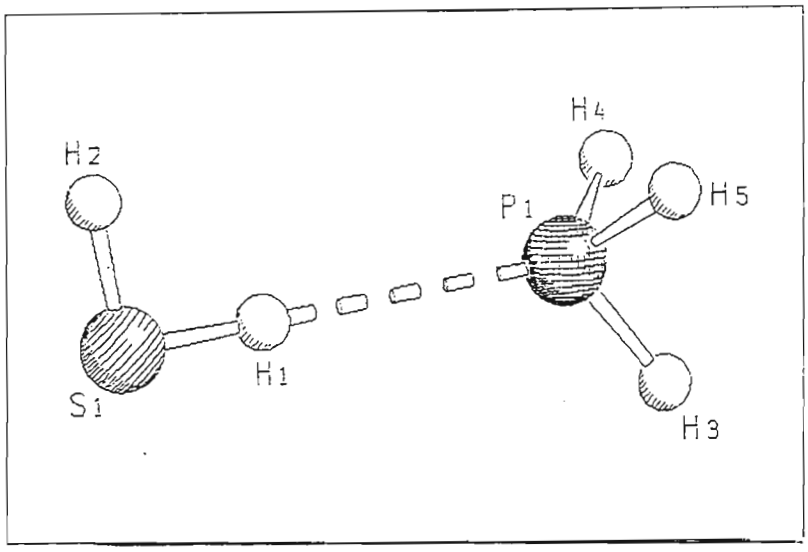

Fig 8.6 The Linear $H_2S.PH_3$ Complex

Table 8.17 Geometrical Parameters for the Most Stable $PH_3.H_2S$ Complex

Complex	Parameter	Complex	Monomer	Difference
$PH_3.H_2S$	r(PH3), r(PH4), r(PH5)/pm	140.5	140.5	0.0
	r(SH1)/pm	133.2	132.9	0.3
	r(SH2)/pm	133.0	132.9	0.1
	R(P..H1)/pm	292.8		
	H1SH2 /deg	93.0	92.8	0.2
	H4PH5 /deg	94.8	94.5	0.3
	H3PH5, H4PH3 /deg	95.1	94.5	0.6
	P..H1S/deg	177.5		

8.3.2 *Energetics*

The binding energy together with the percentage dispersion energy contribution and the BSSE, calculated at the MP2/6-31G** level of theory and basis set are collected in Table 8.18 for the $PH_3.H_2S$ complex.

Table 8.18 The Binding Energies of the $PH_3.H_2S$ Complex

Complex	$\Delta E'$ /kJ mol^{-1}	ΔE /kJ mol^{-1}	BSSE /kJ mol^{-1}	$\%\Delta E_{Disp}$
$PH_3.H_2S$	-0.7	-4.1	3.4	51.4

This complex is weakly bonded (-0.7 kJ mol^{-1}), with the BSSE contributing a large proportion to the uncorrected binding energy. The large dispersion energy contribution (51.4%) is also seen in all of the other complexes containing the hydrides of the second row elements.

8.3.3 *Mulliken Charge Analysis*

The Mulliken charge analysis for the $PH_3.H_2S$ complex is reported in Table 8.19. The proton donor gains -0.011 e charge from the proton acceptor; this charge has its origin mostly from H1 of the proton donor.

Table 8.19 Mulliken Charge Analysis for the $PH_3.H_2S$ Complex

Atom	Atomic Charge /e		Difference
	Complex	Monomer	/e
H1	0.079	0.066	0.013
S	-0.150	-0.132	-0.018
H2	0.060	0.066	-0.006
			-0.011
P	0.147	0.162	-0.015
H3	-0.044	-0.054	0.010
H4	-0.046	-0.054	0.008
H5	-0.046	-0.054	0.008
			0.011

This results in the increase of the SH1 bond distance, resulting from charge loss in the SH1 bonding orbital. The hydrogens of the proton acceptor also undergo a negative charge loss on complexation, this eventually results in an increase in the proton acceptor's bond angles due to a decrease in the lone pair - bonded pair electron repulsive force compared with the bonded pair - bonded pair electron repulsive force in the SH bonds.

8.3.4 *Vibrational Properties of the $PH_3.H_2S$ Complex*

The calculated vibrational spectrum and ratios of the complex to monomer intensities at the MP2/6-31G** level are collected in Tables 8.20 and 8.21 respectively for the $PH_3.H_2S$ complex. The plots of the normal modes of vibration are shown in fig 8.7. This complex, being weakly hydrogen bonded, does not exhibit any major wavenumber shifts on complexation. The ν_1 and ν_2 modes, being the stretching modes of the free and bonded SH bonds of the proton donor, are red shifted by 16 and 26 cm^{-1} respectively. This, coupled with the blue shift of ν_5 (9 cm^{-1}), is characteristic of the trends followed by hydrogen bonded complexes. The ν_3 and ν_4 modes, the symmetric stretching modes, and ν_6 and ν_7, the symmetric bending modes of the proton acceptor, are slightly perturbed from their monomer wavenumbers on complexation. The ν_{11} and ν_{12} modes, the antisymmetric stretching and bending modes of the proton acceptor, are also slightly perturbed on complexation. The intermolecular modes include the hydrogen bond stretching mode occurring at 64 cm^{-1}, much lower in magnitude than that in the $NH_3.H_2O$ complex (202 cm^{-1}) supporting the weakness of this hydrogen bond. The in- and out of plane hydrogen bond bending modes occur at 152 cm^{-1} and 262 cm^{-1} respectively, with ν_9 and ν_{14} being the wagging modes of the proton acceptor occurring at 9 and 65 cm^{-1} respectively. The ν_{15} torsional mode occurs at 6 cm^{-1}. Once again the magnitudes of the wavenumbers of the intermolecular modes are lower than those found in the $NH_3.H_2O$ complex, further reinforcing the weakness of this hydrogen bonded complex.

Table 8.20 Calculated Wavenumber Shifts on complexation in the $PH_3.H_2S$ Complex

Symmetry Species	Mode	Complex Wavenumbers /cm^{-1}	Monomer Wavenumbers /cm^{-1}	Shift[a] /cm^{-1}
a'	ν_1	2855	2871	-16
	ν_2	2819	2845	-26
	ν_3	2556	2546	10
	ν_4	2538	2531	7
	ν_5	1278	1269	9
	ν_6	1183	1184	-1
	ν_7	1080	1078	2
a"	ν_{11}	2554	2546	8
	ν_{12}	1182	1184	-2

(a) Shift = Complex - Monomer

The ratios of the complex to monomer intensities in the $PH_3.H_2S$ complex are reported in Table 8.21. From Table 8.21, the major intensity enhancements occurring on complexation occur in ν_2 and ν_5 by 4.92 and 1.26-fold respectively. The intensity of the bending mode (ν_5) of the proton donor is enhanced, while the corresponding mode of the proton acceptor experiences an intensity decrease. The reason for the intensity decrease could be explained on the basis of the direction of the dipole moment being reversed in the proton acceptor, thus on hydrogen bond formation the charge redistribution is not in the direction of the dipole axis of the proton acceptor but opposite to it, hence resulting

in the intensity decrease.

Table 8.21 The Ratios of the Complex to Monomer Intensity values in the $PH_3.H_2S$ Complex

Symmetry Species	Mode	Complex A_c/km mol^{-1}	A_c/A_m
a'	ν_1	6.8	1.04
	ν_2	19.2	4.92
	ν_3	78.8	0.79
	ν_4	42.6	1.04
	ν_5	9.6	1.26
	ν_6	16.9	0.85
a"	ν_{11}	81.3	0.82
	ν_{12}	16.1	0.82

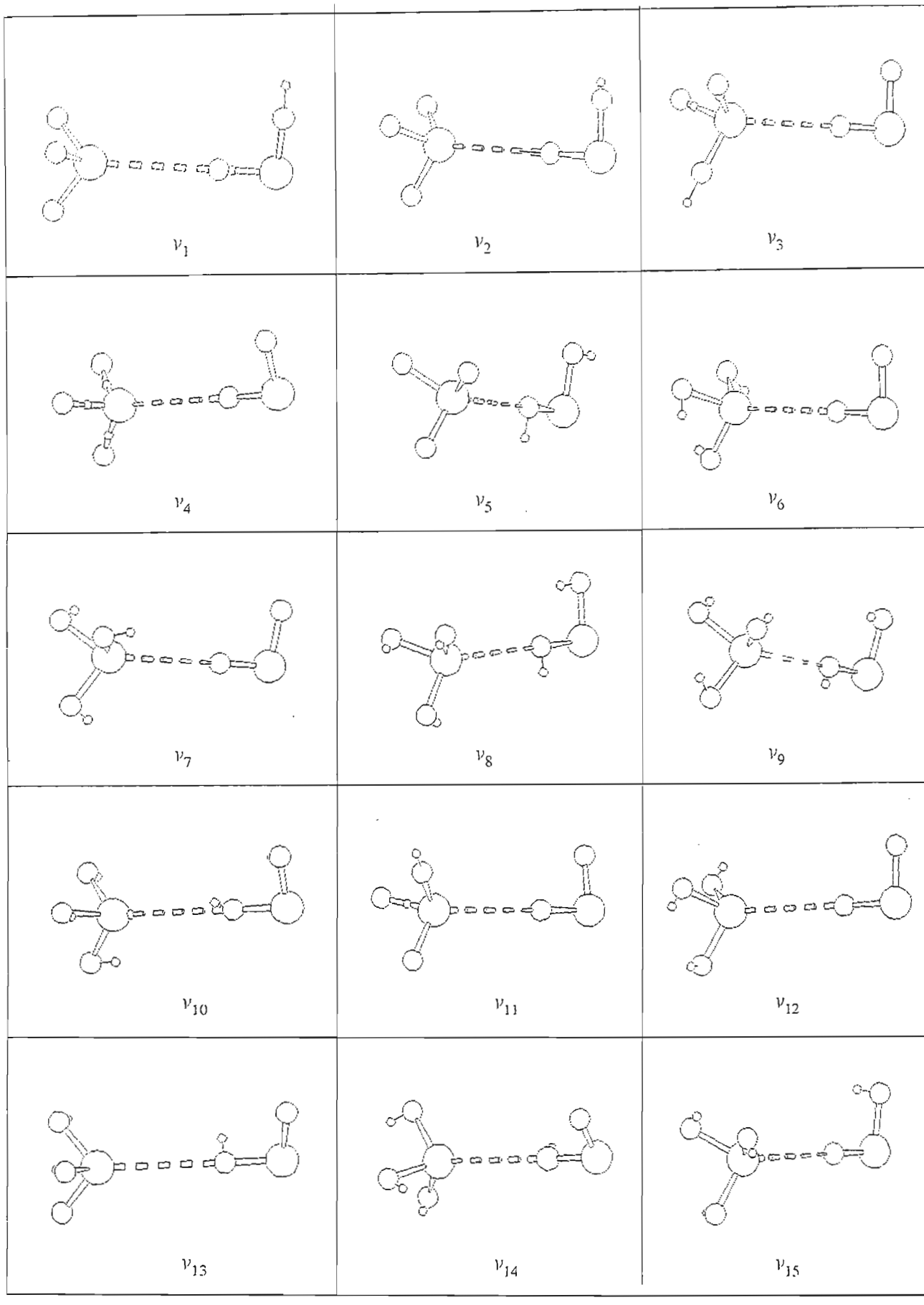

Fig 8.7 Graphical Representation of the $PH_3.H_2S$ Complex Vibration modes

8.4 *The $CH_4.H_2Y$ Complexes (Y= O,S)*

8.4.1 *Geometries*

The structures optimized for the $CH_4.H_2O$ complex comprised CH_4 proton donor to the oxygen of H_2O, with hydrogens eclipsed and staggered in the proton donor and acceptor (figs 8.8 and 8.9) and H_2O the proton donor to the face of the methane tetrahedron (fig 8.10). It is well known that the ability of CH to donate a proton decreases in the order of the type of hybridisation at the carbon atom; $C(sp) > C(sp^2) > C(sp^3)$.[347] Hence one would expect CH_4 to be a weak proton donor compared with H_2O. Previous ab initio studies[283-285,287-290] carried out on the $CH_4.H_2O$ complex report CH_4 acting as the proton donor to H_2O, except for the study of Szczesniak and co-workers[286]; their study involved the use of large basis sets at the near Hartree-Fock level of theory. At this level of theory and basis set they located both complex structures to be local minima on the PES, but the complex having H_2O as proton donor to the methane was found to be the global minimum structure. On attempting to optimize a structure (fig 8.11) similar to that of Szczesniak et al,[286] the resultant structure was found to be a saddle point on the PES. Our study at the MP2/6-31G** level of theory and basis set located the complex having CH_4 as proton donor to H_2O as the local minimum energy structure, while the optimization of the structure having the proton donor-acceptor roles reversed resulted in a saddle point on the PES.

Since H_2S is a stronger acid than H_2O, one would expect H_2S to be proton donor in the complex with methane. Three structures were optimized, two having H_2S as proton donor to methane with the free hydrogen of H_2S eclipsed (fig 8.12) and staggered (fig 8.13) with respect to those of methane respectively and the third structure with methane proton donor to H_2S (fig 8.14), similar to that of the $CH_4.H_2O$ complex.

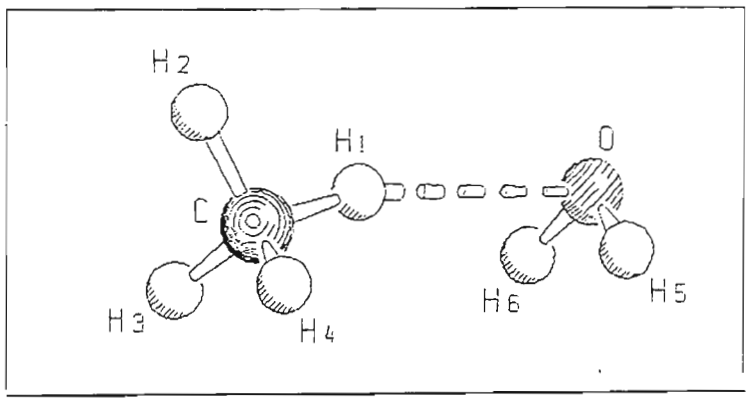

Fig 8.8 The Linear Eclipsed $CH_4.H_2O$ Complex

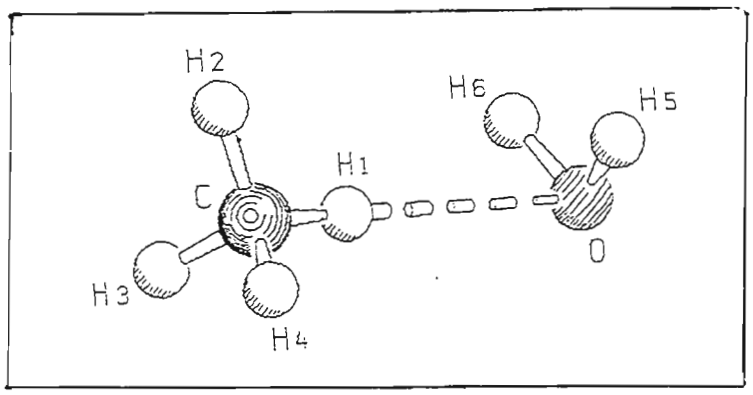

Fig 8.9 The Linear Staggered $CH_4.H_2O$ Complex

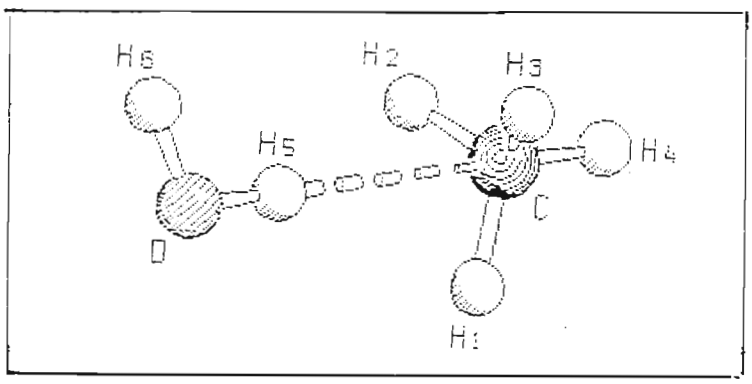

Fig 8.10 The Linear Staggered $H_2O.CH_4$ Complex

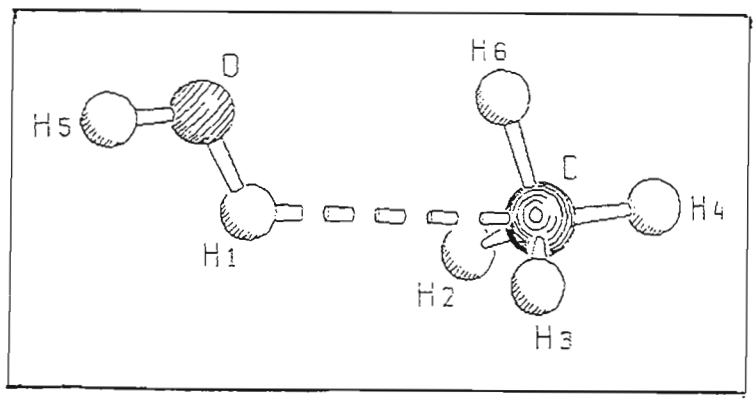

Fig 8.11 The Linear $H_2O.CH_4$ Complex

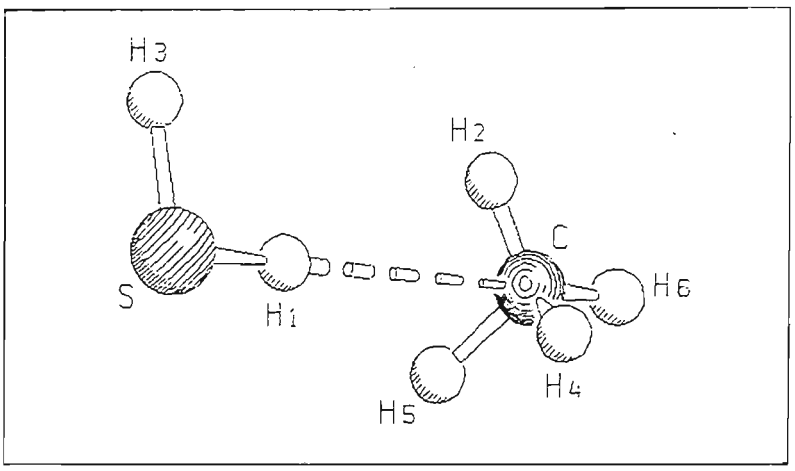

Fig 8.12 The Linear Eclipsed $CH_4.H_2S$ Complex

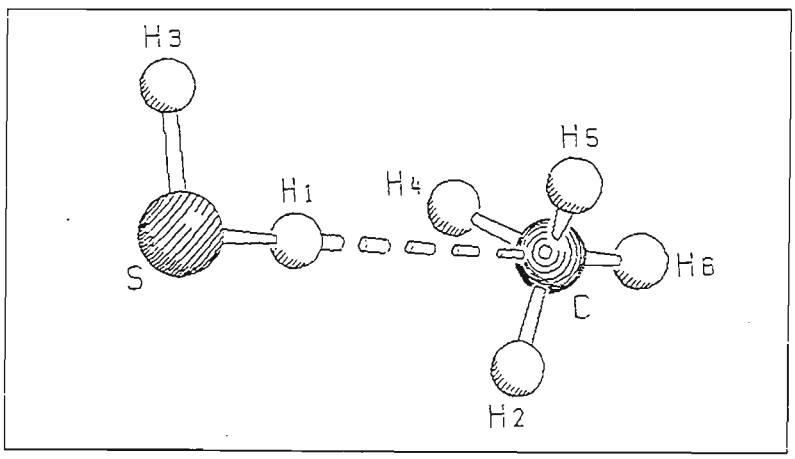

Fig 8.13 The Linear Staggered $CH_4.H_2S$ Complex

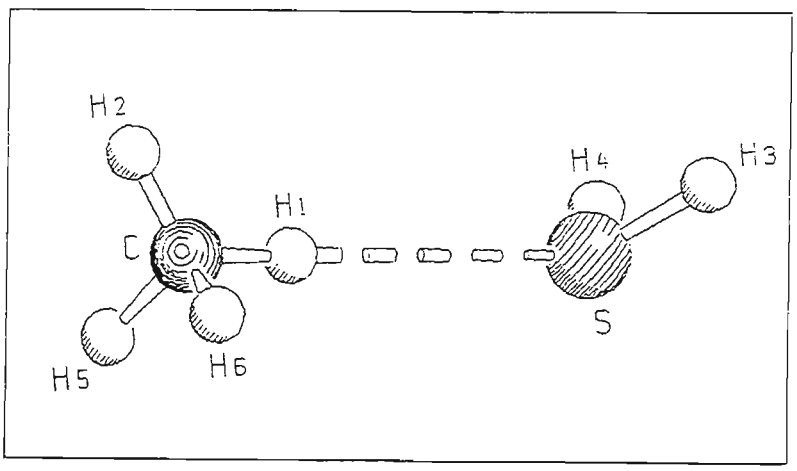

Fig 8.14 The Linear Staggered $H_2S.CH_4$ Complex

The changes in the geometrical parameters in the $CH_4.H_2O$ complex are collected in Table 8.22.

Table 8.22 Geometrical Parameters for the Most Stable $CH_4.H_2O$ Complex

Complex	Parameter	Complex	Monomer	Difference
$CH_4.H_2O$	r(CH2), r(CH3), r(CH4)/pm	108.6	108.4	0.2
	r(CH1)/pm	108.5	108.4	0.1
	r(OH5), r(OH6)/pm	96.2	96.1	0.1
	R(H1..O)/pm	256.0		
	H5OH6 /deg	103.7	103.9	-0.2
	H3CH1, H4CH1 /deg	109.9	109.5	0.4
	H2CH1 /deg	109.4	109.5	-0.1
	CH1..O/deg	167.5		

The major changes occurring in the geometrical parameters occur in the H3CH1 and H4CH1 bond angles by 0.4°. This increase could be due to the repulsion of the hydrogens in the proton acceptor with the hydrogens (H3 and H4) of the proton donor. The remaining geometrical parameters undergo minimal changes on complexation. The H1..O distance of 256 pm coupled with the angle of 167.5° suggests this complex is of the van der Waals type, as in the case of the $MH_4.HX$ series. The microwave studies[281] supporting the structure with H_2O as proton donor to CH_4 along the face of the methane tetrahedron report a C..O distance of 283 pm with a slightly non-linear hydrogen bond.

Our calculated C..O distance (364.5 pm) supports those of Sennikov et al[290] and Sokalski[291] at the MP2/6-31G** and RHF/6-31G** levels of theory, who report C..O separations of 370 and 380 pm respectively. The geometrical parameters for the lowest energy $CH_4.H_2S$ structure are collected in Table 8.23.

Table 8.23 Geometrical Parameters for the Most Stable $CH_4.H_2S$ Complex

Complex	Parameter	Complex	Monomer	Difference
$CH_4.H_2S$	r(CH4), r(CH5)/pm	108.6	108.4	0.2
	r(CH6)/pm	108.5	108.4	0.1
	r(CH2)/pm	108.6	108.4	0.2
	r(SH1)/pm	133.0	132.9	0.1
	r(SH2)/pm	133.0	132.9	0.1
	R(H1..S)/pm	287.3		
	H1SH3/deg	92.9	92.8	0.1
	H2CH6/deg	109.6	109.5	0.1
	H2CH5, H2CH4/deg	109.3	109.5	-0.2
	H6CH5, H6CH4/deg	109.4	109.5	-0.1
	CH1..S/deg	179.8		

The major change in the geometrical parameters involves the decrease in the proton acceptor bond angles (H2CH5, H2CH4) by 0.2°. The CH1..S angle is close to linearity, with a CH1..S distance of 287.3 pm, suggesting possibly a trend towards the conventional

hydrogen bonded type complex. Since this structure is a transition state structure further analysis of the geometrical parameters would be mere speculation.

8.4.2 *Energetics*

The binding energy, together with the percentage dispersion energy contribution and the BSSE calculated at the MP2/6-31G** level of theory and basis set, are collected in Table 8.24 for the $CH_4.H_2O$ complex.

Table 8.24 Binding Energies of the $CH_4.H_2O$ Complex

Complex	$\Delta E'$ /kJ mol^{-1}	ΔE /kJ mol^{-1}	BSSE /kJ mol^{-1}	$\%\Delta E_{Disp}$
$CH_4.H_2O$	0.69	-8.09	8.78	-[a]

a - not determined (due to the $CH_4.H_2O$ complex being unbound at the SCF level)

From Table 8.24, the $CH_4.H_2O$ complex is plagued by BSSE and is unbonded at the correlated level of theory. Similar findings were also observed by Szczesniak et al[286]; as the C-H bond penetrates the oxygen lone-pair electronic field the BSSE increases rapidly. The spurious effects of BSSE in the complex are strongly expressed by Szczesniak et al[286] and must be accounted for; this led to incorrect binding energies obtained by both Sennikov et al[290] and Novoa et al.[285] Latajka and Scheiner[289] had earlier presented a thorough discussion on the BSSE effects in this complex and other weakly bonded complexes. The percentage dispersion energy contribution to the binding energy was found to be over 100%, clearly resulting from the BSSE effects on the interaction energies. The Morokuma energy decomposition analyses is collected in Table 8.25 for the $CH_4.H_2O$ complex.

Table 8.25 Energy Decomposition Analysis of the $CH_4.H_2O$ Complex /kJ mol^{-1}

Complex	ES	EX	CT	PL	MIX	Total
$CH_4.H_2O$	-2.8	5.6	-2.6	-0.18	1.8	1.8

The EX term (5.6 kJ mol^{-1}) is the dominating component in the SCF interaction energy, rendering the complex repulsive at the SCF level of theory. The domination of the EX term arises from the steric repulsion of the hydrogens of methane with those of water. Hence this complex is not governed by electrostatic forces involving a dipole-octupole interaction, as suggested by Szczesniak et al.[286] The early study by Morokuma et al[10] showed the ES and EX terms to balance each other, thus rendering the complex stable, with neglect of BSSE. The MP2 energies for the different structures in the $CH_4.H_2S$ complex are reported in Table 8.26.

Table 8.26 MP2 Energies of the $CH_4.H_2S$ Complexes /Hartrees

Structure	E_{MP2}
I	-439.17551069217
II	-439.17550969217
III	-439.17529089659

Structure I was found to have the lowest MP2 energy. Since no local minimum energy structure was optimized for these complexes, it would be futile to calculate the binding energies and carry out the Mulliken charge analyses for these complexes. Unlike the $CH_4.H_2O$ complex, having water as the proton donor, this complex has the corresponding structure as the least stable energetically. Structure I, having H_2S as proton donor was

found to have the lowest MP2 energy, followed by structure II.

8.4.3 *Mulliken Charge Analysis*

The Mulliken charge analysis for the $CH_4.H_2O$ complex is reported in Table 8.27.

Table 8.27 Mulliken Charge Analysis for the $CH_4.H_2O$ Complex

Atom	Atomic Charge /e		Difference /e
	Complex	Monomer	
H5	0.340	0.337	0.003
O	-0.664	-0.674	0.010
H6	0.340	0.337	0.003
			0.016
C	-0.492	-0.473	-0.019
H1	0.133	0.118	0.015
H2	0.122	0.118	0.004
H3	0.110	0.118	-0.008
H4	0.110	0.118	-0.008
			-0.016

The negative charge donation (-0.016 e) occurs from the proton acceptor to the donor. Most of this charge originates from the oxygen of the proton acceptor and H1 of the proton donor. The hydrogens of the proton donor eclipsing those of H_2O gain negative

charge (-0.008 e), resulting in a greater repulsion with the bonded CH1 electrons, thus resulting in an increase in the H3CH1 and H4CH1 bond angles.

8.4.4 *Vibrational Properties of the $CH_4.H_2Y$ Complexes*

The calculated vibrational spectra, potential energy distributions and infrared intensities at the MP2/6-31G** level of theory for the $CH_4.H_2Y$ complexes are collected in Tables 8.28 - 8.33. The plots of the normal modes of vibration of $CH_4.H_2O$ are shown in fig 8.15.

In the case of the proton donor the a' CH stretching modes, ν_2, ν_3 and ν_4, are red-shifted by 2, 14 and 13 cm^{-1}, while the bending modes, ν_6, ν_7 and ν_8, are blue shifted by 9, 12 and 1 cm^{-1} respectively. In the case of the a" modes of the proton donor, ν_{13} and ν_{15}, being the antisymmetric stretching and bending modes, are red and blue shifted by 20 and 17 cm^{-1} respectively. The red and blue shifting of the stretching and bending modes of the proton donor follows the trend of a hydrogen bonded complex. The water symmetric stretching and bending modes are red shifted by 17 cm^{-1} and 2 cm^{-1} while the antisymmetric stretching mode is red shifted by 20 cm^{-1}. Overall the wavenumber shifts are less than 20 cm^{-1}, being only slightly perturbed from their corresponding monomer bands.

Table 8.28 Calculated Wavenumber Shifts on complexation in the $CH_4.H_2O$ Complex

Symmetry Species	Mode	Complex Wavenumber /cm^{-1}	Monomer Wavenumber /cm^{-1}	Shift[(a)] /cm^{-1}
a'	ν_1	3883	3900	-17
	ν_2	3287	3289	-2
	ν_3	3275	3289	-14
	ν_4	3130	3143	-13
	ν_5	1681	1683	-2
	ν_6	1632	1623	9
	ν_7	1414	1402	12
	ν_8	1403	1402	1
a"	ν_{12}	4019	4039	-20
	ν_{13}	3269	3289	-20
	ν_{14}	1634	1623	11
	ν_{15}	1419	1402	17

(a) Shift = Complex - Monomer

The calculated wavenumber shifts occurring on complexation in the $CH_4.H_2S$ complex are collected in Table 8.29. The major wavenumber shift occurring on complexation occurs in ν_2 and ν_{13} (15 cm^{-1}), with the remaining modes shifted by less than 20 cm^{-1}. The trend of the wavenumber shifts in this complex is like those in a traditional hydrogen bonded

complex, involving the red and blue shifts in the stretching and bending modes of the proton donor respectively. The magnitude of the intermolecular mode having the negative wavenumber (-11 cm^{-1}) is indicative of a transition state structure.

Table 8.29 Calculated Wavenumber Shifts on complexation in the $CH_4.H_2S$ Complex

Symmetry Species	Mode	Complex Wavenumber /cm^{-1}	Monomer Wavenumber /cm^{-1}	Shift[(a)] /cm^{-1}
a'	ν_1	3277	3289	-12
	ν_2	3274	3289	-15
	ν_3	3129	3143	-14
	ν_4	2866	2871	-5
	ν_5	2840	2845	-5
	ν_6	1623	1623	0
	ν_7	1406	1402	4
	ν_8	1401	1402	-1
	ν_9	1270	1269	1
a"	ν_{13}	3274	3289	-15
	ν_{14}	1622	1623	-1
	ν_{15}	1405	1402	3

(a) Complex - Monomer

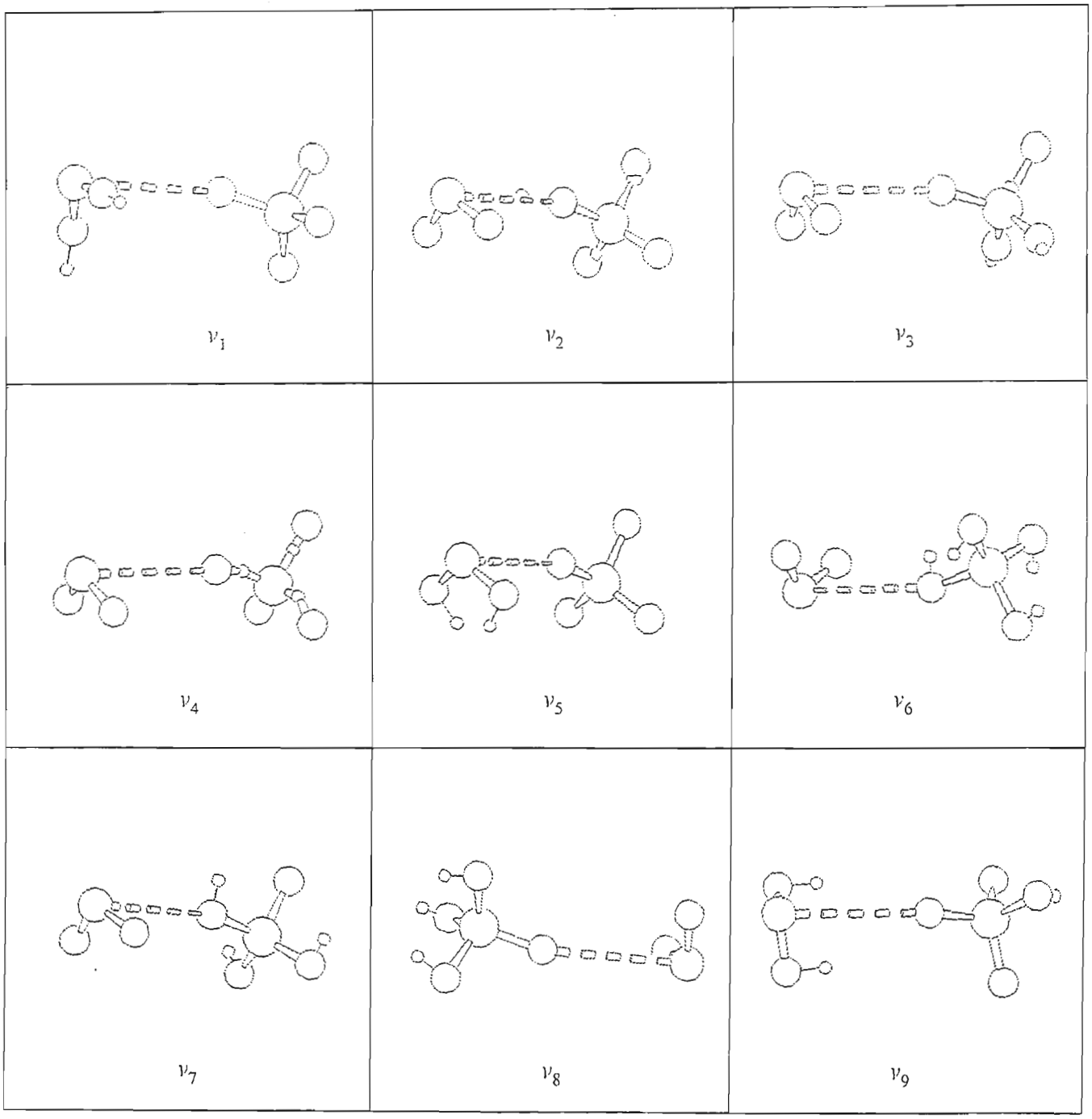

Fig 8.15 Graphical Representation of the CH_4 .H_2O Complex Vibration modes

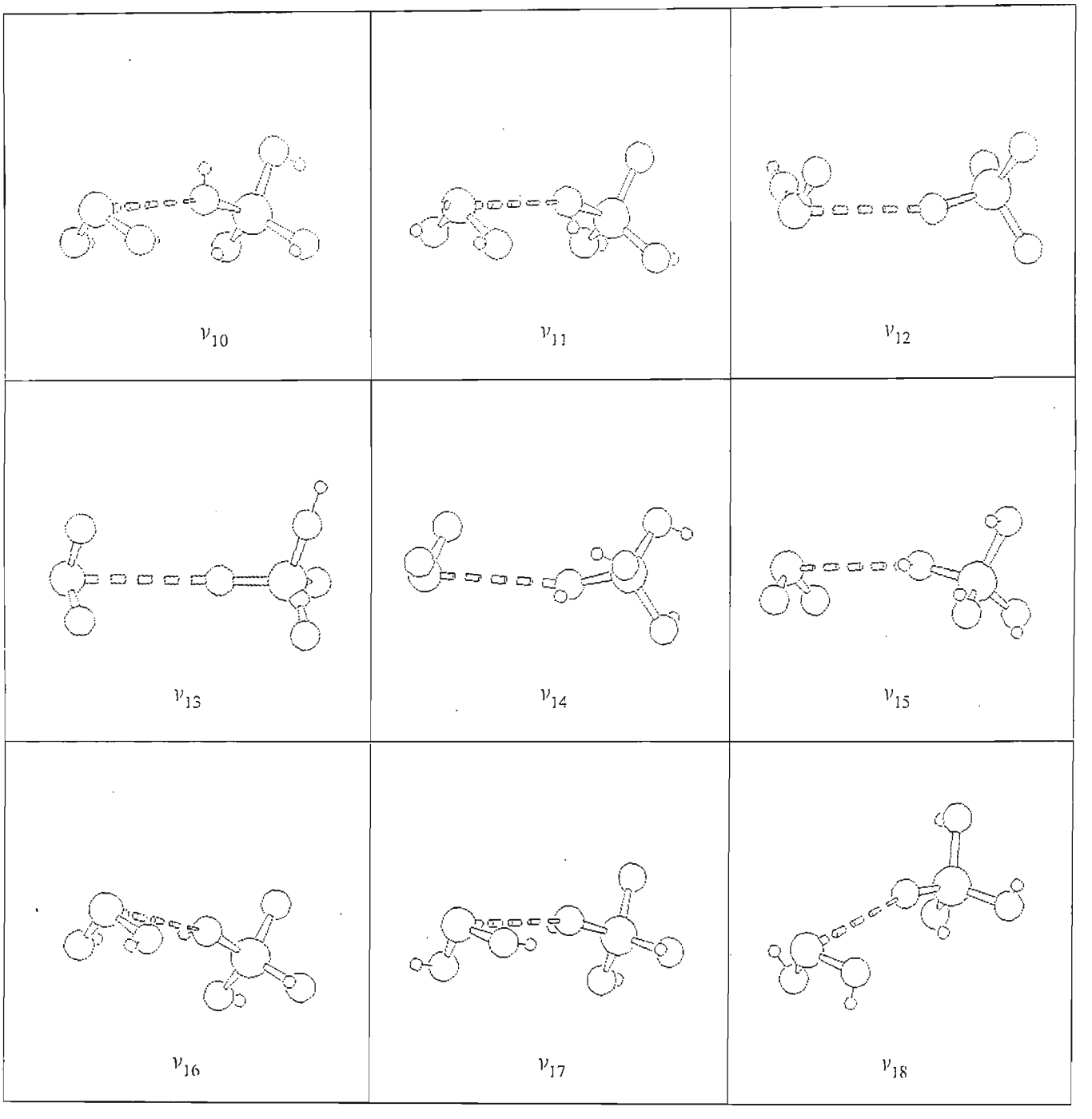

Fig 8.15 Graphical Representation of the CH_4 .H_2O Complex Vibration modes

The symmetry coordinate descriptions for the various modes in the $CH_4.H_2O$ complex are collected in Table 8.30. The symmetry coordinates for the proton donor were generated using the symmetry coordinates for a C_{3v} molecule, since on complexation the local symmetry of methane is reduced from T_d to C_{3v}. In the case of the proton acceptor the symmetry coordinates were similar to those in the monomer. The symmetry coordinates for the intermolecular modes were generated according to the rules of Wilson et al.[70] The percentage PED's of the vibrational modes in the $CH_4.H_2O$ complex are collected in Table 8.31. The ν_1, ν_{12} and ν_{13} modes have 100% PED from their corresponding symmetry coordinate descriptions. These modes are due to the symmetric and antisymmetric stretching modes of the proton acceptor and the antisymmetric stretching of the proton donor respectively. The ν_2, ν_3 and ν_4 modes have contributions to their PED's from both the bonded and non-bonded CH bonds of the proton donor. The proton acceptor ν_5 mode also has a small contribution to its PED from the proton donor mode. In the case of the intramolecular modes of the proton donor, there is no contribution from the symmetry coordinates of the proton acceptor. The intermolecular modes, on the other hand, show a large degree of mixing in the PED's amongst the symmetry coordinates of both the proton donor and acceptor. The wagging and twisting modes of the proton acceptor are coupled with the symmetric and antisymmetric bending modes of the proton donor respectively.

Table 8.30 Symmetry Coordinates for the $CH_4.H_2O$ Complex

Complex	Symmetry Coordinate	Description
$CH_4.H_2O$	$S_1 = 1/\sqrt{2}(\Delta r_3 + \Delta r_4)$	H_2O symmetric stretch
	$S_2 = \Delta r_2$	CH stretch (bonded)
	$S_3 = \Delta r_5$	CH stretch
	$S_4 = 1/\sqrt{2}(\Delta r_6 + \Delta r_7)$	CH_2 symmetric stretch
	$S_5 = 1/\sqrt{6}(2\Delta\theta_1 - \Delta\theta_2 - \Delta\theta_3)$	HOH bend
	$S_6 = 1/\sqrt{6}(2\Delta\beta_1 - \Delta\beta_2 - \Delta\beta_3)$	CH_3 bend
	$S_7 = 1/\sqrt{6}(2\Delta\alpha_1 - \Delta\alpha_2 - \Delta\alpha_3)$	CH_3 bend
	$S_8 = 1/\sqrt{6}(\Delta\alpha_1 + \Delta\alpha_2 + \Delta\alpha_3 - \Delta\beta_1 - \Delta\beta_2 - \Delta\beta_3)$	CH_3 symmetric bend
	$S_9 = \Delta R$	H..O stretch
	$S_{10} = \Delta\pi_1$	CH..O in plane bend
	$S_{11} = 1/\sqrt{2}(\Delta\theta_2 + \Delta\theta_3)$	HOH wag
	$S_{12} = 1/\sqrt{2}(\Delta r_1 - \Delta r_2)$	H_2O antisymmetric stretch
	$S_{13} = 1/\sqrt{2}(\Delta r_6 - \Delta r_7)$	CH_2 antisymmetric stretch
	$S_{14} = 1/\sqrt{2}(\Delta\theta_1 - \Delta\theta_2)$	HOH twist
	$S_{15} = 1/\sqrt{2}(\Delta\beta_2 - \Delta\beta_3)$	CH_2 antisymmetric bend
	$S_{16} = 1/\sqrt{2}(\Delta\alpha_2 - \Delta\alpha_3)$	CH_2 antisymmetric bend
	$S_{17} = \Delta\pi_2$	CH..O out of plane bend

Table 8.30 Continued

	$S_{18} = \Delta\gamma$	torsion about H-bond

The in- and out of plane CH..O bending modes have large contributions from the CH..O stretching and the antisymmetric bending modes of the proton donor. The CH..O stretching mode at 99 cm^{-1} also has a contribution from the wagging mode of the proton acceptor. The coupling of the symmetry coordinates in the PED's of the intermolecular modes suggest the weakness in the CH..O bond as was reflected earlier.

Table 8.31 Wavenumbers and %PEDs in the $CH_4.H_2O$ Complex

Symmetry Species	Wavenumbers /cm^{-1}	%PEDs
a'	3883	$100S_1$
	3287	$76S_2 + 11S_3 + 12S_4$
	3275	$65S_3 + 34S_4$
	3130	$54S_3 + 24S_4 + 22S_2$
	1681	$93S_5 + 4S_8 + 3S_1$
	1632	$54S_6 + 46S_7$
	1414	$44S_6 + 54S_7$
	1403	$98S_8 + 2S_5$
	226	$87S_{11} + 15S_6$
	146	$44S_{10} + 38S_9 + 17S_8$

Table 8.31 Continued

	99	$54S_9 + 41S_{11}$
a"	4019	$100S_{12}$
	3269	$100S_{13}$
	1634	$53S_{16} + 46S_{15}$
	1419	$46S_{16} + 53S_{14}$
	206	$96S_{14} + 4S_{15}$
	107	$100S_{17}$
	14	$100S_{18}$

The changes in the intensities of the vibrational modes on complexation in the $CH_4.H_2O$ complex are collected in Table 8.32. The ratios of the complex / monomer intensities are close to unity except for ν_2. The intensities of the H_2O stretching modes are slightly enhanced on complexation. Overall the weakness of the CH..O bond is once again reflected by the absence of any significant intensity enhancement. The intermolecular HOH wagging, in plane hydrogen bond bending and the torsional modes exhibit high intensity values of 262.9, 89.5 and 55.2 km mol^{-1} respectively.

Table 8.32 Ratios of Complex to Monomer Intensity values in the $CH_4.H_2O$ Complex

Symmetry Species	Mode	Complex A_c/km mol^{-1}	A_c/A_m
a'	ν_1	5.4	1.28
	ν_2	2.7	0.12
	ν_3	21.6	1.01
	ν_4	4.1	-[(a)]
	ν_5	75.7	0.97
	ν_6	0.1	-[(a)]
	ν_7	9.3	0.82
	ν_8	11.1	0.98
a"	ν_{12}	37.1	1.09
	ν_{13}	24.6	1.15
	ν_{14}	0.1	-[(a)]
	ν_{15}	9.9	0.87

(a) The monomer modes are infrared inactive

The ratios of the complex / monomer intensities in the $CH_4.H_2S$ complex are collected in Table 8.33. The major intensity enhancement occurring on complexation in the $CH_4.H_2S$ complex occurs in ν_8 by 1.73-fold. The proton donor stretching mode intensities are decreased 0.74 and 0.65-fold, respectively, while the bending mode is enhanced by 1.25-fold. In the case of the proton acceptor the intensity enhancements are close to unity

except for ν_8.

Table 8.33 Ratios of Complex to Monomer Intensity values in the $CH_4.H_2S$ Complex

Symmetry Species	Mode	Complex A_c/km mol^{-1}	A_c/A_m
a'	ν_1	23.5	1.11
	ν_2	19.4	0.91
	ν_3	0.6	-[(a)]
	ν_4	2.9	0.74
	ν_5	2.5	0.65
	ν_6	0.2	-[(a)]
	ν_7	12.8	1.09
	ν_8	20.3	1.73
	ν_9	9.5	1.25
a"	ν_{13}	17.7	0.83
	ν_{14}	0.3	-[(a)]
	ν_{15}	12.3	1.05

(a) The monomer modes are infrared inactive

8.5 *The $SiH_4.H_2Y$ Complexes (Y=O,S)*

8.5.1 *Geometries*

The $SiH_4.H_2Y$ complexes have received much less attention than the corresponding methane complexes, both theoretically and experimentally. The study of the $SiH_4.H_2O$ complex, by Sennikov et al,[290] resulted in an interaction between the silicon and the oxygen atom, with the hydrogen atoms of the H_2O eclipsing those of silane. These types of complexes are classed as the electron donor-acceptor type, purely due to an electrostatic interaction involving silicon and oxygen. The structures optimized for this complex comprise Si..O interaction with the hydrogens staggered and eclipsed relative to those of the hydrogens in silane, with a Si..OH angle being perpendicular and obtuse respectively, resulting in four plausible structures as shown in figs 8.16-8.19.

The structure having the Si..OH angle close to 90°, together with the hydrogens of water eclipsing those of silane, was found to be the global minimum on the PES. Our global minimum energy structure supports the structure obtained by Sennikov et al[290] at the MP2/6-31G* level of theory. In the case of the corresponding $SiH_4.H_2S$ complex no studies had been carried out either theoretically or experimentally. Structures similar to those of the $SiH_4.H_2O$ complex were optimized (figs 8.20-8.21). The structure with a Si..S interaction and a less perpendicular Si..SH angle, with the hydrogens of H_2S staggered with respect to those of silane was found to be the global minimum, with the other structures being saddle points on the PES. The changes in the geometrical parameters in the most stable $SiH_4.H_2O$ complex are collected in Table 8.34.

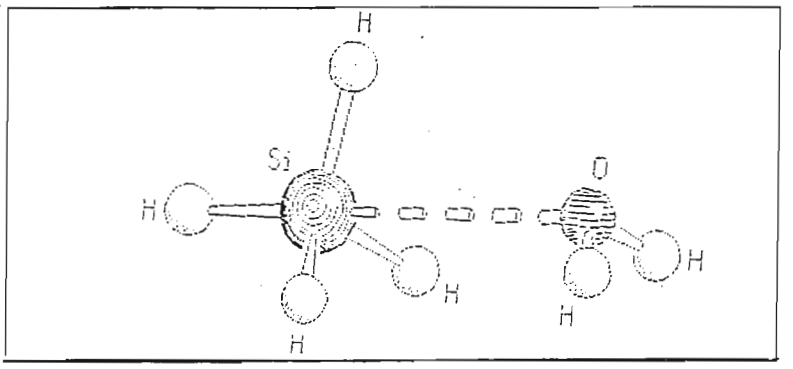

Fig 8.16 The Linear Tetrahedral Eclipsed $SiH_4.H_2O$ Complex

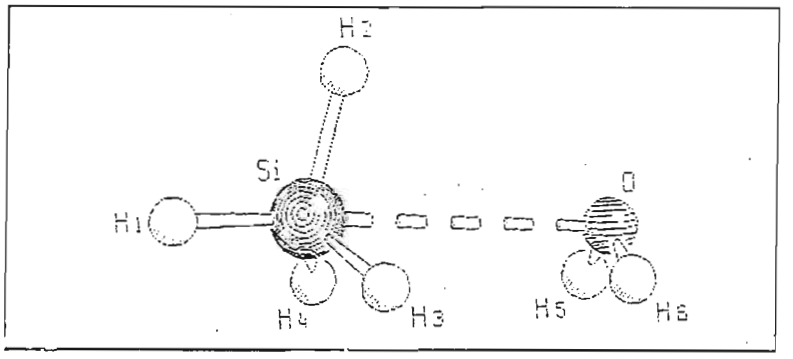

Fig 8.17 The Linear Perpendicular Eclipsed $SiH_4.H_2O$ Complex

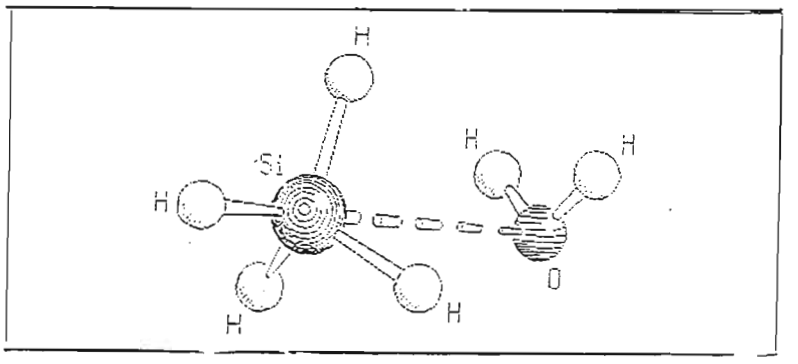

Fig 8.18 The Linear Tetrahedral Staggered $SiH_4.H_2O$ Complex

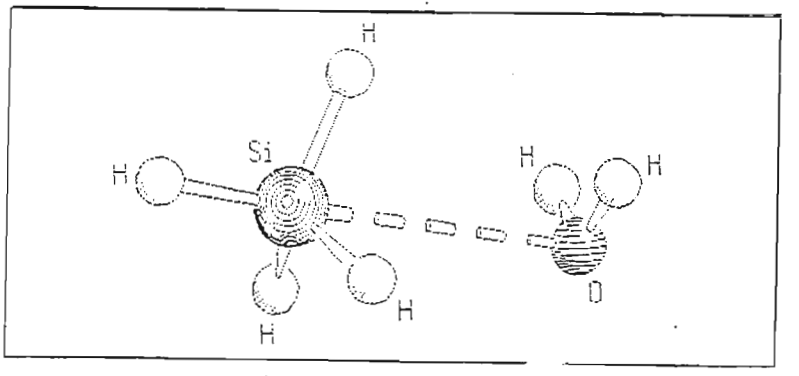

Fig 8.19 The Linear Perpendicular Staggered $SiH_4.H_2O$ Complex

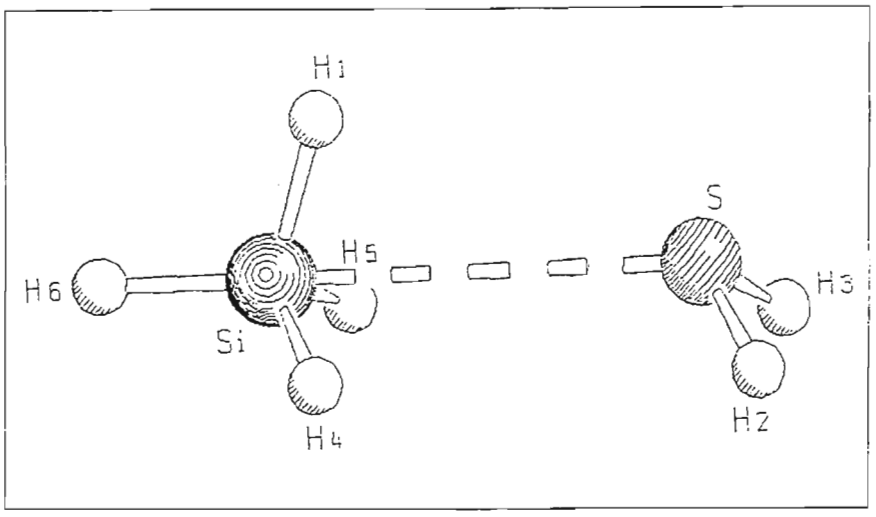

Fig 8.20 The Linear Tetrahedral Eclipsed $SiH_4.H_2S$ Complex

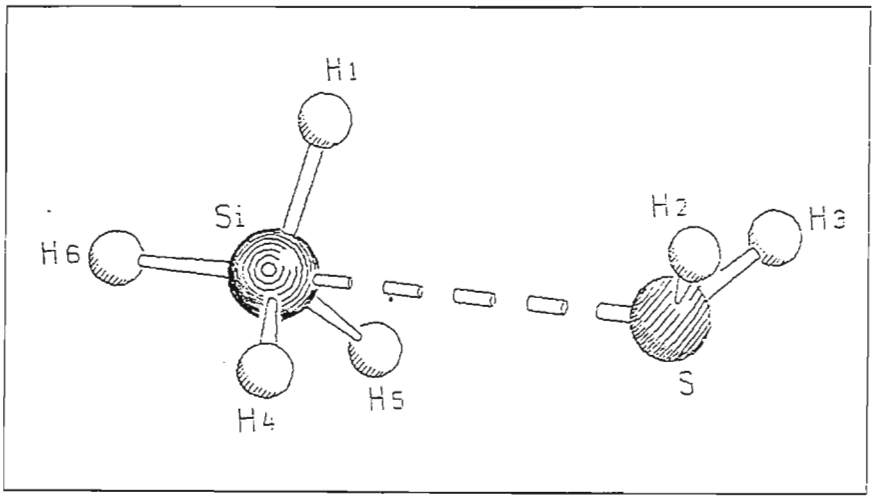

Fig 8.21 The Linear Tetrahedral Staggered $SiH_4.H_2S$ Complex

Table 8.34 Geometrical Parameters for the Most Stable $SiH_4.H_2O$ Complex

Complex	Parameter	Complex	Monomer	Difference
$SiH_4.H_2O$	r(SiH1)/pm	147.0	147.1	-0.1
	r(SiH6)/pm	147.7	147.1	0.6
	r(SiH4), r(SiH5)/pm	147.3	147.1	0.2
	R(Si..O)/pm	328.1		
	r(OH2), r(OH3)/pm	96.3	96.1	0.2
	H2OH3 /deg	103.9	103.9	0.0
	H1SiH6/deg	108.8	109.5	-0.7
	H1SiH4, H1SiH5 /deg	108.4	109.5	-1.1
	Si..OH2/deg	89.9		

On complexation the major changes in the geometrical parameters occur in the H1SiH4 and H1SiH5 bond angles by 1.1°. These changes in the bond angles are due to the steric repulsion between the hydrogens of water eclipsing those of silane. The values of the H1SiH4 and H1SiH5 angles (110.6°) reported by Sennikov et al[290] are much greater than those optimized in this study. The SiH6 distance increases by 0.6 pm due to the charge transfer from the oxygen lone pair electrons to the antibonding orbitals of the electropositive silicon. Sennikov et al[290] obtained a Si..O distance of 319.6 pm, less than our value of 328.1 pm. The changes in the geometrical parameters in the $SiH_4.H_2S$ complex are collected in Table 8.35.

Table 8.35 Geometrical Parameters for the Most Stable $SiH_4.H_2S$ Complex

Complex	Parameter	Complex	Monomer	Difference
$SiH_4.H_2S$	r(SiH1)/pm	147.3	147.1	0.2
	r(SiH6)/pm	147.6	147.1	0.5
	r(SiH4), r(SiH5)/pm	147.3	147.1	0.2
	R(Si..S)/pm	393.6		
	r(SH3), r(SH2)/pm	133.0	132.9	0.1
	H3SH4/deg	92.8	92.8	0.0
	H1SiH6/deg	109.0	109.5	-0.5
	H1SiH4, H1SiH5/deg	109.9	109.5	0.4
	Si..SH3/deg	115.0		

The SiH6 bond length increases by 0.5 pm while the H6SiH1 angle decreases by 0.5° on complexation. The increase in the SiH6 bond distance results from the charge donation from the donor to the antibonding orbitals of the SiH6 bond. The H6SiH1 angle decreases due to the steric repulsion of the hydrogens of H_2S eclipsing those of silane. The geometrical parameters of H_2S remain almost unperturbed on complexation, similar to the case of the $SiH_4.H_2O$ complex. The Si..S distance of 393.6 pm is much longer than that in the $SiH_4.H_2O$ complex, suggesting this electron donor-acceptor complex to be weaker. The angular orientation of the H_2S molecule compared with that of H_2O in the $SiH_4.H_2O$ complex is less perpendicular while in the $H_2S.HX$ series the orientation about the sulphur of H_2S was perpendicular. This change in the orientation about the sulphur was attributed

to the hybridisation at Y in the $H_2Y.HX$ complexes. In the case of the $SiH_4.H_2O$ complex the negatively charged hydrogens (H3 and H4) exert an attractive force on the positively charged hydrogens (H5 and H6) of the water sub-unit, thus forcing them closer together. In the case of the $SiH_4.H_2S$ complex, the orientation of the hydrogens in both silane and hydrogen sulphide are staggered with respect to each other, thus the electrostatic forces exerted by the hydrogens are not as strong as in the case of the $SiH_4.H_2O$ complex.

8.5.3 *Energetics*

The binding energies calculated at the MP2/6-31G** level together with the percentage dispersion energy contributions are collected in Table 8.36 for the $SiH_4.H_2Y$ complexes.

Table 8.36 The Binding Energies for the $SiH_4.H_2Y$ Complexes

Complex	$\Delta E'$ /kJ mol^{-1}	ΔE /kJ mol^{-1}	BSSE /kJ mol^{-1}	$\%\Delta E_{Disp}$
$SiH_4.H_2O$	-1.50	-13.7	12.3	98.0
$SiH_4.H_2S$	-1.09	-3.77	2.68	-[a]

a - not determined (due to this complex being unbound at the SCF level)

From Table 8.36, the $SiH_4.H_2O$ complex is more strongly bonded than the $SiH_4.H_2S$ complex. The role of dispersion plays a greater role in the $SiH_4.H_2O$ complex, probably arising from the greater attractive force of the eclipsed hydrogens in the case of the water complex than the staggered hydrogens in the $SiH_4.H_2S$ complex. In the case of both these complexes the BSSEs are large and could lead to drastic errors in the binding energies if omitted. Our uncorrected binding energy for the $SiH_4.H_2O$ complex is close to that

obtained by Sennikov et al[290] at the MP2/6-31G* level of theory (-10.13 kJ mol^{-1}). The Morokuma energy decomposition analyses for the $SiH_4.H_2Y$ complexes are collected in Table 8.37.

The exchange repulsion is the dominating term in both the $SiH_4.H_2O$ (8.9 kJ mol^{-1}) and $SiH_4.H_2S$ (5.2 kJ mol^{-1}) complexes. The magnitude of the exchange repulsion is greater in the $SiH_4.H_2O$ complex due to the steric effects of the eclipsed hydrogens. The ES term is the dominating attractive force, followed by the CT term in both complexes. There is a greater degree of charge transfer occurring in the water than in the hydrogen sulphide complex. At the SCF level the $SiH_4.H_2S$ complex is unbonded (0.7 kJ mol^{-1}) while the $SiH_4.H_2O$ complex is weakly bonded (-0.1 kJ mol^{-1}).

Table 8.37 Energy Decomposition Analysis of the $SiH_4.H_2Y$ Complexes /kJ mol^{-1}

Complex	ES	EX	CT	PL	MIX	Total
$SiH_4.H_2O$	-6.9	8.9	-3.7	-0.6	2.2	-0.1
$SiH_4.H_2S$	-3.8	5.2	-0.8	-0.2	0.3	0.7

8.5.4 *Mulliken Charge Analysis*

The Mulliken charge analysis in the $SiH_4.H_2O$ complex is collected in Table 8.38. The charge donation occurs from water to silane (-0.028 e) in the $SiH_4.H_2O$ complex. A large proportion of this charge has its origin from the oxygen of the electron donor. The charge influx to the electron acceptor occurs through silicon and eventually to H4 and H5. The gain of negative charge in H4 and H5 results in the electrostatic repulsion between these hydrogens, thus resulting in an increase in the H1SiH4 and H1SiH5 bond angles. The Mulliken charge analysis in the $SiH_4.H_2S$ complex is reported in Table 8.39. The charge donation occurs from SiH_4 to H_2S (-0.001 e) which is the reverse of that in the $SiH_4.H_2O$

complex. Most of the charge loss occurs at silicon (0.025 e) and the hydrogens of the electron acceptor. This charge is distributed to the hydrogens and the sulphur of the electron donor. The increase in the bond lengths and angles could be attributed to the gain of charge in the antibonding orbitals of the electron donor (due to the increased repulsion of the hydrogens in the electron donor).

Table 8.38 Mulliken Charge Analysis for the $SiH_4.H_2O$ Complex

Atom	Atomic Charge /e		Difference
	Complex	Monomer	/e
O	-0.657	-0.674	0.017
H2	0.342	0.336	0.006
H3	0.342	0.336	0.006
			0.029
Si	0.690	0.667	0.023
H1	-0.158	-0.167	0.009
H4	-0.190	-0.167	-0.023
H5	-0.190	-0.167	-0.023
H6	-0.181	-0.167	-0.014
			-0.028

Table 8.39 Mulliken Charge Analysis for the $SiH_4.H_2S$ Complex

Atom	Atomic Charge /e		Difference /e
	Complex	Monomer	
S	-0.137	-0.132	-0.005
H2	0.068	0.066	0.002
H3	0.068	0.066	0.002
			-0.001
Si	0.692	0.667	0.025
H1	-0.171	-0.167	-0.004
H4	-0.172	-0.167	-0.005
H5	-0.172	-0.167	-0.005
H6	-0.177	-0.167	-0.010
			0.001

8.5.6 *Vibrational Properties of the $SiH_4.H_2O$ Complex*

The calculated vibrational spectra and infrared intensities at the MP2/6-31G** level of theory for the $SiH_4.H_2Y$ complexes are shown in Tables 8.40 - 8.43. The plots of the normal modes of vibrations are collected in figs 8.22 and 8.23 for the $SiH_4.H_2O$ and $SiH_4.H_2S$ complexes respectively.

Table 8.40 Calculated Wavenumber Shifts on complexation in the $SiH_4.H_2O$ Complex

Symmetry Species	Mode	Complex Wavenumber /cm^{-1}	Monomer Wavenumber /cm^{-1}	Shift[(a)] /cm^{-1}
a'	ν_1	3879	3900	-21
	ν_2	2370	2355	15
	ν_3	2340	2355	-15
	ν_4	2331	2345	-14
	ν_5	1678	1683	-5
	ν_6	1023	1017	6
	ν_7	979	972	7
	ν_8	978	972	6
a"	ν_{12}	4015	4039	-24
	ν_{13}	2347	2355	-8
	ν_{14}	1029	1017	12
	ν_{15}	979	972	7

(a) Complex - Monomer

The major wavenumber shifts occurring on complexation occur in ν_1 and ν_{12}, the symmetric and antisymmetric stretching modes of the electron donor respectively. The remaining vibrational modes are slightly shifted from their monomer positions with magnitudes less than 20 cm^{-1}. In the case of the electron acceptor, the symmetric

stretching modes are red shifted except for ν_2. The blue shifting of ν_2 results from the position of this hydrogen being off-axis to the electron donor hence having a greater degree of vibrational freedom on executing the stretching mode in the complex. The silane symmetric bending modes are slightly perturbed from their monomer positions. The intermolecular modes include ν_9 (248 cm^{-1}) and ν_{10} (179 cm^{-1}), being the geared and antigeared rocking modes of both SiH_4 and H_2O respectively, and ν_{11} (78 cm^{-1}) which is the Si..O stretching mode. The ν_{16} (268 cm^{-1}) and ν_{17} (164 cm^{-1}) modes incorporate the out of plane rocking modes of the electron donor and acceptor. Lastly ν_{18} (34 cm^{-1}) involves the torsional mode about the Si..O axis. The magnitude of the wavenumber shifts are negligible when compared with the shifts observed in strongly hydrogen bonded complexes like the $NH_3.H_2O$ complex. The ratio of the complex to monomer intensities in the $SiH_4.H_2O$ complex are collected in Table 8.41. The major changes in the intensities occur in ν_1, where the intensity of the symmetric stretching mode in the electron donor is almost doubled. The ν_4, ν_6 and ν_{14} modes have no intensity ratios, since their monomer modes were infrared inactive (a_1 and e modes of silane). The intensity ratios for the electron acceptor are all less than unity. The weakness of this complex is emphasised in the small intensity changes on complexation.

The calculated vibrational spectrum of the $SiH_4.H_2S$ complex is collected in Table 8.42. The major wavenumber shift occurring in this complex occurs in ν_4 (11 cm^{-1}). The remaining vibrational modes are all shifted by less than 10 cm^{-1} from their monomer wavenumbers. The electron acceptor symmetric stretching (ν_1) and bending modes (ν_5) are both red shifted by 7 and 2 cm^{-1} respectively, similar to those in the $SiH_4.H_2O$ complex. The ν_2 mode involves the stretching of the SiH bond in the plane of the electron acceptor, while ν_3 involves the stretching of the SiH bonds staggered with respect to the hydrogens of the electron acceptor. The ν_4 mode is due to the stretching of the SiH bond along the Si..S axis. The symmetric stretching modes of the electron donor are red shifted while the

bending modes, ν_7 and ν_8, are blue and red shifted by 4 and 3 cm^{-1} respectively.

Table 8.41 Ratios of the Complex to Monomer Intensities in the $SiH_4.H_2O$ Complex

Symmetry Species	Mode	Complex A_c/km mol^{-1}	A_c/A_m
a'	ν_1	9.2	2.19
	ν_2	127.6	0.78
	ν_3	103.9	0.64
	ν_5	72.1	0.93
	ν_7	185.7	0.99
	ν_8	188.3	1.02
a"	ν_{12}	39.6	1.17
	ν_{13}	180.9	0.97
	ν_{15}	160.8	0.86

The antisymmetric stretching and bending modes of the electron donor are red and blue shifted respectively. The trend in the wavenumber shifts in both the $SiH_4.H_2O$ and $SiH_4.H_2S$ complexes are consistent with one another. The symmetric intermolecular modes comprise the in plane rocking modes (151 and 82 cm^{-1}) with ν_{11} (49.7 cm^{-1}) the Si..S stretching mode. The ν_{16} (162 cm^{-1}) and ν_{17} (49.8 cm^{-1}) modes are the out of plane geared and antigeared rocking modes of both electron donor and acceptor, while ν_{18} (22 cm^{-1}) is the torsional mode about the Si..S bond.

Table 8.42 Calculated Wavenumber Shifts on complexation in the $SiH_4.H_2S$ Complex

Symmetry Species	Mode	Complex Wavenumber /cm^{-1}	Monomer Wavenumber /cm^{-1}	Shift[a] /cm^{-1}
a'	ν_1	2838	2845	-7
	ν_2	2354	2355	-1
	ν_3	2346	2355	-9
	ν_4	2334	2345	-11
	ν_5	1267	1269	-2
	ν_6	1017	1017	0
	ν_7	976	972	4
	ν_8	969	972	-3
a"	ν_{12}	2864	2871	-7
	ν_{13}	2354	2355	-1
	ν_{14}	1019	1017	2
	ν_{15}	976	972	4

(a) Complex - Monomer

The ratios of the complex to monomer intensities for the $SiH_4.H_2S$ complex are reported in Table 8.43.

Table 8.43 Ratios of the Complex to Monomer Intensities in the $SiH_4.H_2S$ Complex

Symmetry Species	Mode	Complex A_c/km mol^{-1}	A_c/A_m
a'	ν_1	2.8	0.67
	ν_2	155.3	0.95
	ν_3	102.3	0.63
	ν_5	7.1	0.93
	ν_7	175.2	0.94
	ν_8	229.3	1.23
a"	ν_{12}	4.7	0.72
	ν_{13}	153.7	0.94
	ν_{15}	175.9	0.94

The major intensity enhancement occurs in ν_8 by 1.23-fold. The remaining vibrational modes have intensity reductions. A plausible reason for the intensity decreases could be the weakness of this complex resulting from the minimal charge redistribution (0.001 e) on complexation (Table 8.39) which is a direct function of the intensities in this complex.

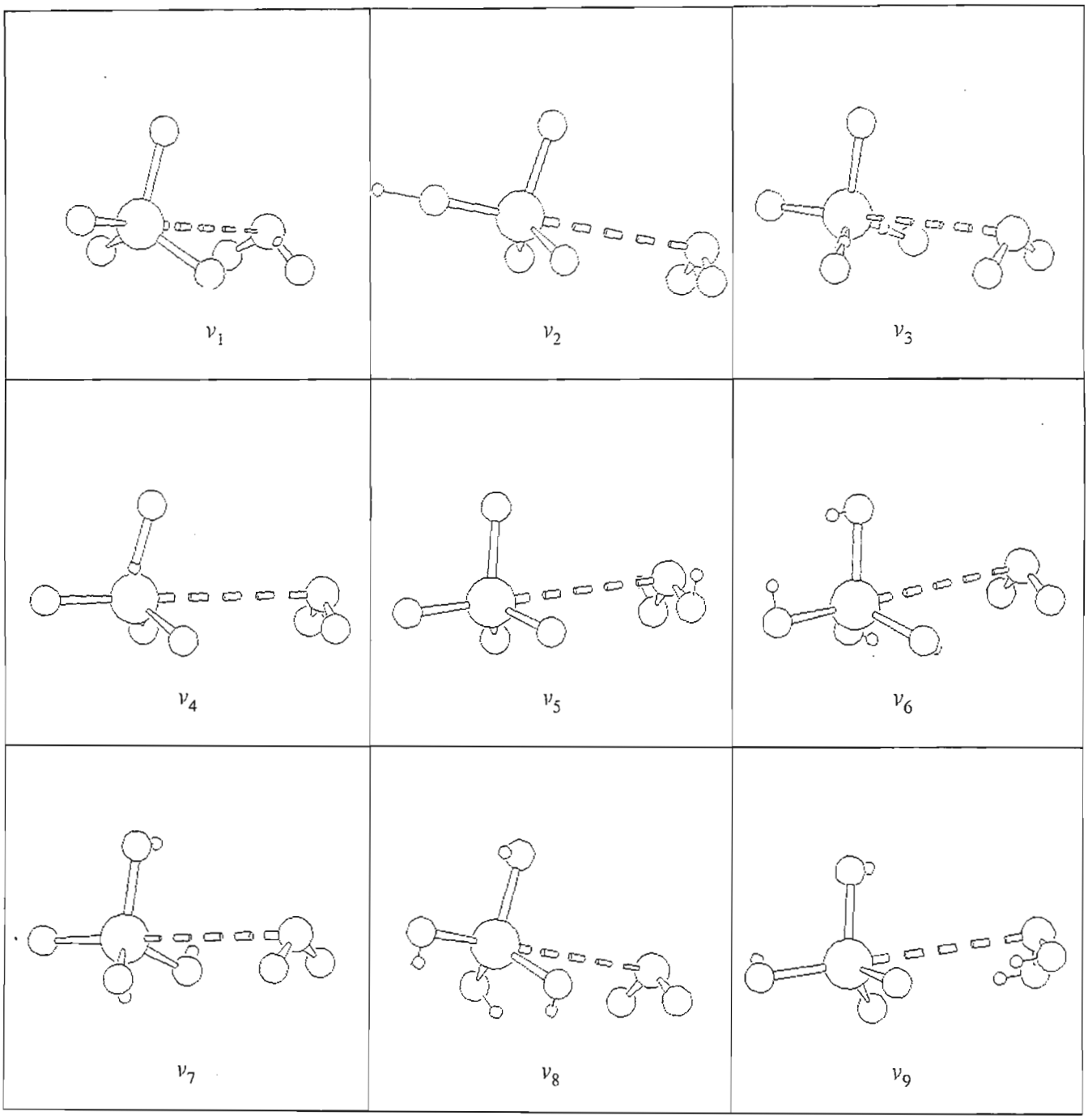

Fig 8.22 Graphical Representation of the $SiH_4 . H_2O$ Complex Vibration modes

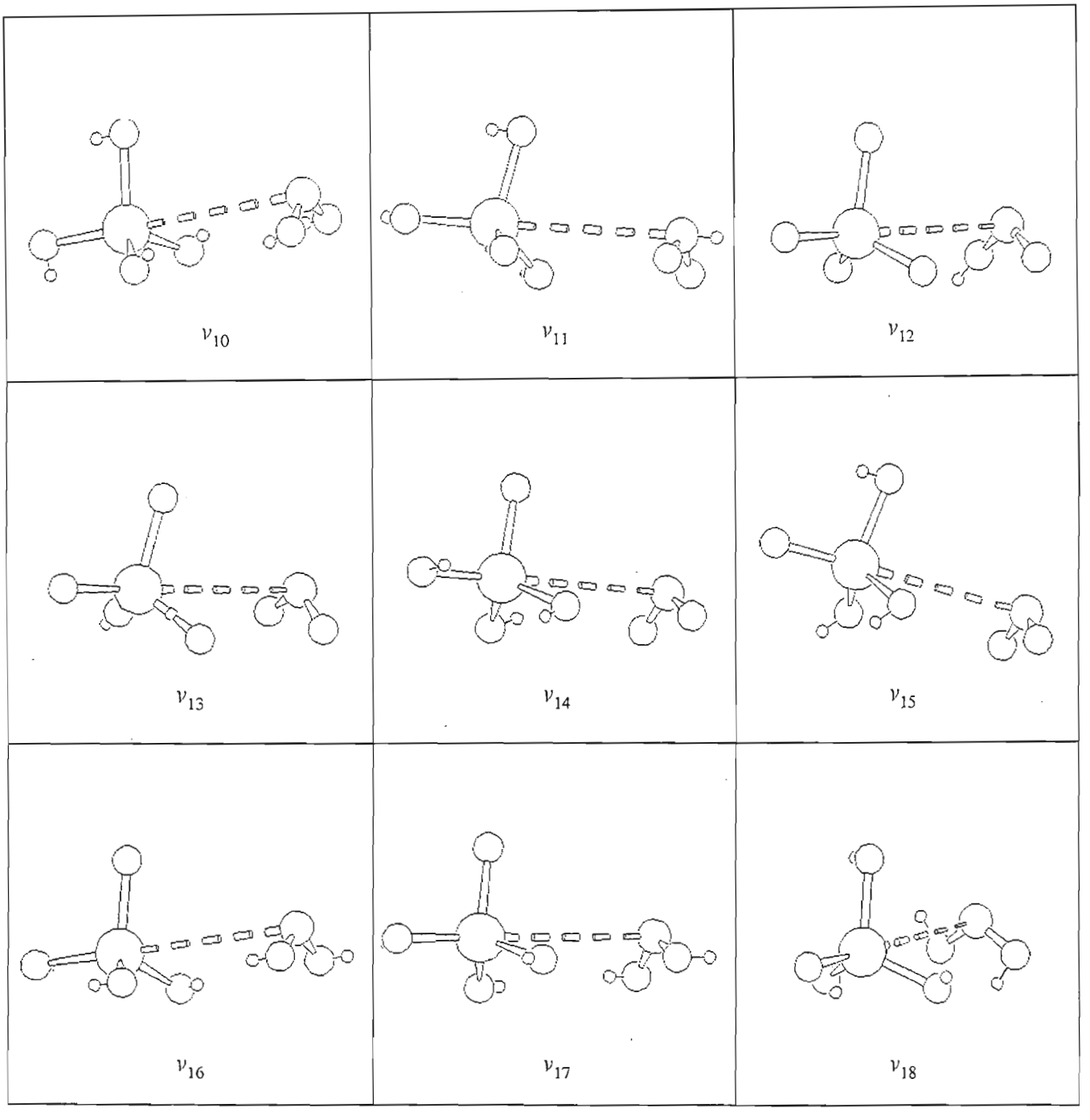

Fig 8.22 Graphical Representation of the $SiH_4 .H_2O$ Complex Vibration modes

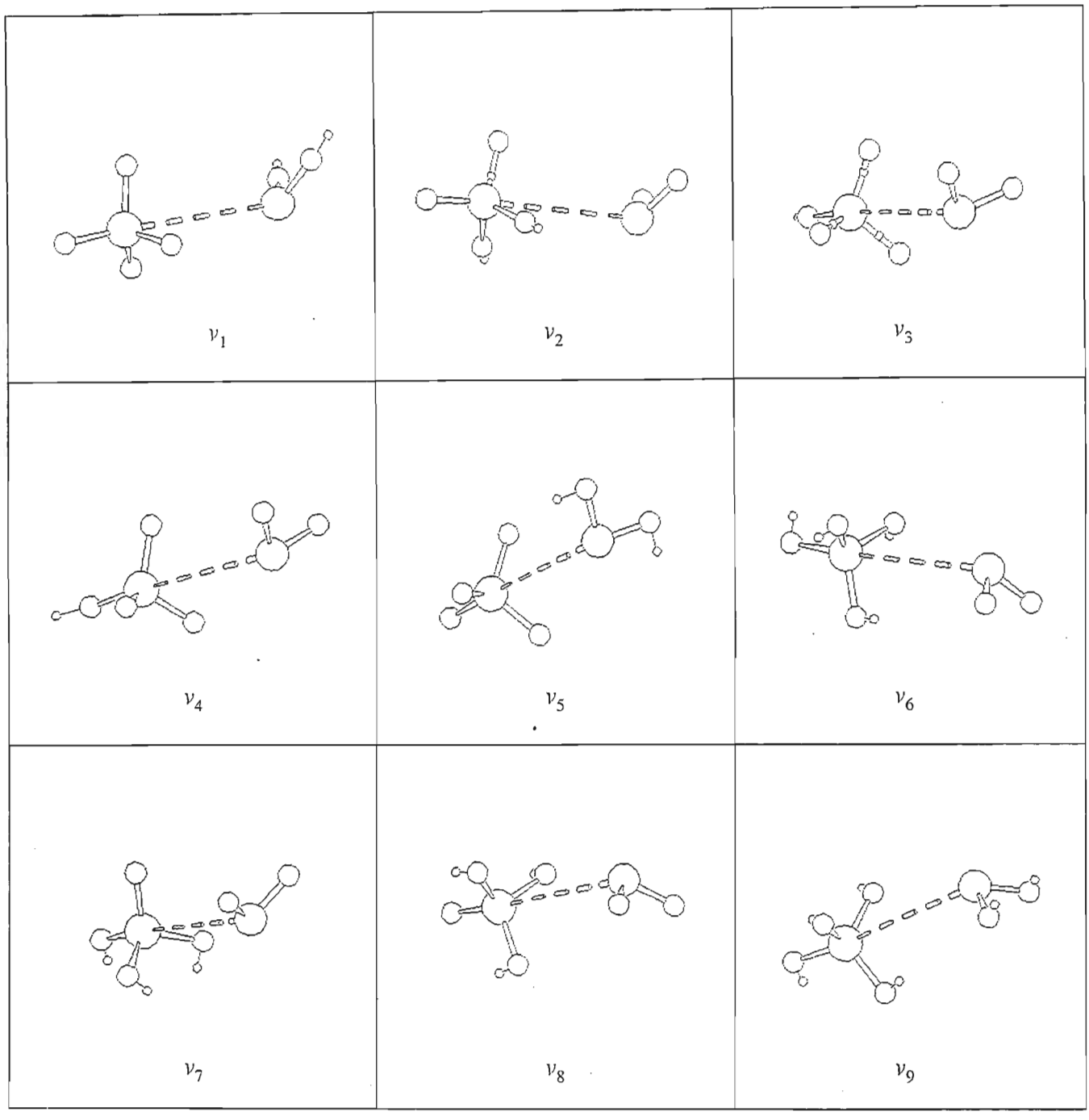

Fig 8.23 Graphical Representation of the $SiH_4 . H_2S$ Complex Vibration modes

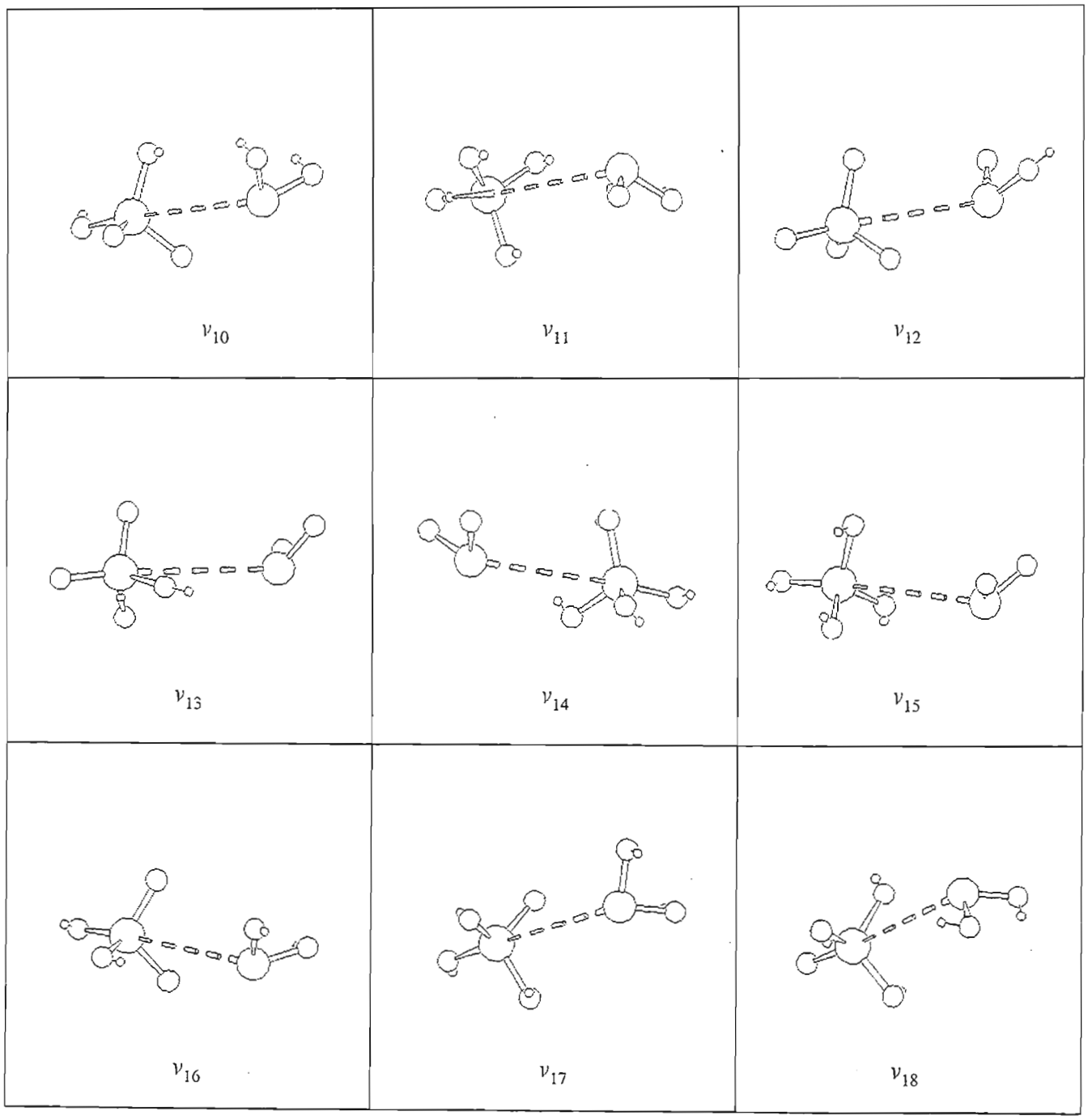

Fig 8.23 Graphical Representation of the $SiH_4 . H_2S$ Complex Vibration modes

8.6 *The $CH_4.AH_3$ Complexes (A= N,P)*

8.6.1 *Geometries*

In the case of the $CH_4.NH_3$ complexes, two structures (figs 8.24 and 8.25) were optimized, the eclipsed and staggered conformers with methane as proton donor to the nitrogen of ammonia. The staggered conformer was found to be the global minimum structure in support of the previous ab initio studies.[287,291] In the case of the $CH_4.PH_3$ complex, structures similar to those of the $CH_4.NH_3$ complexes were optimized (figs 8.26 and 8.27) however, in this case, the eclipsed structure was found to be the global minimum structure. No previous theoretical or experimental studies were found on the $CH_4.PH_3$ complex during this project for comparison. The geometrical parameters for the $CH_4.NH_3$ complex are collected in Table 8.44. The major changes in the geometrical parameters occur in the methane bond angles by 1.4°. The changes in the other geometrical parameters are minimal. The increases in the methane bond angles result from the gain of negative charge from the electron donor, thus creating a greater repulsive force among the hydrogens at the face of the methane tetrahedron. This negative charge gain also results in the increase of the CH2, CH3 and CH4 bond lengths due to the charge migration into the antibonding orbitals. The Mulliken charge analysis further verifies the direction of flow of negative charge in this complex. The H..N distance of 274 pm and CH..N bond angle of 180° qualifies this complex as being a hydrogen bonded complex. Our calculated H..N distance agrees well with the calculated value of 272.8 pm obtained by Yan et al[287] at the same level of theory and basis set.

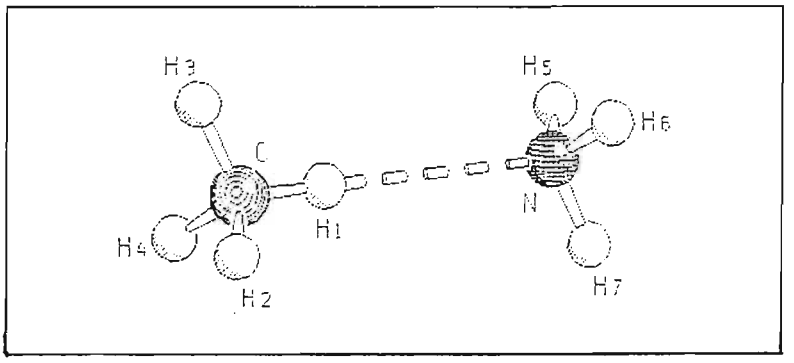

Fig 8.24 The Linear Staggered $CH_4.NH_3$ Complex

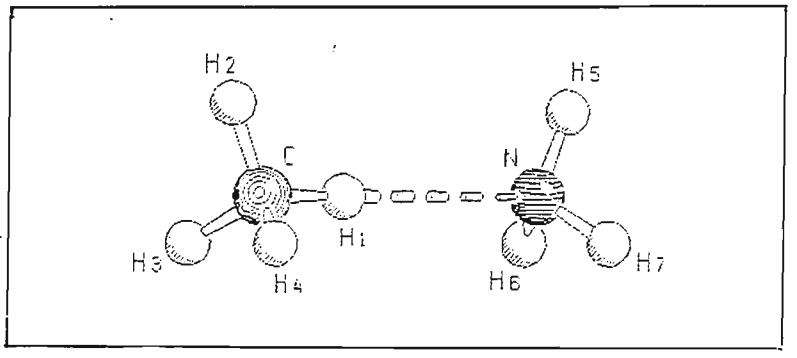

Fig 8.25 The Linear Eclipsed $CH_4.NH_3$ Complex

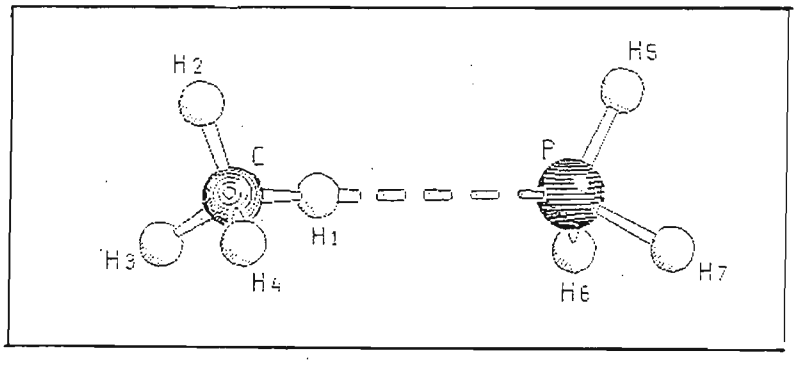

Fig 8.26 The Linear Eclipsed $CH_4.PH_3$ Complex

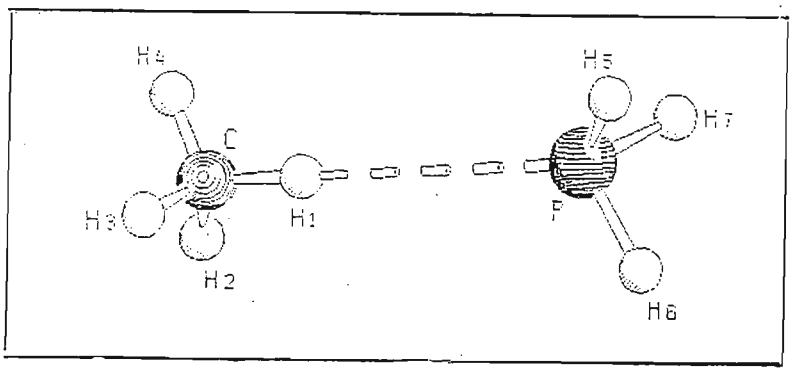

Fig 8.27 The Linear Staggered $CH_4.PH_3$ Complex

Table 8.44 Geometrical Parameters for the Most Stable $CH_4.NH_3$ Complex

Complex	Parameter	Complex	Monomer	Difference
$CH_4.NH_3$	r(CH1)/pm	108.5	108.4	0.1
	r(CH2), r(CH3), r(CH4)/pm	108.6	108.4	0.2
	R(H1..N)/pm	274.0		
	r(NH5), r(NH6), r(NH7)/pm	101.2	101.1	0.1
	H2CH1, H3CH1, H4CH1/deg	109.8	108.4	1.4
	H7NH6, H7NH5, H5NH6/deg	106.3	106.1	0.2
	CH1..N/deg	180.0		

The changes in the geometrical parameters in the $CH_4.PH_3$ complex are collected in Table 8.45. The trend in the changes of the geometrical parameters in the $CH_4.NH_3$ complex are duplicated in the $CH_4.PH_3$ complex. The major change occurring in the geometrical parameters occurs in the proton donor bond angles (1.2°). The increase in the methane bond angles cannot be explained on the basis of an electrostatic model as in the case of the $CH_4.NH_3$ complex, since the direction of the dipole moment of PH_3 is opposite to that of NH_3. The H1..P distance of 341.5 pm and CH1..P angle of 180°, classifies this complex as being hydrogen bonded. Phosphorus being less electronegative than hydrogen results in the phosphine hydrogens bearing a slightly negative charge, thus exerting an

attractive force on the hydrogens of CH_4, which results in an increase of the methane bond angles.

Table 8.45 Geometrical Parameters for the Most Stable $CH_4.PH_3$ Complex

Complex	Parameter	Complex	Monomer	Difference
$CH_4.PH_3$	r(CH1)/pm	108.5	108.4	0.1
	r(CH2), r(CH3), r(CH4)/pm	108.6	108.4	0.2
	R(H1..P)/pm	341.3		
	r(PH5), r(PH6), r(PH7)/pm	140.6	140.5	0.1
	H2CH1, H3CH1, H4CH1/deg	109.6	108.4	1.2
	H7PH6, H7PH5, H5PH6/deg	94.6	94.5	0.1
	CH1..P/deg	180.0		

8.6.2 *Energetics*

The binding energies together with the percentage dispersion energy contributions for the $CH_4.AH_3$ complexes are collected in Table 8.46.

From Table 8.46, the $CH_4.NH_3$ complex is observed to be more strongly bonded than the $CH_4.PH_3$ complex by 3.3 kJ mol^{-1}, with the forces of dispersion being totally responsible

for binding the $CH_4.PH_3$ complex. This effect results from the eclipsed H..H attractive forces and not the CH..P electrostatic interaction. The BSSE plays a major role in both complexes, contributing 80% and 40% to the interaction energy in the $CH_4.PH_3$ and $CH_4.NH_3$ complexes respectively. The BSSE effects in $CH_4.NH_3$ were also observed by Yan et al[287] to play a large role (64%) in the corrected interaction energy. The role of the dispersion energy and the effects of the BSSE are once again emphasised as one descends a group in the periodic table.

Table 8.46 Binding Energies of the $CH_4.AH_3$ Complexes

Complex	$\Delta E'$ /kJ mol^{-1}	ΔE /kJ mol^{-1}	BSSE /kJ mol^{-1}	$\%\Delta E_{Disp}$
$CH_4.NH_3$	-3.6	-5.8	2.3	41.8
$CH_4.PH_3$	-0.3	-1.5	1.2	-[a]

a - not determined (due to the $CH_4.PH_3$ complex being unbound at the SCF level)

The Morokuma energy decomposition analyses for the $CH_4.AH_3$ complexes are collected in Table 8.47. In the $CH_4.NH_3$ complex the EX term dominates the SCF component of the interaction energy. The CT term is the dominant attractive force followed by the ES and PL terms. The $CH_4.NH_3$ complex is bonded at the SCF level of theory (-3.3 kJ mol^{-1}) while the $CH_4.PH_3$ complex is non-bonded (0.7 kJ mol^{-1}). This is as expected, based on the large contribution of dispersion to the interaction energy in the $CH_4.PH_3$ complex. The early energy decomposition analysis studies by Morokuma et al,[10] neglecting BSSE effects, report the SCF binding energy of the $CH_4.NH_3$ complex to be governed by the CT term (2.9 kJ mol^{-1}), with the EX term being slightly lower in energy (2.0 kJ mol^{-1}). The $CH_4.NH_3$ complex may thus be classed as a pseudo EX-CT type complex, while

$CH_4.PH_3$ is classed as a dispersion type complex.

Table 8.47 Energy Decomposition Analysis of the $CH_4.AH_3$ Complexes /kJ mol^{-1}

Complex	ES	EX	CT	PL	MIX	Total
$CH_4.NH_3$	-2.8	7.2	-4.3	-2.8	0.6	-3.3
$CH_4.PH_3$	-1.5	2.6	-0.4	-0.2	0.2	0.7

8.6.3 *Mulliken Charge Analysis*

The Mulliken charge analyses for the $CH_4.AH_3$ complexes are collected in Tables 8.48 and 8.49 depicting the flow of negative charge on complexation. The net charge donation occurs from the proton acceptor to the donor; most of this negative charge (-0.010 e) has its origin from the proton acceptor and H1 of the proton donor. The H2, H3 and H4 hydrogens of the proton donor gain negative charge (-0.013 e), thus increasing the repulsion between them, hence resulting in an increase in the bond angles subtended by these hydrogens, as was observed in the changes in the geometrical parameters.

Table 8.48 Mulliken Charge Analysis for the $CH_4.NH_3$ Complex

Atom	Atomic Charge /e		Difference /e
	Complex	Monomer	
N	-0.784	-0.785	0.001
H5	0.265	0.262	0.003
H6	0.265	0.262	0.003
H7	0.265	0.262	0.003
			0.010
C	-0.495	-0.473	-0.022
H1	0.169	0.118	0.051
H2	0.105	0.118	-0.013
H3	0.105	0.118	-0.013
H4	0.105	0.118	-0.013
			-0.010

Table 8.49 Mulliken Charge Analysis for the $CH_4.PH_3$ Complex

Atom	Atomic Charge /e		Difference /e
	Complex	Monomer	
P	0.162	0.162	0.000
H5	-0.053	-0.054	0.001
H6	-0.053	-0.054	0.001
H7	-0.053	-0.054	0.001
			0.003
C	-0.482	-0.473	-0.009
H1	0.142	0.118	0.024
H2	0.112	0.118	-0.006
H3	0.112	0.118	-0.006
H4	0.112	0.118	-0.006
			-0.003

In the $CH_4.PH_3$ complex, the proton donor gains negative charge (-0.003 e) from the acceptor, as in the $CH_4.NH_3$ complex. The major amount of negative charge loss is experienced by H1 of the proton donor (-0.024 e). The H2, H3 and H4 atoms of the proton donor once again acquire negative charge (-0.006 e), thus resulting in the repulsion of these hydrogens and hence an increase in the internal bond angles subtended by them.

8.6.4 *Vibrational Properties of the $CH_4.AH_3$ Complexes*

The calculated vibrational spectra, potential energy distributions and infrared intensities at the MP2/6-31G** level of theory for the $CH_4.AH_3$ complexes are shown in Tables 8.50 - 8.56. The plots of the normal modes of vibrations are shown in figs 8.28 and 8.29 for the $CH_4.NH_3$ and $CH_4.PH_3$ complexes respectively.

Table 8.50 Calculated Wavenumber Shifts on complexation in the $CH_4.NH_3$ Complex

Symmetry Species	Mode	Complex Wavenumber /cm^{-1}	Monomer Wavenumber /cm^{-1}	Shift[(a)] /cm^{-1}
a_1	ν_1	3561	3564	-3
	ν_2	3276	3289	-13
	ν_3	3123	3142	-19
	ν_4	1397	1402	-5
	ν_5	1112	1122	-10
e	ν_7	3719	3721	-2
	ν_8	3267	3289	-22
	ν_9	1723	1728	-5
	ν_{10}	1633	1623	10
	ν_{11}	1420	1402	18

(a) Shift = Complex - Monomer

The major wavenumber shifts occur in ν_3, ν_8 and ν_{11}, the proton donor symmetric and antisymmetric stretching and antisymmetric bending modes respectively. The ν_8 mode of the proton donor is red shifted by 22 cm^{-1}, while ν_{10} and ν_{11} are blue shifted by 10 and 18 cm^{-1}. The CH stretching mode and the symmetric bending modes are all red shifted. The trends observed in the strong hydrogen bonded complexes involving the red shift of the symmetric stretching modes and the blue shift of the bending modes in the proton donor are not obeyed. The symmetry coordinate descriptions used to describe the different vibrational modes are collected in Table 8.51.

Table 8.51 Symmetry Coordinates for the $CH_4.AH_3$ Complexes

Complex	Symmetry Coordinate	Description
$CH_4.NH_3$	$S_1 = \Delta r_1$	CH stretch
	$S_2 = 1/\sqrt{3}(\Delta r_2 + \Delta r_3 + \Delta r_4)$	CH_3 symmetric stretch
	$S_3 = 1/\sqrt{3}(\Delta r_6 + \Delta r_7 + \Delta r_8)$	AH_3 symmetric stretch
	$S_4 = 1/\sqrt{6}(\Delta\alpha_1 + \Delta\alpha_2 + \Delta\alpha_3 - \Delta\beta_1 - \Delta\beta_2 - \Delta\beta_3)$	CH_3 symmetric bend
	$S_5 = 1/\sqrt{6}(\Delta\theta_1 + \Delta\theta_2 + \Delta\theta_3 - \Delta\tau_1 - \Delta\tau_2 - \Delta\tau_3)$	AH_3 symmetric bend
	$S_6 = \Delta R$	H..A stretch
	$S_{7a} = 1/\sqrt{2}(\Delta r_3 - \Delta r_4)$	CH_3 antisymmetric stretch
	$S_{8a} = 1/\sqrt{2}(\Delta r_7 - \Delta r_8)$	AH_3 antisymmetric stretch
	$S_{9a} = 1/\sqrt{2}(\Delta\alpha_2 - \Delta\alpha_3)$	CH_3 antisymmetric bend

Table 8.51 Continued

	$S_{10a} = 1/\sqrt{2}(\Delta\beta_2 - \Delta\beta_3)$	CH_3 rock
	$S_{11a} = 1/\sqrt{2}(\Delta\theta_2 - \Delta\theta_3)$	AH_3 antisymmetric bend
	$S_{12a} = 1/\sqrt{2}(\Delta\tau_2 - \Delta\tau_3)$	AH_3 rock
	$S_{13a} = \Delta\gamma_1$	libration
	$S_{7b} = 1/\sqrt{6}(2\Delta r_2 - \Delta r_3 - \Delta r_4)$	CH_3 antisymmetric stretch
	$S_{8b} = 1/\sqrt{6}(2\Delta r_6 - \Delta r_7 - \Delta r_8)$	AH_3 antisymmetric stretch
	$S_{9b} = 1/\sqrt{6}(2\Delta\alpha_1 - \Delta\alpha_2 - \Delta\alpha_3)$	CH_3 antisymmetric bend
	$S_{10b} = 1/\sqrt{6}(2\Delta\beta_1 - \Delta\beta_2 - \Delta\beta_3)$	CH_3 rock
	$S_{11b} = 1/\sqrt{6}(2\Delta\theta_1 - \Delta\theta_2 - \Delta\theta_3)$	AH_3 antisymmetric bend
	$S_{12b} = 1/\sqrt{6}(2\Delta\tau_1 - \Delta\tau_2 - \Delta\tau_3)$	AH_3 rock
	$S_{13b} = \Delta\gamma_2$	libration
a_2	$S_{14} = \Delta\phi$	torsion about CH..A bond

The symmetry coordinates for the proton acceptor were similar to those used for the monomer since there was little perturbation in the geometrical parameters of the proton acceptor on complexation. In the case of the proton donor the T_d symmetry was lowered to C_{3v}. Hence the symmetry coordinates characteristic of a C_{3v} molecule were used in the case of the proton donor. The percentage potential energy distributions amongst the various vibrational modes in the $CH_4.NH_3$ complex are reported in Table 8.52.

Table 8.52 Wavenumbers and %PEDs in the $CH_4.NH_3$ Complex

Complex	Symmetry Species	Wavenumbers /cm^{-1}	%PED
$CH_4.NH_3$	a_1	3562	$100S_3$
		3276	$75S_1 + 25S_2$
		3123	$75S_2 + 25S_1$
		1397	$100S_4$
		1111	$93S_5 + 7S_3$
		76	$100S_6$
	e_a	3718	$100S_{8a}$
		3267	$100S_{7a}$
		1723	$88S_{12a} + 12S_{13a}$
		1633	$53S_{9a} + 45S_{10a}$
		1420	$44S_{9a} + 56S_{10a}$
		163	$81S_{13a} + 10S_{9a}$
		35	$57S_{11a} + 43S_{13a}$
	e_b	3718	$100S_{8b}$
		3267	$100S_{7b}$
		1723	$88S_{12b} + 12S_{13b}$
		1633	$53S_{9b} + 45S_{10b}$

Table 8.52 Continued

		1420	$44S_{9b} + 56S_{10b}$
		163	$81S_{13b} + 10S_{9b}$
		35	$57S_{11b} + 43S_{13b}$
	a_2	3	$100S_{14}$

In the case of the a_1 modes, the NH_3 stretching mode has $100\%S_3$ while the corresponding bending mode has $7\%S_3$ and $93\%S_5$ respectively. The methane symmetric stretching modes have contributions from both the S_1 and S_2 symmetry coordinates, resulting from the lowering of symmetry from T_d to C_{3v} on complexation. The methane symmetric bending mode on the other hand is totally unperturbed on complexation. The e_a and e_b modes in the case of the proton donor show a similar trend, with the antisymmetric stretching modes being unperturbed while the remaining modes all have contributions from other symmetry coordinates. The H..N stretching mode occurring at 76 cm^{-1} is totally unperturbed by the other intermolecular modes, further emphasising the weakness of this interaction. The CH..N degenerate bending mode occurs at 163 cm^{-1}, having minimal contributions from the bending modes of the proton donor and acceptor. The degenerate rocking of both sub-units occurs at 35 cm^{-1} with contributions from the symmetry coordinates of both the proton donor and acceptor. The torsional mode about the CH..N bond occurs at 3 cm^{-1}, belonging to the a_2 symmetry species; this mode is unperturbed due to symmetry considerations. The changes in the intensities of the vibrational modes in the $CH_4.NH_3$ complex are collected in Table 8.53.

Table 8.53 Ratios of the Complex to Monomer Intensity values in the $CH_4.NH_3$ complex

Symmetry Species	Mode	Complex A_c/km mol^{-1}	A_c/A_m
a_1	ν_1	0.001	0.005
	ν_2	0.3	0.001
	ν_5	150.8	0.69
e	ν_7	1.0	1.25
	ν_8	28.5	1.34
	ν_9	16.0	0.75
	ν_{10}	0.2	0.25
	ν_{11}	11.0	0.94

The ν_3 and ν_4 modes correspond to ν_1 and ν_2 of the methane monomer, which are both infrared inactive, and hence their corresponding intensities are not given in Table 8.53. The major intensity enhancements occur in ν_7 and ν_8 by factors of 1.25 and 1.34 respectively. The remaining intensity ratios are all below unity, further providing evidence of the weakness of the bond in this complex. The wavenumber shifts in the $CH_4.PH_3$ complex are collected in Table 8.54.

Table 8.54 Calculated Wavenumber Shifts on Complexation in the $CH_4.PH_3$ Complex

Symmetry Species	Mode	Complex Wavenumber /cm^{-1}	Monomer Wavenumber /cm^{-1}	Shift[(a)] /cm^{-1}
a_1	ν_1	3282	3289	-7
	ν_2	3130	3142	-12
	ν_3	2530	2531	-1
	ν_4	1400	1402	-2
	ν_5	1081	1078	3
e	ν_7	3274	3289	-15
	ν_8	2546	2546	0
	ν_9	1626	1623	3
	ν_{10}	1410	1402	8
	ν_{11}	1183	1184	-1

(a) Complex - Monomer

The major wavenumber shifts occurring on complexation occur in ν_2 and ν_7 by -12 and -15 cm^{-1} respectively. These red shifts are due to the symmetric CH_3 and antisymmetric CH_3 stretching vibrations respectively. The remaining wavenumber shifts are less than 10 cm^{-1}, once again stressing the weakness of this complex. The symmetry coordinates used in the description of the vibrational modes of $CH_4.PH_3$ were identical to those used in the $CH_4.NH_3$ complex and hence will not be repeated. The percentage symmetry coordinate distributions amongst the vibrational modes are collected in Table 8.55.

Table 8.55 Wavenumbers and %PEDs in the $CH_4.PH_3$ Complex

Complex	Symmetry Species	Wavenumbers /cm^{-1}	%PED
$CH_4.PH_3$	a_1	3282	$24S_1 + 76S2_2$
		3130	$77S_1 + 23S_2$
		2532	$100S_3$
		1401	$100S_4$
		1082	$100S_5$
		40	$100S_6$
	e_a	3274	$100S_{7a}$
		2548	$100S_{8a}$
		1626	$51S_{9a} + 49S_{10a}$
		1409	$49S_{9a} + 51S_{10a}$
		1184	$100S_{12a}$
		90	$74S_{13a} + 25S_{11a}$
		28	$57S_{11a} + 43S_{13a}$
	e_b	3274	$100S_{7b}$
		3548	$100S_{8b}$
		1626	$51S_{9b} + 49S_{10b}$
		1409	$49S_{9b} + 51S_{10b}$

Table 8.55 Continued

		1184	$100S_{12b}$
		90	$74S_{13b} + 25S_{11b}$
		28	$57S_{11b} + 43S_{13b}$
	a_2	3	$100S_{14}$

Both ν_1 and ν_2 have contributions from symmetry coordinates S_1 and S_2 as in the case of the $CH_4.NH_3$ complex. The symmetric stretching mode of the proton acceptor and the bending modes of both proton donor and acceptor have symmetry coordinate contributions solely due to their own symmetry coordinates. In the e symmetry species, the stretching modes are unperturbed by the symmetry coordinates of the other vibrational modes. The antisymmetric bending mode of the proton donor is greatly perturbed by those coordinates describing the antisymmetric vibrational modes of the same species. The H..P stretching mode occurs at 40 cm^{-1} with 100% symmetry coordinate contribution from S_6. The degenerate libration occurs at 90 cm^{-1} with a contribution from the antisymmetric PH_3 bending mode. The in- and out of phase rocking of both sub-units occur at 28 cm^{-1}, considerably lower than in the $CH_4.NH_3$ complex. Lastly the torsional mode about the CH..P bond occurs at 3 cm^{-1}, similar to its value in the $CH_4.NH_3$ complex. The changes in the intensities of the $CH_4.PH_3$ complex are collected in Table 8.56.

Table 8.56 Ratios of the Complex to Monomer Intensity values in the $CH_4.PH_3$ complex

Symmetry Species	Mode	Complex A_c/km mol^{-1}	A_c/A_m
a_1	ν_1	11.2	0.95
	ν_3	45.8	1.12
	ν_5	40.8	1.26
e	ν_7	22.8	1.07
	ν_8	93.4	0.95
	ν_9	6.2	0.53
	ν_{10}	10.0	0.47
	ν_{11}	18.4	0.56

The changes in the intensities on complexation are all minimal with ν_{10}, the CH_3 antisymmetric bending mode, being considerably weakened. The overall small complex/ monomer intensity ratios in the $CH_4.PH_3$ complex are due to this complex being weakly bonded.

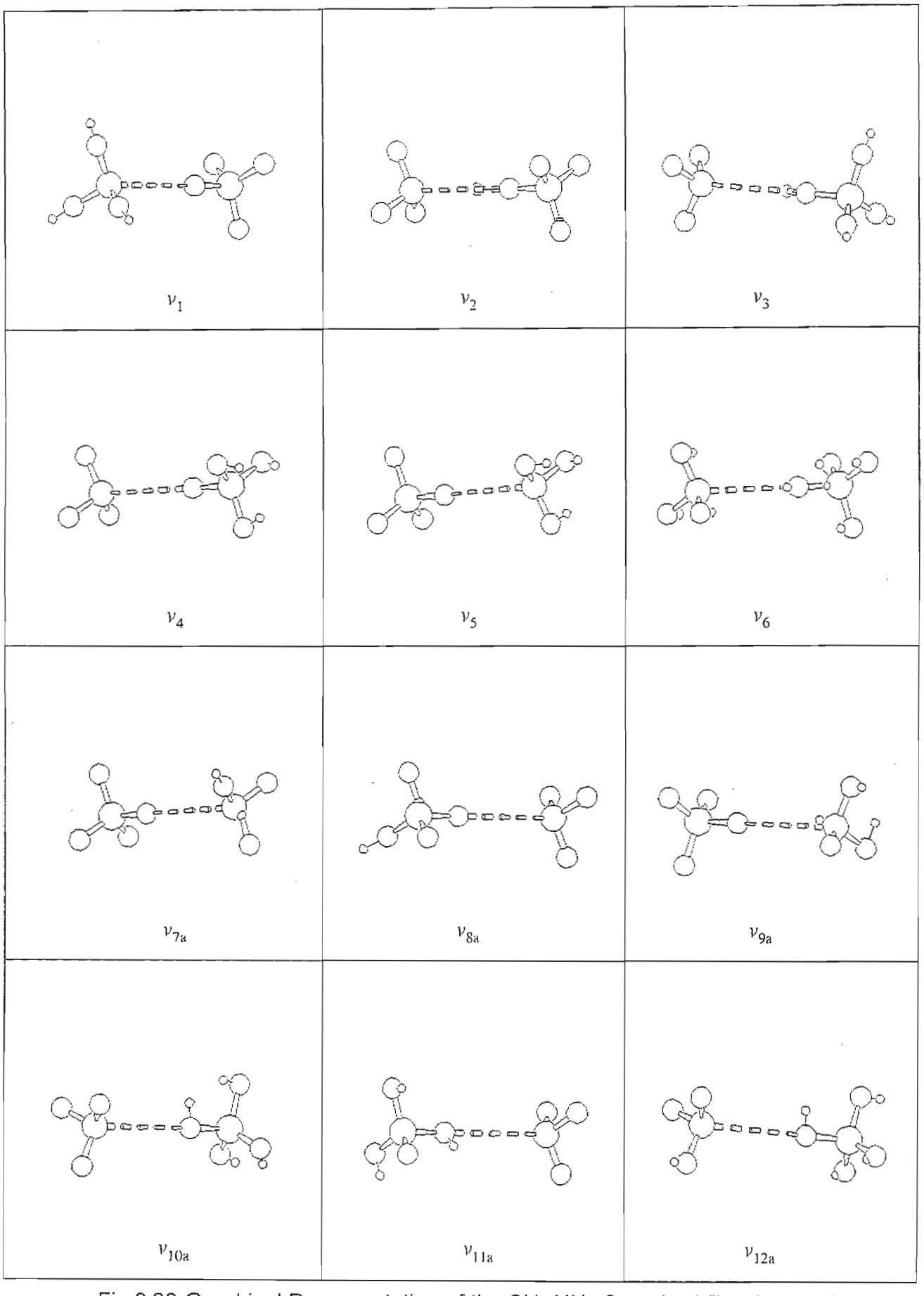

Fig 8.28 Graphical Representation of the $CH_4.NH_3$ Complex Vibration modes

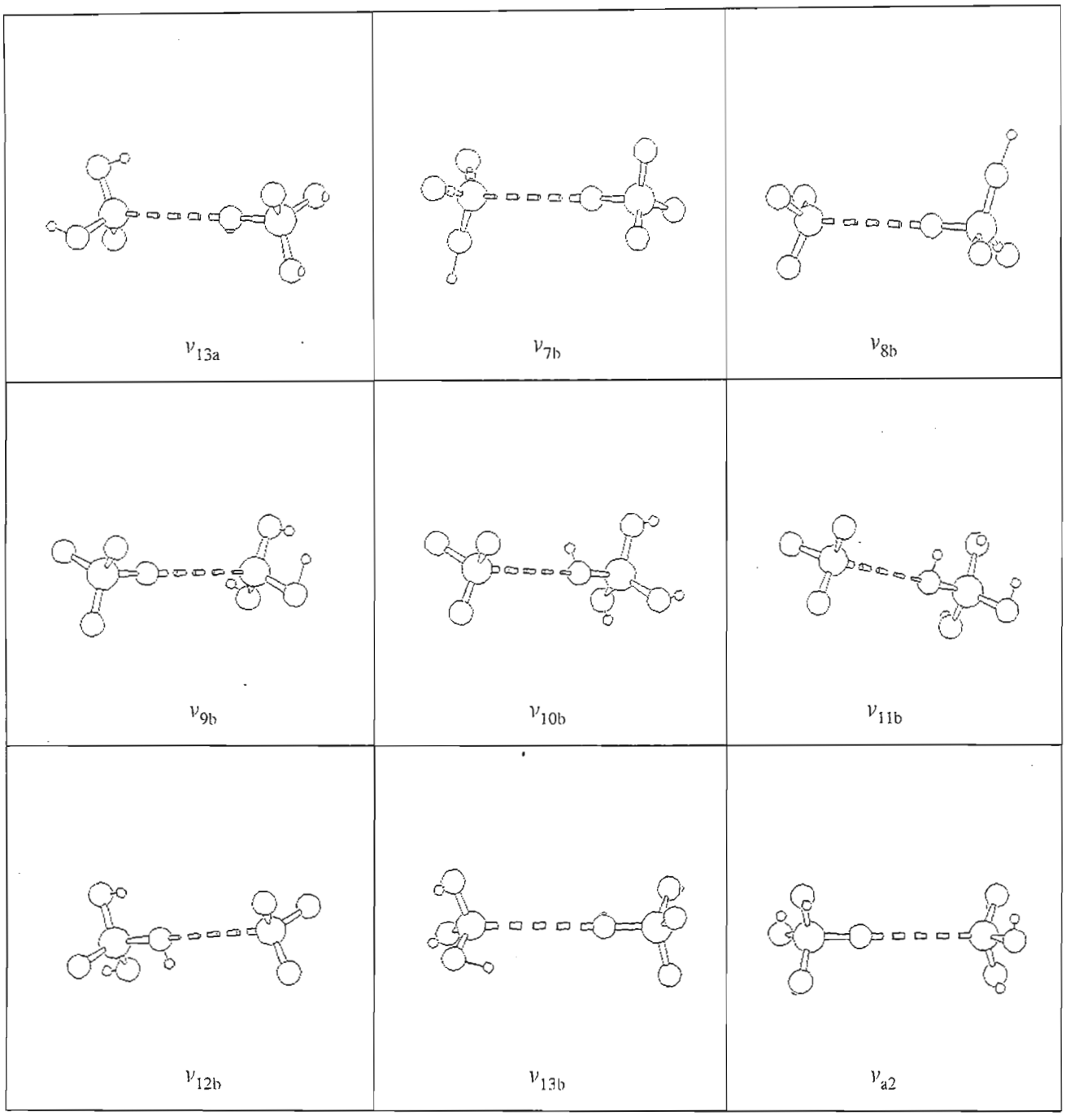

Fig 8.28 Graphical Representation of the $CH_4.NH_3$ Complex Vibration modes

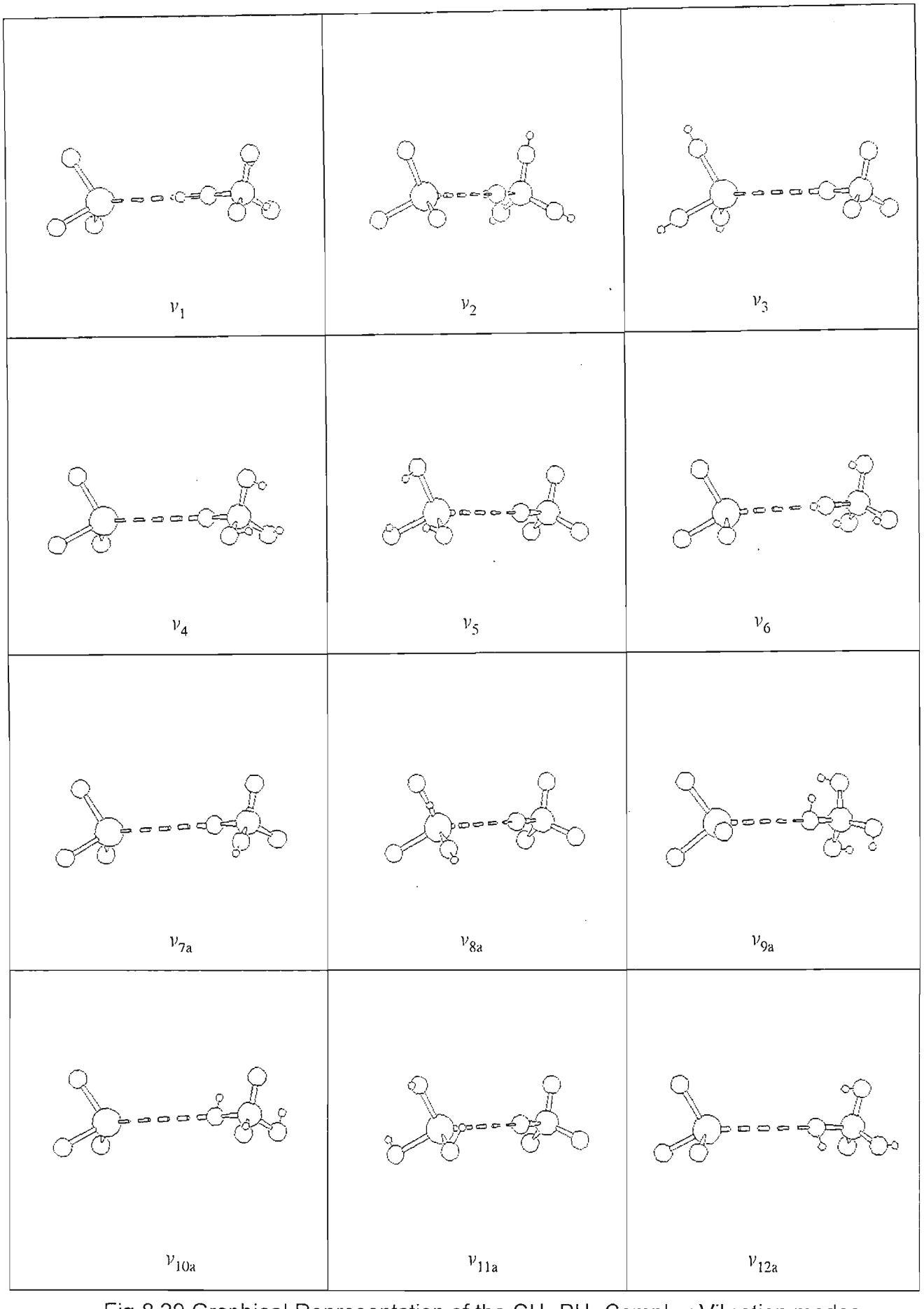

Fig 8.29 Graphical Representation of the CH_4.PH_3 Complex Vibration modes

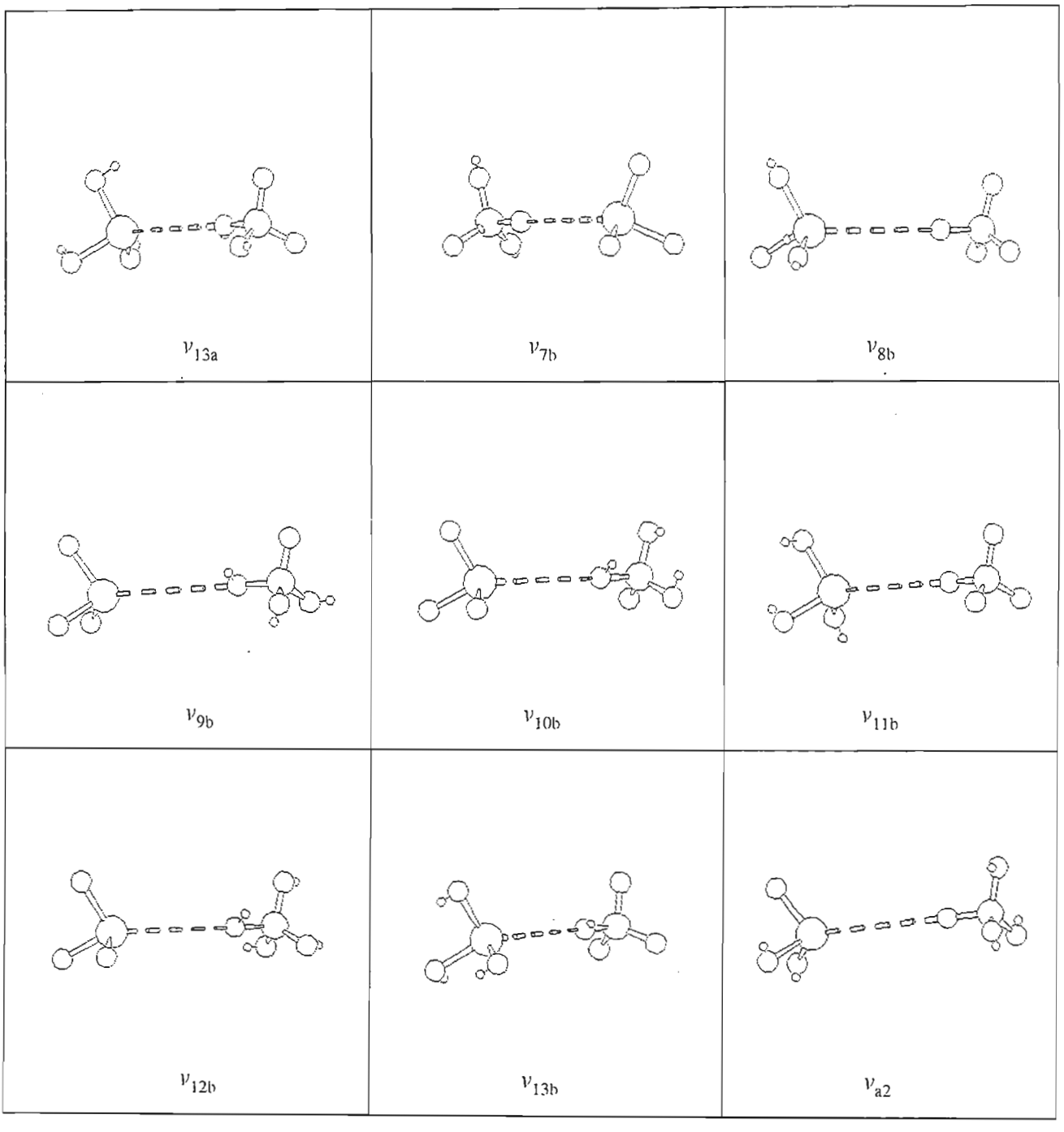

Fig 8.29 Graphical Representation of the $CH_4.PH_3$ Complex Vibration modes

8.7 *The $SiH_4.AH_3$ Complexes (A=N,P)*

8.7.1 *Geometries*

The structures optimized for these complexes comprise the eclipsed (fig 8.30 and 8.31) and staggered (fig 8.32 and 8.33) conformers, having C_{3v} symmetry with a Si..A interaction. The eclipsed structures were found to be saddle points while the staggered conformers were local minima on the PES. The changes in the geometrical parameters in the $SiH_4.NH_3$ complex are collected in Table 8.57.

In the $SiH_4.NH_3$ complex the major changes in the geometrical parameters occur in the SiH7 bond length and the HSiH bond angles, which increase by 1.1 pm and decrease by 2.1° respectively. The increase in the SiH7 bond distance can be explained by the gain of negative charge from the electron donor into the SiH7 antibonding orbital. Our calculated value for the Si..N distance (309.9 pm) is in good agreement with that of a theoretical calculation of Gordon et al[297] and the experimental gas phase studies of Rossi and Jasinski[295], who report values of 318 pm at the MP2/6-31G* level of theory and 313.1 pm respectively. Gordon et al[297] also commented on the effect of the addition of correlation to decrease the Si..N bond from 333 to 318 pm.

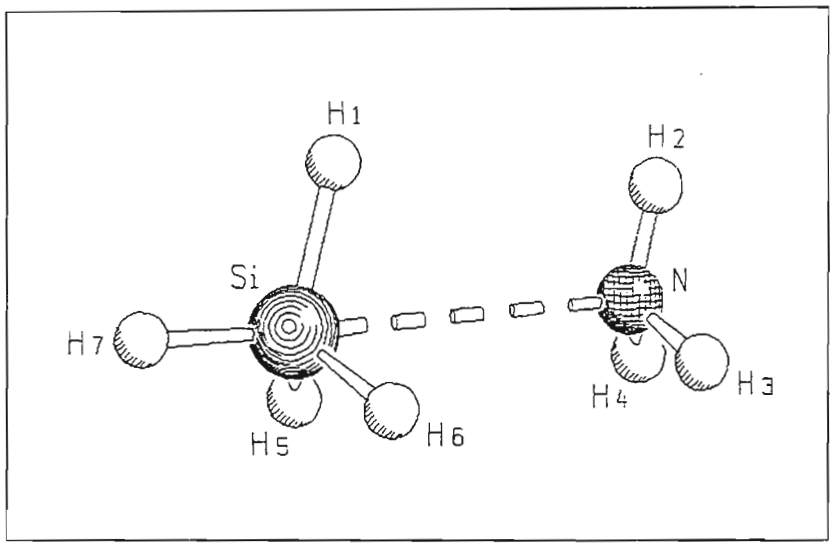

Fig 8.30 The Linear Eclipsed $SiH_4.NH_3$ Complex

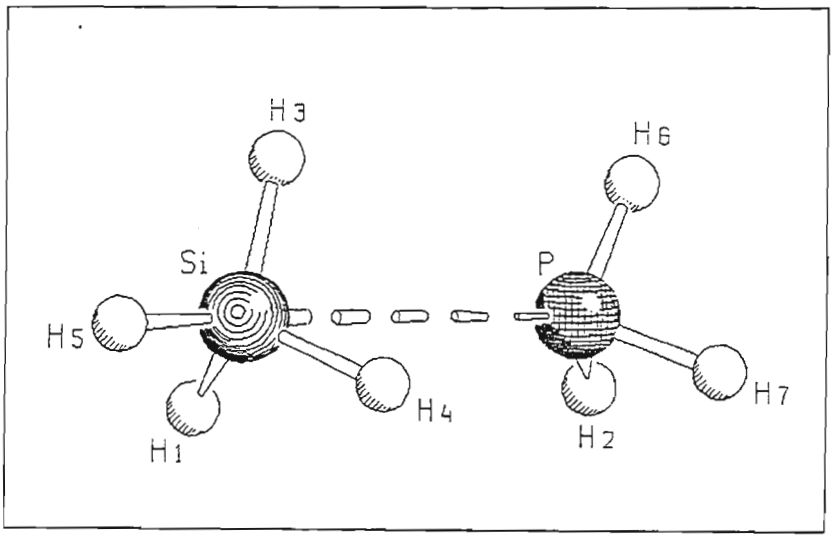

Fig 8.31 The Linear Eclipsed $SiH_4.PH_3$ Complex

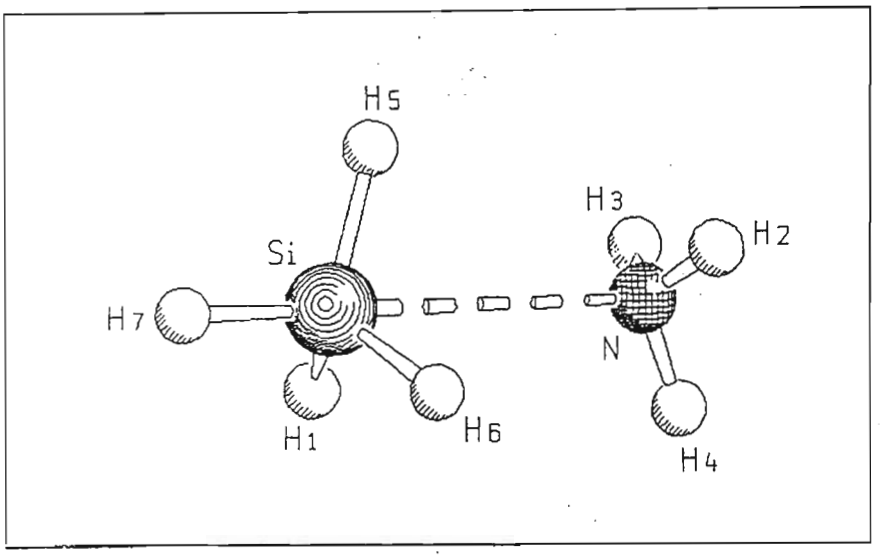

Fig 8.32 The Linear Staggered $SiH_4.NH_3$ Complex

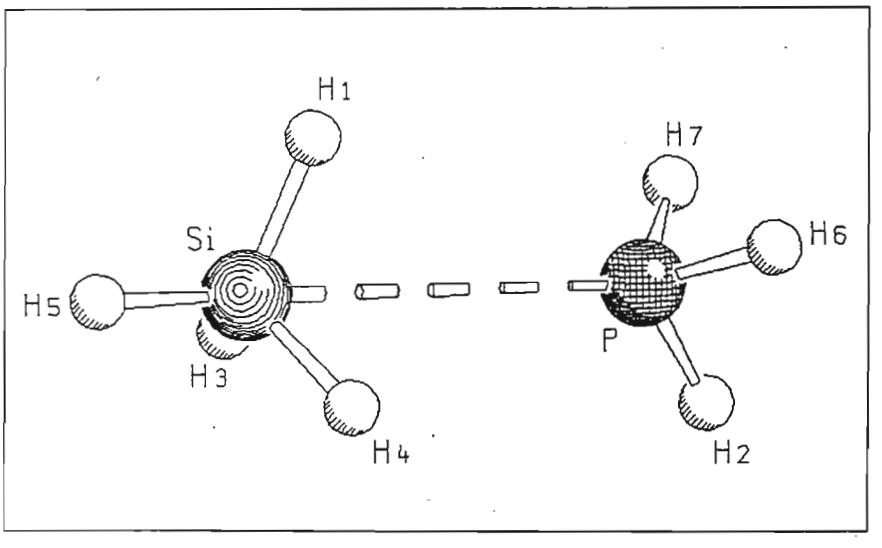

Fig 8.33 The Linear Staggered $SiH_4.PH_3$ Complex

Table 8.57 Geometrical Parameters for the Most Stable $SiH_4.NH_3$ Complex

Complex	Parameter	Complex	Monomer	Difference
$SiH_4.NH_3$	r(SiH1), r(SiH5), r(SiH6)/pm	147.2	147.1	0.1
	r(SiH7)/pm	148.2	147.1	1.1
	r(NH2), r(NH3), r(NH4)/pm	101.3	101.1	0.2
	R(Si..N)/pm	309.9		
	H7SiH1, H7SiH5, H7SiH6/deg	111.6	109.5	2.1
	H2NH3, H2NH4, H3NH4/deg	106.6	106.1	0.5

The changes in the geometrical parameters in the $SiH_4.PH_3$ complex are collected in Table 8.58.

On complexation the electron donor and acceptor undergo minimal changes in their geometrical parameters, with the major change (0.4°) occurring in the silane bond angles, H3SiH5, H5SiH1 and H4SiH5, as in the $SiH_4.NH_3$ complex. The Si..P distance is much larger than the Si..N distance, probably resulting from the difference in the van der Waals radii of phosphorus and nitrogen, thereby allowing a greater charge penetration into the vacant d-orbitals of silicon in the $SiH_4.NH_3$ complex. The minimal changes occurring in the geometrical parameters for this series of complexes are an indication of the weakness of the Si..A bond in these complexes.

Table 8.58 Geometrical Parameters for the Most Stable $SiH_4.PH_3$ Complex

Complex	Parameter	Complex	Monomer	Difference
$SiH_4.PH_3$	r(SiH1), r(SiH3), r(SiH4)/pm	147.3	147.1	0.2
	r(SiH5)/pm	147.6	147.1	-0.1
	r(PH2), r(PH6), r(PH7)/pm	140.6	140.5	0.1
	R(Si..P)/pm	403.5		
	H1SiH5, H3SiH5, H4SiH5/deg	109.9	109.5	0.4
	H7PH2, H6PH2, H7PH6/deg	94.6	94.5	0.1

8.7.2 *Energetics*

The binding energies together with the percentage dispersion energy contributions for the $SiH_4.AH_3$ complexes are collected in Table 8.59.

The $SiH_4.PH_3$ complex is totally governed by dispersion while the $SiH_4.NH_3$ complex has a 34.8% dispersion energy contribution. The BSSE contributions to the corrected interaction energies amount to 52.5% and 76.9% in the $SiH_4.NH_3$ and $SiH_4.PH_3$ complexes respectively. The $SiH_4.NH_3$ complex is more strongly bonded than the $SiH_4.PH_3$ complex by 86.2%.

Table 8.59 The Binding Energies of the $SiH_4.AH_3$ Complexes

Complex	$\Delta E'$ /kJ mol^{-1}	ΔE /kJ mol^{-1}	BSSE /kJ mol^{-1}	$\%\Delta E_{Disp}$
$SiH_4.NH_3$	-6.6	-13.7	7.1	34.8
$SiH_4.PH_3$	-1.0	-3.9	2.9	-[a]

a - not determined (due to the $SiH_4.PH_3$ complex being unbound at the SCF level)

The Morokuma energy decomposition analyses for the $SiH_4.AH_3$ complexes are collected in Table 8.60.

Table 8.60 Energy Decomposition Analyses of the $SiH_4.AH_3$ Complexes /kJ mol^{-1}

Complex	ES	EX	CT	PL	MIX	Total
$SiH_4.NH_3$	-22.3	23.8	-4.3	-2.4	0.8	-4.4
$SiH_4.PH_3$	-4.6	6.3	-1.0	-0.3	0.5	0.9

The SCF interaction energy (0.9 kJ mol^{-1}) for $SiH_4.PH_3$ suggests this complex to be unbound at the SCF level of theory. In the case of the $SiH_4.NH_3$ complex the SCF interaction energy is attractive (-4.4 kJ mol^{-1}). The ES term dominates the attractive component of the SCF interaction energy in the $SiH_4.NH_3$ and $SiH_4.PH_3$ complexes by 22.3 and 4.6 kJ mol^{-1} respectively.

8.7.3 *Mulliken Charge Analysis*

The Mulliken charge analyses for the $SiH_4.AH_3$ complexes are collected in Tables 8.61

and 8.62 respectively.

Table 8.61 Mulliken Charge Analysis for the $SiH_4.NH_3$ Complex

Atom	Atomic Charge /e		Difference /e
	Complex	Monomer	
N	-0.778	-0.786	0.008
H2	0.271	0.262	0.009
H3	0.271	0.262	0.009
H4	0.271	0.262	0.009
			0.034
Si	0.713	0.667	0.046
H1	-0.182	-0.167	-0.015
H5	-0.182	-0.167	-0.015
H6	-0.182	-0.167	-0.015
H7	-0.200	-0.167	-0.033
			-0.034

In the $SiH_4.NH_3$ complex, negative charge donation (-0.034 e) occurs from NH_3 to SiH_4. The H7 atom lying collinear with the Si..N bond gains most of the charge (-0.033 e), with the balance of charge averaged amongst the hydrogens of silane. The negative charge acquired by these hydrogens results in an increase in the repulsive forces between them, thus forcing their bond angles to increase. On complexation the silicon becomes more

electropositive due to negative charge loss to the hydrogens of silane. The Mulliken charge analysis in the $SiH_4.PH_3$ complex is collected in Table 8.62.

Table 8.62 Mulliken Charge Analysis for the $SiH_4.PH_3$ Complex

Atom	Atomic Charge /e		Difference /e
	Complex	Monomer	
P	0.156	0.162	-0.006
H2	-0.053	-0.054	0.001
H6	-0.053	-0.054	0.001
H7	-0.053	-0.054	0.001
			-0.003
Si	0.693	0.667	0.026
H1	-0.171	-0.167	-0.004
H3	-0.171	-0.167	-0.004
H4	-0.171	-0.167	-0.004
H5	-0.178	-0.167	-0.011
			0.003

In this complex the electron donor donates negative charge (-0.003 e) to the electron acceptor. The trend of negative charge donation is reversed when compared with that in the $SiH_4.NH_3$ complex. The reversal of charge donation is due to phosphorus being less electropositive than silicon, thus withdrawing negative charge from silane. The hydrogens

of PH_3 also acquire positive charge due to charge donation to the phosphorus atom.

8.7.5 *Vibrational Properties of the $SiH_4.AH_3$ Complexes*

The calculated vibrational spectra, potential energy distributions and infrared intensities at the MP2/6-31G** level of theory for the $SiH_4.AH_3$ complexes are shown in Tables 8.63 - 8.69. The plots of the normal modes of vibrations are described in figs 8.34 and 8.35 for the $SiH_4.NH_3$ and $SiH_4.PH_3$ complexes respectively.

On complexation, ν_3, the stretching mode of the SiH bond along the Si..N axis undergoes a major red shift of 48 cm^{-1}. The NH_3 symmetric and antisymmetric stretching modes, together with the silane SiH_3 symmetric stretching mode, undergo red shifts of magnitude close to 10 cm^{-1}. The ammonia symmetric and antisymmetric bending modes undergo blue and red shifts of 5 and 6 cm^{-1} respectively. The remaining modes are only slightly perturbed from the corresponding monomer modes.

Table 8.63 Calculated Wavenumber Shifts on complexation in the $SiH_4.NH_3$ Complex

Symmetry Species	Mode	Complex Wavenumber /cm^{-1}	Monomer Wavenumber /cm^{-1}	Shift[(a)] /cm^{-1}
a_1	ν_1	3561	3571	-10
	ν_2	2343	2355	-12
	ν_3	2297	2345	-48
	ν_4	1121	1116	5
	ν_5	965	972	-7
e	ν_7	3718	3728	-10
	ν_8	2356	2355	1
	ν_9	1718	1724	-6
	ν_{10}	1033	1017	16
	ν_{11}	971	972	-1

(a) Complex - Monomer

The wavenumber shifts in the $SiH_4.PH_3$ complex are collected in Table 8.64. The major wavenumber shift occurring in this complex occurs in ν_3 (-13 cm^{-1}). This shift is due to the stretching of the SiH bond collinear with the Si..P axis. The wavenumbers of the remaining vibrational modes remain almost unperturbed from their monomer values.

Table 8.64 Calculated Wavenumber Shifts on complexation in the $SiH_4.PH_3$ Complex

Symmetry Species	Mode	Complex Wavenumber /cm^{-1}	Monomer Wavenumber /cm^{-1}	Shift[(a)] /cm^{-1}
a_1	ν_1	2532	2531	1
	ν_2	2345	2355	-10
	ν_3	2332	2345	-13
	ν_4	1085	1078	7
	ν_5	967	972	-5
e	ν_7	2548	2546	2
	ν_8	2353	2355	-2
	ν_9	1183	1184	-1
	ν_{10}	1018	1017	1
	ν_{11}	975	972	3

(a) Complex - Monomer

The symmetry coordinate descriptions for the vibrational modes are collected in Table 8.65.

Table 8.65 Symmetry Coordinates of the $SiH_4.AH_3$ Complexes

Complex	Symmetry Coordinate	Description
$SiH_4.AH_3$	$S_1 = 1/\sqrt{3}(\Delta r_5 + \Delta r_6 + \Delta r_7)$	AH_3 symmetric stretch
	$S_2 = \Delta r_4$	SiH stretch
	$S_3 = 1/\sqrt{3}(\Delta r_1 + \Delta r_2 + \Delta r_3)$	SiH_3 symmetric stretch
	$S_4 = 1/\sqrt{6}(\Delta\theta_1 + \Delta\theta_2 + \Delta\theta_3 - \Delta\tau_1 - \Delta\tau_2 - \Delta\tau_3)$	SiH_3 symmetric bend
	$S_5 = 1/\sqrt{6}(\Delta\alpha_1 + \Delta\alpha_2 + \Delta\alpha_3 - \Delta\beta_1 - \Delta\beta_2 - \Delta\beta_3)$	AH_3 symmetric bend
	$S_6 = \Delta R$	Si..A stretch
	$S_{7a} = 1/\sqrt{2}(\Delta r_2 - \Delta r_3)$	SiH_3 antisymmetric stretch
	$S_{8a} = 1/\sqrt{2}(\Delta r_6 - \Delta r_7)$	AH_3 antisymmetric stretch
	$S_{9a} = 1/\sqrt{2}(\Delta\alpha_2 - \Delta\alpha_3)$	SiH_3 antisymmetric bend
	$S_{10a} = 1/\sqrt{2}(\Delta\beta_2 - \Delta\beta_3)$	SiH_3 rock
	$S_{11a} = 1/\sqrt{2}(\Delta\theta_2 - \Delta\theta_3)$	AH_3 antisymmetric bend
	$S_{12a} = 1/\sqrt{2}(\Delta\tau_2 - \Delta\tau_3)$	AH_3 rock
	$S_{13a} = \Delta\gamma_1$	libration
	$S_{7b} = 1/\sqrt{6}(2\Delta r_1 - \Delta r_2 - \Delta r_3)$	SiH_3 antisymmetric stretch
	$S_{8b} = 1/\sqrt{6}(2\Delta r_5 - \Delta r_6 - \Delta r_7)$	AH_3 antisymmetric stretch
	$S_{9b} = 1/\sqrt{6}(2\Delta\alpha_1 - \Delta\alpha_2 - \Delta\alpha_3)$	SiH_3 antisymmetric bend

Table 8.65 Continued

	$S_{10b} = 1/\sqrt{6}(2\Delta\beta_1 - \Delta\beta_2 - \Delta\beta_3)$	SiH_3 rock
	$S_{11b} = 1/\sqrt{6}(2\Delta\theta_1 - \Delta\theta_2 - \Delta\theta_3)$	AH_3 antisymmetric bend
	$S_{12b} = 1/\sqrt{6}(2\Delta\tau_1 - \Delta\tau_2 - \Delta\tau_3)$	AH_3 rock
	$S_{13b} = \Delta\gamma_2$	libration
	$S_{14} = \Delta\phi$	torsion about Si..A

The percentage potential energy distributions amongst the various vibrational modes in the $SiH_4.NH_3$ complex are collected in Table 8.66. The a_1 intramolecular modes have 100% symmetry coordinate contribution. A similar situation exists in the case of the e symmetry species except for the electron acceptor antisymmetric bending mode. The ν_{10} and ν_{11} modes have symmetry coordinate distribution from other symmetry coordinates (S_{12a} and S_{9a}). The Si..N stretching mode has 15% contribution from S_4, the symmetric bending mode of silane. The intermolecular vibrational modes belonging to the e symmetry species, viz., the libration and rocking modes of the electron donor and acceptor have symmetry coordinate contributions from the bending modes of the electron donor. The a_2 mode has a 100% contribution from the torsional symmetry coordinate.

Table 8.66 Wavenumbers and %PEDs in the $SiH_4.NH_3$ Complex

Symmetry Species	Wavenumbers /cm^{-1}	%PED
a_1	3561	$100S_1$
	2343	$100S_2$
	2297	$100S_3$
	1121	$100S_4$
	965	$100S_5$
	87	$84S_6 + 15S_4$
e_a	3718	$100S_{8a}$
	2356	$100S_{7a}$
	1719	$100S_{11a}$
	1033	$74S_{9a} + 25S_{12a}$
	972	$92S_{10a} + 6S_{9a}$
	315	$90S_{12a} + 10S_{11a}$
	134	$42S_{13a} + 47S_{11a}$
e_b	3718	$100S_{8b}$
	2356	$100S_{7b}$
	1719	$100S_{11b}$
	1033	$74S_{9b} + 25S_{12b}$

Table 8.66 Continued

	972	$92S_{10b} + 6S_{9b}$
	315	$90S_{12b} + 10S_{11b}$
	134	$42S_{13b} + 47S_{11b}$
a_2	39	$100S_{14}$

The percentage potential energy distribution amongst the different symmetry coordinates for the $SiH_4.PH_3$ complex are collected in Table 8.67.

The a_2 mode has 100% symmetry coordinate distribution to its corresponding symmetry coordinate, with the Si..P stretching mode having 4% symmetry coordinate contribution from the PH_3 symmetric bending mode. In the case of the e species, the intramolecular stretching modes of the electron donor and acceptor have symmetry coordinate contributions solely due to their own symmetry coordinates. The bending modes of the electron donor and acceptor are perturbed by one another. The libration and rocking modes having symmetry coordinate contributions from the bending modes of the electron acceptor. The trend of having different symmetry coordinates contributing to a particular mode is consistent in the $SiH_4.AH_3$ complexes for the bending modes. This arises since those fundamentals lie close to each other.

Table 8.67 Wavenumbers and %PEDs in the $SiH_4.PH_3$ Complex

Symmetry Species	Wavenumbers /cm^{-1}	%PED
a_1	2532	$100S_1$
	2354	$100S_2$
	2332	$100S_3$
	1085	$100S_4$
	967	$100S_5$
	50	$97S_6 + 4S_5$
e_a	2548	$100S_{8a}$
	2354	$100S_{7a}$
	1183	$97S_{9a}$
	1018	$64S_{12a} + 35S_{10a}$
	976	$60S_{10a} + 34S_{11a}$
	160	$70S_{13a} + 26S_{11a}$
	53	$50S_{11a} + 47S_{10a}$
e_b	2548	$100S_{8b}$
	2354	$100S_{7b}$
	1183	$100S_{9b}$
	1018	$64S_{12b} + 35S_{10b}$

Table 8.67 Continued

	976	$60S_{10b} + 34S_{11b}$
	160	$70S_{13b} + 26S_{11b}$
	53	$50S_{11b} + 47S_{10b}$
a_2	22	$100S_{14}$

The changes in the intensities of the $SiH_4.AH_3$complexes are collected in Tables 8.68 and 8.69. The intensities of the symmetric stretching and bending modes for the electron acceptor are not shown in Table 8.68 since their corresponding monomer bands are infrared inactive. The major intensity enhancement occurs in ν_7, the antisymmetric stretching mode of NH_3; this results from the low monomer intensity value. The general trend with this type of weak complex follows weak intensity enhancements on complexation.

Table 8.68 Ratios of the Complex to Monomer Intensity values in the $SiH_4.NH_3$ complex

Symmetry Species	Mode	Complex A_c/km mol^{-1}	A_c/A_m
a_1	ν_1	0.2	1.00
	ν_2	30.2	0.18
	ν_4	155.7	0.72
	ν_5	254.0	1.36
e	ν_7	3.4	4.25
	ν_8	179.3	1.09
	ν_9	16.0	0.77
	ν_{11}	145.0	0.77

The changes in the complex / monomer intensity ratios in the $SiH_4.PH_3$ complex are collected in Table 8.69.

The intensity ratios on complexation are close to unity, with ν_5 and ν_8 being enhanced by 1.36 and 1.50 respectively. This occurs as a consequence of the charge acquired by the hydrogens of silane on complexation, which enhances the dipole moment vector, hence resulting in an intensity enhancement on execution of the bending mode. The intensity ratios are even lower in this complex compared with the corresponding NH_3 complex,. hence further emphasizing the weakness of this complex.

Table 8.69 Ratios of the Complex to Monomer Intensity values for the $SiH_4.PH_3$ complex

Symmetry Species	Mode	Complex A_c/km mol^{-1}	A_c/A_m
a_1	ν_1	43.8	1.07
	ν_2	95.2	0.58
	ν_4	27.3	0.84
	ν_5	254.3	1.36
e	ν_7	88.2	0.89
	ν_8	147.9	1.50
	ν_9	17.6	0.89
	ν_{11}	168.9	0.91

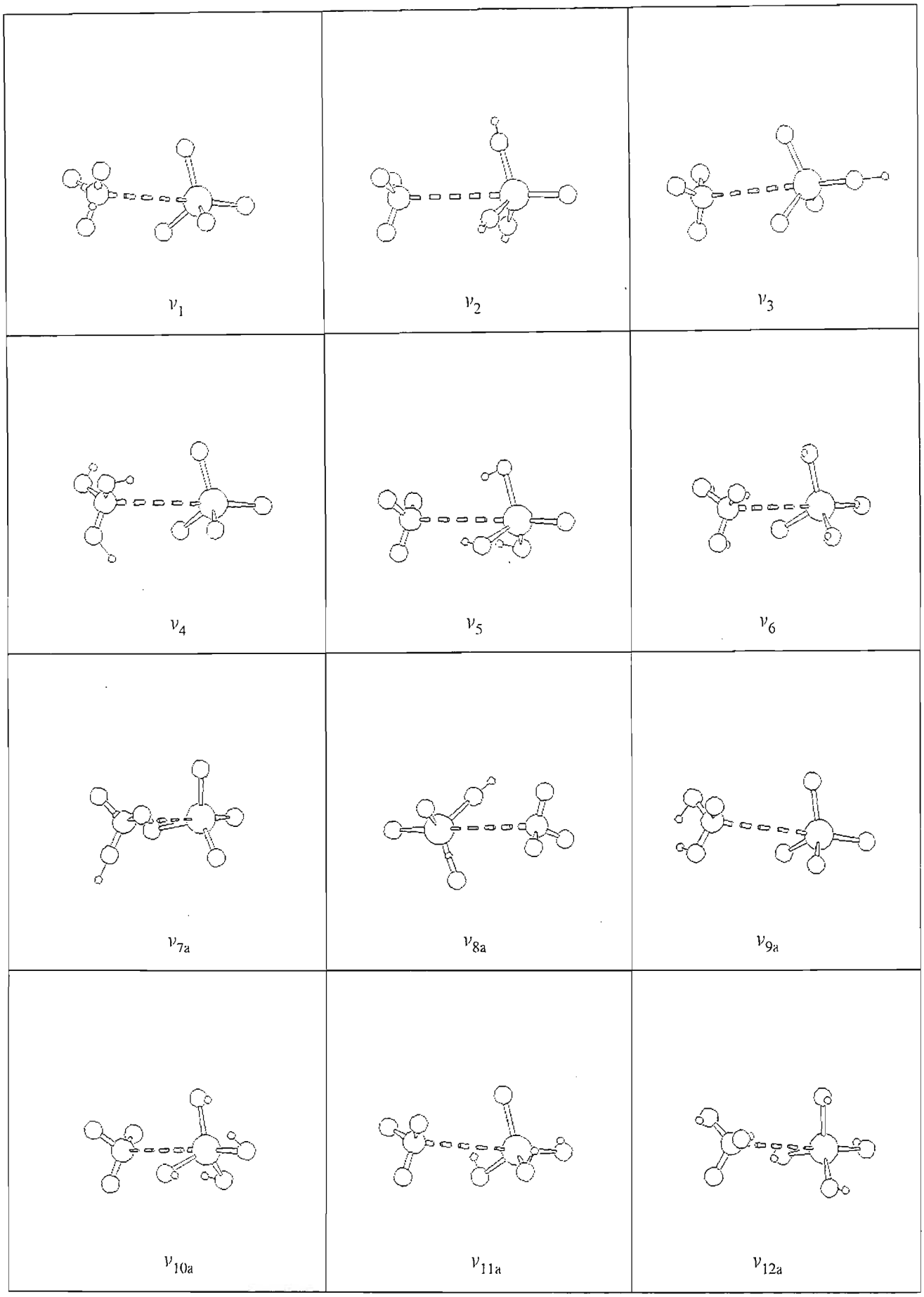

Fig 8.34 Graphical Representation of the $SiH_4.NH_3$ Complex Vibration modes

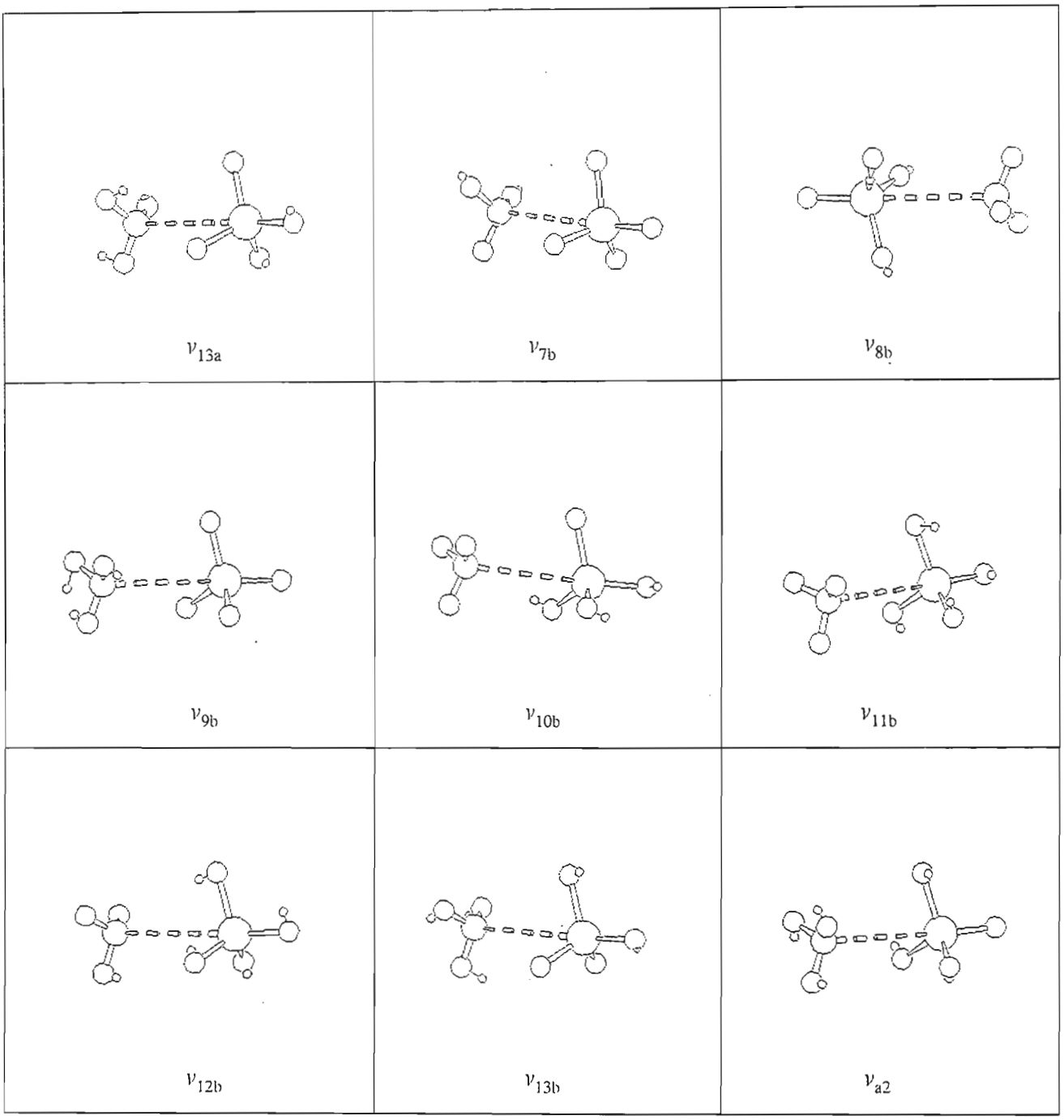

Fig 8.34 Graphical Representation of the $SiH_4.NH_3$ Complex Vibration modes

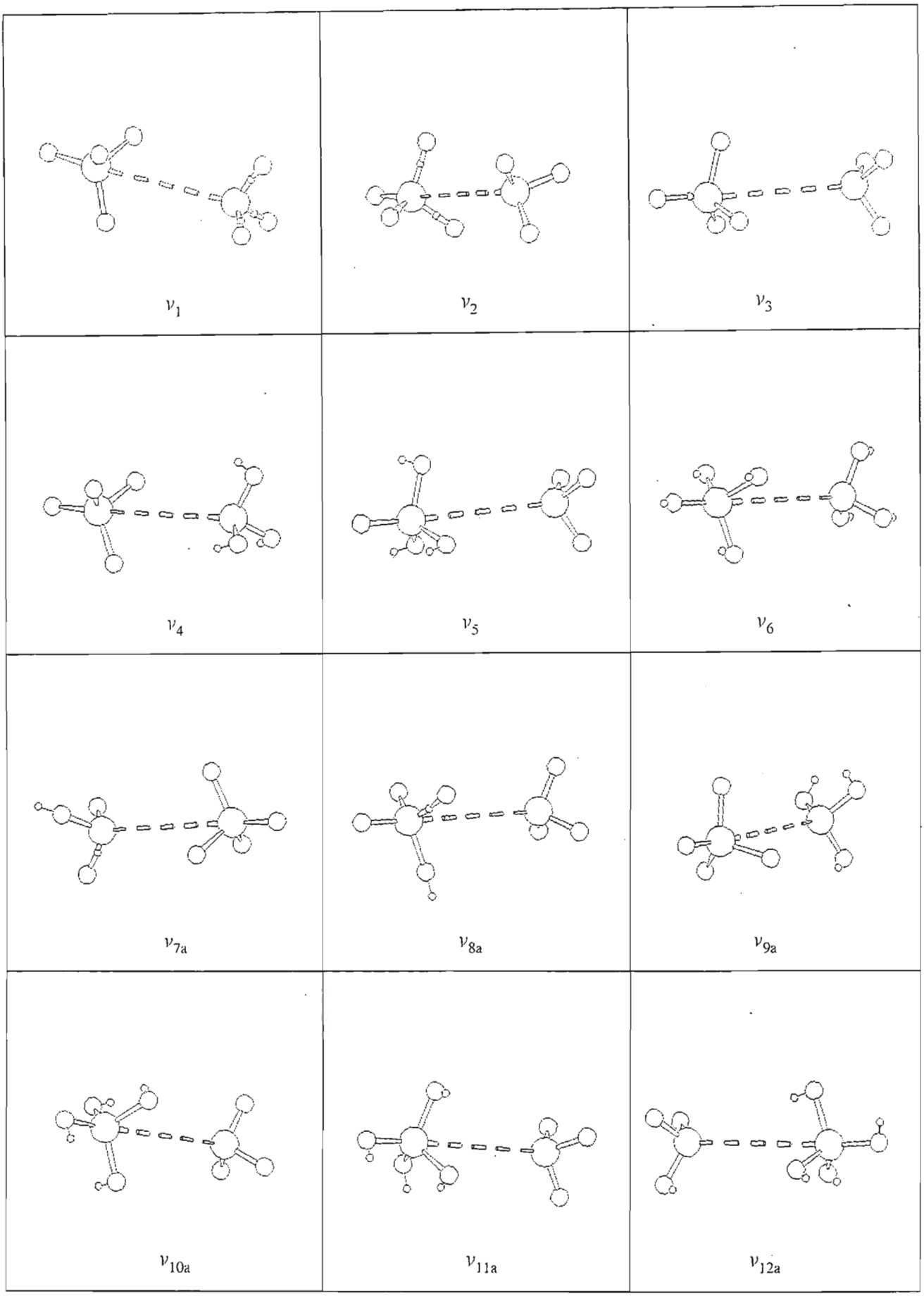

Fig 8.35 Graphical Representation of the $SiH_4.PH_3$ Complex Vibration modes

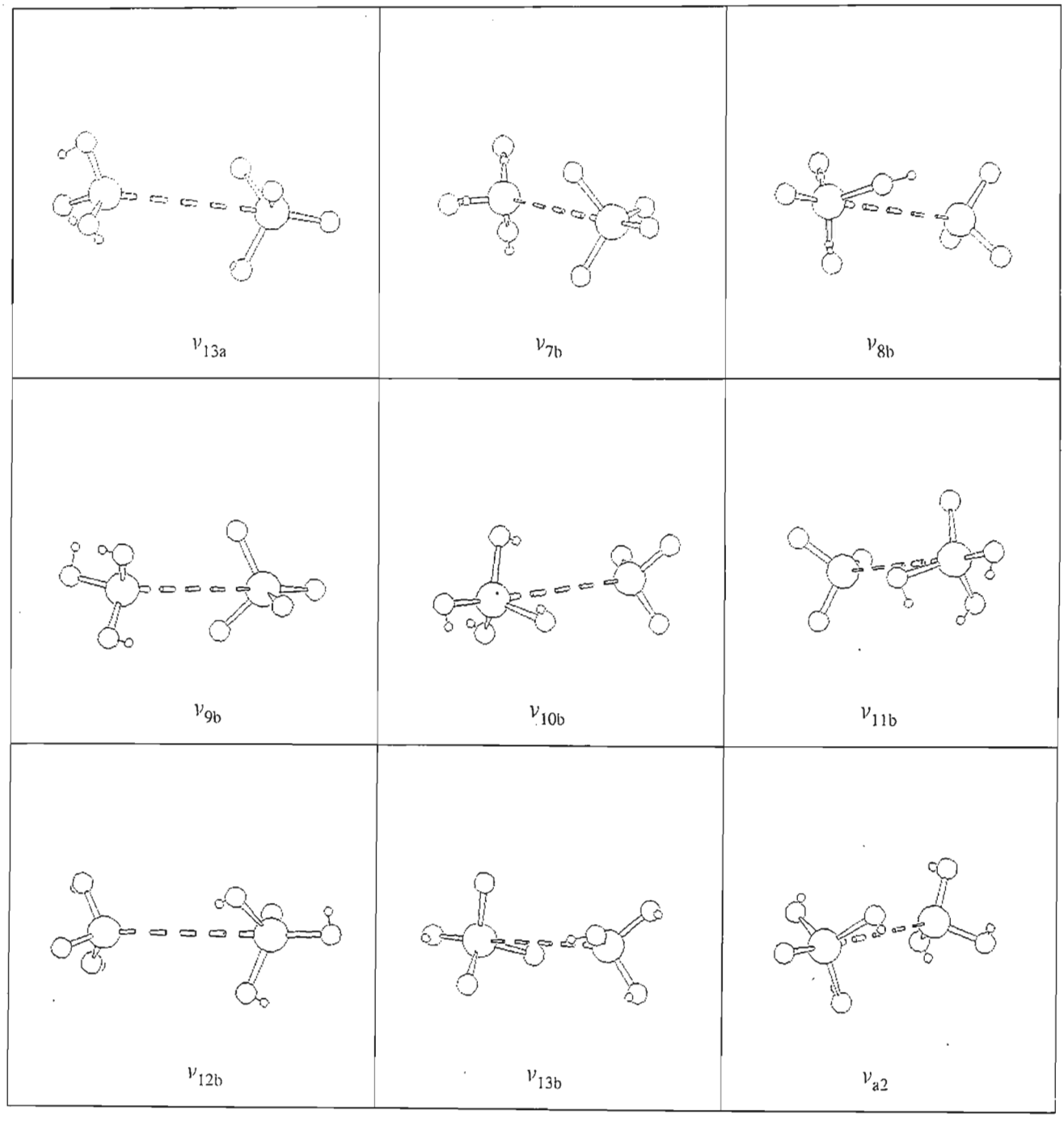

Fig 8.35 Graphical Representation of the $SiH_4.PH_3$ Complex Vibration modes

Chapter Nine

Summary and Conclusions

In this chapter, some correlations will be presented for the relationships between the various calculated parameters, e.g. geometrical parameters, net Mulliken charges transferred, corrected MP2 binding energies, wavenumber shifts and intensity ratios in the different complexes. The new systems studied in this project consisting of the complexes $CH_4.PH_3$, $SiH_4.HCl$, $SiH_4.H_2S$, and $SiH_4.YH_3$ follow the same trends as those observed for the more common complexes in the series.

9.1 The Homodimers

9.1.1 Correlation of Hydrogen Bond Characteristics with the MP2 Corrected Interaction Energies

Table 9.1 presents a summary of the hydrogen bond lengths, angles, percentage dispersion energy contributions and corrected MP2 interaction energies for the homodimers. Fig 9.1 shows a plot of the H..B distance against the corrected MP2 interaction energies for the homodimers. From fig 9.1 it is observed that the homodimers with the largest H..B distances are the most unstable. The linear trend in the correlation is remarkable, with the HF and PH_3 dimers being on either side of the best straight line fit of the data points. The HF dimer has a much shorter H..B separation, probably resulting from the vibrational averaging effects of the dimer during the proton donor-acceptor interchange. The phosphine dimer has a doubly bifurcated interaction and hence due to steric factors the P..H separation is expected to be much longer. The plot of the AH..B bond angle against the corrected MP2 energies is shown in fig 9.2. The trend followed in this correlation is almost linear with the exception of the ammonia dimer. AH..B angles for the homodimers are close to linearity except for the cyclic species, having more than one major site of

Table 9.1 Summary of the Geometrical Parameters and the Corrected MP2 Interaction Energies for the Homodimers

Homodimer	R(H..B) /pm	AH..B /deg	$\%\Delta E_{disp}$	$\Delta E'$(MP2) /kJ mol^{-1}
$(HF)_2$	178.3	180.0	37.0	-8.0
$(HCl)_2$	260.8	175.6	42.8	-5.6
$(H_2O)_2$	194.5	170.2	9.4	-19.6
$(H_2S)_2$	284.0	178.2	57.4	-4.3
$(NH_3)_2$	245.5	123.7	26.8	-10.5
$(PH_3)_2$	356.2	165.3	99.3	-10.6
$(CH_4)_2$	317.8	180.0	95.5	-0.74

For further comparison, fig 9.3 depicts the percentage dispersion energy contribution in the different homodimers. The trend followed by the second row hydrides, having a greater dispersion energy contribution to the binding energy, is clearly shown. This further emphasises the need for the incorporation of larger basis sets when studying complexes in the second and higher rows, where a complete description of the bonding region is required in theoretical calculations of this nature.

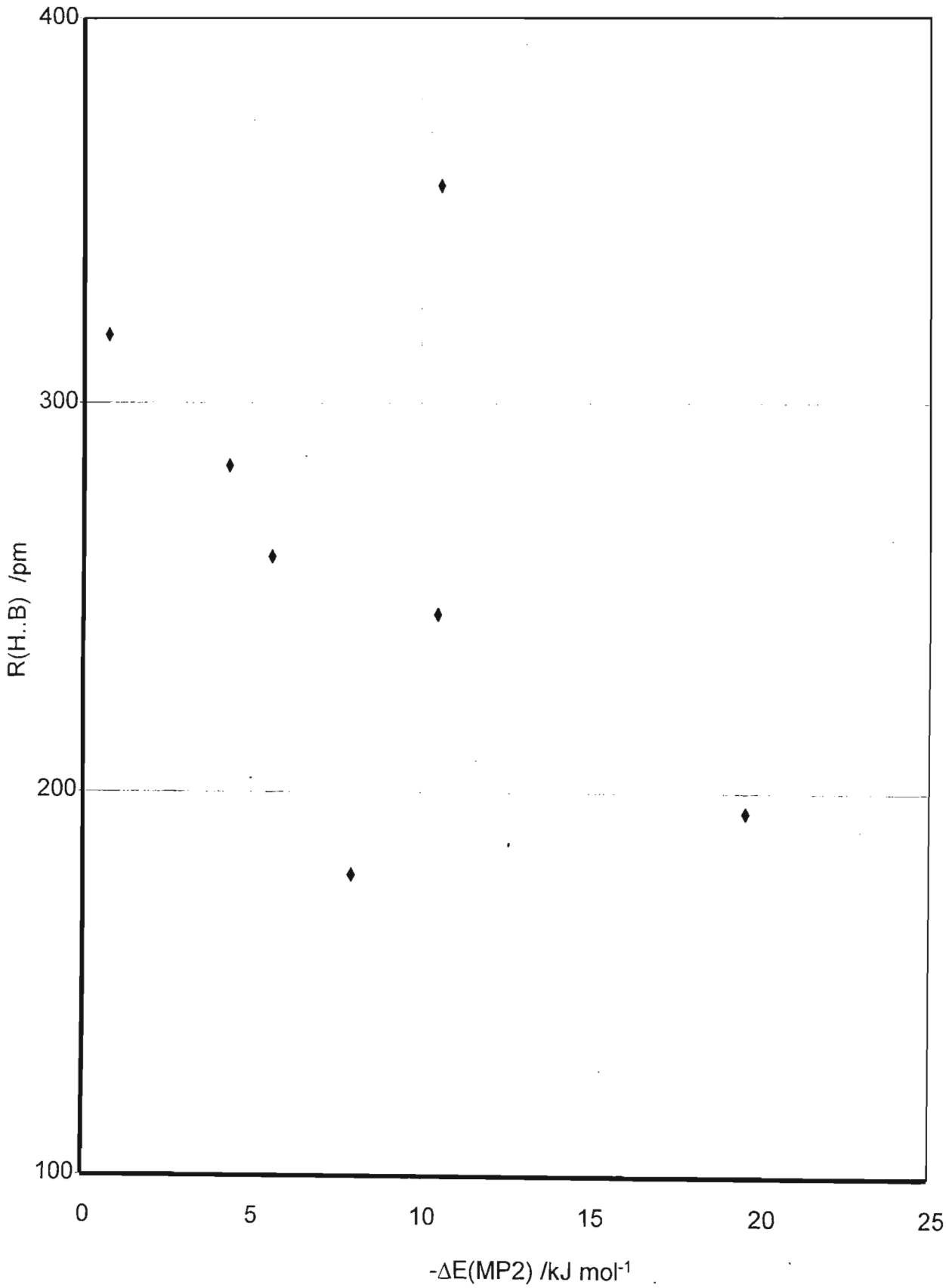

Fig 9.1 Plot of the H..B distance against -ΔE(MP2)

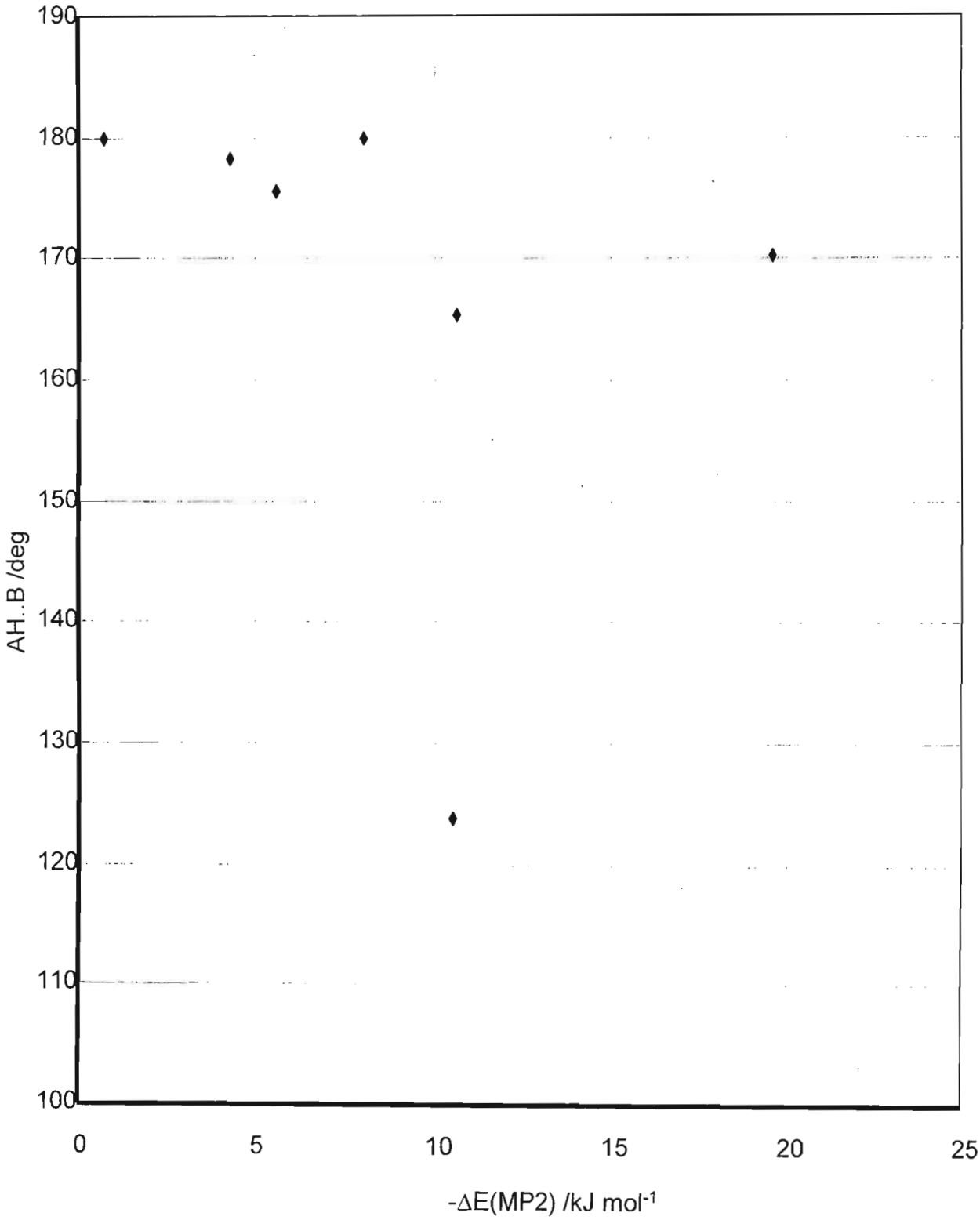

Fig 9.2 Plot of AH..B angle against -ΔE(MP2)

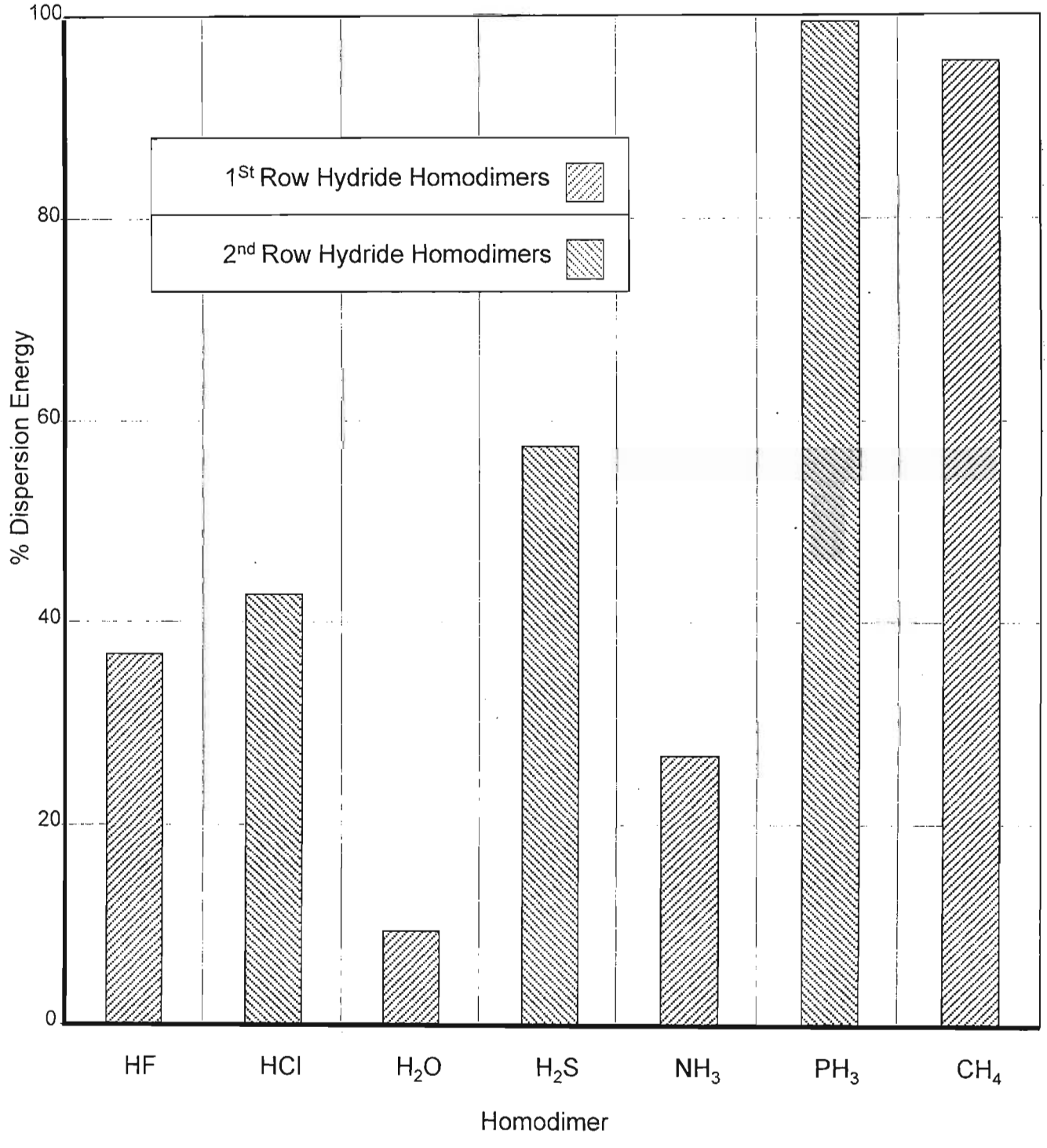

Fig 9.3 Plot of Percentage Dispersion Energy for the Homodimers

9.1.2 Correlation of the Changes in the AH Bond Lengths with the Net Mulliken Charges Transferred

Table 9.2 correlates the changes in the AH bond length with the net Mulliken charge transferred on dimerization. Fig 9.4 shows a plot of the net Mulliken charge transferred against the changes in the AH bond length.

Table 9.2 Summary of the Net Mulliken Charge Transferred and the Changes in the AH Bond Lengths

Homodimer	Net Mulliken Charge Transferred /e	Δr(AH) /pm
$(HF)_2$	0.037	0.6
$(HCl)_2$	0.013	0.4
$(H_2O)_2$	0.012	0.6
$(H_2S)_2$	0.009	0.3
$(NH_3)_2$	0.000	0.2
$(PH_3)_2$	0.000	0.2
$(CH_4)_2$	0.002	0.1

From fig 9.4, the greater the Mulliken charge transferred, the greater the change in the AH bond length. The HF dimer undergoes the largest net Mulliken charge transfer and hence has the largest change in the HF bond length. In the water dimer there is a slight

deviation from this trend, even though it also undergoes a similar net Mulliken charge transfer to the HF dimer. The change in the OH bond length is not as significant. The YH_3 dimers, having centrosymmetric structures, show no net Mulliken charge transfer hence do not follow the trend of the other homodimers.

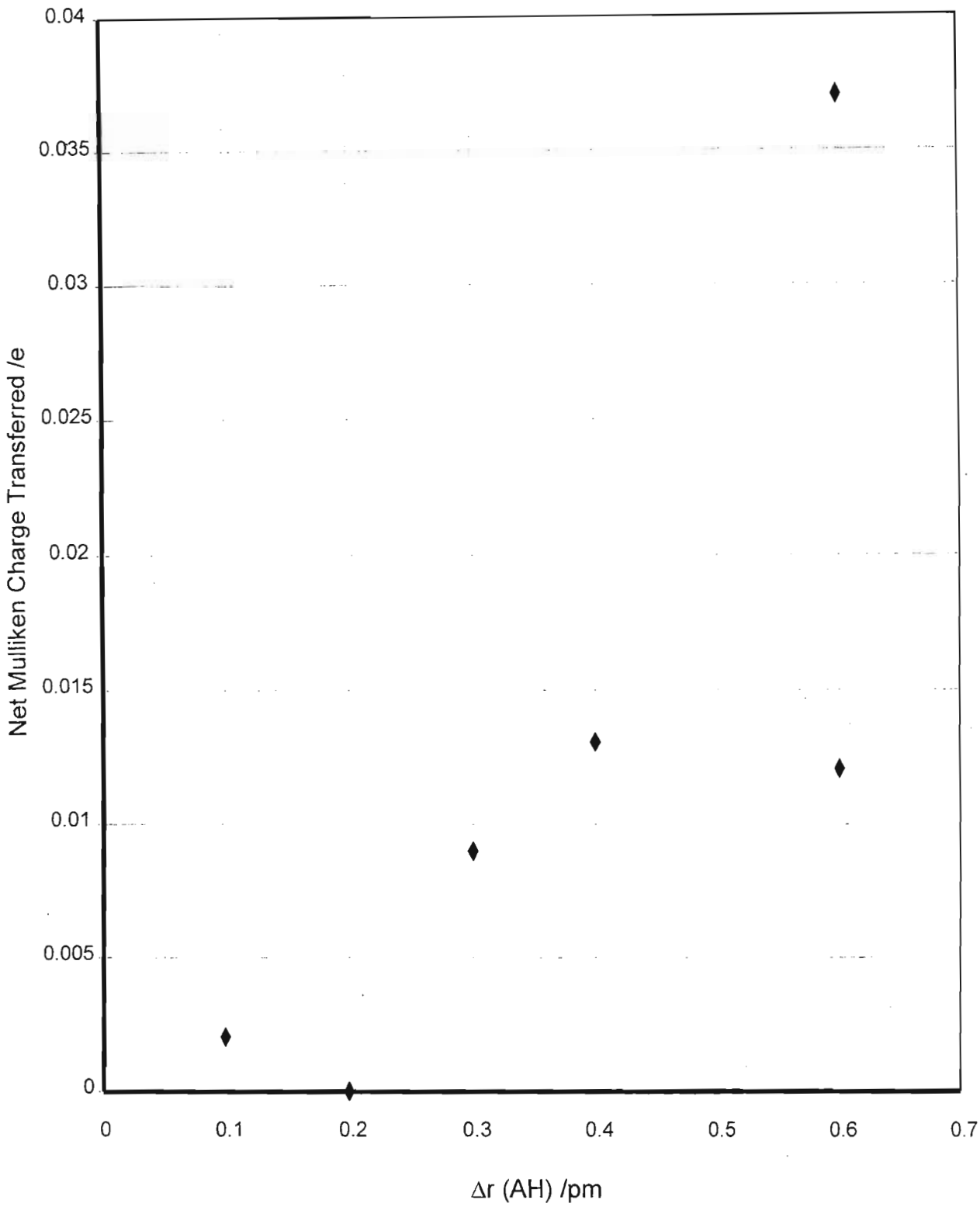

Fig 9.4 Plot of Net Mulliken Charge transferred against Δr (AH)

9.1.3 Correlation of the Geometrical Parameters with the Wavenumber Shifts and the Ratios of the Complex to Monomer Intensities

Table 9.3 summarises the changes in the AH bond lengths, AH stretching wavenumber shifts and complex to monomer intensity ratios.

Table 9.3 Summary of the Changes in the AH Bond Lengths, AH Stretching Wavenumber Shifts and the Complex to Monomer Intensity Ratios

Homodimer	$\Delta r(AH)$ /pm	$-\Delta\nu(AH)$ /cm^{-1}	I_c/I_m
$(HF)_2$	0.6	115	5.4
$(HCl)_2$	0.4	43	6.1
$(H_2O)_2$	0.6	41	18.8
$(H_2S)_2$	0.3	14	1.5
$(NH_3)_2$	0.2	23	0.0
$(PH_3)_2$	0.2	-1	0.0
$(CH_4)_2$	0.1	-3	0.7

The changes in the wavenumber shifts of the AH bonds are almost proportional to the corresponding extensions of the AH bonds, as seen in fig 9.5. This trend is in support of the Nakamoto, Margoshes and Rundle rule[347] depicting a linear relationship between $\Delta\nu(AH)$ and $\Delta r(AH)$. The largest changes in the AH bond length occur in the HF and H_2O dimers, however the largest wavenumber shift occurs in the HF dimer. The AH stretching modes in both the methane and phosphine dimers undergo blue shifts on dimerization with

the smallest changes in the AH bond lengths. The relationship shown in fig 9.5 is similar to that in fig 9.4. Hence one may conclude that the net amount of Mulliken charge transferred during dimerization is proportional to the magnitude of the wavenumber shift in the AH bonds.

The plot of the complex / monomer intensity ratios for the AH stretching mode against the change in the AH bond distance also shows no clear relationship, as shown in fig 9.6. The water dimer has the largest complex / monomer intensity ratio for the AH stretching mode, followed by the HCl dimer. The YH_3 dimers undergo no intensity enhancement, consistent with their having the smallest wavenumber shifts in the AH stretching vibrations.

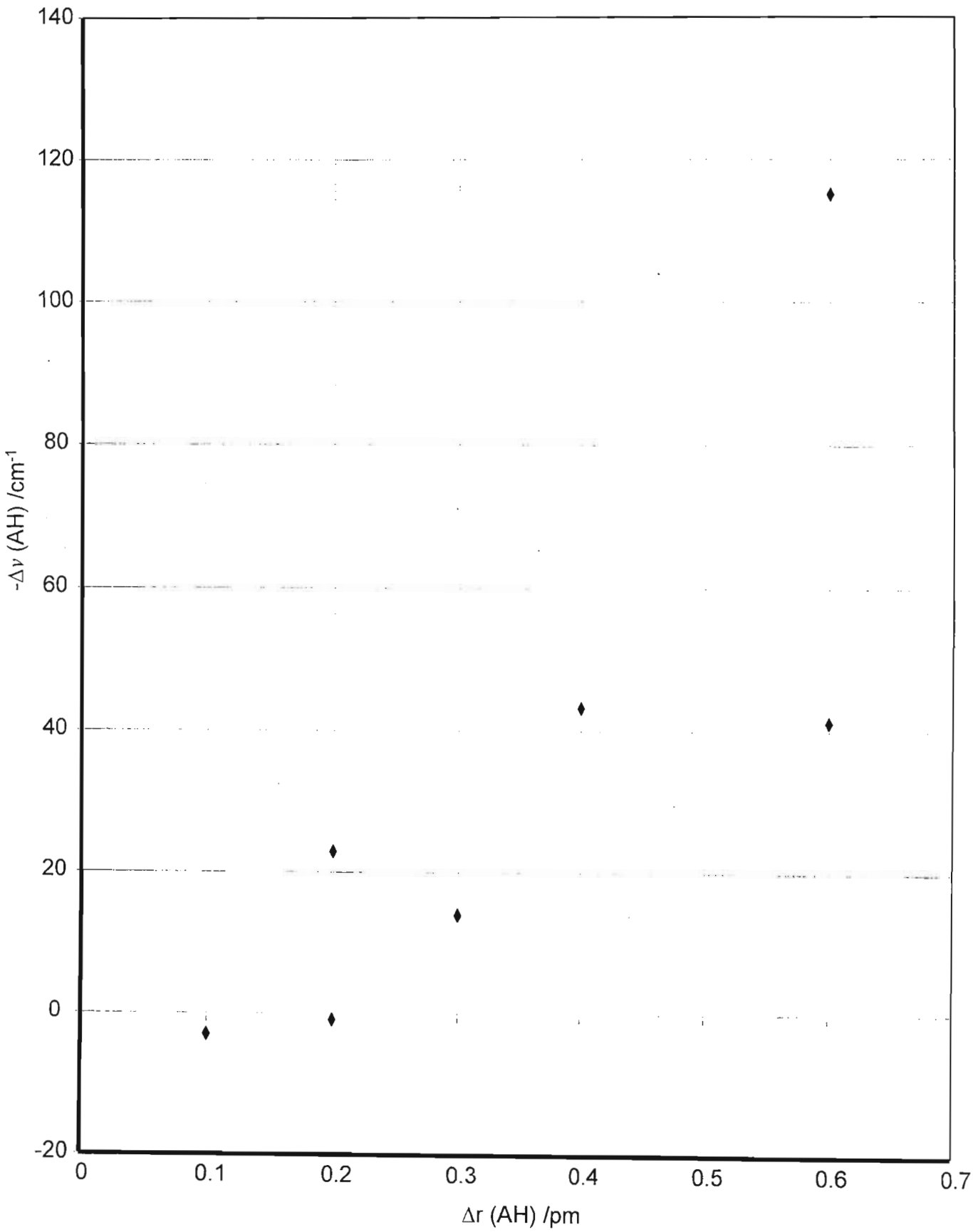

Fig 9.5 Plot of $-\Delta\nu$ (AH) against Δr (AH)

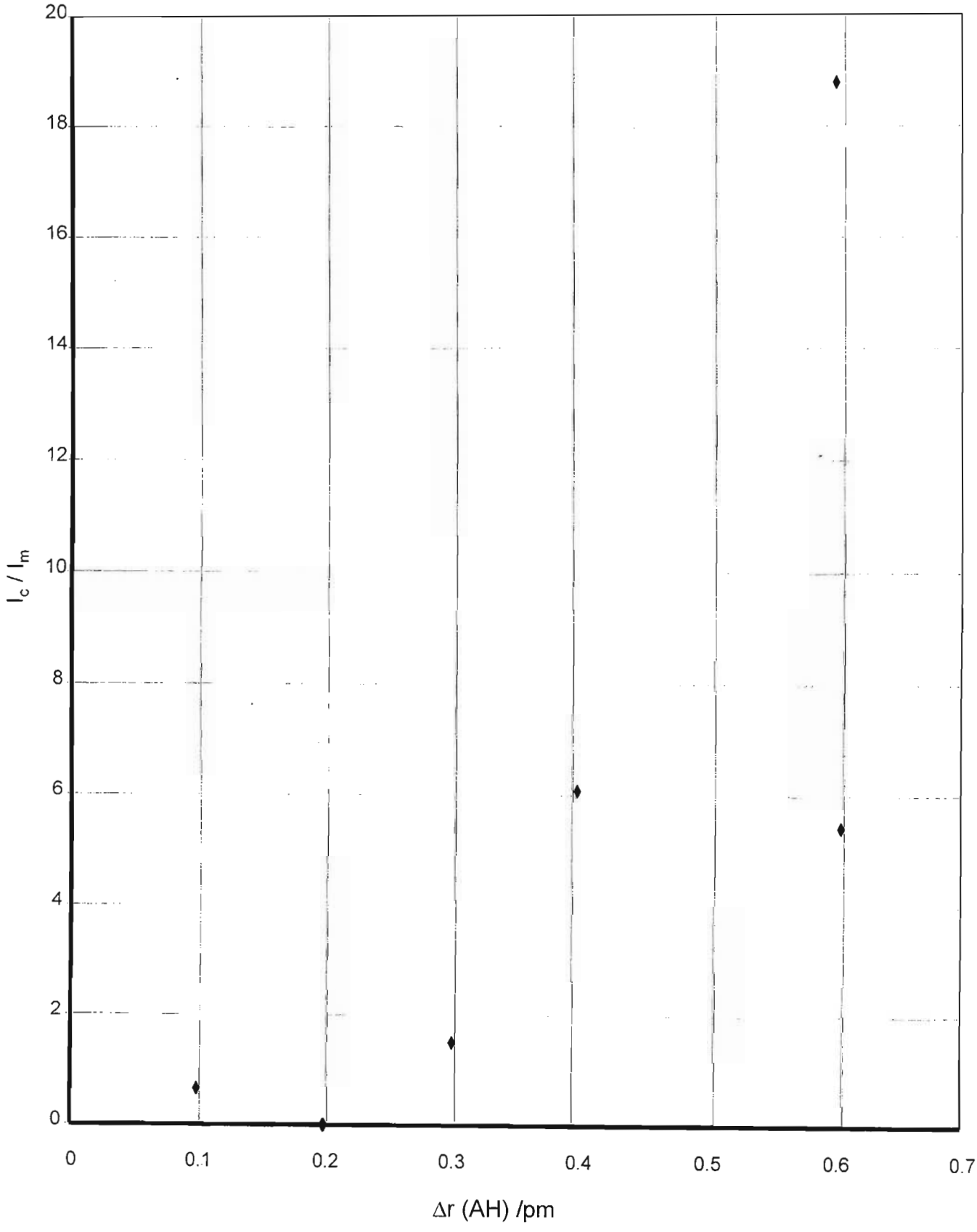

Fig 9.6 Plot of I_c / I_m against Δr (AH)

9.2 ***The HF Complexes***

9.2.1 Correlation of Hydrogen Bond Characteristics with the MP2 Corrected Interaction Energies

Table 9.4 presents a summary of the hydrogen bond lengths together with the corrected MP2 interaction energies. Fig 9.7 shows a plot of the H..B distance against the corrected MP2 interaction energy for the HF complexes. From fig 9.7, the plot of the H..B distance against the corrected MP2 interaction energies, the trend is seen to be an inversely proportional relationship. The NH_3.HF complex is the most stable, with the MH_4.HF complexes being the least stable. In the case of the NH_3.HF complex, the proton of HF is centrally located between the nitrogen and fluorine atoms, thus stabilising the complex. In the MH_4.HF complexes, there is also a secondary interaction, resulting in the deviation of these two data points on the graph from the trend followed by the other HF complexes. The shorter the H..B distance the more stable is the complex energetically. Fig 9.8 shows that the FH..B angle is almost invariant to the corrected MP2 interaction energy with the exception of the MH_4.HF complexes. This is expected since these complexes have a secondary interaction.

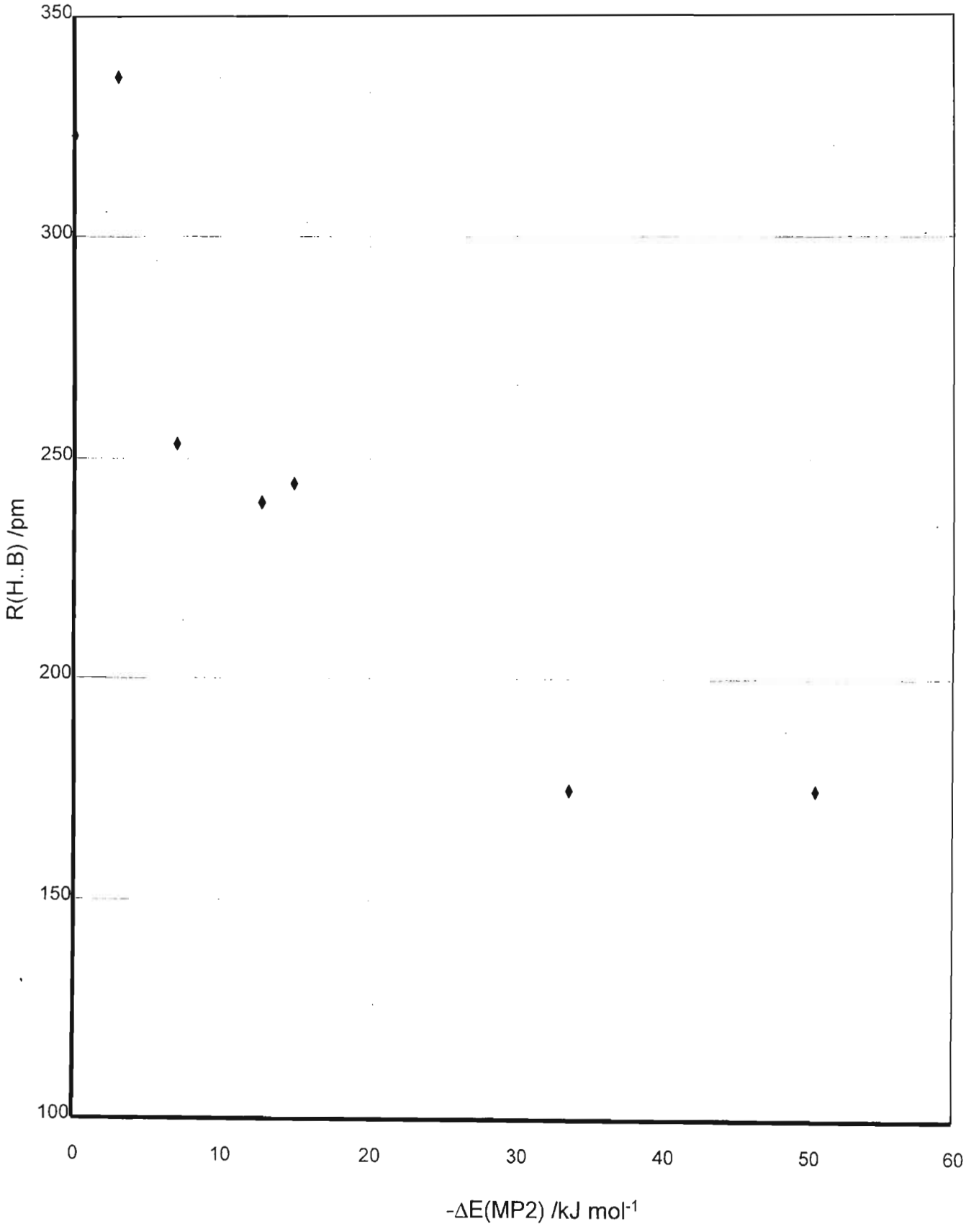

Fig 9.7 Plot of the H..B distance against -ΔE(MP2)

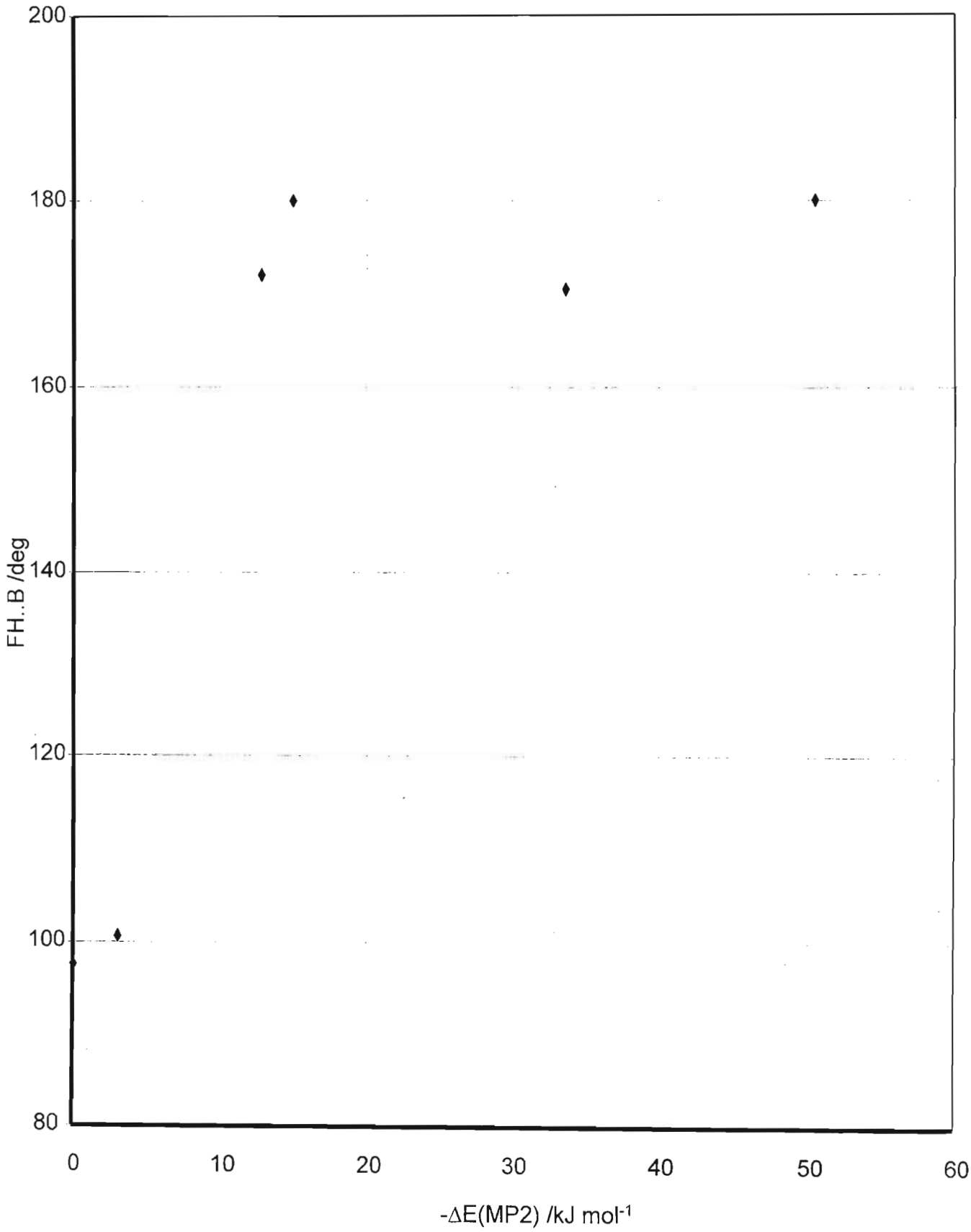

Fig 9.8 Plot of FH..B angle against -ΔE(MP2)

Table 9.4 Summary of the Geometrical Parameters and the Corrected MP2 Interaction Energies for the HF Complexes

Complex	R(H..B) /pm	FH..B /deg	$\%\Delta E_{Disp}$	$\Delta E(MP2)$ /kJ mol^{-1}
$HF.H_2O$	174.9	170.3	1.8	-33.7
$HF.H_2S$	239.6	172.0	9.2	-12.8
$HF.NH_3$	174.8	180.0	2.2	-50.5
$HF.PH_3$	244.0	180.0	3.9	-14.9
$HF.CH_4$	336.3	100.8	74.8	-3.1
$HF.SiH_4$	322.9	97.6	100.0	-0.1

From fig 9.9, the plot of the percentage dispersion energy for the different HF complexes, a similar trend to that for the homodimers is observed. The percentage dispersion energy contribution in the second row complexes with HF is found to be greater than those of the corresponding first row complexes. As one moves in the right in the periodic table, the percentage dispersion energy contribution also decreases correspondingly. The MH_4.HF complexes have the highest dispersion energy contributions for the first and second row hydride complexes with HF respectively.

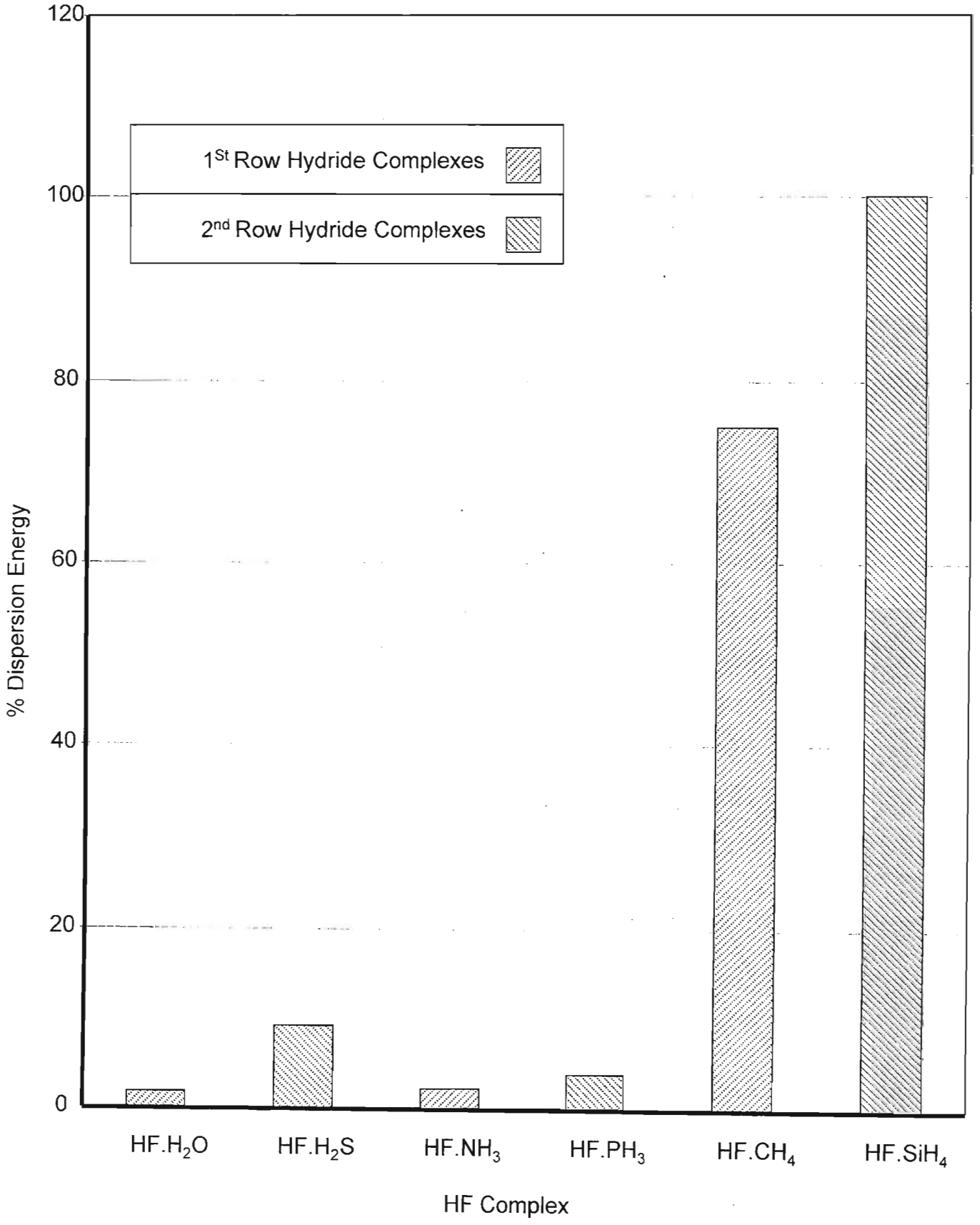

Fig 9.9 Plot of Percentage Dispersion Energy for the HF Complexes

9.2.1 Correlation of the HF Bond Lengths with the Net Mulliken Charges Transferred

Table 9.5 collects the changes in the HF bond distances and the net Mulliken charges transferred. From fig 9.10, which plots the net Mulliken charge transferred against the change in the HF bond distance, a directly proportional relationship is obtained. The complex with the largest amount of net Mulliken charge transferred (NH_3.HF) undergoes the greatest change in the HF bond length. The second row hydride complexes with HF experience smaller changes in the HF bond lengths on complexation coupled with the decreased net Mulliken charges transferred on complexation, as seen in Table 9.5.

Table 9.5 Summary of the Net Mulliken Charges Transferred and the Changes in HF Bond Lengths

Complex	Net Mulliken Charge Transferred /e	Δr(HF) /pm
H_2O.HF	0.039	1.4
H_2S.HF	0.015	0.6
NH_3.HF	0.040	2.4
PH_3.HF	0.024	0.7
CH_4.HF	0.016	0.2
SiH_4.HF	0.022	0.2

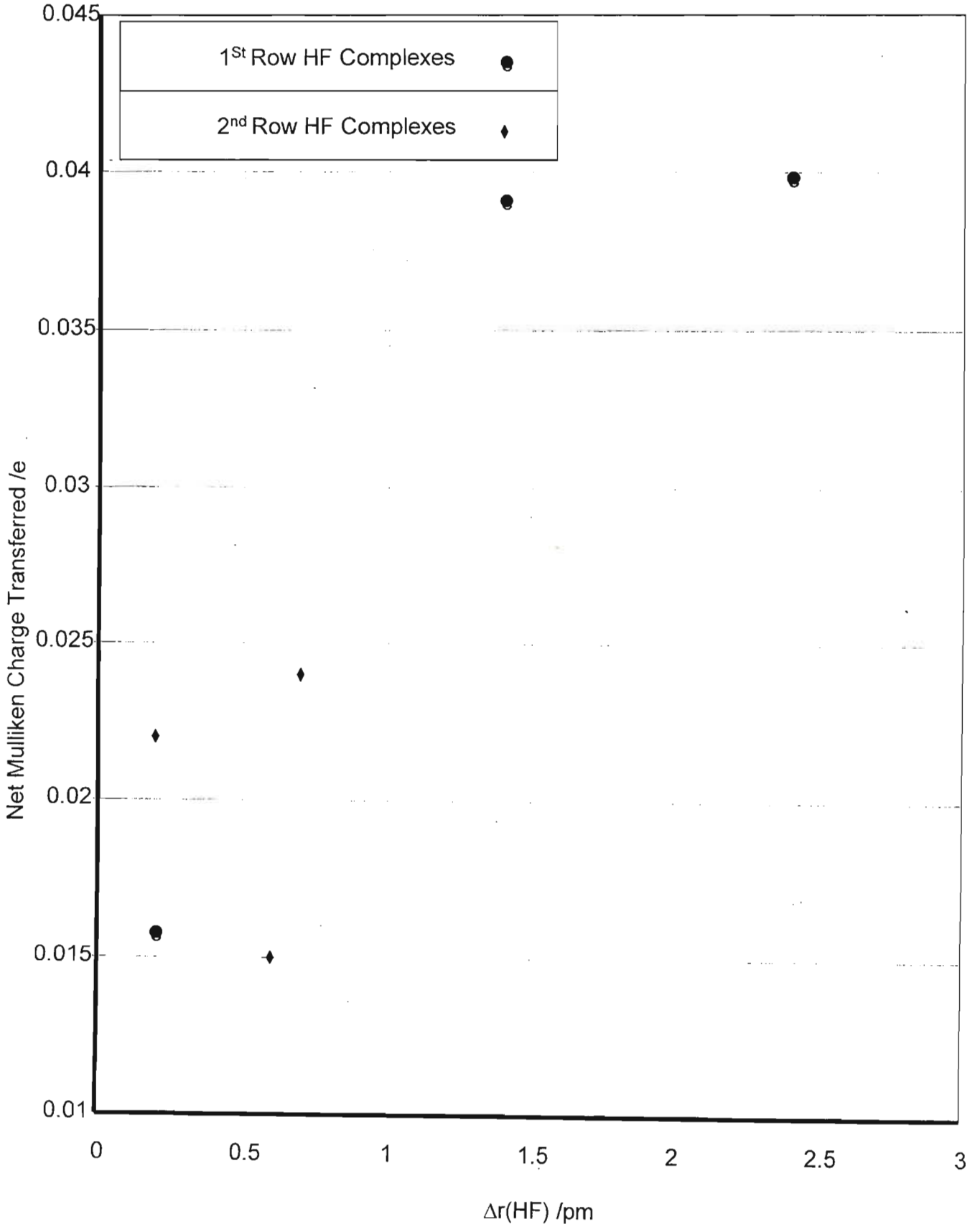

Fig 9.10 Plot of Net Mulliken Charge Transferred against Δr(HF)

9.2.3 Correlation of the Geometrical Parameters with the Wavenumber Shifts and the Ratios of the Complex to Monomer Intensities for the HF Stretching Mode in the HF Complexes

Table 9.6 summarises the changes in the HF bond lengths, wavenumber shifts and complex to monomer intensity ratios.

Table 9.6 Summary of the Changes in the HF Bond Distances, Stretching Wavenumber Shifts from the Monomer Position and the Complex to Monomer Intensity Ratios

Complex	Δr(HF) /pm	$-\Delta\nu$(HF) /cm^{-1}	I_c/I_m
H_2O.HF	1.4	292	4.96
H_2S.HF	0.6	139	5.43
NH_3.HF	2.4	544	12.25
PH_3.HF	0.7	160	6.25
CH_4.HF	0.2	22	0.97
SiH_4.HF	0.2	30	0.95

The relationship seen in fig 9.11, the plot of the HF stretching wavenumber shift against the change in the corresponding bond length depicts an exceptionally linear relationship thus following the Nakamoto, Margoshes and Rundle rule[347]. The complex with the greatest change in the HF bond distance also undergoes the largest wavenumber shift. The NH_3.HF complex experiences the greatest change in the HF bond length, with the MH_4.HF complexes the least. Once again this is due to these complexes having a secondary interaction, thus resulting in a greater charge redistribution, rather than being

localised in the hydrogen bonding region.

One can also conclude that the wavenumber shifts in the HF stretching mode for the first row hydride complexes are much larger than those in the second row hydride complexes. From a comparison of $-\Delta\nu$(HF) and -ΔE(MP2), a direct proportionality exists following the Badger-Bauer rule.[348] Fig 9.12 depicts the plot of the complex / monomer intensity ratios for the HF stretching mode against the changes in the HF bond length on complexation. The HF complexes with the first row hydrides show a linear relationship, with the NH_3.HF complex having the largest I_c/I_m ratio and change in the HF bond length, with the CH_4.HF complex having the smallest. For the second row hydride complexes with HF a similar linear trend is observed, with the PH_3.HF complex having the largest I_c/I_m ratio and change in the HF bond length.

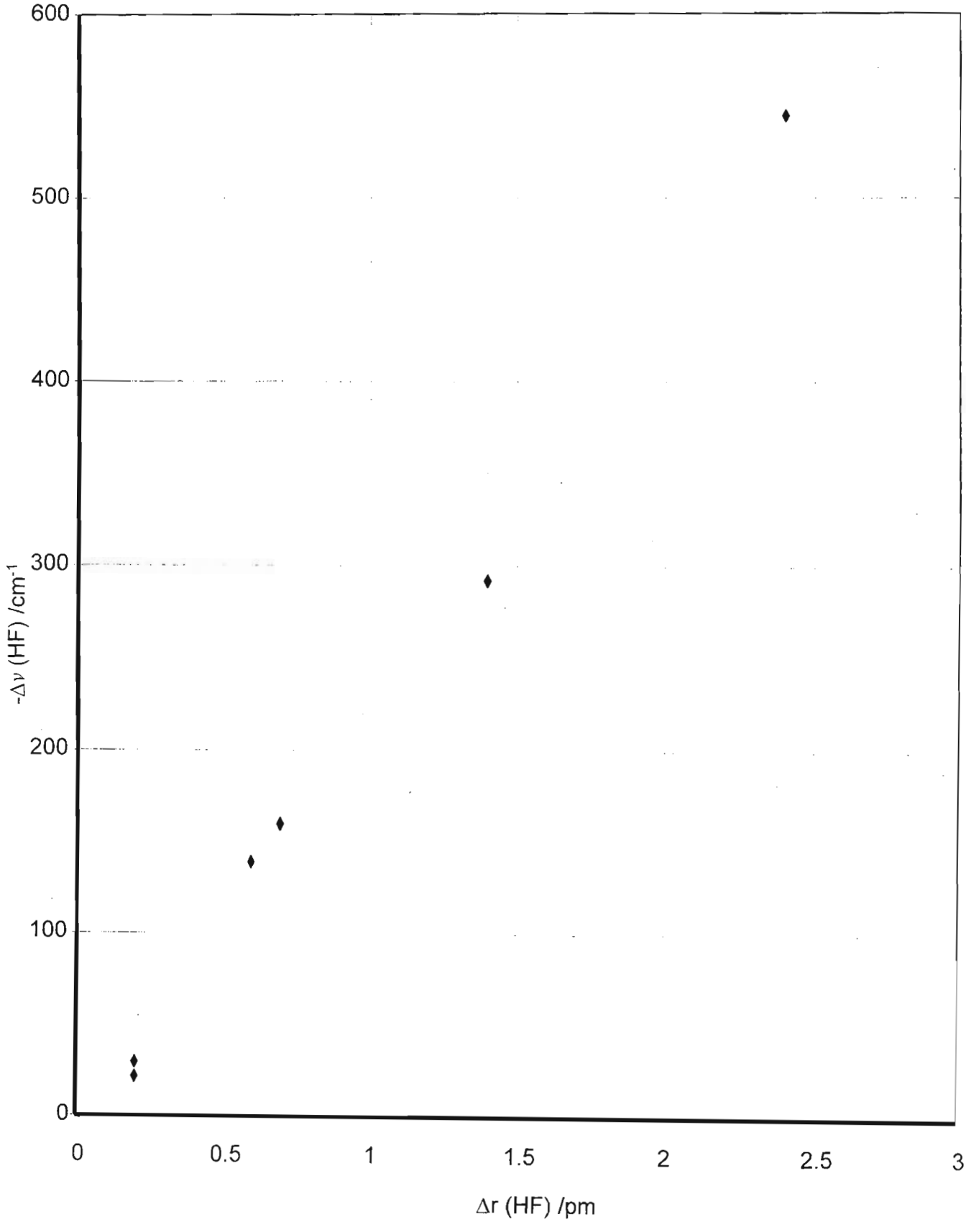

Fig 9.11 Plot of $-\Delta\nu$ (HF) against Δr (HF)

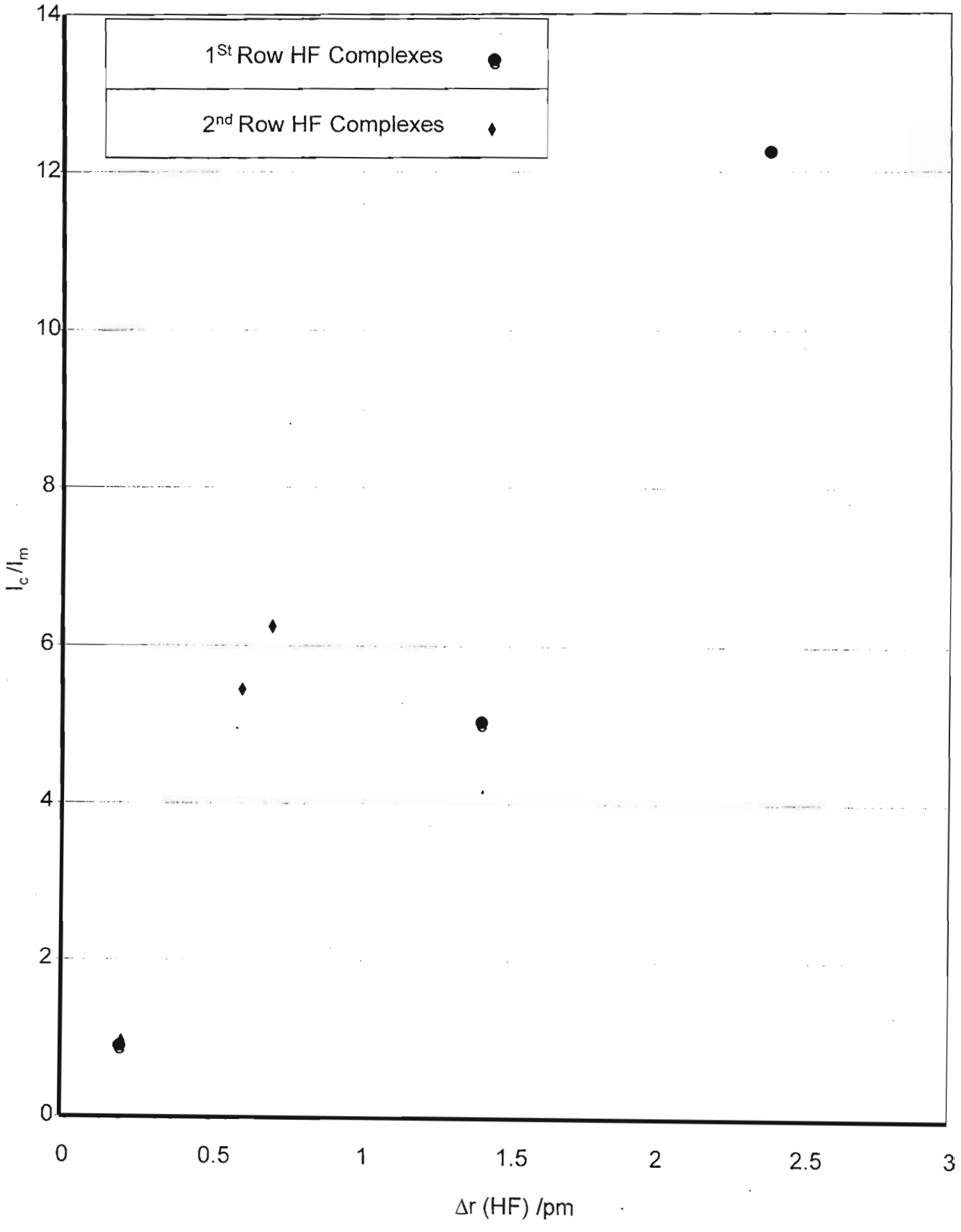

Fig 9.12 Plot of I_c/I_m against Δr (HF)

*9.3 **The HCl Complexes***

9.3.1 Correlation of Hydrogen Bond Characteristics with the MP2 Corrected Interaction Energies

Table 9.7 presents the summary of the hydrogen bond lengths (H..B) together with the corrected MP2 interaction energies for the HCl complexes. Fig 9.13 displays a plot of the hydrogen bond length against the corrected MP2 interaction energy. In the case of the first row hydride complexes with HCl, the NH_3.HCl complex is most stable with the shortest H..B distance.

Table 9.7 Summary of the Geometrical Parameters and the Corrected MP2 Interaction Energies for the HCl Complexes

Complex	R(H..B) /pm	ClH..B /deg	$\%\Delta E_{Disp}$	ΔE(MP2) /kJ mol^{-1}
HCl.HF	195.6	180.0	50.1	-11.1
HCl.H_2O	186.3	175.4	18.3	-19.7
HCl.H_2S	253.0	178.4	35.1	-6.4
HCl.NH_3	177.5	180.0	19.4	-39.9
HCl.PH_3	258.2	180.0	32.8	-10.6
HCl.CH_4	264.1	180.0	82.1	-1.9
HCl.SiH_4	213.0	180.0	81.8	-2.2

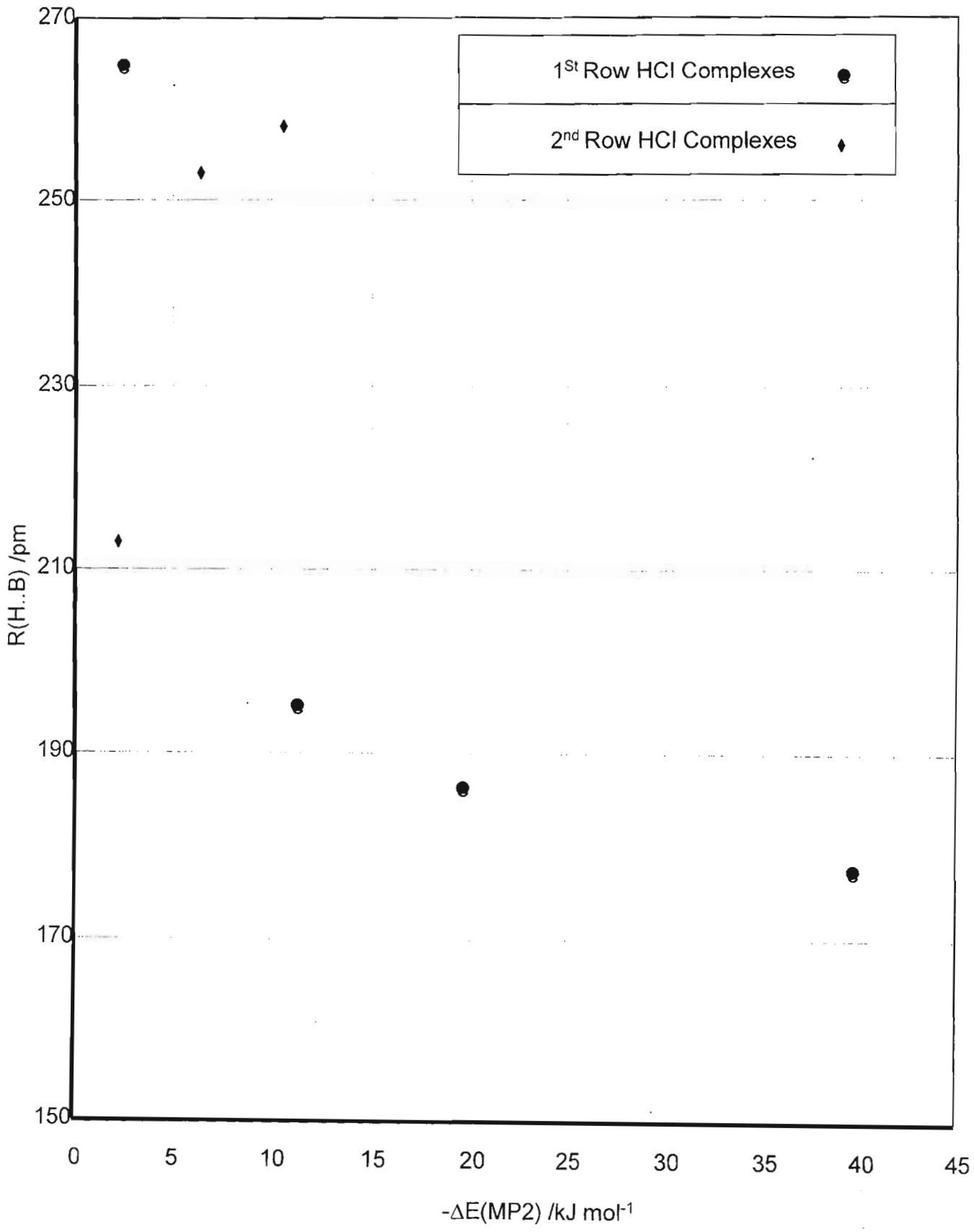

Fig 9.13 Plot of R(H..B) against -ΔE(MP2)

The trend followed by the HF complexes, shown in fig 9.9, is repeated, with the second row hydride complexes with HCl having a greater dispersion energy contribution to their interaction energies than the corresponding first row hydride complexes (fig 9.14).

9.3.2 Correlation of Changes in the HCl Bond Lengths with the Net Mulliken Charges Transferred

Table 9.8 collects the changes in the HCl bond distances and the net Mulliken charges transferred in the HCl complexes.

Table 9.8 Summary of the Net Mulliken Charges Transferred and the Changes in HCl Bond Length

Complex	Net Mulliken Charge Transferred /e	Δr(HCl) /pm
HF.HCl	0.036	0.7
H_2O.HCl	0.046	1.8
H_2S.HCl	0.025	0.7
NH_3.HCl	0.064	4.8
PH_3.HCl	0.033	1.0
CH_4.HCl	0.006	0.2
SiH_4.HCl	0.006	0.2

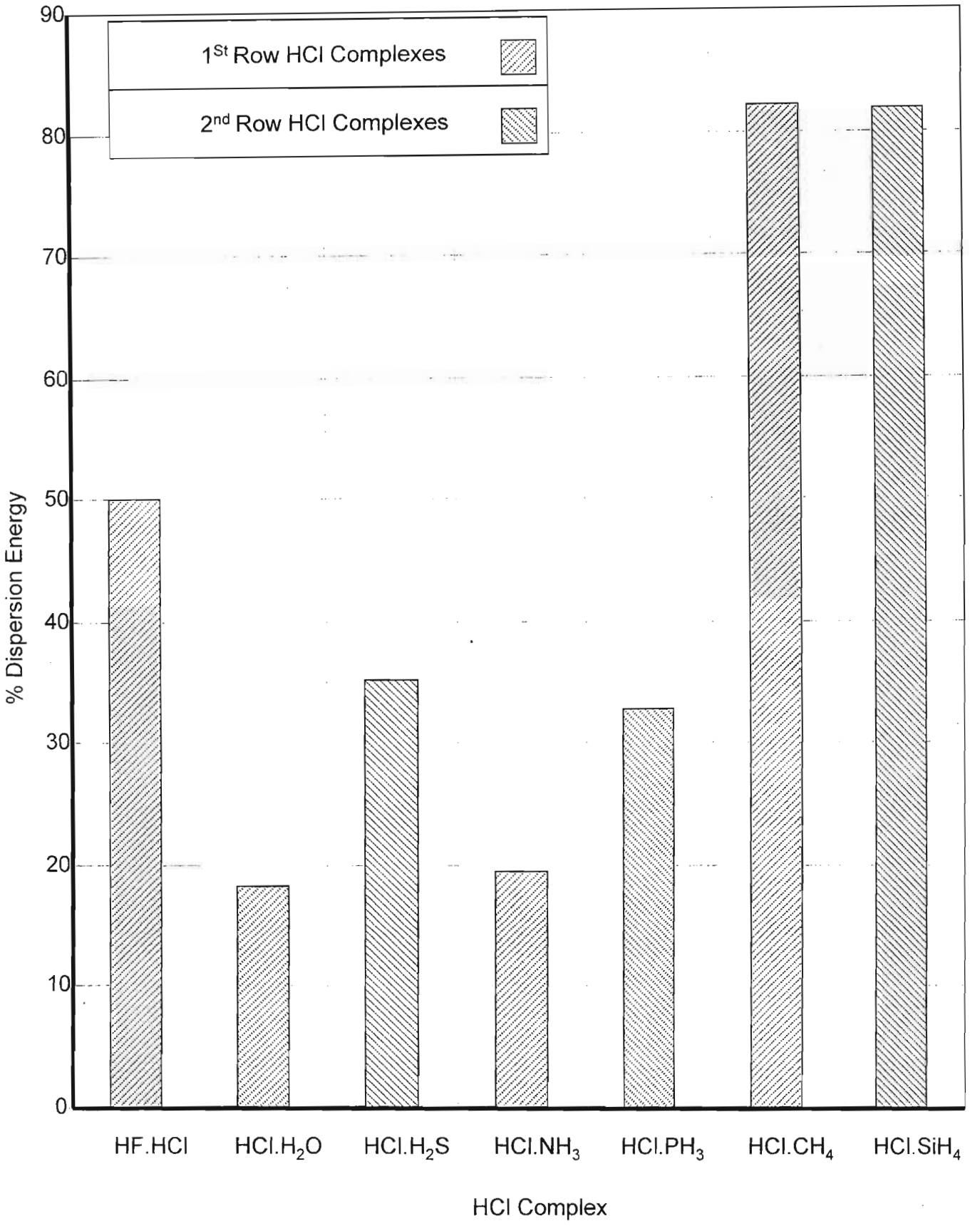

Fig 9.14 Plot of Percentage Dispersion Energy for the HCl Complexes

Fig 9.15, the plot of the net Mulliken charge transferred against the change in the HCl bond distance, depicts a directly proportional relationship. This relationship is more pronounced in these complexes compared with the HF complexes. It should also be noted that in the HCl complexes the hydrogen bond interaction is more localised with no secondary interactions, as was the case in the corresponding HF complexes. The NH_3.HCl complex undergoes the greatest net Mulliken charge transfer, coupled with the largest change in the HCl bond length, similar to the NH_3.HF complex.

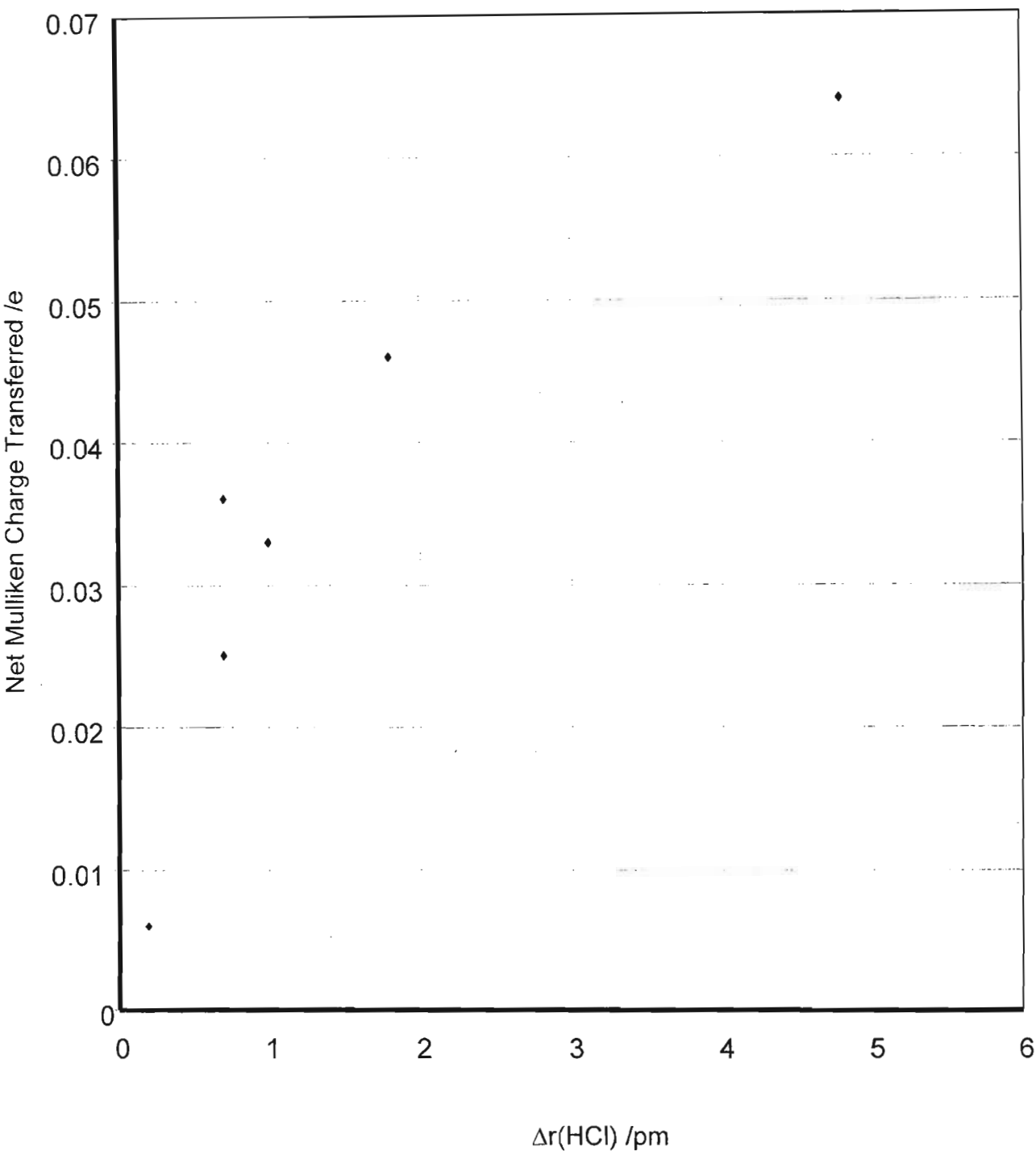

Fig 9.15 Plot of Net Mulliken Charge Transferred against Δr(HCl)

9.3.3 Correlation of the Geometrical Parameters with the Wavenumber Shifts and the Ratios of the Complex to Monomer Intensities for the HCl Stretching Mode in the HCl Complexes

Table 9.9 summarises the changes in the HCl bond lengths, wavenumber shifts and complex to monomer intensity ratios.

Table 9.9 Summary of the Changes in the HCl Bond Lengths, Stretching Wavenumber Shifts from the Monomer Positions and the Complex to Monomer Intensity Ratios

Complex	Δr(HCl) /pm	$-\Delta\nu$(HCl) /cm^{-1}	I_c/I_m
HF.HCl	0.7	74	11.97
H_2O.HCl	1.8	270	30.05
H_2S.HCl	0.7	26	0.1
NH_3.HCl	4.8	547	75.89
PH_3.HCl	1.0	145	19.9
CH_4.HCl	0.2	16	0.85
SiH_4.HCl	0.2	31	4.22

The plot (fig 9.16) of the wavenumber shifts against the changes in the HCl bond distances shows a linear relationship. This linear trend is similar to that in the HF complexes. The first row hydride complexes exhibit larger wavenumber shifts than the second row hydride complexes with HCl. This trend was also observed in the corresponding HF complexes, however, the magnitudes of the HCl wavenumber shifts for

the MH_4.HCl complexes are smaller. The Badger-Bauer rule[348] also holds in these complexes as in the HF complexes. In the case of the relationship of the intensity ratios against the changes in the HCl bond lengths (fig 9.17), once again a linear relationship is observed. Overall, in both sets of HX complexes, the greater the HX intensity ratios the greater is the change in the HX bond distance. The NH_3.HCl complex exhibits the largest I_c/I_m ratio, with the largest change in the HCl distances. The magnitudes of the I_c/I_m ratios for the second row hydride complexes are smaller than those for the first row hydride complexes.

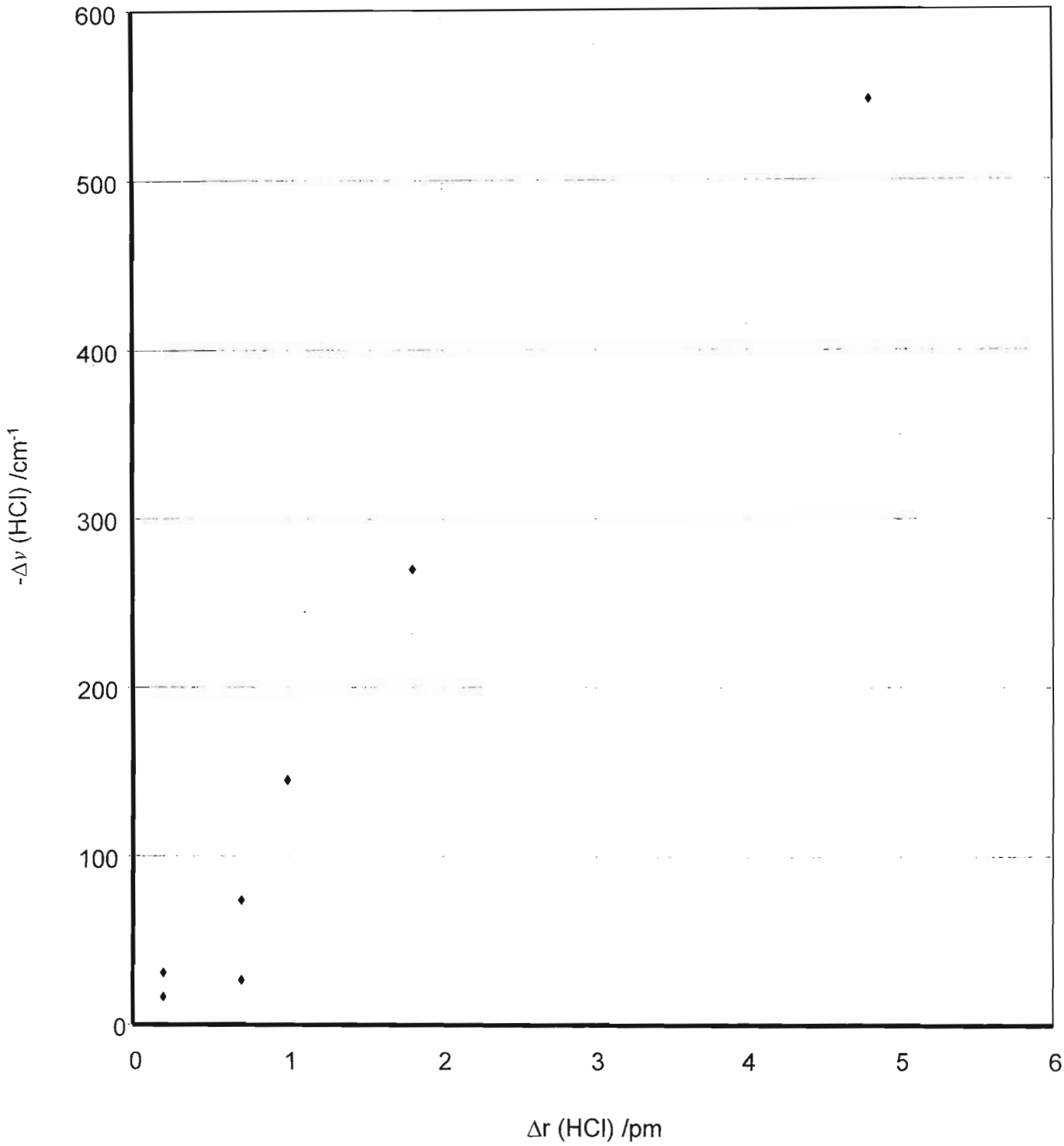

Fig 9.16 Plot of $-\Delta\nu$ (HCl) against Δr (HCl)

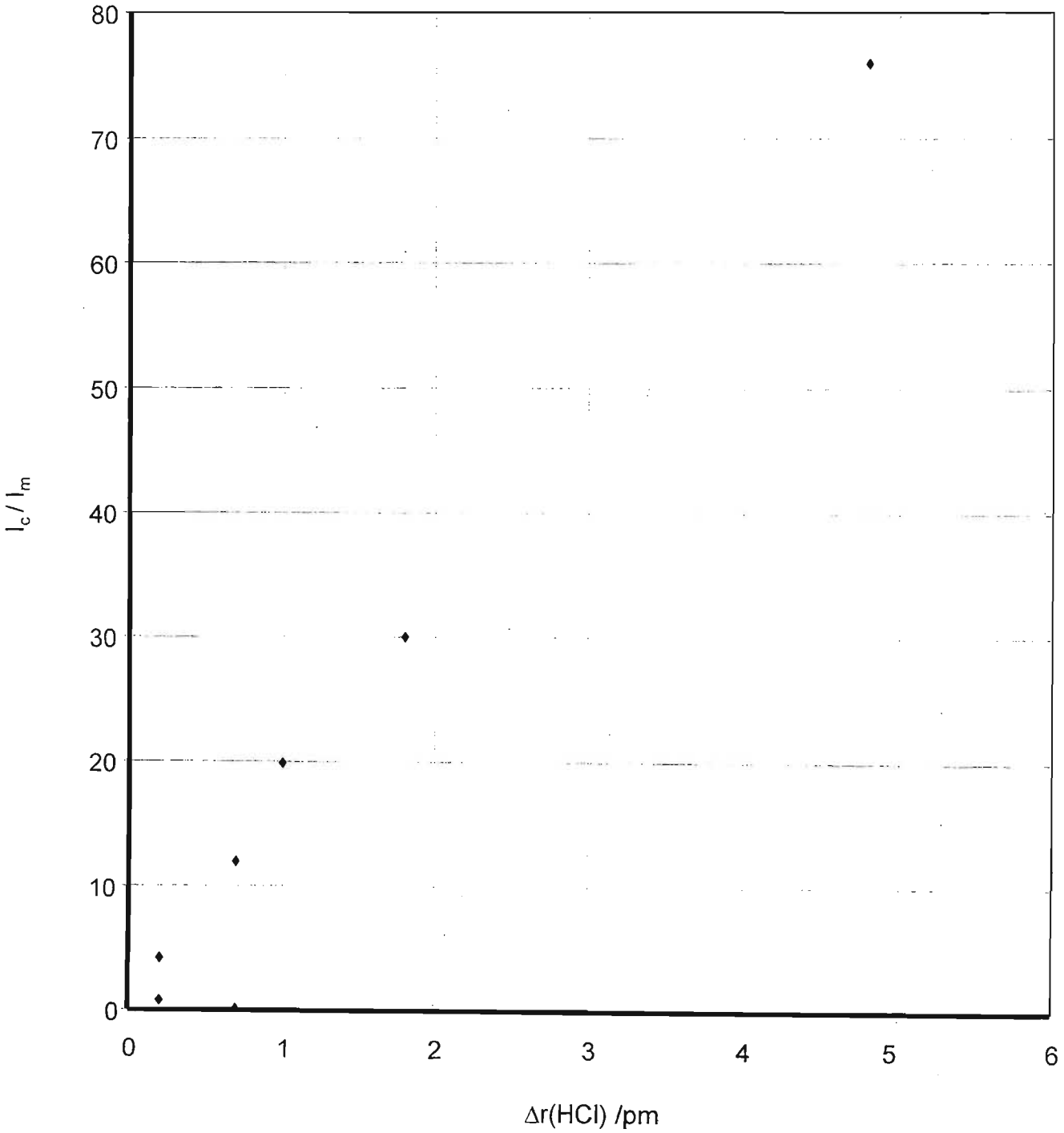

Fig 9.17 Plot of I_c/I_m against Δr(HCl) in the HCl Complexes

9.4 The $NH_3.H_2O$, $PH_3.H_2S$ and $H_2S.H_2O$ Complexes

The only complex having water as the acid is the $NH_3.H_2O$ complex. Hence no comparisons could be made with other complexes in which water is the acid. The complexes having H_2S as proton donor are $H_2S.H_2O$ and $PH_3.H_2S$. Summarising the major results for these three complexes, the stronger the interaction, the shorter is the hydrogen bond distance, the larger the role the dispersion energy plays in the second row complexes ($PH_3.H_2S$) (as observed in the HF, HCl and homodimer complexes), the greater the change in the AH bond length and the greater the net amount of Mulliken charge transferred on complexation. With regard to the wavenumber shifts, the strongest bound complex ($NH_3.H_2O$) has the largest wavenumber shift (-173 cm^{-1}) and the weakest bound complex ($PH_3.H_2S$) the smallest wavenumber shift (-26 cm^{-1}). A similar trend to the wavenumber shifts is also observed for the intensity ratios.

9.5 The Methane Complexes

9.5.1 Correlation of Hydrogen Bond Characteristics with the MP2 Corrected Interaction Energies

Table 9.10 presents the summary of the hydrogen bond lengths and angles together with the corrected MP2 interaction energies.

Table 9.10 Summary of the Geometrical Parameters and the Corrected MP2 Interaction Energies for the Methane Complexes

Complex	R(H..B) /pm	CH..B /deg	$\%\Delta E_{Disp}$	$-\Delta E(MP2)$ /kJ mol^{-1}
$CH_4.H_2O$	256.0	167.5	-	-0.7
$CH_4.NH_3$	274.0	180.0	41.8	3.6
$CH_4.PH_3$	341.3	180.0	-	0.3

The trend of the first row hydride complex being more strongly bonded than the second row hydride complex is once again repeated. In the case of the dependence of the hydrogen bond angle on the corrected MP2 interaction energy, the trend towards a linear hydrogen bonded complex is reinforced. The $CH_4.NH_3$ complex has 41.8% dispersion energy contribution to the binding energy of the complex. The other methane complexes in this series are unbound at the SCF level, hence calculation of the percentage dispersion energy was not carried out.

9.4.2 Correlation of the Changes in the CH Bond Lengths with the Net Mulliken Charges Transferred

Table 9.11 collects the changes in the CH bond distances and the Mulliken charge shifts. The net Mulliken charge transferred shows no dependence on the change in the CH bond length, since the value of $\Delta r(CH)$ was 0.1 pm in all the methane complexes.

Table 9.11 Summary of the Net Mulliken Charges Transferred and the Changes in the CH Bond Lengths

Complex	Net Mulliken Charge Transferred /e	$\Delta r(CH)$ /pm
$CH_4.H_2O$	0.016	0.1
$CH_4.NH_3$	0.010	0.1
$CH_4.PH_3$	0.003	0.1

9.4.3 Correlation of the Geometrical Parameters with the Wavenumber Shifts and the Ratios of the Complex to Monomer Intensities for the CH Stretching Modes in the Methane Complexes

Table 9.12 summarises the changes in the CH bond lengths, wavenumber shifts and complex to monomer intensity ratios. The $\Delta\nu(CH)$ and I_c/I_m values show no dependence on $\Delta r(CH)$, since the $\Delta r(CH)$ values are all constant. Hence no conclusion can be made regarding the relationship between the vibrational properties and the changes in the CH bond distances.

Table 9.12 Summary of the Changes in the CH Bond Lengths, Stretching Wavenumber Shifts from the Monomer Positions and the Complex to Monomer Intensity Ratios

Complex	Δr(CH) /pm	$-\Delta\nu$(CH) /cm^{-1}	I_c/I_m
$CH_4.H_2O$	0.1	14	0.12
$CH_4.NH_3$	0.1	13	0.00
$CH_4.PH_3$	0.1	12	0.00

9.5 The Silane Complexes

These complexes have a Si..A interaction and hence cannot be classed as hydrogen bonded complexes. Based on the type of interaction and the low magnitudes of the binding energies, these complexes should be more properly regarded as van der Waals complexes.

9.5.1 Correlation of Hydrogen Bond Characteristics with the MP2 Corrected Interaction Energies

Table 9.13 presents a summary of the Si..A bond distances together with the corrected MP2 interaction energies.

From fig 9.18 there exists a relationship between the Si..A distance and the corrected MP2 interaction energies except for $SiH_4.NH_3$. The $SiH_4.NH_3$ complex is the most stable, with the shortest Si..A separation, and the $SiH_4.PH_3$ complex the least stable with the largest Si..A separation. The contribution of the dispersion energy to the binding energy is greater for the $SiH_4.H_2O$ complex and smaller for the $SiH_4.NH_3$ complex. A possible explanation for this could be due to the Si..N interaction being more electrostatic in nature. The complexes with the second period hydrides are unbound at the SCF level, thus

it is not possible to compute the percentage dispersion energy contributions to the interaction energy in those cases.

Table 9.13 Summary of the Si..A Bond Distances and the Corrected MP2 Interaction Energies for the Silane Complexes

Complex	R(Si..A) /pm	$\%\Delta E_{Disp}$	$-\Delta E(MP2)$ /kJ mol^{-1}
$SiH_4.H_2O$	328.1	98.0	1.5
$SiH_4.H_2S$	393.6	-	1.1
$SiH_4.NH_3$	309.9	34.8	6.5
$SiH_4.PH_3$	403.5	-	0.9

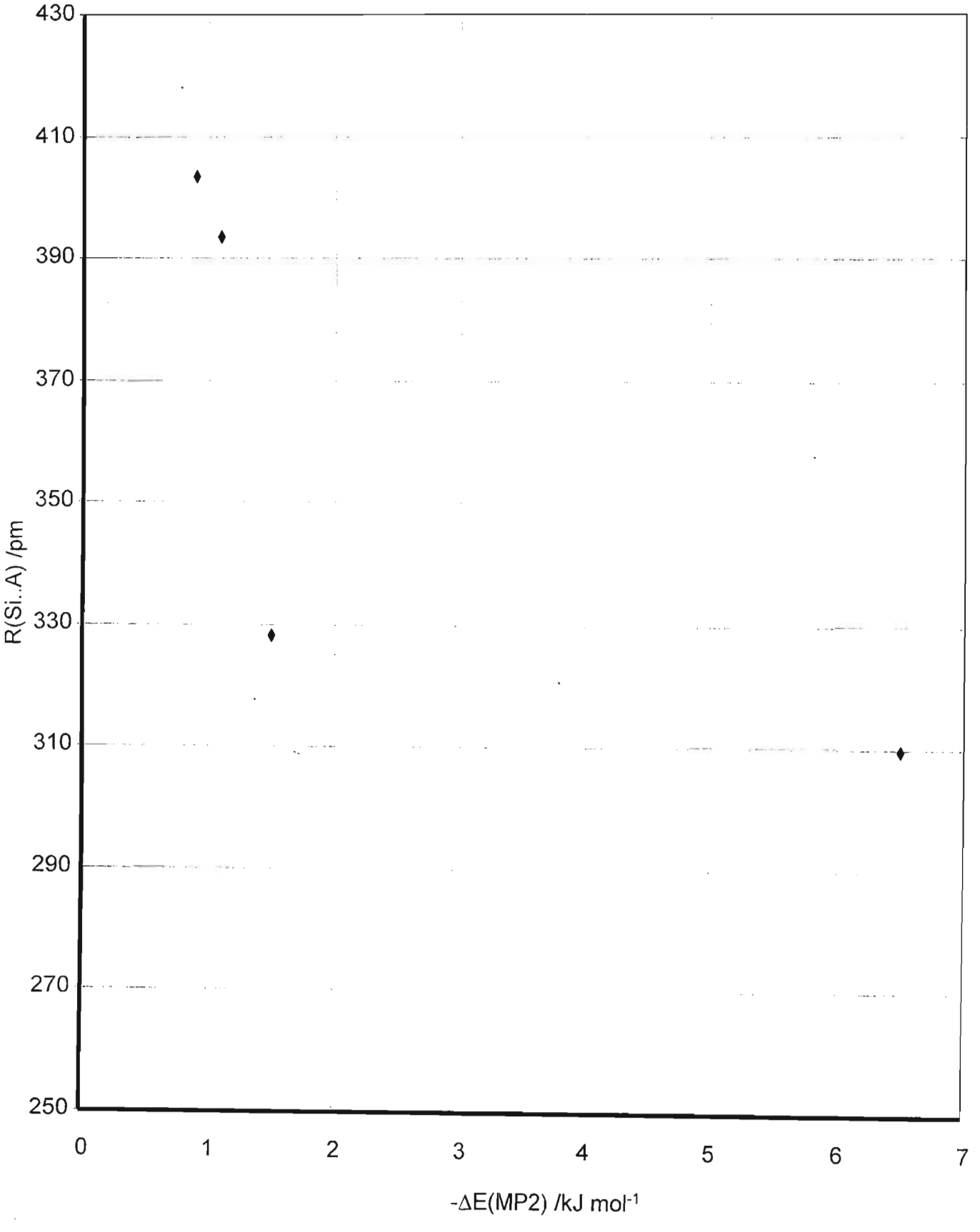

Fig 9.18 Plot of R(Si..A) distance against -ΔE(MP2)

9.5.2 Correlation of the Changes in the SiH Bond Lengths with the Net Mulliken Charges Transferred

Table 9.14 collects the changes in the SiH bond distances collinear with the Si..O interaction and the Mulliken charge shifts. The net Mulliken charge transferred as a function of Δr(SiH) shows the complex undergoing the greatest charge transfer to have the largest change in the SiH bond length, i.e. the $SiH_4.NH_3$ complex. In the case of the $SiH_4.PH_3$ complex, the SiH bond distance decreases on complexation; this is a consequence of the dipole moment of PH_3 being in the opposite direction to those in the other hydrides.

Table 9.14 Summary of the Net Mulliken Charges Transferred and the Changes in the SiH Bond Lengths

Complex	Net Mulliken Charge Transferred /e	Δr(SiH) /pm
$SiH_4.H_2O$	0.029	0.6
$SiH_4.H_2S$	0.001	0.5
$SiH_4.NH_3$	0.034	1.1
$SiH_4.PH_3$	0.003	-0.1

9.5.3 Correlation of the Geometrical Parameters with the Wavenumber Shifts and the Ratios of the Complex to Monomer Intensities for the SiH Stretching Mode in the Silane Complexes

Table 9.15 summarises the changes in the SiH bond lengths, wavenumber shifts and complex to monomer intensity ratios. No relationships are found between the changes in the SiH bond distances and the wavenumber shifts or the intensity ratios of the SiH stretching vibration. In the $SiH_4.H_2O$ complex, the I_c/I_m ratio has the largest value, and the largest SiH wavenumber shift on complexation. The poor correlation of the data points could result from the nature of the bonding in these complexes.

Table 9.15 Summary of the Changes in the SiH Bond Distances, Stretching Wavenumber Shifts from the Monomer Positions and the Complex to Monomer Intensity Ratios

Complex	Δr(SiH) /pm	$-\Delta\nu$(SiH) /cm^{-1}	I_c/I_m
$SiH_4.H_2O$	0.6	21	2.19
$SiH_4.H_2S$	0.5	7	0.67
$SiH_4.NH_3$	1.1	10	1.00
$SiH_4.PH_3$	-0.1	-1	1.07

Chapter Ten

Matrix Isolation Infrared Spectroscopy of the $(CH_4)_2$, $CH_4.HCl$, $CH_4.H_2S$ and $CH_4.NH_3$ Complexes in Argon and Nitrogen Matrices

10.1 The CH_4 Dimer

10.1.1 Introduction

The methane dimer has one methane molecule as proton donor to the face of the other methane molecule, as predicted by our calculations. Earlier studies of the methane spectrum in nitrogen matrices by Nelander[349] assigned bands at 3034.2, 3031.38, 3021.17 and 3013.65 cm^{-1} to the R(1), R(0), Q(1) and P(1) rovibrational lines with the corresponding lines in the bending region at 1310.72, 1307.28, 1302.37 and 1299.16 cm^{-1}. These lines appeared only on temperature annealing, whereby the upper rotational levels become populated and on decreasing the temperature, these lines diminished in intensity. In our experiments the formation of the bands on temperature recycling was irreversible. Hence the bands formed in our study are not due to rotational fine structure.

10.1.2 The Matrix Isolated Spectrum

10.1.2.1 Experimental

In argon matrices no dimer bands were observed. In concentrated nitrogen matrices (200/1), the intensity of the monomer band decreased on temperature recycling to 35 K, and led to the growth of a shoulder on the high frequency side at 3029.7 cm^{-1} and a new intense band at 3009.6 cm^{-1}. Likewise, in the bending region the monomer band at 1305.3 cm^{-1} gave rise to shoulders at 1309.7 and 1297.0 cm^{-1} together with an intense band at 1301.5 cm^{-1}. These wavenumbers are listed in Table 10.1. Also the relative intensities of the complex /

monomer bands from Table 6.50 in chapter 6 show decreases for the ν_1, ν_6 and ν_9 modes and increases for ν_2, ν_5 and ν_{13}. The spectra are shown in figs. 10.1 and 10.2. These features justify our conclusion regarding the predicted structure of the dimer.

Table 10.1 Matrix Band Assigments for the CH_4 Dimer Spectrum in Nitrogen Matrices

Region	Observed Wavenumber /cm^{-1}	Computed Wavenumber /cm^{-1}	Ratio[a]	Assignment
CH_4 ν_3	3029.7	3281	1.08	Dimer ν_1
	3021.5	3278	1.08	Monomer ν_3
	3019.8	3278	1.08	Dimer ν_9
	3009.6	3276	1.09	Dimer ν_2
CH_4 ν_4	1309.7	1405	1.07	Dimer ν_5
	1305.3	1404	1.08	Monomer ν_4
	1301.5	1403	1.08	Dimer ν_{14}
	1297.0	1401	1.08	Dimer ν_6

(a) Ratio = Computed / Observed

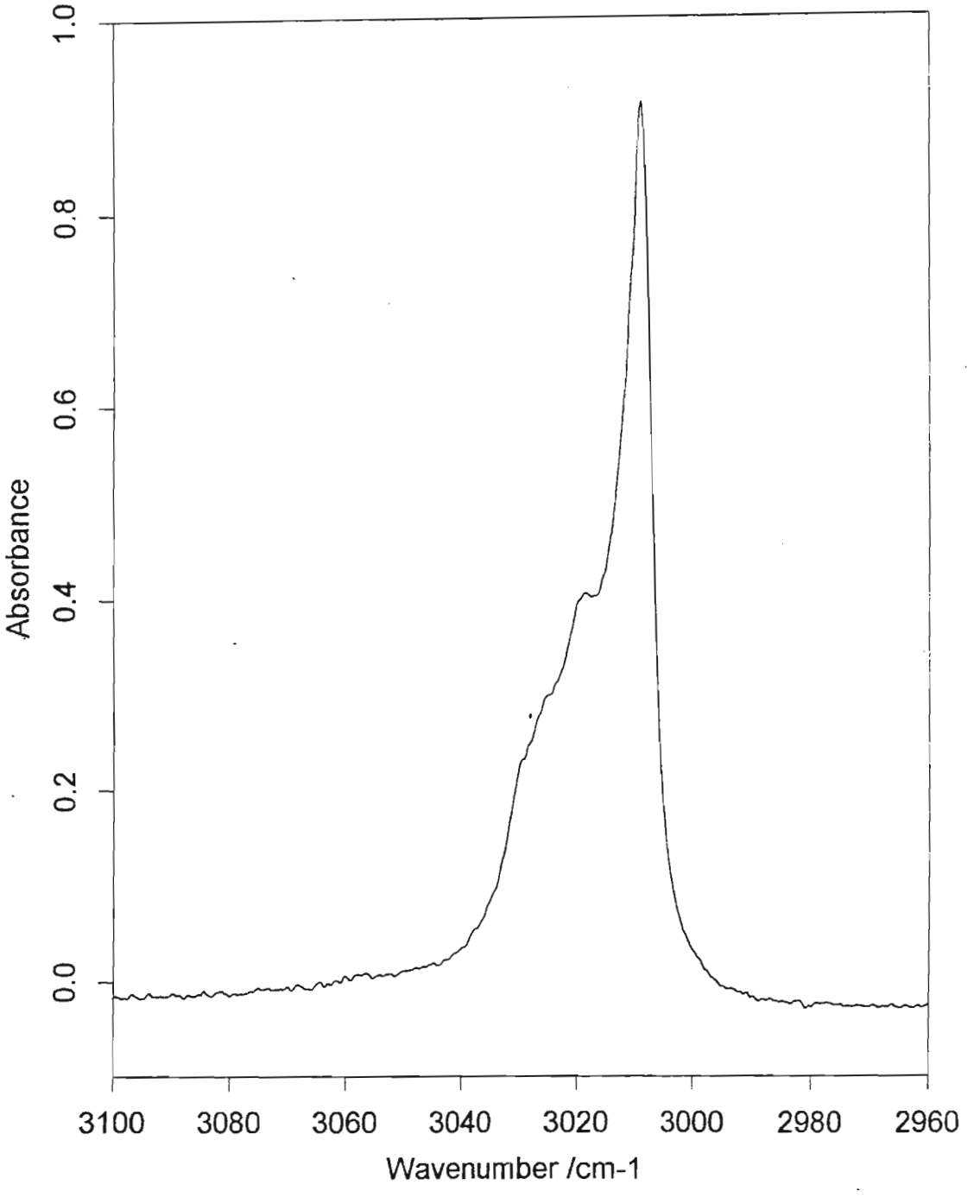

Fig 10.1 CH Stretching Region of Methane in Nitrogen

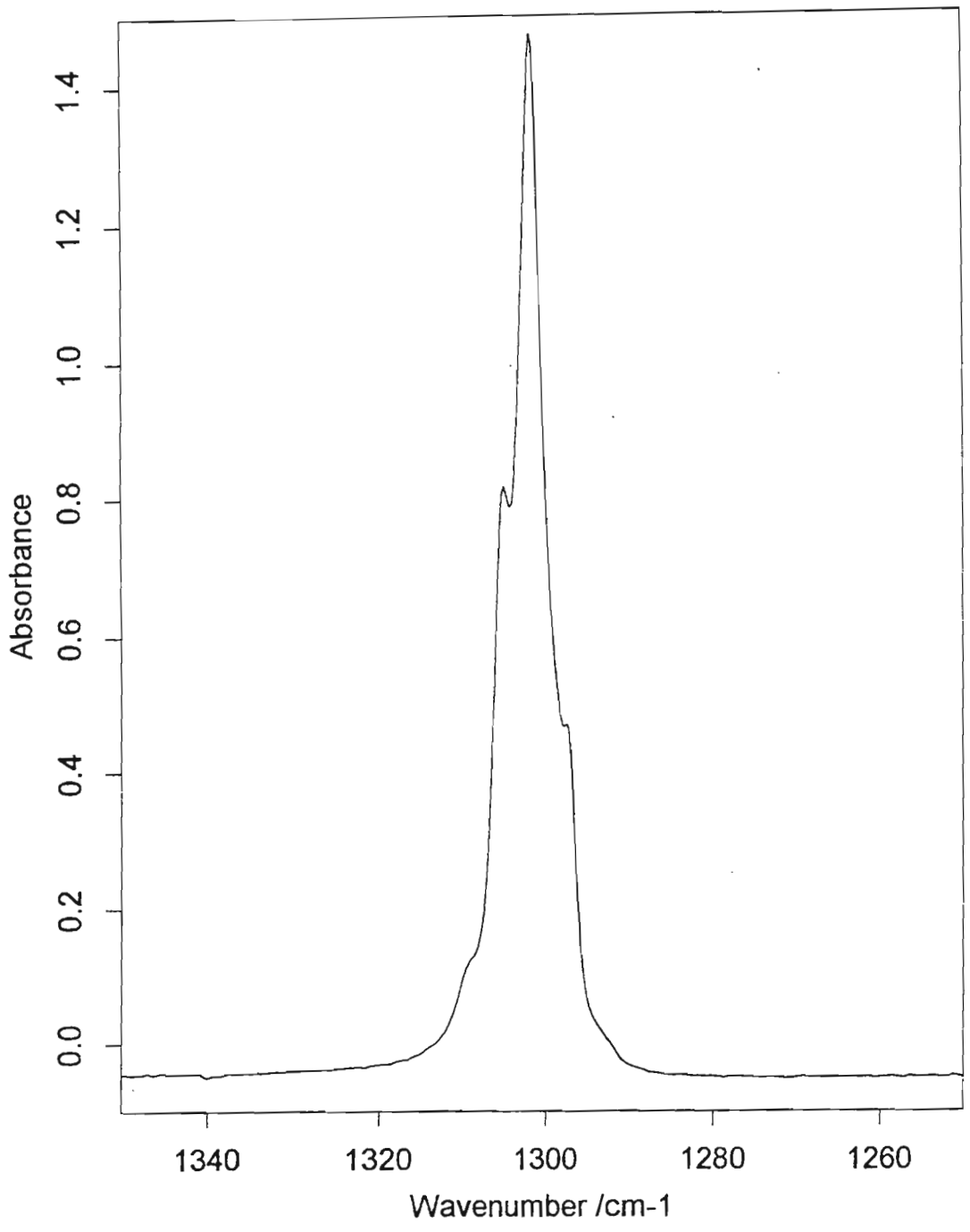

Fig 10.2 HCH Bending Region of Methane in Nitrogen

10.2 The CH_4.HCl Complex

10.2.1 Introduction

The monomers in this complex have been extensively studied,[118-120,350] with well defined matrix isolated spectra. Hence, the spectra of the monomer and higher aggregate species in the case of HCl will not be discussed.

10.2.2 The Matrix Isolated Infrared Spectrum

The bands due to the monomer, dimer and polymer matrix isolated species were evident in the complex spectrum when compared with the monomer HCl spectrum.

The spectrum of methane in argon showed no formation of dimer or any higher aggregate species, in contrast to the nitrogen matrix. The complex bands were easily identifiable in the argon matrix. Table 10.2 collects the wavenumbers for the CH_4.HCl complex in the argon and nitrogen matrices. The complex spectra with M/A/A of 1200/1/1 in an argon matrix are shown in figs. 10.3 and 10.4 and in a nitrogen matrix in fig 10.5.

Table 10.2 Wavenumber Assignments for the CH_4.HCl Complex in Argon and Nitrogen Matrices

Region	Observed Wavenumber /cm^{-1}		Computed Wavenumber /cm^{-1}	Ratio[a]	Assignment
	N_2 Matrix	Ar Matrix			
CH_4 ν_3		3020.3	3277	1.08	Complex (ν_1)
	3018.6	3018.5	3289	1.09	Monomer
		3016.3	3270	1.08	Complex (ν_6)
		3014.9	3270	1.08	Complex (ν_6)
CH_4 ν_1	-[b]	-[b]	3143		Monomer
	-[b]	-[b]	3127		Complex (ν_2)
HCl	2848.8	2849.9	3128	1.10 (Ar) 1.10 (N_2)	Monomer
	2838.9	-[b]	3112	1.10	Complex (ν_3)
CH_4 ν_2	-[b]	-[b]	1623		Monomer
	-[b]	-[b]	1624		Complex (ν_7)
CH_4 ν_4		1305.1	1407	1.08	Complex (ν_8)
		1302.7	1407	1.08	Complex (ν_8)
		1301.9	1400	1.07	Complex (ν_4)

Table 10.2 Continued

	1305.1	1302.0	1402	1.08 (Ar) 1.07 (N_2)	Monomer

(a) Ratio = Computed / Observed

(b) Not observed

The assignments of the bands were accomplished as follows. The ν_3 mode of methane belongs to the f_2 symmetry species (ir active) in the monomer; on complexation the T_d symmetry of methane is reduced to C_{3v}, thus resulting in the appearance of a_1 and e symmetry species. The a_1 symmetry vibrational mode is expected to lie on the high frequency side of the parent monomer band (ν_3). The band at 3018.5 cm^{-1} in argon was assigned to the monomer ν_3 mode of methane as it was also observed in the methane/argon spectrum. The remaining complex bands correlating with ν_3 of the monomer were assigned to the 3016.3 and 3014.9 cm^{-1} absorptions, since they were the only new bands to have formed on the low frequency side in the complex spectrum. These bands were not observed in nitrogen matrices. The degeneracy of ν_6 is slightly lifted, probably resulting from cage effects leading to the distortion of the C_{3v} symmetry in the complex. The ratios of the computed / experimental wavenumbers are consistent with each other. In the HCl stretching region in argon, there was no evidence of any complex bands. Barnes et al[265] observed a new band 16 cm^{-1} to the low frequency side of the monomer band. In the nitrogen matrix a new band was observed, red shifted 9.9 cm^{-1} from the monomer band, assigned to the complex band. This band was not observed in either of the HCl spectra in the nitrogen and argon matrices and appeared in the complex spectrum only after annealing to 35 K. The shift of this band is fairly close to our calculated wavenumber shift of -16 cm^{-1}. The band arising from the infrared inactive ν_1 monomer mode of methane was not observed in the complex spectrum

in either argon or nitrogen matrices due to its inherent weakness. The bands arising from the infrared inactive ν_2 band in the monomer were also not observed in either argon or nitrogen matrices. From the monomer, ν_4, bending mode of methane, our calculations predicted complex band formation on the high frequency (degenerate) and on the low frequency side of the monomer band. Once again, the degeneracy of ν_8 in the complex is slightly lifted resulting in a wavenumber difference of 2.4 cm^{-1}. The only new band to appear on the low frequency side (1301.9 cm^{-1}) was assigned to ν_4 of the complex. In summary the complex is more evident in argon than in nitrogen matrices, due to the greater ability of the larger cage of the argon matrix to accommodate the complex. Our calculated wavenumber shifts are in reasonable agreement with the experimental matrix shifts of this complex.

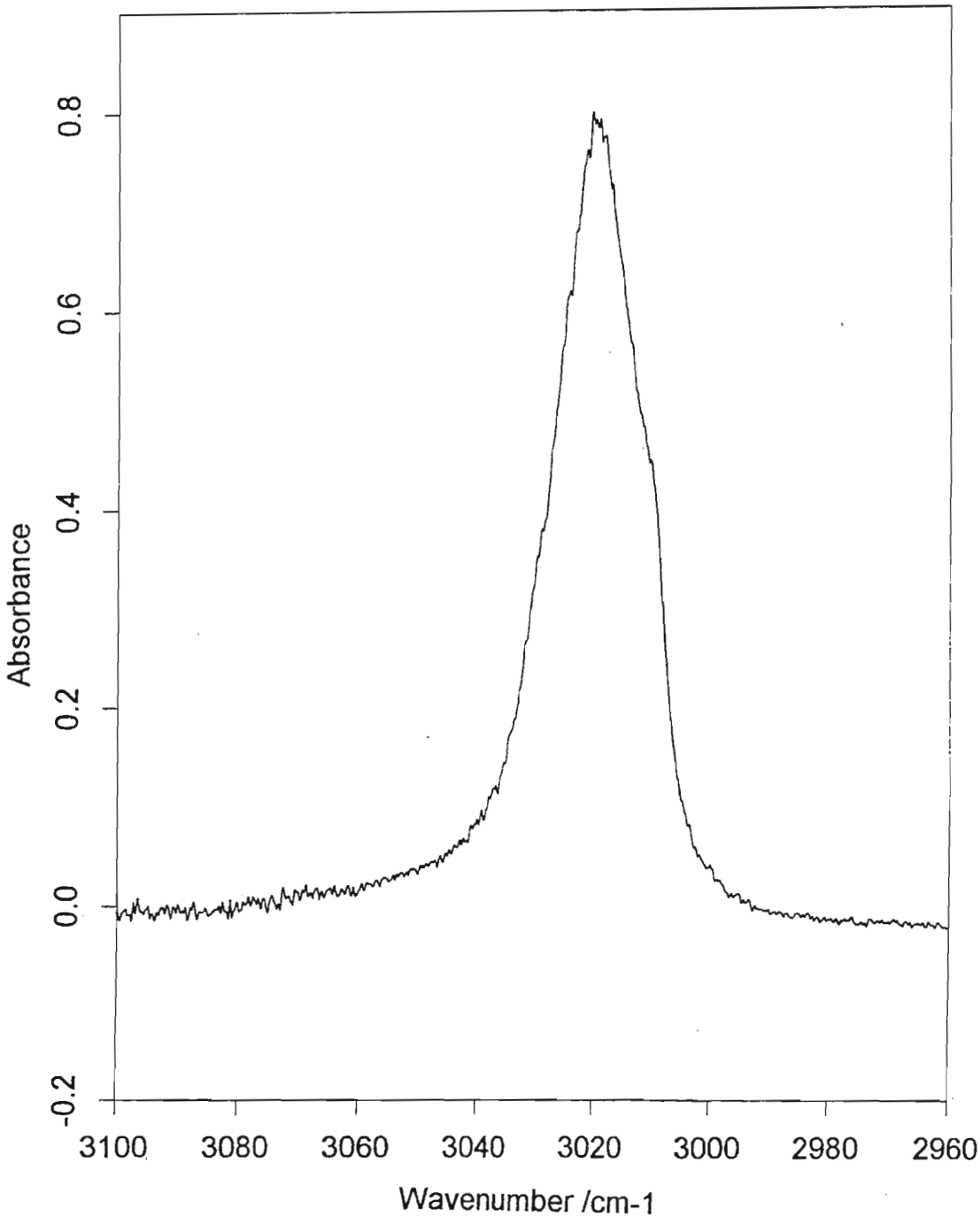

Fig 10.3 CH Stretching Region of Methane - Hydrogen Chloride Complex in Argon

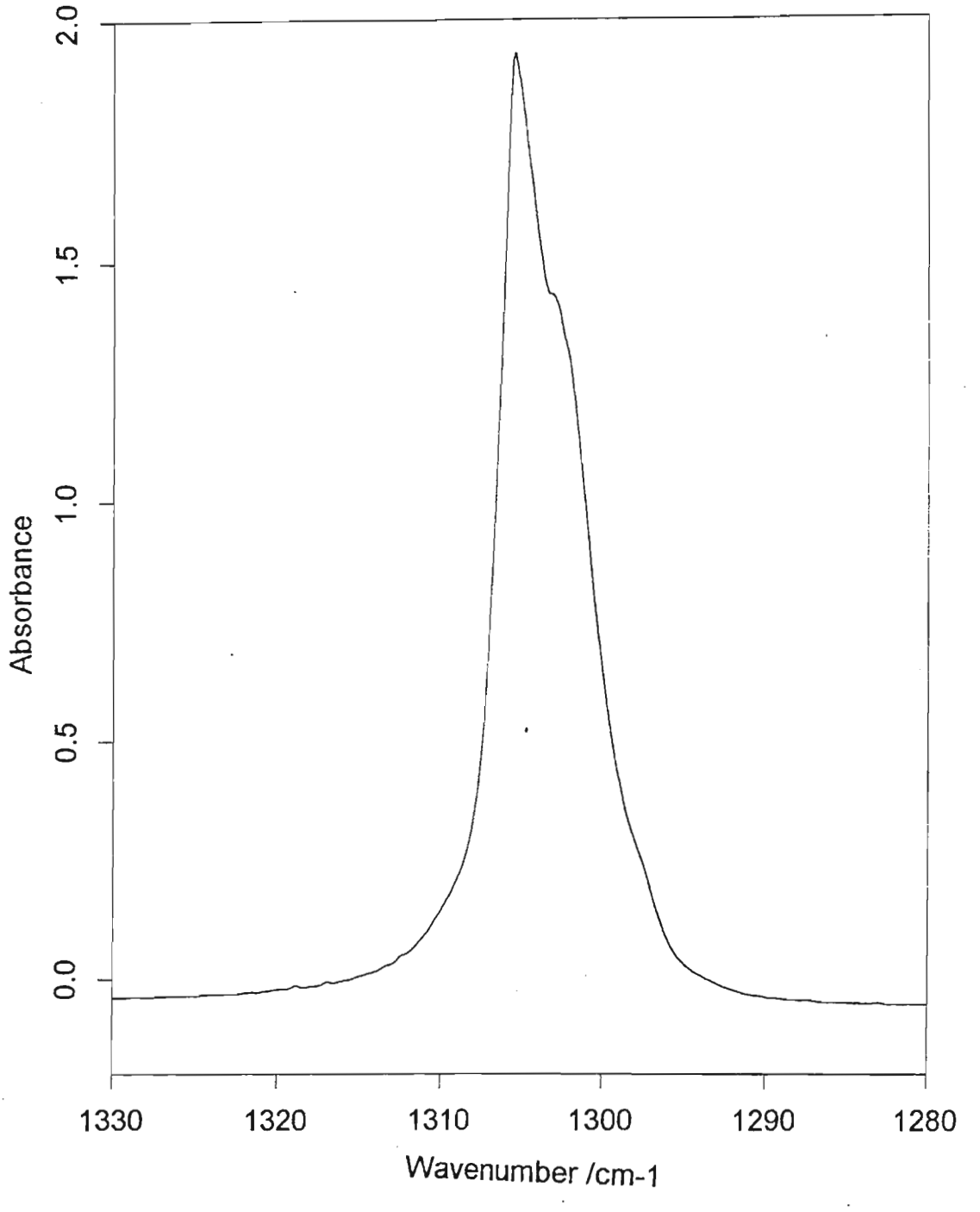

Fig 10.4 HCH Bending Region of Methane - Hydrogen Chloride Complex in Argon

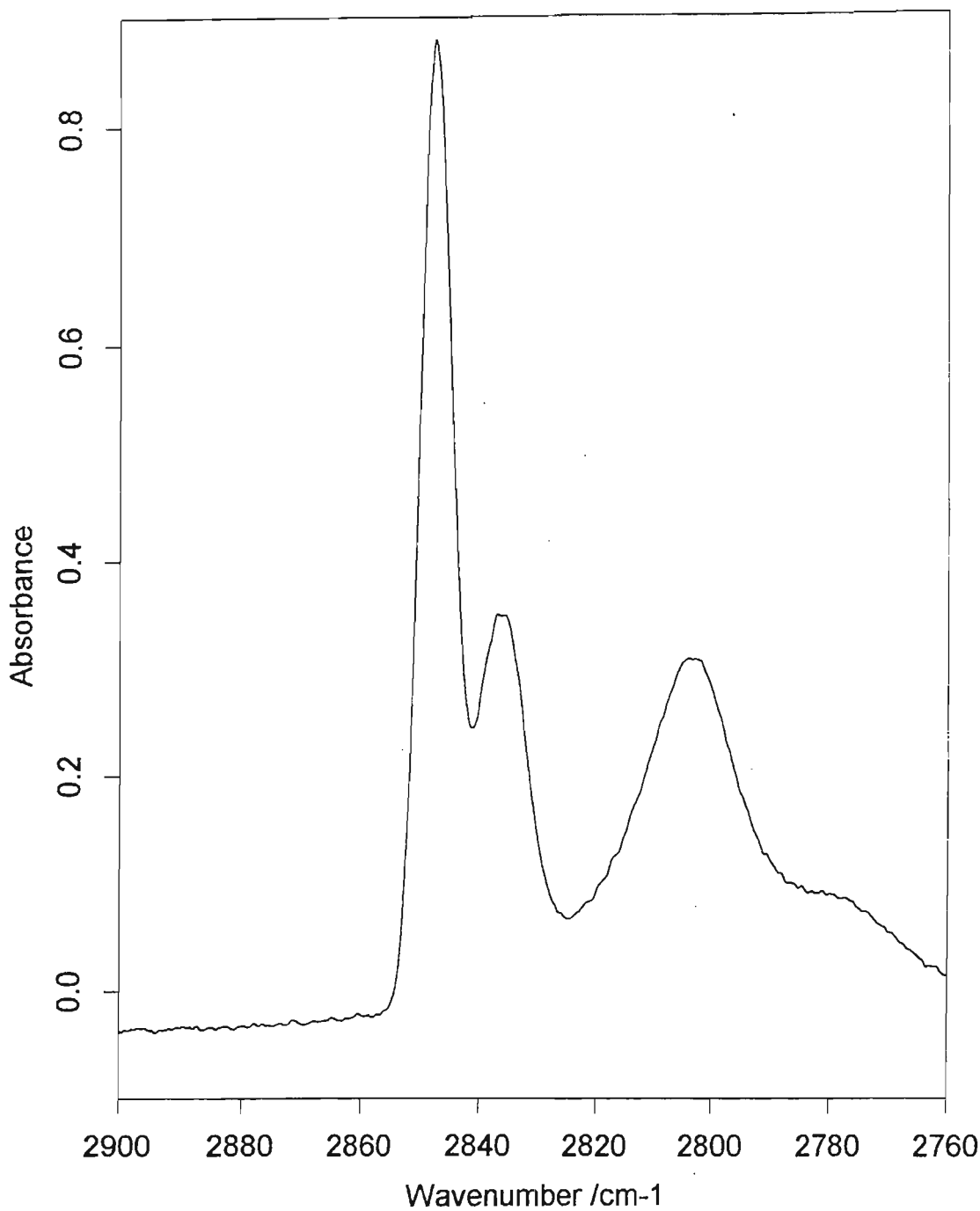

Fig 10.5 HCl Stretching Region of Methane - Hydrogen Chloride Complex in Nitrogen

10.3 The $CH_4.H_2S$ Complex

10.3.1 Introduction

The hydrogen sulphide spectrum has been extensively studied in various matrices.[159-161,349,350] Hence, the spectra of the monomer and higher aggregate species will not be discussed. To our knowledge no experimental matrix isolation studies have been carried out for this complex in either argon or nitrogen matrices.

10.3.2 The Matrix Isolated Spectrum

Table 10.3 collects the wavenumbers for the matrix isolated $CH_4.H_2S$ complex in a nitrogen matrix. Figs. 10.6 to 10.8 show the spectra for this complex.

In the CH_4 ν_3 region, three new bands are expected to form, with ν_3 having the lowest intensity, as predicted by our calculated spectrum. Three new bands were observed on the low frequency side of the methane monomer degenerate symmetric stretching vibration. These bands were assigned to ν_1, ν_2 and ν_{13} based on their relative intensities on complexation. A new, weak band at 2849.9 cm^{-1} was also observed on complexation and was assigned to the ν_3 complex band arising from the infrared-inactive methane symmetric stretching mode in the monomer. The appearance of this band suggests distortion of the methane tetrahedron on complexation with hydrogen sulphide, thus rendering this band infrared active. In the H_2S ν_3 antisymmetric stretching region, one new band was seen -7.4 cm^{-1} from the corresponding monomer band. This band was assigned to the ν_4 complex band. In the H_2S ν_1 region, one new band was seen at 2618.5 cm^{-1}, shifted -2.5 cm^{-1} from its corresponding monomer band. The appearance of this band suggests that H_2S is the proton donor in this complex, otherwise this band would have appeared close to the monomer position for the antisymmetric stretching mode. A difference of 5.7 cm^{-1} exists between the ν_4 and ν_5 SH

stretching modes, further emphasising the inequivalence of these modes and hence supporting hydrogen sulphide as being the proton donor to methane.

Table 10.3 Wavenumber Assignments for the $CH_4.H_2S$ Complex in a Nitrogen Matrix

Region	Observed Wavenumber /cm^{-1}	Computed Wavenumber /cm^{-1}	Ratio[a]	Assignment
CH_4 ν_3	3014.2	3277	1.09	Complex ν_1
	3017.4	3289	1.09	Monomer ν_3
	3008.9	3274	1.09	Complex ν_{13}
	3011.9	3274	1.09	Complex ν_2
CH_4 ν_1	2849.9	3129	1.10	Complex ν_3
H_2S ν_3	2631.6	2871	1.09	Monomer ν_3
	2624.2	2866	1.09	Complex ν_4
H_2S ν_1	2621.0	2845	1.09	Monomer ν_1
	2618.5	2840	1.08	Complex ν_5
CH_4 ν_2	-[b]	1623		Complex ν_6
	-[b]	1622		Complex ν_{14}
CH_4 ν_4	1302.2	1402	1.08	Monomer ν_4
	-[b]	1402		Complex ν_7
	1304.3	1401	1.07	Complex ν_8

Table 10.3 Continued

	-[b]	1402		Complex ν_{15}
H_2S ν_2	1181.2	1269	1.08	Monomer ν_2
	1179.5	1270	1.08	Complex ν_9

(a) Ratio = Computed / Observed

(b) Not Observed

In the methane ν_2 bending region no new bands were observed. However in the methane ν_4 bending region, one new band was observed at 1304.3 cm^{-1} which was assigned to the ν_8 complex band. Our calculations predicted the appearance of two more new bands in this region, blue shifted from their corresponding monomer bands. These bands were not observed. In the H_2S ν_2 bending region our calculations predicted one new band slightly blue shifted from its corresponding monomer band. A new band was observed at 1179.5 cm^{-1}, blue shifted 1.7 cm^{-1} from the H_2S (ν_2) band. Based on the above similarities of our calculated spectrum with the matrix isolated ir spectrum, one can conclude that hydrogen sulphide is the proton donor to methane.

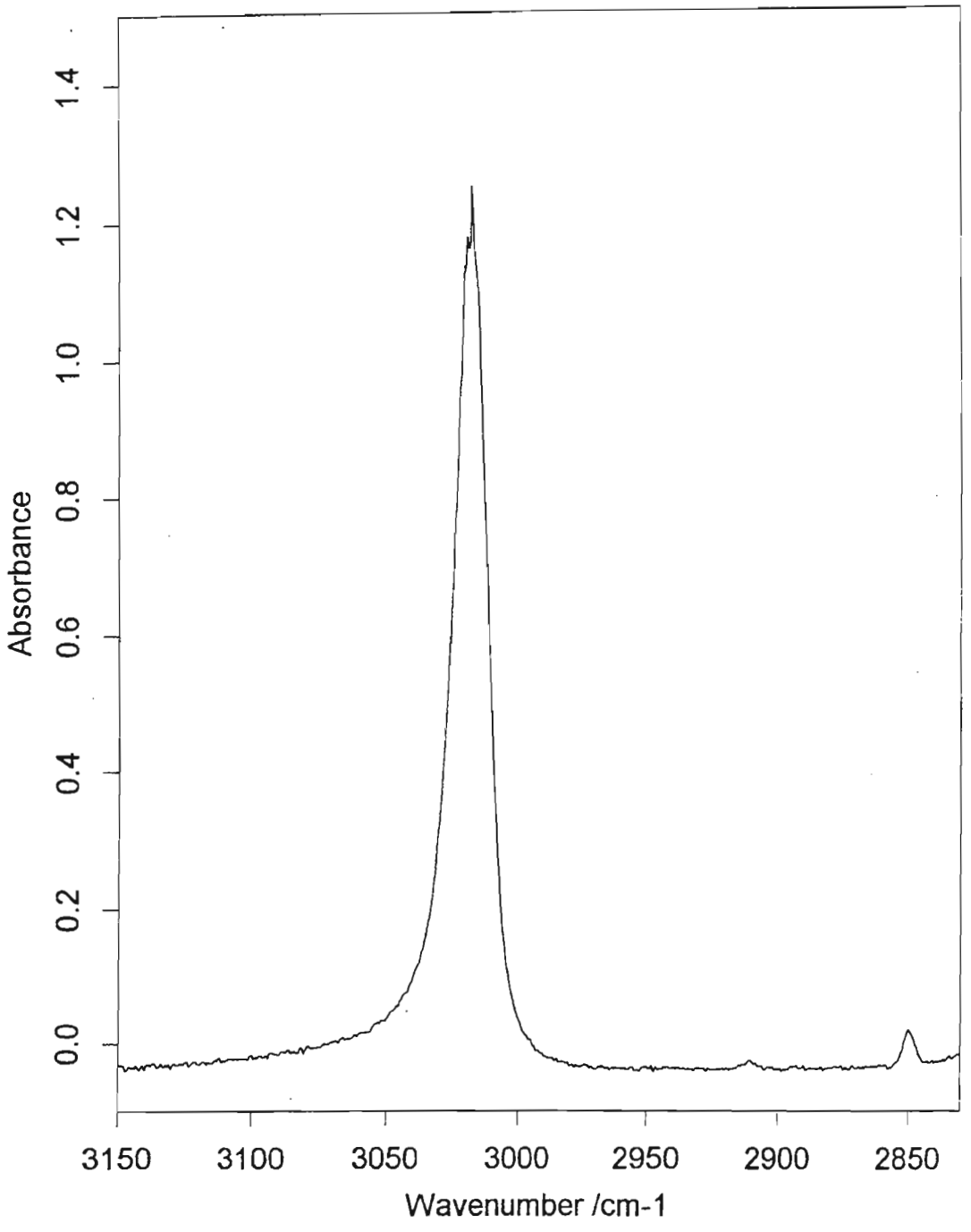

Fig 10.6 CH Stretching Region of Methane - Hydrogen Sulphide Complex in Nitrogen

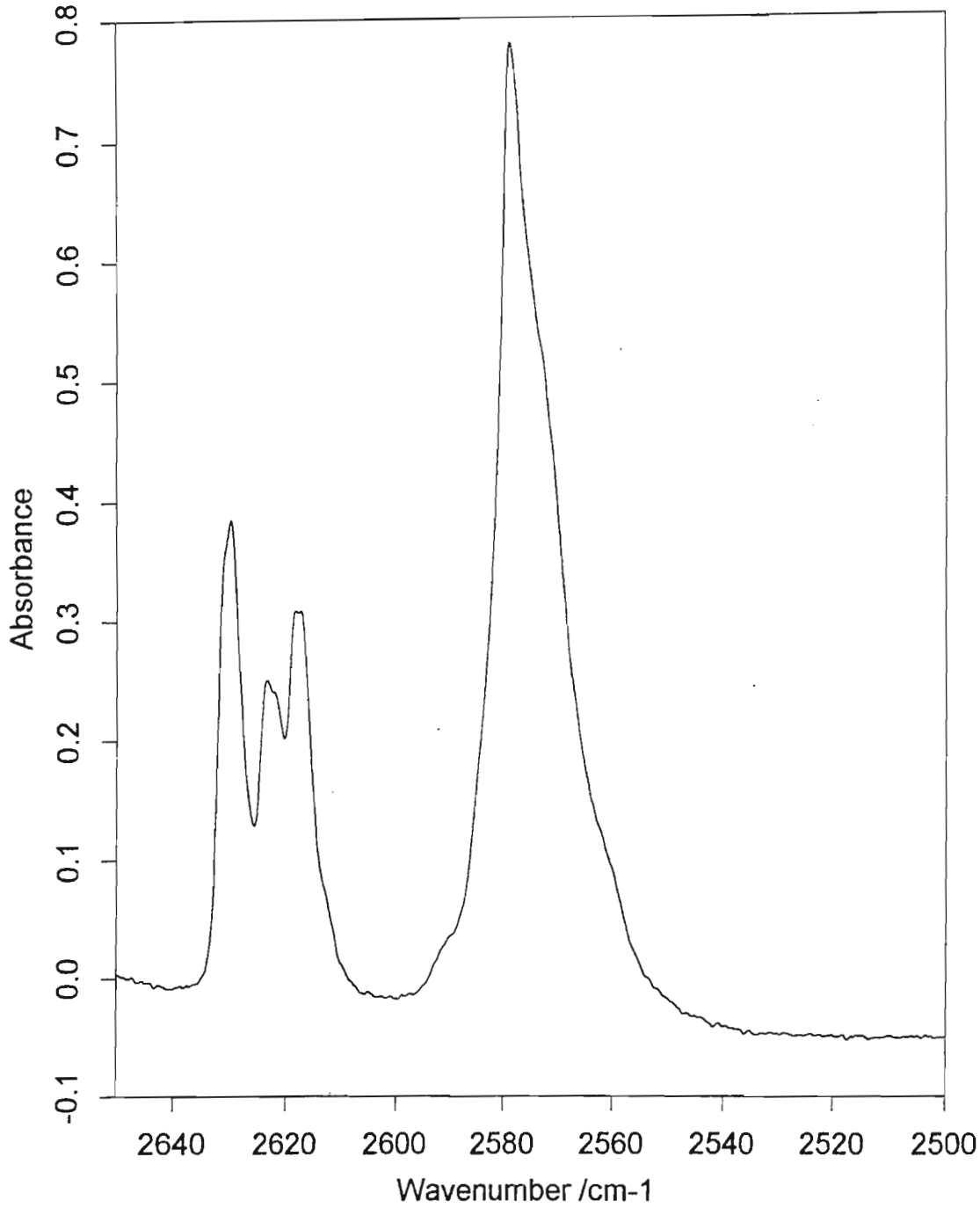

Fig 10.7 SH Stretching Region of Methane - Hydrogen Sulphide Complex in Nitrogen

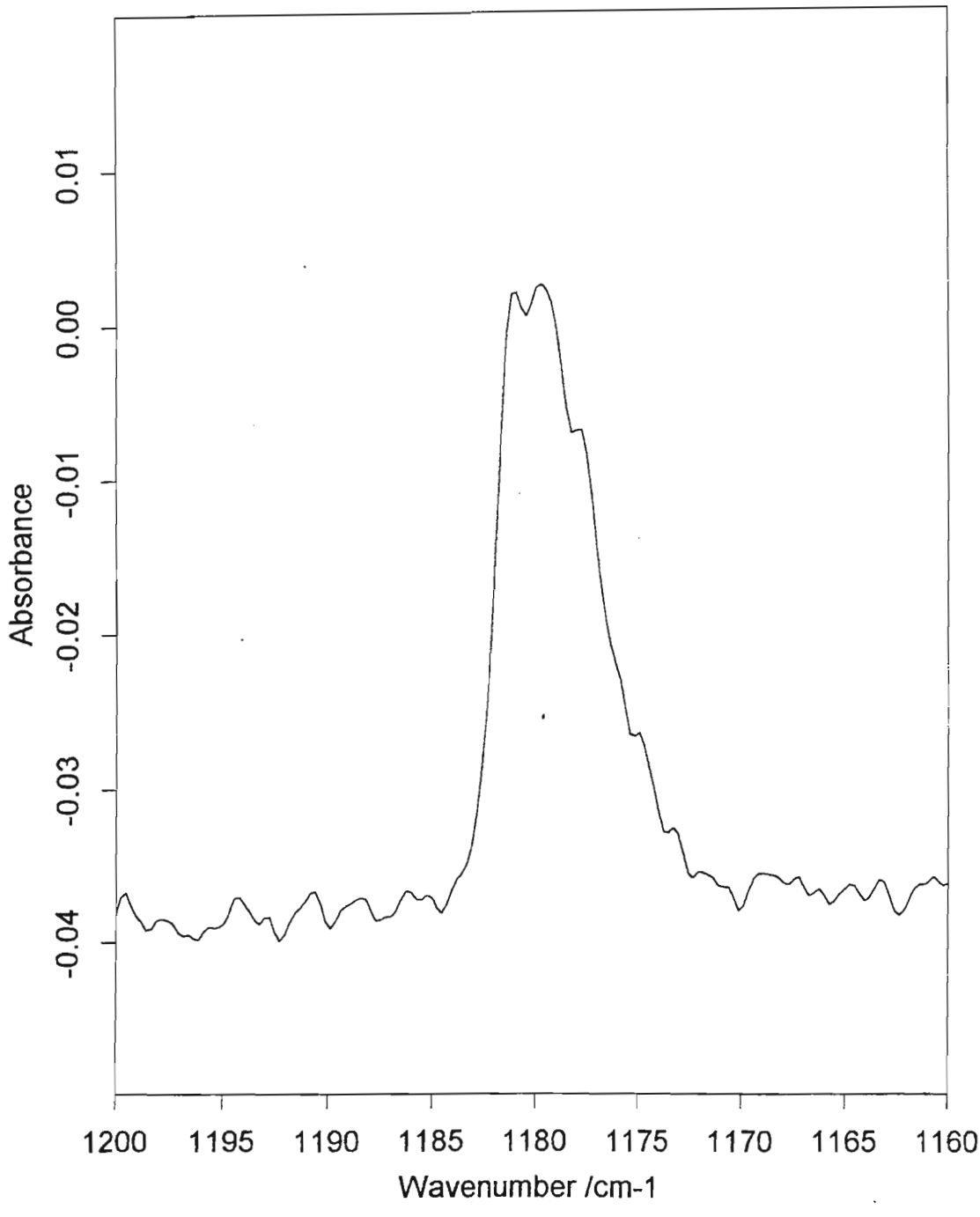

Fig 10.8 HSH Bending Region of Methane - Hydrogen Sulphide Complex in Nitrogen

10.4 The $CH_4.NH_3$ Complex

10.4.1 Introduction

The monomers in this complex have been extensively studied, with well defined matrix isolated spectra. Hence, the spectra of the monomers of methane and ammonia and those of the higher aggregate species of ammonia will not be discussed in detail. To our knowledge no experimental matrix isolation studies have been carried out for this complex in either argon or nitrogen matrices.

10.4.2 The Matrix Isolated Spectrum

No new bands were observed in either nitrogen or argon matrices for this complex, but the experimental spectra are shown in figs. 10.9 to 10.13. The wavenumbers are tabulated in Table 10.4.

The nitrogen matrix spectrum of methane and ammonia is displayed, showing clearly the ammonia monomer, dimer and trimer band positions. The ease of formation of the ammonia dimer compared with the formation of a methane-ammonia complex probably led to non-complexation of the methane-ammonia complex as observed in the immediate appearance of the dimer and trimer ammonia bands before temperature annealing.

Table 10.4 Matrix Band Assignments for the CH_4 and NH_3 in a Nitrogen Matrix

Molecule	Observed Wavenumber /cm^{-1}	Assignment
CH_4	3017.4	Monomer ν_3
	1302.2	Monomer ν_4
NH_3	3435.4	Monomer ν_3
	3425.5	Dimer ν_1
	3400.6	Dimer ν_2
	3389.2	Trimer
	3375.9	Trimer
	3328.3	Monomer ν_1
	3306.9	Trimer
	3243.8	Dimer ν_4
	3232.1	Trimer
	3205.1	Trimer
	1644.8	Dimer ν_{14}
	1620.5	Monomer ν_4
	1048	Trimer
	1018	Dimer ν_7

Table 10.4 Continued

	1013	Monomer ν_2
	992	Monomer ν_2
	980	Monomer ν_2

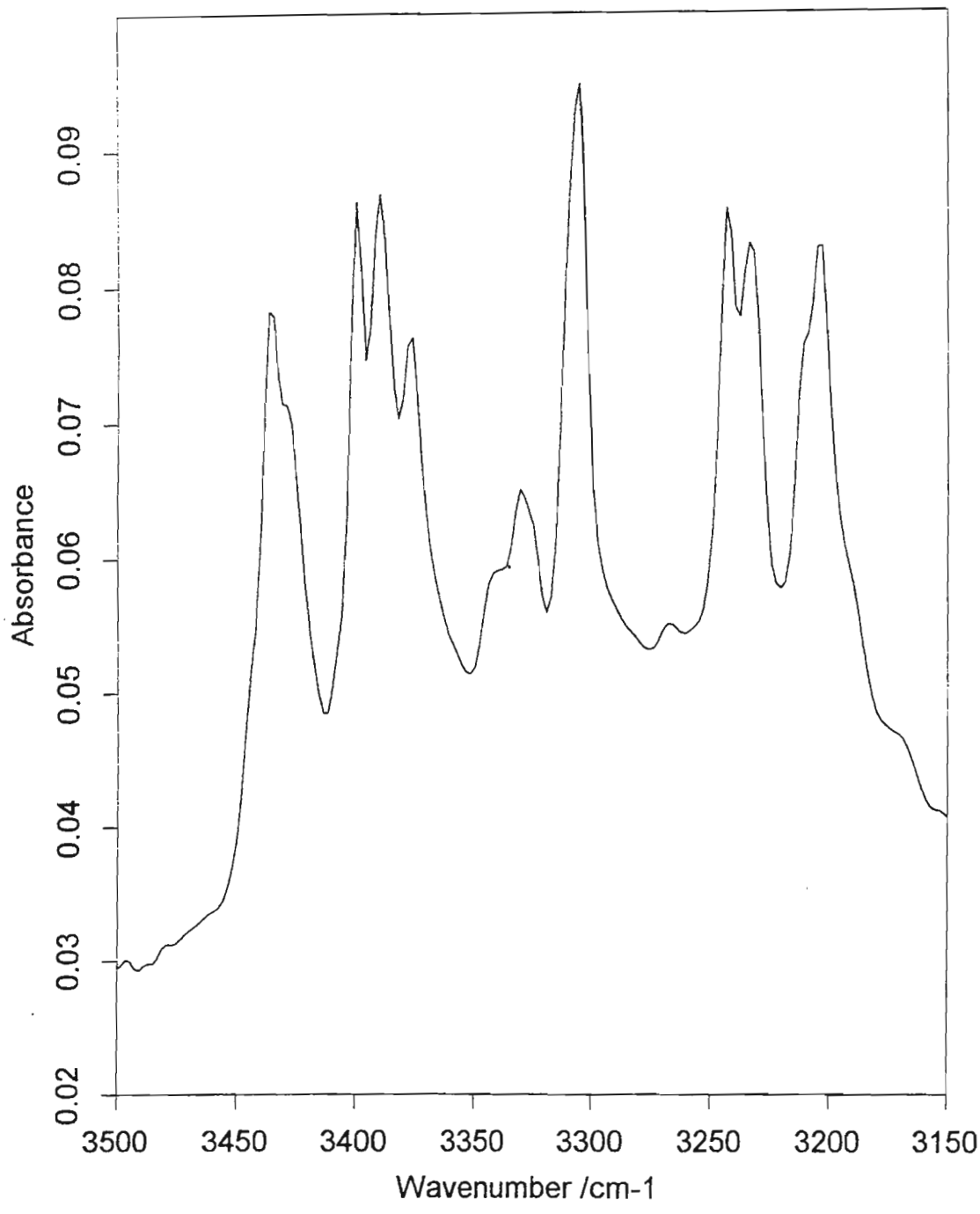

Fig 10.9 NH Stretching Region of Methane and Ammonia in Nitrogen

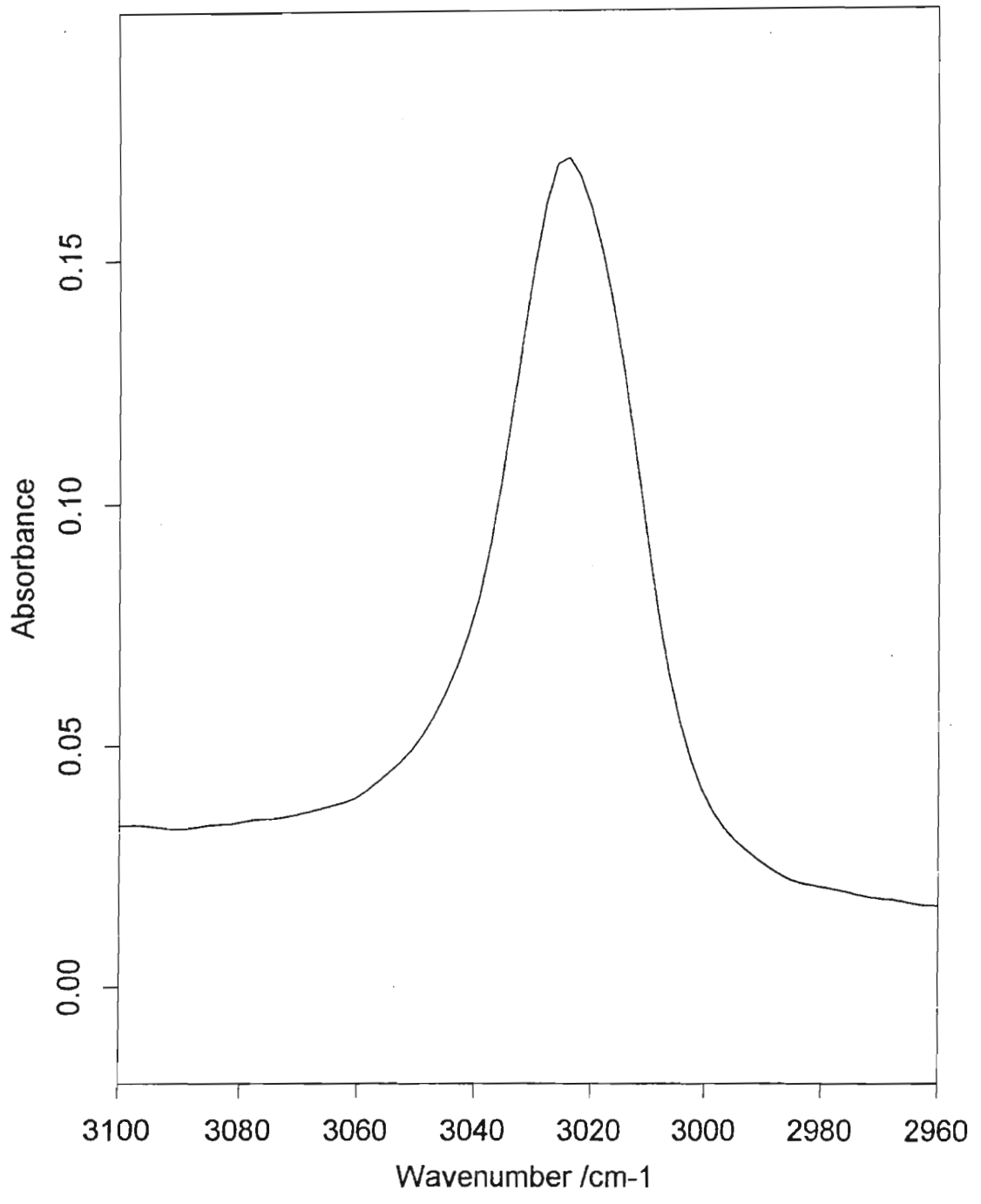

Fig 10.10 CH Stretching Region of Methane and Ammonia in Nitrogen

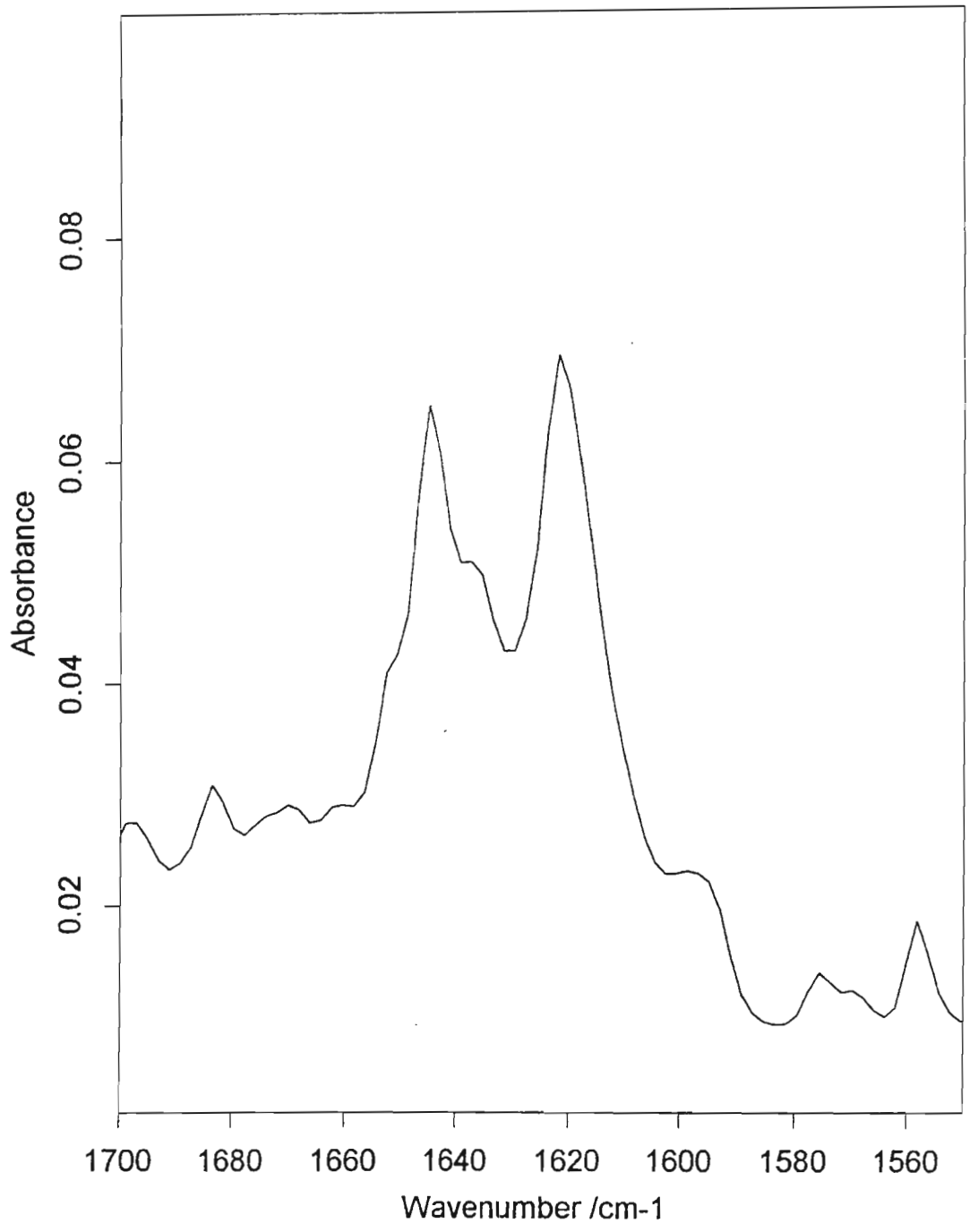

Fig 10.11 Antisymmetric HNH Bending Region of Methane and Ammonia in Nitrogen

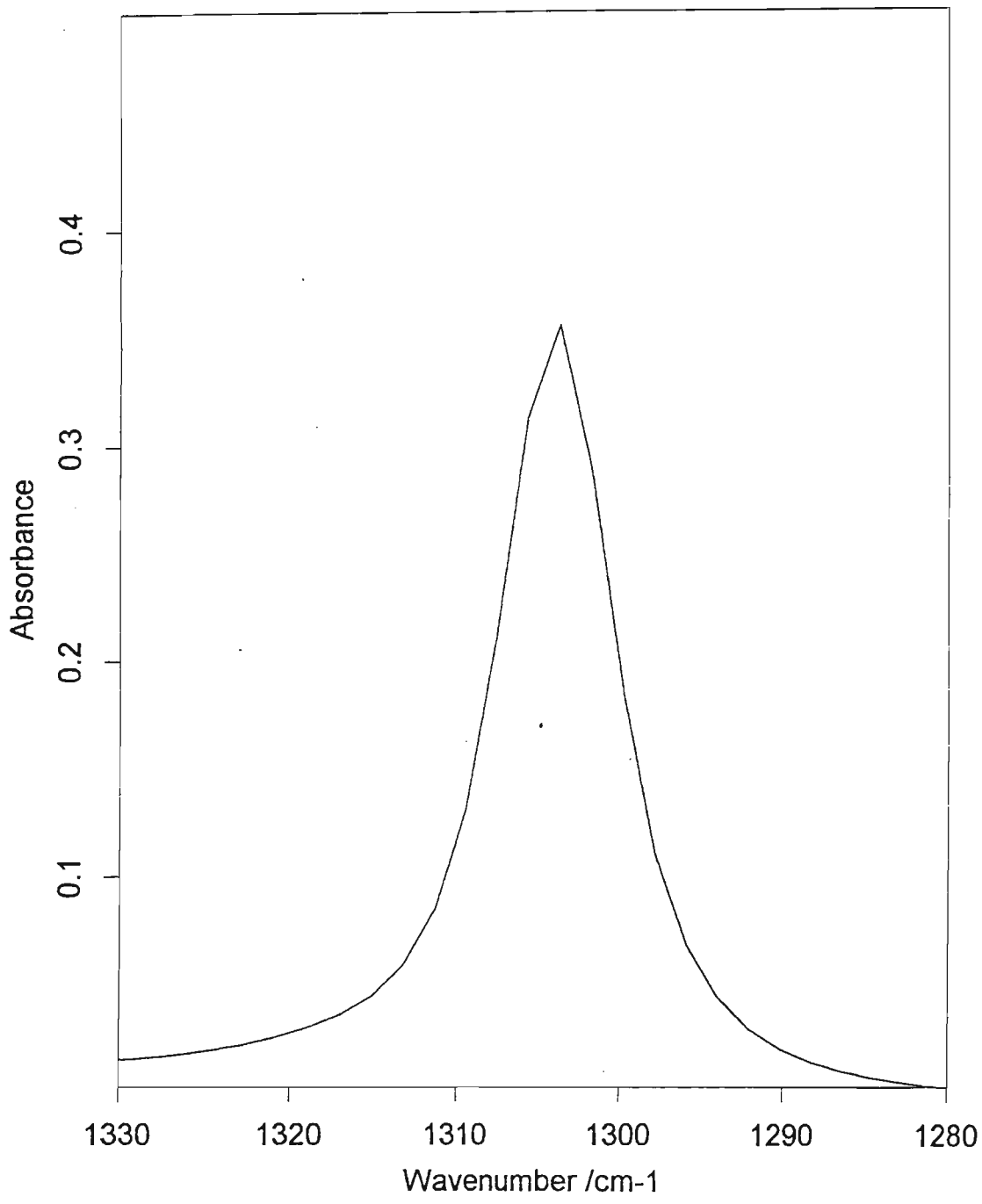

Fig 10.12 HCH Bending Region of Methane and Ammonia in Nitrogen

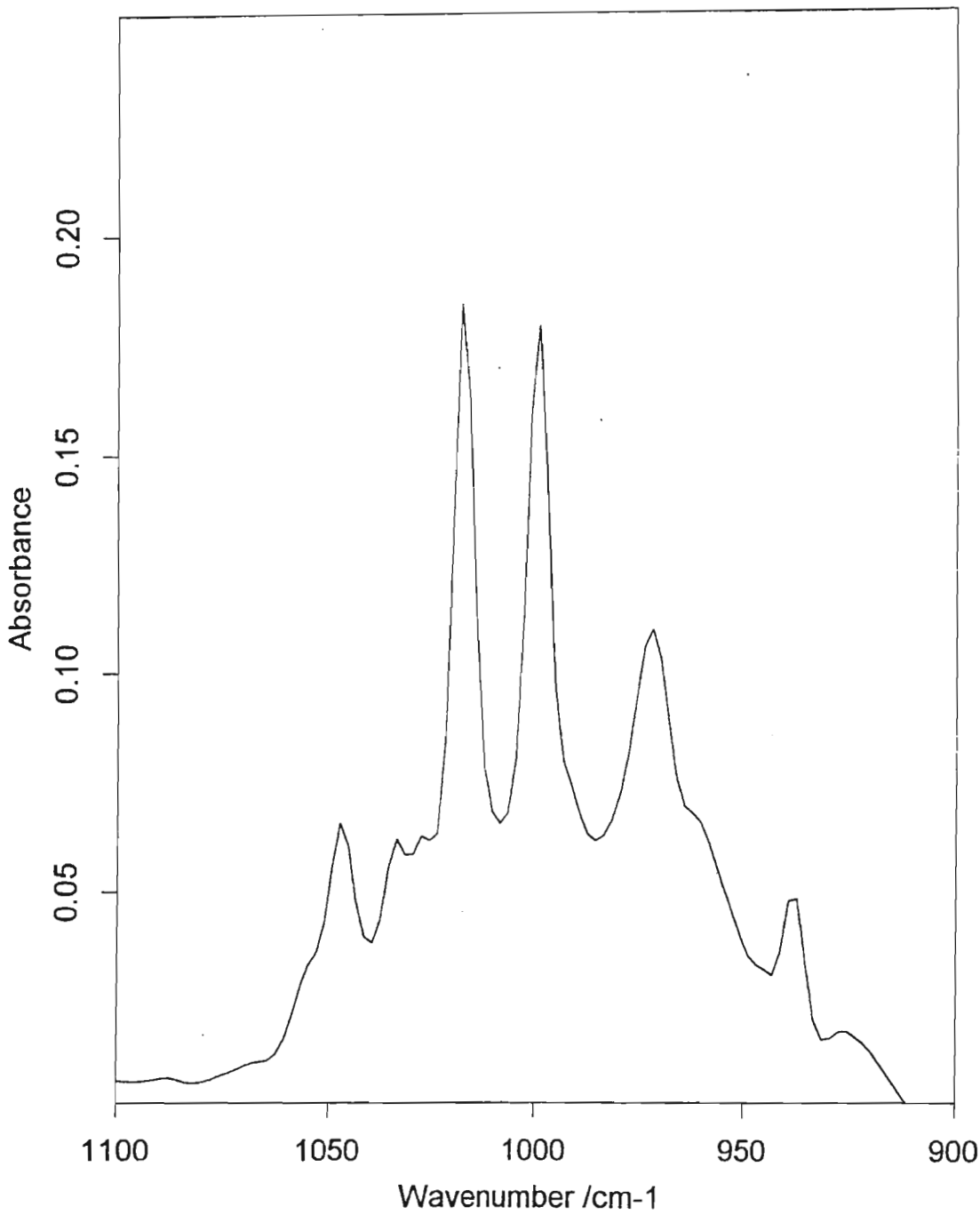

Fig 10.13 Symmetric HNH Bending Region of Methane and Ammonia in Nitrogen

Chapter Eleven

Summary of Theoretical and Experimental Results

This chapter summarises the results obtained both theoretically and experimentally and the good correlation that exists between the results obtained, thus emphasising the strength of using the matrix isolation technique together with *ab initio* molecular orbital theory in studying molecular interactions. In the case of the hydrogen bonded complexes studied, the trend towards the hydrogen bond angle being close to linearity, coupled with a short AH..B distance, is indicative of a strongly hydrogen bonded complex. However, in the case of the homodimer series, as one moves to the left of the periodic table, the bonding nature changes. These homodimers tend to have a greater contribution from the dispersion energy term than from the electrostatic energy term. The percentage dispersion energy contributions in the second row homodimers are much larger than those of the first row homodimers. Hence one could perhaps be justified in concluding that the percentage dispersion energy contribution to the binding energy increases as one descends the periodic table in the case of the homodimers.

In the case of the vibrational spectra of the homodimers, the conventional red and blue shifts of the symmetric stretching and bending modes in the proton donor are clearly depicted as in the hydrogen bonded complexes. Further, the red shift of the symmetric AH stretching mode as a function of the change in the AH bond length shows two distinct linear proportional trends for the first and second row homodimers respectively. A similar generalisation could also be made for the ratio of the intensities of the AH stretching modes to that of the change in the AH stretching wavenumber shifts, with the exception of the existence of an exponential relationship in the case of the correlation between the intensity ratios and the changes in the AH bond lengths.

In the complexes with HX, the shorter the H..B separation the greater the interaction energy, with the hydrogen bond angle being close to linearity. Two trends can be drawn from the results of the percentage dispersion energy contribution in these complexes; as one moves to the right of the periodic table the percentage dispersion energy contribution increases and as one descends the group a similar trend is also observed. In the case of the MH_4.HF complexes, there is also a tendency for a secondary interaction, which is absent in the case of the MH_4.HCl complexes. Therefore a further generalisation could be made; as one descends group 17 of the periodic table, complexes with MH_4 would have HX as the proton donor due to the decreasing electron donating ability of the X atom on descending group 17. The vibrational spectra of the HX complexes show that as one moves to the left of the periodic table the wavenumber shifts of HX stretching modes decrease rapidly for both the first and second row hydride complexes. In the case of the intensity ratio for the HF stretching mode as a function of the change in the HF bond length, two linear relationships exist for the first and second row hydride complexes, with HF respectively. This is however not the case for the HCl complexes, probably resulting from the decreased electronegativity in the chloride, compared with the fluoride.

In the complexes containing methane as the proton donor, viz., $CH_4.H_2O$, $CH_4.NH_3$ and $CH_4.PH_3$, the hydrogen bond angle was close to linearity with the H_2O complex being unbonded at the correlated level of theory. In the vibrational spectra of these complexes, the proton donor symmetric stretching and bending modes undergo red shifts, unlike those in the conventional hydrogen bonded complexes. In the case of the $CH_4.H_2S$ complex with methane our experimental vibrational spectrum clearly shows the formation of new bands. The wavenumber shifts from our theoretical calculations are seen to be quite close to the experimentally obtained values.

On analysing the results for the electron donor-acceptor complexes of SiH_4, one could classify these complexes as being weakly bonded with large Si..A interaction distances. The

larger the Si..A bond length the weaker is the interaction energy, as in the hydrogen bonded complexes. The trend in the percentage dispersion energy contribution to the binding energy is also the same as in the hydrogen bonded complexes.

The vibrational spectra of the H_2Y complexes show a trend towards red shifts in the case of the electron donor symmetric stretching and bending modes. This trend is however not obeyed by the second row AH_3 complexes. In the silane-ammonia complex the symmetric stretching and bending modes of the electron donor are red and blue shifted respectively. In the phosphine complex the symmetric stretching and bending modes of the electron acceptor are both blue shifted. Hence one could generalise that in the case of the silane complexes with the group 16 hydrides as one descends the group in the periodic table red shifts should be observed for the symmetric stretching and bending modes of the electron donor. In the case of the AH_3 hydrides, as one descends the group in the periodic table blue shifts should be observed for the stretching modes of the electron acceptor.

In addition to the trends observed in this project which aid in predicting the structural, energetic and vibrational properties of similar complexes when descending a group or moving from left to right in the periodic table the following points have to be mentioned.

The use of adequate basis set size is echoed throughout this project when studying complexes containing the second row elements; possibly the inclusion of diffuse functions for providing a better description of the bonding region when complexation occurs would be helpful. This study focused solely on the use of the 6-31G** basis set, due to limitations of CPU resources and for completeness in order to make a reasonable comparison with the different complexes. The calculation of the BSSE by means of the Boys and Bernardi method is still commonly used, despite criticisms from many theoreticians. The Morokuma decomposition analyses further provide vital information regarding the different energy components responsible for the SCF interaction energy. However, the energy terms determined are of qualitative use only since there is a neglect of correlation effects and the Pauli exclusion principle is violated

in the determination of the polarisation term.

The Mulliken charge analysis provides reasonable qualitative information regarding the direction of charge flow on complexation, however one needs also to bear in mind that the determination of the Mulliken charges involves the averaging of the charges on the atoms rather than the determination of each atomic charge uniquely.

Our calculated vibrational wavenumbers were not scaled to account for anharmonic effects, nevertheless our experimental wavenumber shifts compared fairly well with those predicted theoretically. In addition it is worth noting that the new systems studied theoretically viz., $CH_4.H_2S$, $CH_4.PH_3$, $SiH_4.H_2S$ and $SiH_4.YH_3$ also followed similar trends to those systems already studied, emphasising the importance of using consistent levels of theory and basis sets.

Experimentally, new complexes viz., $(CH_4)_2$, $CH_4.NH_3$ and $CH_4.H_2S$ have been identified under cryogenic conditions. It should be emphasised that the experimental matrix isolation studies were confined to the hydrides CH_4, HCl, NH_3 and H_2S simply because of their ready availability and their relative ease of handling. Further, in the experimental section of this project the following point has to be mentioned. The matrix isolation technique provides the ideal medium for molecular interactions to be studied in inert gas matrices, despite the presence of matrix cage effects resulting in band splitting and multiple site trapping. These effects are small, however, and are identified by varying the concentrations of the matrix and absorber species.

Finally, despite the shortcomings of the theoretical model, we have found excellent agreement between theory and experiment in this project.

References

1. P. Hobza and R. Zahradnik, "Intermolecular Complexes, The Role of van der Waals systems in Physical Chemistry and in the Biodisciplines", Elsevier, Amsterdam, 1988.
2. M.D. Joesten and L.J. Schaad, "Hydrogen Bonding", Marcel Dekker, Inc., New York, 1974.
3. M. Rigby, E.B. Smith, W.A. Wakeham and G.C. Maitland, "The Forces Between Molecules", Oxford Science Publications, Clarendon Press, Oxford, 1986.
4. G.C. Maitland, M. Rigby, E.B. Smith and W.A. Wakeham, "Intermolecular Forces, Their Origin and Determination", Oxford Science Publications, Clarendon Press, Oxford, 1981.
5. I.G. Kaplan, "Theory of Molecular Interactions", Elsevier, Amsterdam, 1986.
6. J. Laane, M. Dakkouri, B. van der Veken and H. Oberhammer, "Structures and Conformations of Non-Rigid Molecules", Kluwer Academic Publishers, Dordrecht, 1992.
7. W.M. Latimer and W.H. Rodebush, J. Am. Chem. Soc., *42*, 1419 (1920).
8. G.C. Pimentel and A.L. McClellan, "The Hydrogen Bond", W.H. Freeman and Company, San Francisco, 1960.
9. N.B. Colthup, L.H. Daly and S.E. Wiberly, "Introduction to Infrared and Raman Spectroscopy", 2nd edition, Academic Press, New York, 1975, (a) pp. 459-462, (b) p. 469, (c) pp. 473-476
10. K. Morokuma, Acc. Chem. Res., *10*, 294 (1977).
11. H.A. Benesi and J.H. Hildebrand, J. Am. Chem. Soc., *71*, 2703 (1949).
12. R.S. Mulliken and W.B. Person, Ann. Rev. Phys. Chem., *13*, 107 (1962).
13. D.J. Wales, Mol. Phys., *74*, 1 (1991).
14. T.R. Dyke, B. Howard and W. Klemperer, J. Chem. Phys., *56*, 2442 (1972).
15. S.E. Novick, K.C. Janda, S.L. Holmgren, M. Waldman and W. Klemperer, J.

Chem. Phys., *65*, 114 (1976).

16. A.J. Stone, Chem. Phys. Lett., *83*, 233 (1981).
17. A.D. Buckingham and P.W. Fowler, Can. J. Chem., *63*, 2018 (1985).
18. A.D. Buckingham, P.W. Fowler and J.M. Hutson, Chem. Rev., *88*, 963 (1988).
19. A.D. Buckingham and P.W. Fowler, J. Chem. Phys., *79*, 6426 (1983).
20. A.C. Legon and D.J. Millen, Faraday Disc. Chem. Soc., *73*, 71 (1982).
21. A.C. Legon and D.J. Millen, Acc. Chem. Res., *20*, 39 (1987).
22. V. Magnasco and R. McWeeny, "Weak Interactions between Molecules and their Physical Interpretation", Theoretical Models of Chemical Bonding, Part 4, Z.B. Maksic (editor), Springer-Verlag, Berlin , 1991, pp. 134-169.
23. P. Schuster, G. Zundel and C. Sandorfy, " The Hydrogen Bond, Vol.II, Structure and Spectroscopy", North-Holland Publishing Company, Amsterdam, 1976, pp. 395-400.
24. Z. Kisiel, A.C. Legon and D.J. Millen, J. Chem. Phys., *78*, 2910 (1983).
25. A.C. Legon, D.J. Millen and O. Schrems, J. Chem. Soc., Faraday Trans. 2, *75*, 592 (1979).
26. T.J. Balle, E.J. Campbell, M.R. Keenan and W.H. Flygare, J. Chem. Phys., *71*, 2623 (1979).
27. A.C. Legon, J. Chem. Phys., *87*, 2064 (1983).
28. E. Whittle, D.A. Dows and G.C. Pimentel, J. Chem. Phys., *22*, 1943 (1954).
29. E. Knözinger and O. Schrems, "Vibrational Spectra and Structures, A Series of Advances", Vol. 16, J.R. Durig (editor), Elsevier Scientific Publishing Company, New York, 1987, pp. 141-225.
30. A.J. Barnes, W.J. Orville-Thomas, A. Muller and R. Gaufres, " Matrix Isolation Spectroscopy", D. Reidel Publishing Company, Dordrecht, 1980.
31. S. Cradock and A.J. Hinchcliffe, "Matrix Isolation", Cambridge University Press,

London, 1975.

32. E. Schrödinger, Ann. Physik., *79*, 361 (1926).
33. N.L. Allinger and U. Burkert, " Molecular Mechanics", ACS Monographs Series, Washington, D.C., 1982.
34. N.L. Allinger, J. Am. Chem. Soc., *99*, 8127 (1977).
35. D. Feller and E.R. Davidson in " Reviews in Computational Chemistry", edited by K.B. Lipkowitz and D.B. Boyd, VCH Publishers Inc, New York, 1990, pp. 1-37.
36. M.J.S. Dewar and W. Thiel, J. Am. Chem. Soc., *99*, 4899 (1977).
37. M. Born and J.R. Oppenheimer, Ann. Physik., *84*, 457 (1927).
38. T. Clark, "A Handbook of Computational Chemistry: A Practical Guide to Chemical Structure and Energy Calculations", John Wiley and Sons., New York, 1985, (a) p.12, (b) p. 233.
39. T. Clark in "Recent Experimental and Computational Advances in Molecular Spectroscopy", edited by R. Fausto, Kluwer Academic Publishers, Dordrecht, 1992, p. 369.
40. H.C. Urey and C.A. Bradley, Phys. Rev., *38*, 1969 (1931).
41. J.P. Stewart in "Reviews in Computational Chemistry", edited by K.B. Lipkowitz and D.B. Boyd, VCH Publishers Inc, New York, 1990, pp. 45-78.
42. J.A. Pople, D.P. Santry and G.A. Segal, J. Chem. Phys., *43*, 5129 (1965).
43. J.A. Pople and G. A. Segal, J. Chem. Phys., *43*, 5136 (1985).
44. J.A. Pople, D.L. Beveridge and P.A. Dobosh, J. Chem. Phys., *46*, 2026, (1967).
45. L. Visscher, O. Visser, P.J.C. Aerts, H. Merenga and W.C. Nieuwpoort, Comp. Phys. Commun., *81*, 120 (1994).
46. W.J. Hehre, L. Radom, P.von R. Schleyer and J.A. Pople, " *Ab Initio*

Molecular Orbital Theory", John Wiley and Sons, Inc., New York, 1986, (a) pp. 17-21, (b) pp. 7-18, (c) p. 172, (d) pp. 72-88, (e) pp. 38-40.

47. C. Møller and M.S. Plesset, Phys. Rev., *46*, 618 (1934).
48. C.E. Dykstra, "Quantum Chemistry and Molecular Spectroscopy", Prentice Hall, Englewood Cliffs, New Jersey, 1991, (a) p. 278, (b) p. 282.
49. C.C.J. Roothaan, Rev. Mod. Phys., *23*, 69 (1951).
50. G.G. Hall, Proc. Roy. Soc., A,*205*, 541 (1951).
51. S.F. Boys, Proc. Roy. Soc., A,*200*, 542 (1950).
52. J.C. Slater, Phys. Rev., *34*, 1293 (1929).
53. S.F. Boys and F. Bernardi, Mol. Phys., *19*, 553 (1970).
54. D. Hirst, "A Computational Approach to Chemistry", Blackwell Scientific Publishers, Oxford, 1990, pp. 10-20.
55. N.R. Kestner, M.D. Newton and E.L. Mathers, Int. J. Quant. Chem. Quant. Symp., *17*, 431 (1983).
56. D.W. Schwenke and D.G. Truhlar, J. Chem. Phys., *82*, 2418 (1985).
57. M.D. Newton, J. Chem. Phys., *87*, 4288 (1983).
58. M. Allavena, B. Silvi and J. Capriani, J. Chem. Phys., *76*, 4573 (1982).
59. Z. Latajka and S. Scheiner, J. Chem. Phys., *81*, 407 (1984).
60. M.M. Szczesniak and S. Scheiner, J. Chem. Phys., *84*, 6328 (1986).
61. W. Kolos, Theor. Chim. Acta., *51*, 219 (1979).
62. A. Fadini and F. M. Schnepel, " Vibrational Spectroscopy : Methods and Application", Ellis Horwood Publishers, Chichester, 1989, p. 16.
63. W.W Coblentz, "Investigation of the IR Spectra", Carnegie, Washington, 1962.
64. A. Smekal, Natuurwissenschaften, *43*, 873 (1923).
65. C.V. Raman and K.S. Krishnan, Nature., *121*, 501 (1928).
66. A.P. Scott and L. Radom, J. Phys. Chem., *100*, 16502 (1996).

67. P. Gans, "Vibrating Molecules: An Introduction to the Interpretation of Infrared and Raman Spectra", Chapman and Hall, London, 1971, (a) p. 87, (b) p. 92.

68. J.H. Schachtschneider, " Vibrational Analysis of Polyatomic Molecules", Vol. VI, Shell Development Company Report, Emeryville, CA, 1964.

69. M. Diem, " Introduction to Modern Vibrational Spectroscopy", John Wiley and Sons, New York, 1993, p. 65.

70. E.B. Wilson, Jr, J.C. Decius and P.C. Cross, " Molecular Vibrations: Theory of Infrared and Raman Vibrational Spectra", McGraw-Hall Company, New York, 1955.

71. J.E. Del Bene, J. Comp. Chem., *10*, 603 (1989).

72. W.J. Lafferty, R.D. Suenram and F.J. Lovas, J. Mol. Spect., *123*, 434 (1987).

73. B.J. Howard, T.R. Dyke and W. Klemperer, J. Chem. Phys., *81*, 5417 (1984).

74. H.S. Gutowsky, C. Chuang, J.D. Keen, T.D. Klots and T. Emilsson, J. Chem. Phys., *83*, 2070 (1985).

75. K. von Puttkamer and M. Quack, Mol. Phys., *62*, 1047 (1987).

76. K. von Puttkamer, M. Quack and M.A. Suhm, Mol. Phys., *65*, 1025 (1988).

77. M. Quack and M.A. Suhm, Chem. Phys. Lett., *171*, 517 (1990).

78. M. Quack and K. von Puttkamer, Chem. Phys., *139*, 31 (1989).

79. A.S. Pine and W.J. Lafferty, J. Chem. Phys., *78*, 2154 (1983).

80. A.S. Pine, W.J. Lafferty and B.J. Howard, J. Chem. Phys., *81*, 2939 (1984).

81. A.S. Pine and G.T. Fraser, J. Chem. Phys., *89*, 6636 (1988).

82. E.J. Bohac and R.E. Miller, J. Chem. Phys., *99*, 1537 (1993).

83. A.S. Pine and B.J. Howard, J. Chem. Phys., *84*, 590 (1986).

84. C. Laush and J.M. Lisy, J. Chem. Phys., *101*, 7480 (1994).

85. C. Laush, J.M. Lisy, F. Huisken and A. Kulcke, J. Chem. Phys., *98*, 5982 (1993).

86. D.T. Anderson, S. Davis and D.J. Nesbitt, J. Chem. Phys., *104*, 6225 (1996).

87. L. Andrews and G.L. Johnson, J. Phys. Chem., *88*, 425 (1984).

88. L. Andrews, J.H. English and V.E. Bondybey, J. Chem. Phys., *81*, 3452 (1984).

89. L. Andrews and R.D. Hunt, J. Phys. Chem., *92*, 81 (1988).

90. L. Andrews, S.R. Davis and R.D. Hunt, Mol. Phys., *77*, 993 (1992).

91. L. Andrews, J. Phys. Chem., *88*, 2940 (1984).

92. D.W. Michael, C.E. Dykstra and J.M. Lisy, J. Chem. Phys., *81*, 5998 (1984).

93. P. Jensen, P.R. Bunker, A. Karpfen, M. Kofranek and H. Lischka, J. Chem. Phys., *93*, 6266 (1990).

94. M.J. Frisch, J.E. Del Bene, J.S. Binkley and H.F. Schaefer III, J. Chem. Phys., *84*, 2279 (1986).

95. S.K. Loushin, S. Liu and C.E. Dykstra, J. Chem. Phys., *84*, 2720 (1986).

96. J.E. Del Bene, J. Chem. Phys., *86*, 2110 (1987).

97. M.J. Redmon and J.S. Binkley, J. Chem. Phys., *87*, 969 (1987).

98. P.R. Bunker, M. Kofranek, H. Lischka and A. Karpfen, J. Chem. Phys., *89*, 3002 (1988).

99. S.C. Racine and E.R. Davidson, J. Phys. Chem., *97*, 6367 (1993).

100. D.H. Zhang and J.Z.H. Zhang, J. Chem. Phys., *99*, 6624 (1993).

101. K.A. Peterson and T.H. Dunning, jr, J. Chem. Phys., *102*, 2032 (1995).

102. A. Beyer and A. Karpfen, Chem. Phys., *64*, 343 (1982).

103. Y. Hannachi, B. Silvi and Y. Boutellier, J. Chem. Phys., *97*, 1911 (1992).

104. D.M. Bishop, J. Pipin and B. Kirtman, J. Chem. Phys., *102*, 6778 (1995).

105. D.H. Zhang, Q. Wu, J.Z.H. Zhang, M. von Dirke and Z. Bacic, J. Chem. Phys., *102*, 2315 (1995).

106. W.A. Sokalski, P.C. Hariharan and J.C. Kaufman, J. Phys. Chem., *87*, 2803 (1983).

107. J.D. Dill, L.C. Allen, W.C. Topp and J.A. Pople, J. Am. Chem. Soc., *97*, 7220 (1975).

108. P. Kollman, J. McKelvey, A. Johansson and S. Rothenberg, J. Am. Chem. Soc., *97*, 955 (1975).

109. W.C. Topp and L.C. Allen, J. Am. Chem. Soc., *96*, 5291 (1974).

110. M. Kofranek, H. Lischka and A. Karpfen, Chem, Phys., *121*, 137 (1988).

111. D.R. Yarkony, S.V. O'Neal, H.F. Schaefer III, C.P. Baskin and C.F. Bender J. Chem. Phys., *60*, 855 (1974).

112. H.-C. Chang and W. Klemperer, J. Chem. Phys., *100*, 1 (1994).

113. D.T. Anderson, S. Davis and D.J. Nesbitt, J. Chem. Phys, *105*, 4488 (1996).

114. N. Ohashi and A.S. Pine, J. Chem. Phys., *81*, 73 (1984).

115. A.S. Pine and B.J. Howard, J. Chem. Phys., *84*, 590 (1986).

116. B. Katz, A. Ron and O. Schnepp, J. Chem. Phys., *47*, 5303 (1967).

117. A.J. Barnes, H.E. Hallam and G.F. Scrimshaw, Trans. Faraday Soc., *65*, 3159 (1969).

118. C. Girardet, D. Maillard, A. Schriver and J.P. Perchard, J. Chem. Phys., *67*, 3917 (1977).

119. D. Maillard, A. Schriver, J.P. Perchard, C. Girardet and D. Robert, J. Chem. Phys., *70*, 1511 (1979).

120. D. Maillard, A. Schriver, J.P. Perchard and C. Girardet, J. Chem. Phys., *71*, 505 (1979).

121. A. Furlan, S. Wulfert, A.R.W. McKellar and J.W.C. Johns, J. Mol. Spect., *138*, 282 (1989).

122. P.C. Gomez and P.R. Bunker, J. Mol. Spect., *168*, 507 (1994).

123. P.C. Gomez, P.R. Bunker, A. Karpfen and H. Lischka, J. Mol. Spect., *166*, 441 (1994).

124. P.R. Bunker, V.C. Epa, P. Jensen and A. Karpfen, J. Mol. Spect., *146*, 200 (1991).

125. S.C. Althorpe, D.C. Clary and P.R. Bunker, Chem. Phys. Lett., *187*, 35 (1991).

126. M.D. Schuder, C.M. Lovejoy, R. Lascola and D.J. Nesbitt, J. Chem. Phys., *99*, 4346 (1993).

127. M.J. Frisch, J.A. Pople and J. Del Bene, J. Phys. Chem., *89*, 3664 (1985).

128. R.M. Bentwood, A.J. Barnes and W.J. Orville-Thomas, J. Mol. Spect., *84*, 391 (1980).

129. M. van Thiel, E.D. Becker and G.C. Pimentel, J. Chem. Phys., *27*, 486 (1957).

130. G.P. Ayers and A.D.E. Pullin, Spectrochim. Acta, *32A*, 1629 (1976).

131. G.P. Ayers and A.D.E. Pullin, Spectrochim. Acta, *32A*, 1695 (1976).

132. L. Fredin, B. Nelander and G. Ribbegard, J. Chem. Phys., *66*, 4065 (1977).

133. D.F. Coker, R.E. Miller and R.O. Watts, J. Chem. Phys., *82*, 3554 (1985).

134. R.H. Page, J.G. Frey, Y.-R. Shen and Y.T. Lee, Chem. Phys. Lett., *106*, 373 (1984).

135. J.A. Odutola and T.R. Dyke, J. Chem. Phys., *72*, 5062 (1980).

136. L.A. Curtiss, D.J. Frurip and M. Blander, J. Chem. Phys., *71*, 2703 (1979).

137. K. Kim and K.D. Jordan, J. Phys. Chem., *98*, 10089 (1994).

138. J.E. Del Bene, W.B. Person and K. Szczepaniak, J. Phys. Chem., *99*, 10705 (1995).

139. J.E. Del Bene, J. Phys. Chem., *92*, 2874 (1988).

140. B. van Hensbergen, R. Block and L. Jensen, J. Chem. Phys., *76*, 3161 (1982).

141. K. Morokuma and H. Umeyama, J. Am. Chem. Soc., *99*, 1316 (1977).

142. K. Morokuma, Acc. Chem. Res., *10*, 294 (1977).

143. P.O. Astrand, G. Karlström, A. Engdahl and B. Nelander, J. Chem. Phys., *102*, 3534 (1995).

144. J. Kim, J. Yong, Y. Lee, S. Lee, B.J. Mhin and K.S. Kim, J. Chem. Phys., *102*, 310 (1995).

145. C.J. Marsden, B.J. Smith, J.A. Pople, H.F. Schaefer III and L. Radom, J. Chem. Phys., *95*, 1825 (1991).

146. F.F. Muguet, G.W. Robinson and M.P. Bassez-Muguet, Int. J. Quant. Chem., *39*, 449 (1991).

147. G. de Oliviera and C.E. Dykstra, J. Mol. Struct. (Theochem), *337*, 1 (1995).

148. J.G.C.M. van Duijneveldt-van de Rijdt and F.B. van Duijneveldt, J. Chem. Phys., *97*, 5019 (1992).

149. A.D. Buckingham., J. Mol. Struct., *250*, 111 (1991).

150. S.C. Althorpe and D.C. Clary, J. Chem. Phys., *101*, 3603 (1994).

151. S.M. Cybulski and S. Scheiner, J. Phys. Chem., *93*, 6565 (1989).

152. Y.-B Wang, F.-M. Tao and Y.-H. Pan, J. Mol. Struct. (Theochem), *309*, 235 (1994).

153. K. Szalewicz, S.J. Cole, W. Kolos and R.J. Bartlett, J. Chem. Phys., *89*, 3662 (1988).

154. S.J. Chakravorty and E.R. Davidson, J. Phys. Chem., *97*, 6373 (1993).

155. K.L. Busarow, R.C. Cohen, G.A. Blake, K.B. Laughlin, Y.T. Lee and R.J. Saykally, J. Chem. Phys., *90*, 3937 (1989).

156. J.A. Odutola, R. Viswanathan and T.R. Dyke, J. Am. Chem. Soc., *101*, 4787 (1979).

157. T. Pradeep and C.N.R. Rao, Chem. Phys. Lett., *185*, 496 (1991).

158. M. Sodupe, A. Oliva and J. Bertran, J. Am. Chem. Soc., *117*, 8416 (1995).

159. B. Nelander, J. Chem. Phys., *69*, 3870 (1978).

160. U.P. Agarwal, A. J. Barnes and W.J. Orville-Thomas, Can. J. Chem., *63*, 1705 (1985).

161. E.L. Woodbridge, T.-L. Tso, M.P. McGrath, W.J. Hehre and E.K.C. Lee, J. Chem. Phys., *85*, 6991 (1986).

162. P.F. Fernandez, J.V. Ortiz and E.A. Walters, J. Chem. Phys., *84*, 1653 (1986).

163. J.R. Sabin, J. Am. Chem. Soc., *93*, 3613 (1971).

164. G. de Oliviera and C. E. Dykstra, J. Mol. Struct. (Theochem), *362*, 275 (1996).

165. G.C. Pimentel, M.O. Bulanin and M. van Thiel, J. Chem. Phys., *36*, 500 (1961).

166. G. Ribbegard, Chem. Phys., *8*, 185 (1975).

167. S. Suzer and L. Andrews, J. Chem. Phys., *87*, 5131 (1987).

168. J.P. Perchard, R.B. Bohn and L. Andrews, J. Phys. Chem., *95*, 2707 (1991).

169. G.A. Yeo and T.A. Ford, Struct. Chem., *3*, 75 (1992).

170. A.J. Barnes, J. Mol. Struct., *237*, 19 (1990).

171. T. Nishiya, N. Hirota, H. Shinohar and N. Nishi, J. Phys. Chem., *89*, 2260 (1985).

172. D. Nelson, G.T. Fraser and W. Klemperer, J. Chem. Phys., *63*, 6201 (1985).

173. J.A. Odutola, T.R. Dyke, B.J. Howard and J.S. Muenter, J. Chem. Phys., *70*, 4884 (1979).

174. G.T. Fraser, D. Nelson, A. Charo and W. Klemperer, J. Chem. Phys., *82*, 2536 (1984).

175. D. Nelson, G.T. Fraser, W. Klemperer, F.J. Lovas and R.D. Suenram, J. Chem. Phys., *87*, 6364 (1987).

176. F. Carnovale, J.B. Peel and R.G. Rothwell, J. Chem. Phys., *85*, 6261 (1986).

177. M. Havenith, H. Linnartz, E. Zwart, A. Kips, J.J. ter Meulen and W.L. Meerts, Chem. Phys. Lett., *193*, 261 (1992).

178. J.G. Loeser, C.A. Schmuttenmaer, R.C. Cohen, M.J. Elrod, D.W. Steyert, R.J. Saykally, R.E. Bumgarner and G.A. Blake, J. Chem. Phys., *97*, 4727 (1992).

179. M. Havenith, R.C. Cohen, K.L. Bon, D.-H. Gwo, Y.T. Lee and R.J. Saykally, J. Chem. Phys., *44*, 4776 (1991).

180. H. Linnartz, W.L. Meerts and M. Havenith, Chem. Phys., *193*, 327 (1995).

181. P.A. Kollman and L.C. Allen, J.Am.Chem. Soc., *93*, 4991 (1971).

182. G.A. Yeo and T.A. Ford, J. Mol. Struct., *141*, 331 (1986).

183. G.A. Yeo and T.A. Ford, J. Mol. Struct., *266*, 183 (1992).

184. G.A..Yeo and T.A. Ford, S. Afr. J. Chem., *39*, 243 (1986).

185. Z. Latajka and S. Scheiner, J. Chem. Phys., *84*, 341 (1986).

186. K.P. Sagarik, R. Ahlrichs and S. Brode, Mol. Phys., *57*, 1247 (1986).

187. D.M. Hasset, C.J. Marsden and B.J. Smith, Chem. Phys. Lett., *183*, 449 (1991).

188. S.-Y. Liu, C.E. Dykstra, K. Kolenbrander and J.M. Lisy, J. Chem. Phys., *85*, 2077 (1986).

189. J.W.I. van Bladel, A. van der Avoird and P.E.S. Wormer, J. Chem. Phys., *97*, 4750 (1992).

190. D. Nelson and W. Klemperer, J. Chem. Phys., *87*, 139 (1987).

191. A. van der Avoird, E.H.T. Olthof and P.E.S. Wormer, Faraday Discuss. Chem. Soc., *97*, 43 (1994).

192. E.H.T. Olthof, A. van der Avoird, P.E.S. Wormer, J.G. Loeser and R.J. Saykally, J. Chem. Phys., *101*, 8443 (1994).

193. E.H.T. Olthof, A. van der Avoird and P.E.S. Wormer, J. Chem. Phys., *101*, 8430 (1994).

194. F.-M. Tao and W. Klemperer, J. Chem. Phys., *99*, 5976 (1993).

195. S.M. Cybulski, Chem. Phys. Lett., *228*, 451 (1994).

196. J.H. Rigby, E.B. Smith and J.H. Dymond, J. Chem. Phys., *42*, 2801 (1965).

197. J.J. Novoa, M.H. Whangbo and J.H. Williams, J. Chem. Phys., *94*, 4835 (1991).

198. Y. Nagy, D.F. Weaver and V.H. Smith, jr, Mol. Phys., *85*, 1179 (1995).

199. D.E. Williams and D.J. Craycroft, J. Phys. Chem., *91*, 6365 (1987).

200. M.M. Szczesniak, G. Chalasinski, S.M. Cybulski and S. Scheiner, J. Chem. Phys., *93*, 4243 (1990).

201. S. Tsuzuki and K. Tanabe, J. Phys. Chem., *95*, 2272 (1991).

202. B.J. Palmer and J.L. Anchell, J. Phys. Chem., *99*, 12239 (1995).

203. B.P. Reid, M.J. O'Loughlin and R.K. Sparks, J. Chem. Phys., *83*, 5656 (1985).

204. M. Snels and R. Fantoni, Chem. Phys., *109*, 67 (1986).

205. J.W.I. van Bladel and A. van der Avoird, J. Chem. Phys., *92*, 2837 (1990).

206. K.C. Janda, J.M. Steed, S.E. Novick and W. Klemperer, J. Chem. Phys., 67, 5162 (1977).

207. C. Girardet, A. Schriver and D. Maillard, Mol. Phys., *41*, 779 (1980).

208. M.M. Szczesniak and P. Hobza, J. Phys. Chem., *87*, 2608 (1983).

209. R.M. Bentwood, M.P. Wright and A.J. Barnes, J. Mol. Struct., *118*, 97 (1984).

210. B. Nelander, J. Chem. Phys., *69*, 3870 (1978).

211. R.D. Amos, Chem. Phys., *104*, 145 (1986).

212. A. Les, Theor. Chim. Acta., *66*, 375 (1985).

213. P.G. Del Conde and O.A. Novaro, Theor. Chim. Acta., *51*, 79 (1979).

214. J.W. Bevan, A.C. Legon, D.J. Millen and S.C. Rogers, J. Chem. Soc., Chem. Comm., 341 (1975).

215. J.W. Bevan, Z. Kisiel, A.C. Legon, D.J. Millen and S.C. Rogers, Proc. Roy. Soc., *A372*, 441 (1980).

216. A.C. Legon, D.J. Millen and H.M. North, Chem. Phys. Lett., *135*, 303 (1987).

217. R.K. Thomas, Proc. Roy. Soc., *A344*, 579 (1975).

218. L. Andrews and G.L. Johnson, J. Chem. Phys., *79*, 3670 (1983).

219. G. Cazzoli, P.G. Favero, D.G. Lister, A.C. Legon and D.J. Millen, Chem. Phys. Lett., *117*, 543 (1985).

220. Y. Hannachi, B. Silvi and Y. Boutellier, J. Chem. Phys., *94*, 2915 (1991).

221. Z. Latajka and S. Scheiner, J. Chem. Phys., *87*, 5928 (1987).

222. K. Somasundaram, R.D. Amos and N.C. Handy, Theor. Chim. Acta., *69*, 491 (1986).

223. M.M. Szczesniak, S. Scheiner and Y. Boutellier, J. Chem. Phys., *81*, 5024 (1984).

224. A. Hinchliffe, J. Mol. Struct., *106*, 361 (1984).

225. A.C. Legon and D.J. Millen, Chem. Rev., *86*, 635 (1986).

226. B.S. Ault and G.C. Pimentel, J. Chem. Phys., *77*, 57 (1973).

227. G.P. Ayers and A.D.E. Pullin, Spectrochim. Acta, *32A*, 1641 (1976).

228. A. Schriver, B. Silvi, D. Maillard and J.P. Perchard, J. Phys. Chem., *81*, 2095 (1977).

229. A.C. Legon and L.C. Willoughby, Chem. Phys. Lett., *69*, 280 (1980).

230. G.B. Bacskay, Mol. Phys., *77*, 61 (1992).

231. P. Cope, D.J. Millen and A.C. Legon, J. Chem. Soc., Faraday Trans. 2, *82*, 1189 (1986).

232. Y. Boutellier, M. Allavena and J.M. Leclercq, Chem. Phys. Lett., *84*, 361 (1981).

233. R. Viswanathan and T.R. Dyke, J. Chem. Phys., *77*, 1166 (1982).

234. L.C. Willoughby, A.J. Fillery-Travis and A.C. Legon, J. Chem. Phys., *81*, 20 (1984).

235. R.T. Arlinghaus and L. Andrews, Inorg. Chem., *24*, 1523 (1985).

236. S. Scheiner, J. Chem. Phys., *78*, 599 (1983).

237. M.M. Szczesniak and S. Scheiner, J. Chem. Phys., *83*, 1778 (1985).

238. U.C. Singh and P.A. Kollman, J. Chem. Phys., *80*, 353 (1984).

239. E.J. Goodwin and A.C. Legon, J. Chem. Soc., Faraday Trans. 2, *80*, 51 (1984).

240. Y. Boutellier, Z. Latajka, H. Ratajczak and S. Scheiner, J. Chem. Phys., *94*, 2956 (1991).

241. L. Andrews, Faraday Discuss. Chem. Soc., *86*, 37 (1988).

242. L. Andrews, J. Mol. Struct., *173*, 103 (1988).

243. G.L. Johnson and L. Andrews, J. Am. Chem. Soc., *104*, 3043 (1982).

244. P. Goldfinger and G. Verhaegen, J. Chem. Phys., *50*, 1467 (1968).

245. N.W. Howard and A.C. Legon, J. Chem. Phys., *88*, 4694 (1988).

246. B.S. Ault and G.C. Pimentel, J. Phys. Chem., *77*, 1649 (1973).

247. A.J. Barnes, T.R. Beech and Z. Mielke, J. Chem. Soc., Faraday Trans. 2, *80*, 455 (1984).

248. E. Clementi, J. Chem. Phys., *46*, 3851 (1967).

249. E. Clementi and J. N. Gayles, J. Chem. Phys., *47*, 3837 (1967).

250. R.C. Raffenetti and D.H. Phillips, J. Chem. Phys., *71*, 4534 (1979).

251. Z. Latajka and S. Scheiner, J. Chem. Phys., *81*, 4014 (1984).

252. M.M. Szczesniak, I.J. Kurnig and S. Scheiner, J. Phys. Chem., *89*, 3131 (1988).

253. A.E. Reed, F. Weinhold, L.A. Curtiss and D.J. Pochatko, J. Chem. Phys., *84*, 5687 (1986).

254. G. Corongiu, D. Estrin, G. Murgia, L. Palieri, L. Pisani, J.D. Watts and E. Clementi, Int. J. Quant. Chem., *59*, 119 (1996).

255. R.T. Arlinghaus and L. Andrews, J. Chem. Phys., *81*, 4341 (1984).

256. B. Muller and J. Reinhold, Chem. Phys. Lett., *196*, 363 (1992).

257. Z. Latajka and S. Scheiner, J. Chem. Phys., *81*, 2713 (1984).

258. I.J. Kurnig, M.M. Szczesniak and S. Scheiner, J. Phys. Chem., *90*, 4253 (1986).

259. I.J. Kurnig, M.M. Szczesniak and S. Scheiner, J. Chem. Phys., *87*, 2214 (1987).

260. J.R. Alabart and R. Caballol, Chem. Phys. Lett., *141*, 334 (1987).

261. A.C. Legon and L.C. Willoughby, J. Chem. Soc., Chem. Comm., 997 (1982).

262. A.C. Legon and L.C. Willoughby, Chem. Phys., *74*, 127 (1983).

263. A.C. Legon, B.P. Roberts and A.L. Wallwork, Chem. Phys. Lett., *173*, 107 (1990).

264. Y. Oshima and Y. Endo, J. Chem. Phys., *93*, 6256 (1990).

265. A.J. Barnes, J. Mol. Struct., *100*, 259 (1983).

266. S.R. Davis and L. Andrews, J. Chem. Phys., *86*, 3765 (1987).

267. S.R. Davis and L. Andrews, J. Am. Chem. Soc., *109*, 4768 (1987).

268. S.R. Davis and L. Andrews, J. Phys. Chem., *93*, 1273 (1989).

269. J.S. Craw, R.G.A. Bone and G.B. Bacskay, J. Chem. Soc., Faraday Trans., *89*, 2363 (1993).

270. M.G. Govender and T.A. Ford, S. Afr. J. Chem., *48*, 98 (1995).

271. M.G. Govender and T.A. Ford, J. Mol. Struct. (Theochem), *338*, 141 (1995).

272. G.T. Fraser and R.D. Suenram, J. Chem. Phys., *96*, 7287 (1992).

273. B. Nelander and L. Nord, J. Phys. Chem., *86*, 4375 (1982).

274. A. Engdahl and B. Nelander, J. Chem. Phys., *91*, 6607 (1989).

275. G.A. Yeo and T.A. Ford, Can. J. Chem., *69*, 632 (1991).

276. G.A. Yeo and T.A. Ford, Spectrochim. Acta., *47A*, 485 (1991).

277. Z. Latajka and S. Scheiner, J. Phys. Chem., *94*, 217 (1990).

278. G. Hilpert, G.T. Fraser, R.D. Suenram and E.N. Karyakin, J. Chem. Phys., *102*, 4321 (1995).

279. P.Herbine, T.A. Hu, G. Johnson and T.R. Dyke, J. Chem. Phys., *93*, 5485 (1990).

280. P.A. Stockman, R.E. Bumgarner, S. Suzuki and G.A. Blake, J. Chem. Phys., *96*, 2496 (1992).

281. R.D. Suenram, G.T. Fraser, F.J. Lovas and Y. Kawashima, J. Chem. Phys., *101*, 7230 (1994).

282. L. Dore, R.C. Cohen, C.A. Schmuttenmaer, K.L. Busarow, M.J. Elrod, J.G. Loeser and R.J. Saykally, J. Chem. Phys., *100*, 863 (1994).

283. S.R. Ungemach and H.F. Schaefer III, J. Am. Chem. Soc., *96*, 7898 (1974).

284. D.E. Woon, P. Zeng and D.R. Beck, J. Chem. Phys., *93*, 7808 (1990).

285. J.J. Novoa, B. Tarron, M.H. Whangbo and J.M. Williams, J. Chem. Phys., *95*, 5179 (1991).

286. M.M. Szczesniak, G. Chalsinski, S.M. Cybulski and P. Cieplak, J. Chem. Phys., *98*, 3078 (1993).

287. X. Yan, S. Wang, M. Hodoscek and G.W.A. Milne, J. Mol. Struct. (Theochem),

309, 279 (1994).

288. T. van Mourik and F.B. van Duijneveldt, J. Mol. Struct. (Theochem), *341*, 63 (1995).

289. Z. Latajka and S. Scheiner, J. Comp. Chem., *8*, 674 (1987).

290. P.G. Sennikov, R.I. Sharibdjanov and K.J. Khoudoinazarov, J. Mol. Struct. (Theochem), *270*, 87 (1992).

291. W.A. Sokalski, J. Phys. Chem., *87*, 2803 (1983).

292. M. Orozco and F.J. Luque, J. Mol. Struct. (Theochem), *254*, 31 (1992).

293. R. Fessenden and J.S. Fessenden, Chem. Rev., *61*, 361 (1961).

294. J.J. Watkins, M.D. Sefic and M.A. Ring, Inorg. Chem., *11*, 3146 (1972).

295. A.R. Rossi and J.M. Jasinski, Chem. Phys. Lett., *169*, 399 (1990).

296. B.S. Ault, Inorg. Chem., *20*, 2817 (1981).

297. M.S. Gordon, L.P. Davis and L.W. Burggraf, Chem. Phys. Lett., *163*, 371 (1989).

298. Gaussian 70, W.J. Hehre, W.A. Lathan, M.D. Newton, R. Ditchfield and J.A. Pople, Program No. 236, Quantum Chemistry Program Exchange, Indiana University, Bloomington, IN, 1973.

299. Gaussian 76, J.S. Binkley, R.A. Whiteside, P.C. Hariharan, R. Seeger, W.J. Hehre, M.D. Newton and J.A. Pople, Program No. 368, Quantum Chemistry Program Exchange, Indiana University, Bloomington, IN, 1978.

300. Gaussian 80, J.S. Binkley, R.A. Whiteside, R. Krishnan, R. Seeger, D.J. DeFrees, H.B. Schlegel, S. Topiol, L.R. Kahn and J.A. Pople, Program No. 406, Quantum Chemistry Program Exchange, Indiana University, Bloomington, IN, 1980.

301. Gaussian 82, J.S. Binkley, M.J. Frisch, D.J. DeFrees, K. Raghavachari, R.A. Whiteside, H.B. Schlegel, E.M. Fluder and J.A. Pople, Department of Chemistry, Carnegie-Mellon University, Pittsburgh, PA, 1982.

302. Gaussian 85, R.F. Hout, jr., M.M. Francl, S.D. Kahn, K.E. Dobbs,

E.S. Blurock, W.J. Pietro, D.J. DeFrees, S.K. Pollack, B.A. Levi, R. Steckler and W.J. Hehre, Quantum Chemistry Program Exchange, Indiana University, Bloomington, IN, 1983.

303. Gaussian 86, M.J. Frisch, J.S. Binkley, H.B. Schlegel, K. Raghavachari, C.F. Melius, R.L. Martin, J.J.P. Stewart, F.W. Bobrowicz, C.M. Rohlfing, L.R. Kahn, D.J. DeFrees, R. Seeger, R.A. Whiteside, D.J. Fox, E.M. Fluder and J.A. Pople, Carnegie-Mellon Quantum Chemistry Publishing Unit, Pittsburgh, PA, 1984.

304. Gaussian 88, M.J. Frisch, M. Head-Gordon, H.B. Schlegel, K. Raghavachari, J.S. Binkley, C. Gonzales, D.J. DeFrees, D.J. Fox, R.A. Whiteside, R. Seeger, C.F. Melius, J. Baker, R. Martin, L.R. Kahn, J.J.P. Stewart, E.M. Fluder, S. Topiol and J.A. Pople, Gaussian Inc., Pittsburgh, PA, 1988.

305. Gaussian 90, M.J. Frisch, M. Head-Gordon, G.W. Trucks, J.B. Foresman, H.B. Schlegel, K. Raghavachari, M.A. Robb, J.S. Binkley, C. Gonzalez, D.J. DeFrees, D.J. Fox, R.A. Whiteside, R. Seeger, C.F. Melius, J. Baker, R.L. Martin, L.R. Kahn, J.J.P. Stewart, S. Topiol and J.A. Pople, Gaussian Inc., Pittsburgh, PA, 1990.

306. Gaussian 92, Revision C.4, M.J. Frisch, G.W. Trucks, M. Head-Gordon, P.M. Gill, M.W. Wong, J.B. Foresman, B.G. Johnson, H.B. Schlegel, M.A. Robb, E.S. Replogle, R. Gomperts, R.L. Andres, K. Raghavachari, J.S. Binkley, C. Gonzalez, R.L. Martin, D.J. Fox, D.J. DeFrees, J. Baker, J.J.P. Stewart and J.A. Pople, Gaussian Inc., Pittsburgh, PA, 1992.

307. H.B Schlegel, J. Chem. Phys., *77*, 3676 (1982).

308. B.A. Murtaugh and R.W.H. Sargent, Comp. J., *13*, 185 (1970).

309. S. Huzinaga, Y. Sakai, E. Miyoshi and S. Narita, J. Chem. Phys., *93*, 3319 (1990).

310. W. Kohn and L.J. Sham, Phys. Rev. A., 1133 (1965).

311. J.M. Leclercq, M. Allevana, Y. Boutellier, J. Chem. Phys., *78*, 4606 (1983).

312. G. Alagona, C. Ghio, R. Cammi, J. Tomasi, Int. J. Quantum. Chem., *32*, 227 (1987).

313. J.P. Daudy, P. Claverie , J.P. Malrieu, Int. J. Quant. Chem., *8*, 1 (1974).

314. F.J Olivares del Valle, S. Tolosa, E.A. Ojalvo, J.J. Esperilla, A. Requena, J. Chem. Phys., *84*, 5077 (1986).

315. E.R. Davidson and S.J. Chakravorty, Chem. Phys. Lett., *217*, 48 (1994).

316. H. Umeyama and K. Morokuma, J. Am. Chem. Soc., 99, 1316 (1977).

317. M.R. Peterson and R.A. Poirier, MONSTERGAUSS, University of Toronto, 1981.

318. R.J. Shell and D. Steele, VIBRA90, Department of Chemistry, Royal Holloway and Bedford New College, University of London, 1992.

319. E. Keller, SCHAKAL-92, Kristallographisches Institut der Universitat, Hebelstr. 25, D-7800 Freiburg i. Br., Germany, 1992.

320. J.R. Thomas, B.J. DeLeeuw, G. Vacek, T.D. Crawford, Y. Yamaguchi and H.F. Schaefer III, J. Chem. Phys., 99, 403 (1993).

321. M.D. Harmony, V.W. Laurie, R.L. Kuczkowski, R.H. Schwendeman, D.A. Ramsay, F.J. Lovas, W.J. Lafferty and A.G. Maki, J. Phys. Chem. Ref. Data, 8, 619 (1979).

322. T. Shimanouchi, Tables of Molecular Vibrational Frequencies. Consolidated Vol.I, NSRDS-NBS 39, National Bureau of Standards, Washington, DC, 1972.

323. L.A. Pugh and K.N Rao, in Molecular Spectroscopy: Modern Research, Vol.II, Ed. K.N. Rao, Academic Press, New York, 1976, pp. 165-227.

324. M.A.H. Smith, C.P. Rinsland, B. Fridovich and K.N. Rao, in Molecular Spectroscopy: Modern Research, Vol.III, Ed. K.N. Rao, Academic Press, New York, 1985, pp. 111-248.

325. W.B. Person and J.D. Rogers, Analytiktreffen 1980, Schwingungsspektroskopie, Theorie und Anwendungen, Karl Marx Universität, Leipzig, 1980, pp. 262-300.

326. R.D. Amos, Chem. Phys., 104, 145 (1986).

327. S.J. Cyvin, B.N. Cyvin, I. Elvebredd, G. Hagen and J. Brunvoll, Kgl. Norske Videnskab. Selskab. Skr., 22, 1-14 (1972).

328. S.J. Cyvin, J. Brunvoll, B.N. Cyvin, I. Elvebredd and G. Hagen, Mol. Phys., 14, 43 (1968).

329. I.M. Mills, Theoretical Chemistry, Vol.I, Specialist Periodical Report, Chem. Soc., London, 1974, pp. 59-110.

330. Y. Morino, K. Kuchitsu and S. Yamamoto, Spectrochim. Acta, 24A, 335 (1968).

331. G. Herzberg, Molecular Structure and Molecular Spectra, Vol.II, Infrared and Raman Spectra of Polyatomic Molecules, D.van Nostrand Company, Inc., New York, 1945, pp. 170, 177, 182.

332. G.T. Fraser, J. Chem. Phys., *90*, 2097 (1989).

333. B. Civalleri, E. Garrone and P. Ugliengo, J. Mol. Struct.(Theochem)., *419*, 227 (1997).

334. P. Hobza, Carsky and R. Zahradnik, Coll. Czech. Ch. Com., *44*, 3438 (1979).

335. S. Tolosa and F.J. Olivares del Valle, J. Mol. Struct.(Theochem)., *312*, 109 (1994).

336. Z. Latajka and Y. Boutellier, J. Chem. Phys., *101*, 9793 (1994).

337. J.E. Lowder, L.A. Kennedy, K.G.P. Sulzmann and S.S. Penner, J. Quant. Spect. Radiat. Transf., *10*, 71 (1970).

338. A.J. Barnes and J.D.R. Howells, J. Chem. Soc., Faraday Trans II., *68*, 729 (1972).

339. D.A. Dixon, J. Phys. Chem., *92*, 86 (1988).

340. R.D. Urban and M. Takami, J. Chem. Phys., *102*, 3019 (1995).

341. L.C. Willoughby, Chem. Phys. Lett., *95*, 449 (1983).

342. M.T. Bowers, G.I. Kerly and W.H. Flygare, J. Chem. Phys., *45*, 3399 (1966).

343. J.A. Platts, S.T. Howard and B.R.F. Braeke, J. Am. Chem. Soc., *118*, 2726 (1996).

344. E.L. Coitino, O.N. Ventura and R.M. Sosa, J. Mol. Struct., *254*, 315 (1992).

345. R.F. Hout, B.A. Levi and W.J. Hehre, J. Comp. Chem., *3*, 234 (1982).

346. A. Allerhand and P. von R. Schleyer, J. Am. Chem. Soc., *85*, 1715 (1963).

347. K. Nakamoto, M. Margoshes and R.E. Rundle, J. Am. Chem. Soc., *77*, 6840 (1955).

348. R.M. Badger and S.H. Bauer, J. Chem. Phys., *5*, 839 (1937).

349. B. Nelander, J. Chem. Phys., *82*, 5340 (1985).

350. S.-Y. Tang and C.W. Brown, J. Raman Spec., *2*, 209 (1974).